CRANFIELD UNIVERSITY

SIMON M. WIEDEMANN

DYNAMICS AND CONTROL OF FLEXIBLE ARTICULATED SPACE MANIPULATORS WITH LARGE PAYLOADS

COLLEGE OF AERONAUTICS

PHD THESIS

2002

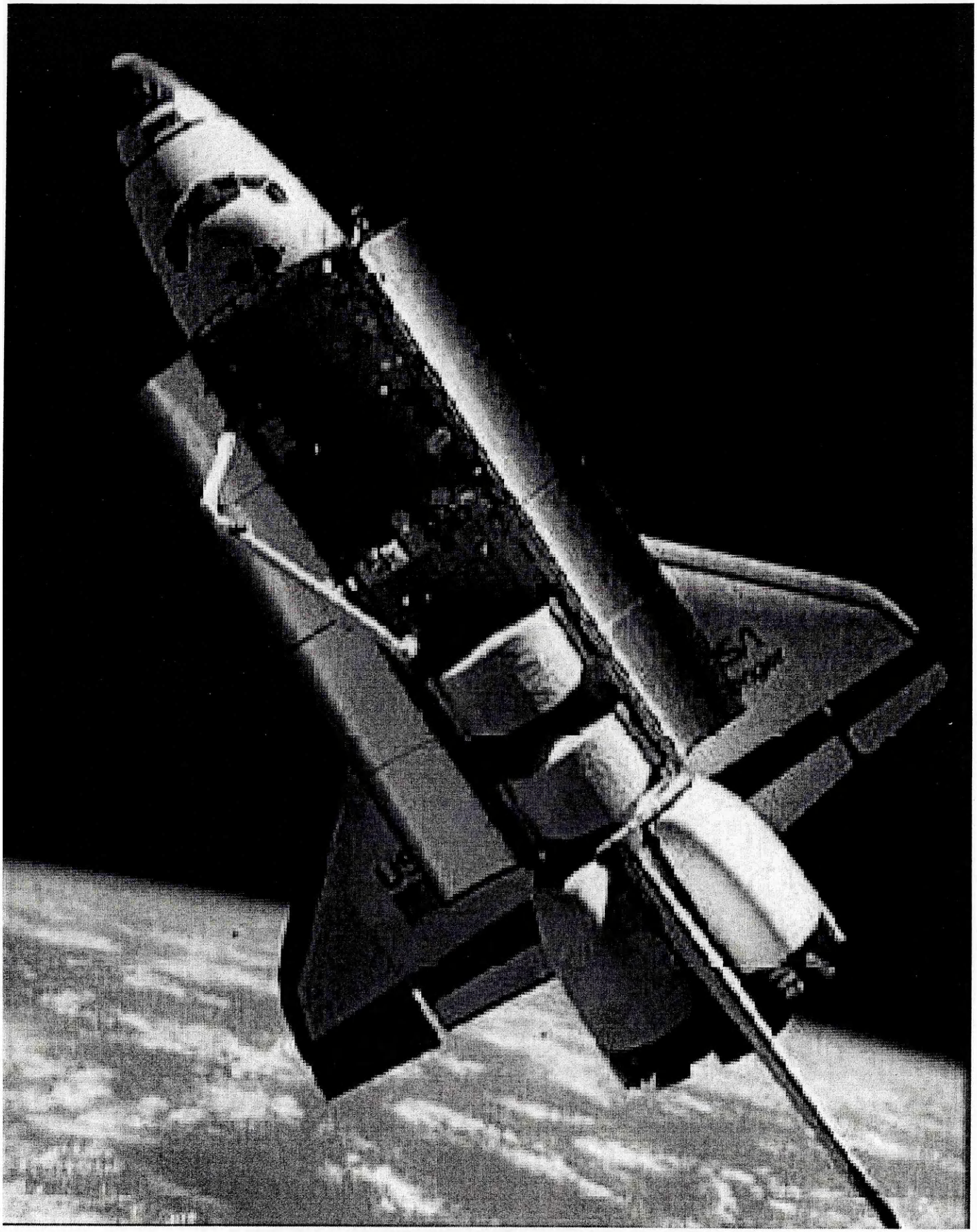

Most of life's failures are people who did not realise
how close they were to success when they gave up.

Thomas Edison

Cranfield University

College of Aeronautics

PhD Thesis

Academic Year 2001

Simon M. Wiedemann

Dynamics and control of flexible articulated space manipulators with large payloads

Supervisor: Prof Colin L. Kirk

March 2002

This thesis is submitted in partial fulfilment of the requirements for the degree of Doctor of Philosophy

ABSTRACT

This thesis studies the dynamics and control of flexible articulated space manipulators with large payloads similar to the Space Shuttle Remote Manipulator System. For dynamic response analyses an exact analytical method to compute natural frequencies and mode shapes of space manipulator systems with varying degrees of complexity is developed.

Dynamic response analyses are performed comparing the results obtained using the exact mode shapes with those obtained when using assumed mode shapes for a series of different manipulator slew manoeuvres and Shuttle thruster firings.

Possible methods for active vibration damping control of the manipulator are discussed, including the methods presented by other researchers. In this thesis it is proposed to use reaction wheels in a closed-loop control scheme, and its advantages and disadvantages compared to other methods are discussed.

The problem of payload capturing and post-capture dynamics are addressed, as well as the dynamics following an emergency braking of the robot. For these cases, a simple method to estimate upper limits of dynamic responses is developed, and results obtained with this method for various example cases are compared with results computed by professional software.

Finally the dynamic responses of a space station to various robot manoeuvres are analysed. These responses can have detrimental effects on micro-gravity and similar experiments. The analyses are performed using a simplified model of the International Space Station and its Mobile Remote Manipulator System.

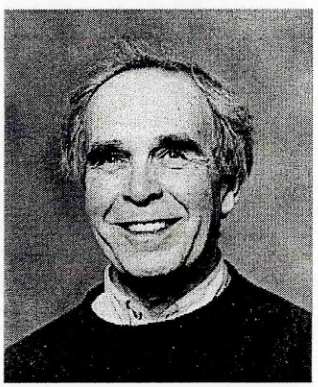

Prof Dr Colin L Kirk

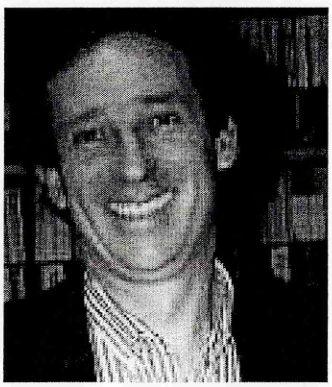

Prof Dr Oskar Wallrapp

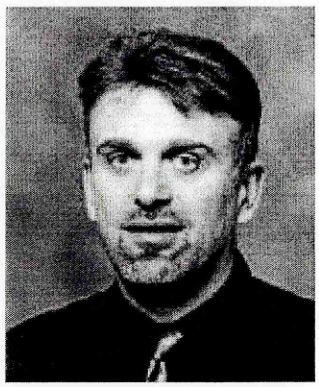

Dr Rade Vignjevic

Think where man's glory begins and ends.
And say my glory was I had such friends.

William Butler Yeats

ACKNOWLEDGEMENT

All the following persons helped in one way or another in order to enable me to come to Cranfield and do this PhD project. I want to say thank you to

- Colin L. Kirk: for the way he has taken interest in this project, for his supervision and his personal friendship. I am deeply indebted, and I hope he has been satisfied with my performance. Everything I know now is due to him. Thank you, Colin.

- Oskar Wallrapp: my admired friend and teacher, who never stopped believing in me, and who introduced me into the wonderful world of flexible bodies. Without his help, his knowledge and his contacts to Cranfield University, I would have never come here.

- Rade Vignjevic: for the computer hardware and software he provided me with.

- Mark, Dave, Jenny, Kristian, Mark, Priah, Richard, Wim and all the others in the PhD offices: for letting me be a part of the group from the very first day I arrived till the day I left.

- my brother Thomas: for his gentle and sensible way of encouraging me. As far as I can remember, he said: "If you do not make use of this chance, I never want to see you again."

- my mother Waltraud: she would always back me up, be it financially or otherwise, if I was in trouble. This gave me the security to start the project without sponsor.

- Barbara, Johannes, Kai, Andreas, Carola, Anders, and all the others back in Germany: I was always welcome whenever I got back for a visit, and I would always find comfort and friendship, being two of the things that kept me going.

- my two very special "buddies" Wolfgang and Odi: Wolfgang in Germany and Odi in Cranfield have always been there for me whenever I got problems, be it technically or personally. They saved me from a lot of stupidities. Thanks, guys.

- Lutz Mauer, Claus Schwientek and the others from the INTEC team: they provided me with a free license for SIMPACK within the boundaries of this PhD project. Without SIMPACK, the verifications of the various results would have been much more difficult or simply impossible.

- the unsung heroes of the various software companies, which are usually forgotten: without such incredible tools like MATHEMATICA, this project could have never been undertaken.

Cranfield, 2001
Simon Wiedemann

TABLE OF CONTENTS

LIST OF FIGURES

CHAPTER 1: INTRODUCTION

In recent years a considerable quantity of research has been devoted to the dynamics and vibration control of single and multi-link robotic manipulators, subjected to disturbances arising from rotational manoeuvres by torque motors about one or more revolute joints. Of particular interest in respect of space research is the vibration of flexible robotic systems, such as the Space Shuttle Remote Manipulator System (in the following, the abbreviation "RMS" indicates a general remote manipulator system, whereas "SRMS" is solely used for the Shuttle Remote Manipulator System) and the Space Station Mobile Remote Manipulator System (MRMS). Such structures are essentially lightweight and hence flexible, in contrast to stiff industrial robots, and can be subject to vibration when performing various manoeuvres in space. This thesis uses the SRMS as the basis for vibration and dynamic analysis, being the only system in actual use.

A sample of the relevant literature is given in [1]-[20], [23], [28], [30]-[38] and for the SRMS in [1]-[10], [25] and [44]. However, most papers give little detailed information about the operation of the SRMS or its dynamic characteristics with the exception of [5], [9] and [69], which give a limited quantity of numerical results. The SRMS is designed by SPAR Aerospace, Toronto, Canada, who appear to be reluctant to release more than superficial technical information.

The major concerns regarding vibration of a robotic manipulator such as the SRMS relate to possible fatigue damage in the drive mechanisms ([1]), such as the high reduction gear trains and damping out residual vibrations following a movement of the payload after a rotational slew or a translation of the extended SRMS / payload, using Shuttle thrusters. Thus during construction, say on the International Space Station (ISS), considerable time can elapse in waiting for residual vibrations to decay ([5], [9]). Hence a study of passive and active, closed-loop damping is essential to reduce the decay time and so enable payloads to be accurately placed. Similarly with the MRMS, bang-bang translations of the payload along the main truss with shoulder joint locked (see figure 1.1) leads to vibrations which can be detrimental to micro-gravity environmental conditions on the Space Station and associated experimental work.

The literature reveals that only two-dimensional planar motion of the SRMS has been considered in vibration analysis. However, flexible multi-body programmes such as SIMPACK are able to analyse three-dimensional motion of multi-link systems. Thus in the present study we consider only planar motion of single, double and triple articulated SRMS type robots with large payloads rigidly attached at the free end, or end effector, allowing for rigid body motion of the Shuttle. Initially however, to simplify the problem, the base of the SRMS is assumed to be attached to an inertially fixed joint but in a later section this joint is allowed to be free and comparison with the two cases is made.

1.1 CONTRIBUTION TO KNOWLEDGE

This thesis studies the following situations of dynamic response of the SRMS and MRMS, as shown in detail in the contents:

1. rotational manoeuvres of the SRMS with various joints free or fixed, using bang-bang control by means of electric motors, comparing the cases of Shuttle fixed against Shuttle free boundary conditions
2. translational manoeuvres with the SRMS / payload extended perpendicular to the payload bay, using Shuttle Vernier thrusters
3. dynamics of the SRMS due to payload / satellite capture ([69])
4. influence of SRMS interactive forces on Shuttle out-of-plane motion
5. dynamic interaction of MRMS and the Space Station.

The major contribution to knowledge in the thesis is the use of the exact eigenvalue analysis of a three-link robot, with two flexible links, yielding exact natural frequencies and mode shapes for use in transient response analyses. This approach does not appear to exist in the current literature, which for a three-link system has been studied by [35] using assumed mode shapes and allowing for planar rigid body Shuttle motion. [35] does not however justify the use of approximate mode shapes by comparing approximate eigenvalues with the exact results as given in this thesis.
A further major contribution is the study of the effect of a wide range of payloads with overhang and various orientations of the three-link RMS with joints free or locked, and the effect on natural frequencies and mode shapes for the first few important modes.
The structure of the thesis is given in section 1.5, but here the general approach to the complex analysis of the three-link system is given.
The classical solution to the Bernoulli-Euler beam with various boundary conditions is well known (see for example [41]). However, when large end masses and rotary inertias are present with torsion springs to represent the effect of mechanically locked joints, the resulting eigenvalue analysis becomes extremely tedious even for a single beam. When a second elastic beam is connected at the elbow joint (see figure 1.1) and a third rigid end effector coupled to a rigid payload is included, the complexity increases by an order of magnitude or more.
It was thus decided to proceed in stages from a single link attached to an inertially fixed base, or shoulder joint, to formulate the eigenvalue determinant and verify the programme against known eigenvalues for simple beams, as for example given in [55].
The next step was to formulate the eigenvalue determinant for two connected elastic beams with a third rigid beam / payload, again with the shoulder joint inertially fixed. This restriction was later removed , allowing the Shuttle to be free.
A search of the literature reveals virtually no information on the vibration response of the SRMS with joints free, locked or a combination of free and locked joints. There is also nothing available on the effect of payload size or SRMS configuration. In this thesis it is shown that with one or more joints free the dynamic response due to step function torques at the joints is negligibly small. This is primarily due to the links then being basically pinned-pinned or pinned-clamped for the payload arm. Thus the natural frequencies are higher than when the joints are locked and thus the dynamic responses are small. With all joints locked we essentially have a cantilever beam with much lower natural frequency and hence larger response. Therefore in this situation the major SRMS vibration response occurs when the system has locked joints, with torsional stiffnesses due to gear box and gear tooth flexure, and this fact has not been

reported in the literature to the author's knowledge. Although details of the SRMS manoeuvre sequences could not be found in the literature [7] states that slews performed by astronaut tele-operation take place with only one joint free at a time. For example the shoulder joint can be fixed with slew taking place about the elbow joint. Alternatively the slew could occur about the wrist joint with the other joints locked. In these situations the dynamic response is greater than with all joints free. This aspect of the subject is again absent in the literature.

For the study of the single link system, the analysis given in [48] and [53] are similar to the single link analysis here, taking account of end payload inertia and mass, shoulder drive or hub inertia and various restraints by springs. The papers however do not relate to the SRMS and [53] considers torsional shaft flexibility between the hub and the motor rotor only and assumes zero overhang of the payload at the free end, where the payload is very small with a mass comparable to that of the flexible link itself. [53] also comments on the use by other workers of approximate mode shapes but makes no comparison of approximate and exact natural frequency results.

This thesis investigates active damping or closed-loop control of vibration in the lowest mode using collocated sensors and reaction wheels mounted near to the ends of the two flexible links. [9] considers active damping of the SRMS with feedback to the epicyclic gear / drive motors. However, this thesis shows that with joints free, which is obviously a requirement for use of the drive motors as active dampers, the vibration levels are very small, hence this method appears to be inapplicable. Few papers consider the use of reaction wheels, but [64] has considered the use of a tip mounted reaction wheel and a proof mass actuator for damping out slew induced vibrations. This thesis shows that reaction wheel damping or any other kind of active damping is only relevant to the case of all joints locked where the SRMS is essentially a series of cantilever beams with additional root torsional springs. Thruster firing is then the major cause of significant flexural oscillation, which is similar to the case of hard capture of a satellite with small relative velocity.

Currently there is no active damping on the SRMS and as far as is known on the MRMS. Probably the main reason is due to the complexity of adding, say, a reaction wheel or wheels to one or more links of the system, and the associated sensors and software. Since vibration is only important with all joints locked, then two reaction wheels mounted near to the free ends of the flexible links will be adequate and that case is considered in the thesis, for motion of the SRMS in its plane of symmetry due to Shuttle thruster firing or satellite capture.

A further significant contribution to knowledge is the comparison of the exact eigenvalues for the single link with large payloads and torsion spring restraints at the shoulder, with approximate methods using assumed mode shapes to represent the link flexibility in the equations of motion. It is shown that Rayleigh's principle is verified if a sufficient number of assumed mode shapes is taken, so that the approximate natural frequencies converge towards the exact values. This fact has not to the author's knowledge been proved for the single link RMS under consideration. Thus use of approximate mode shapes for single or multi-link systems will require many assumed mode shapes. Consequently to avoid the excessive computational burden of using many assumed mode shapes in the equations of motion, the exact mode shapes are used throughout this thesis. Clearly these have to be determined, together with the

exact eigenvalues or natural frequencies, for each case of different payloads and link configurations.
Initially the open-loop response of the SRMS is considered, to obtain information on the likely magnitudes of vibration response. Implementation of active damping using reaction wheels would not require any type of system identification due to the method of using collocated sensors / actuators ([65]) as proposed in this thesis, thus yielding an autonomous closed-loop active damping system.
However, the topic of SRMS system identification has apparently received no attention in the literature except for [9], which confirms the statement made in many SRMS related papers that the payload dimensions are known in practice before operating the SRMS. This thesis therefore gives no consideration to methods of system identification.
The thesis considers planar motion of the SRMS / payload in the plane of symmetry of the Shuttle, assuming that pitch, roll or yaw motion is controlled by Vernier thrusters during translation of the Shuttle / SRMS / payload by longitudinal thrusting, or during rotations of the various SRMS links due to slew manoeuvres.
It is noted however that the SRMS shoulder joint is mounted offset from the Shuttle longitudinal axis at the side of the payload bay. It is also some considerable distance from the Shuttle centre of mass. Thus slew accelerations / decelerations of the payload will give shoulder joint reactions causing rigid body roll, yaw and pitch of the Shuttle. The problem will exist at the end of a slew manoeuvre and if further thruster action is needed to recover the Shuttle initial orientation, which will further excite SRMS vibrations.
One further aspect, for example, is the roll motion produced by elevating the payload about the shoulder joint, which will cause lateral vibration of the SRMS which will not be damped out by a reaction wheel mounted for damping planar vibrations. This extended problem is far more complex than the present treatment and would require multi-axis closed-loop vibration control, which has not been considered in the related literature.
The thesis restricts the analysis only to out-of-plane Shuttle rigid body motion, say roll motion, due to a rigid body RMS slew about the shoulder joint, which provides information of the roll acceleration and the level of RMS / Shuttle interaction.

1.2 SOFTWARE TOOLS

The following software tools were used on a Pentium II processor PC with 266 MHz clock.

MATHEMATICA:
This is a very strong tool for any mathematical application. Since it is capable of handling also symbolic calculations, all the numerical and symbolical results presented in this thesis are computed using the MATHEMATICA code. In particular, all the elements of the various determinants to compute the natural frequencies and mode shapes of a robot with one or more flexible links as well as the elements of the various mass and stiffness matrices for equations of motion are derived with MATHEMATICA.

As one means to check the analytical results, a programme using the finite element method was developed with MATHEMATICA by the author for two-dimensional beam structures. It was however found that due to ill-conditioning of the system matrices, the finite element method could only give the natural frequencies for relatively small payloads, but in these cases the agreement between the analytical and the finite element method results was within the limits of numerical accuracy. As another source of verification the professional finite element programme MSC / NASTRAN (Version 70.5) was used, but here the natural frequencies and mode shapes even for only a single flexible link system were not computed correctly for larger payloads, probably also due to ill-conditioning, and no further attempt was made to set up the more complex configurations. The analytical results are however proven to be correct by various means as shown in the following chapters, and also by using BEAM and SIMPACK.

BEAM and SIMPACK:
Theses two software tools were provided by INTEC GmbH, Wessling, Germany. BEAM is a pre-processor, which allows for the set-up of straight beam structures subject to dynamical and kinematic boundary conditions and the computation of the natural frequencies and mode shapes of such structures.
The data created with BEAM can be used in SIMPACK (**SI**mulation of **M**ulti-body systems **PACK**age), a programme to set up and simulate three-dimensional mutli-body mechanisms, including flexible bodies.
Since BEAM does not allow for the computation of the exact natural frequencies and mode shapes of robot systems as presented in this thesis, verifications of the numerical results of the presented exact solutions and of dynamic response analyses are performed using a relatively large number of assumed mode shapes created with BEAM in SIMPACK. The agreement between the various results serves two purposes, first the verification of the exact solutions and second the comparison with assumed mode shapes approximations as usually used by the various researchers.

1.3 ASSUMPTIONS

In agreement with the majority of the related literature ([5], [9]-[17], [19], [23]-[27], etc.), the following assumption are made for all the following analyses:

- locked gear box drives are approximated as linear torsion springs
- the joints have radii $r_i = 0$ to avoid unnecessary complexity due to offsets from the root of the link to the centre of the motor armature
- the links are assumed to be Bernoulli-beams
- the deflections of the links are small and allow for linearisation, thus they are always perpendicular to the undeformed link axis
- axial deflections of the beams are neglected due to small centrifugal forces for low slew rates
- the payload is rigid
- the centres of mass of the joints are aligned with the undeformed link axes
- the connection of the last link with the payload is rigid

- any motions and elastic deflections in dynamic response analyses are assumed to take place relative to an inertia frame that coincides with the system centre of mass, which in reality stays fixed on the orbit about the earth; as the SRMS / payload is rotated, say perpendicular to the Shuttle, the combined system centre of mass will remain on the orbit, and thus the Shuttle will move away from the orbit, opposite to the motion of the payload, but as this motion takes place slowly its effect on the SRMS vibrations is neglected
- it is assumed that the joint gear box ratios are very high, so that the reaction torques at the input side can be neglected (for example for the SRMS, the shoulder joint ratio is 1:1842, and the maximum output torque is 1298 Nm, so that the reaction torque at the input side is 0.7 Nm)
- geometric stiffening effects are neglected due to the low slew rates
- except for some analyses in chapter 2.10 all models are planar.

1.4 THE SHUTTLE REMOTE MANIPULATOR SYSTEM (SRMS)

Since the SRMS is the only existing manipulator working in space, it will be referred to and compared with repeatedly throughout this thesis, and some of its known design characteristics will be the foundation for some general assumptions concerning large flexible space manipulators in this thesis. Figure 1.1 shows a schematic of the stowed SRMS and introduces some of the common technical terms related to the SRMS or space manipulators in general.

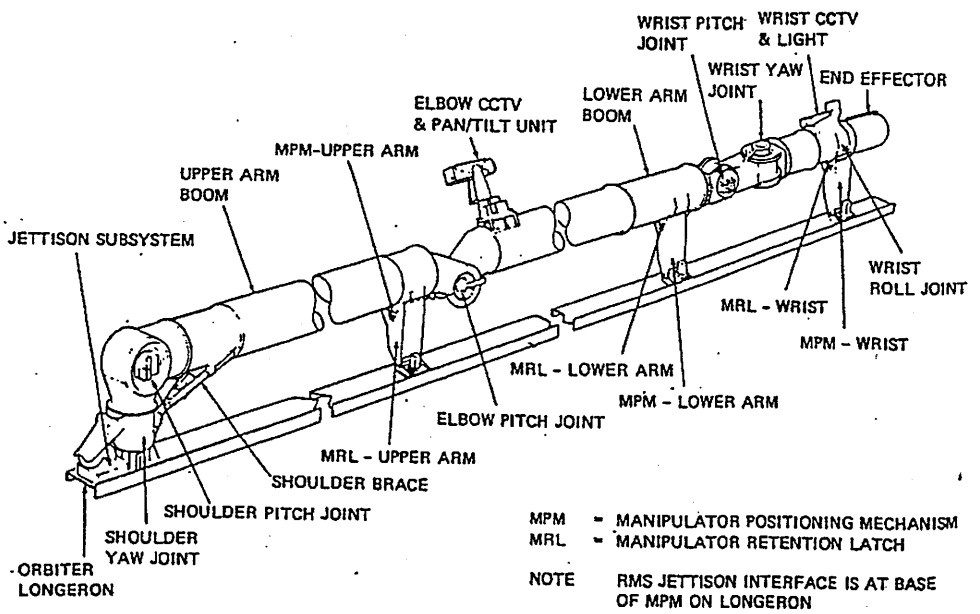

Figure 1.1: Sketch of the stowed SRMS and technical terms ([3])

1.5 STRUCTURE OF THESIS

The organisation of this thesis is shown by the following chapter by chapter account.

Chapter 2:
This chapter applies the method to compute exact natural frequencies and mode shapes to a planar single flexible link robot with fixed base subject to various dynamical boundary conditions. The boundary conditions are reproduced as exactly as the available literature on the SRMS allows. Some examples of dynamic responses to randomly chosen excitations are given, where assumed mode shape approximations are compared with the results when the exact mode shapes are used. Also the magnitude of interaction between a single link rigid robot and the Space Shuttle are assessed by some examples.

Chapter 3:
Here the exact analyses of the natural frequencies and mode shapes of the single flexible link are extended to a planar single flexible link with fixed base and articulated end effector. This step by step increase of the system complexity allows for steady control of the results, for example by comparison with previous results when the simpler systems are imitated, or by comparison to a rigid double pendulum, when the link stiffnesses are chosen so as to approach infinity.

Chapter 4:
This chapter investigates the natural frequencies and mode shapes of a planar double flexible link robot with fixed base and gives some examples of dynamic responses to arbitrary assumed excitations.

Chapter 5:
The system is extended to the fully developed planar double flexible link with fixed base and articulated end effector. Again the exact natural frequencies and mode shapes are computed.

Chapter 6:
Until now the robot was always assumed to have a fixed base. In practice this is the case in the ground test bed, where the links and a test payload are supported by low friction (air) bearings and can only move in a plane, or if the robot is on a space station so that the station mass is very much larger than that of the robot, or if the Shuttle carrying the robot is attitude controlled while the robot is operated.
In the general case the robot base is mounted on a Shuttle that is free to float in space. The effect of the free base on the natural frequencies and mode shapes of the planar manipulator system is investigated.

Chapter 7:
This chapter gives a series of examples of worst case open-loop dynamic responses due to slew manoeuvres of the manipulator system or due to Shuttle thruster firings. The results for a fixed and a free base robot are compared. The chapter allows for estimating the likely magnitude of dynamic responses and to evaluate various control methods.

Chapter 8:
This chapter shows two examples of how the manipulator can be automatically

operated, using either an inverse dynamics method or Lyapunov's direct method. Although attitude control of the manipulator is not a main topic of this thesis, the chapter is included to show that if excitations other than bang-bang accelerations act on the manipulator, the robot elastic vibration amplitudes in dynamic response analyses are much smaller.

Chapter 9:
Here the possibility of controlling the elastic deflections of the manipulator using reaction wheels is investigated and proven to be feasible within sensible boundaries of additional hardware space and available electric energy. The achievable damping ratios are shown to be able to reduce the waiting time for vibrations to damp down to acceptable levels significantly.

Chapter 10:
This investigates some worst case dynamic responses of the SRMS due to emergency braking during operation, and a simple method to estimate upper limits of dynamic responses is given.

Chapter 11:
A simplified flexible dynamic model of the International Space Station carrying the MRMS is set up, and the magnitudes of dynamic responses of the space station to robot operations are investigated from the point of view of disturbances of micro-gravity or similar experiments.

Chapter 12:
A summary of the thesis is given in the last chapter.

CHAPTER 2: SINGLE LINK WITH FIXED BASE

Although very few single link robot systems exist, this chapter deals with the basic mechanics and dynamics of such a system, since the single link is an integral part of the multi-link robot. Also, the study of a single link system is the foundation for the formulation of the dynamics of the multi-link system.

2.1 JOINTS AND TORQUE MOTORS

The mechanical design and thus the dynamical behaviour of the joints heavily influence the overall behaviour of the manipulator, since they determine the boundary conditions for the flexible links in addition to the payload mass inertia.
For the further analyses the gear system of the joints is assumed to be a backdriveable epicyclic gear train with an electric motor, such as that of the Space Shuttle Remote Manipulator System (SRMS). This assumption gives rise to a series of considerable consequences that are to be developed subsequently. Figure 2.1 shows a cut away of an SRMS joint, in which a considerable speed reduction is achieved using a complex epicyclic gear train system.

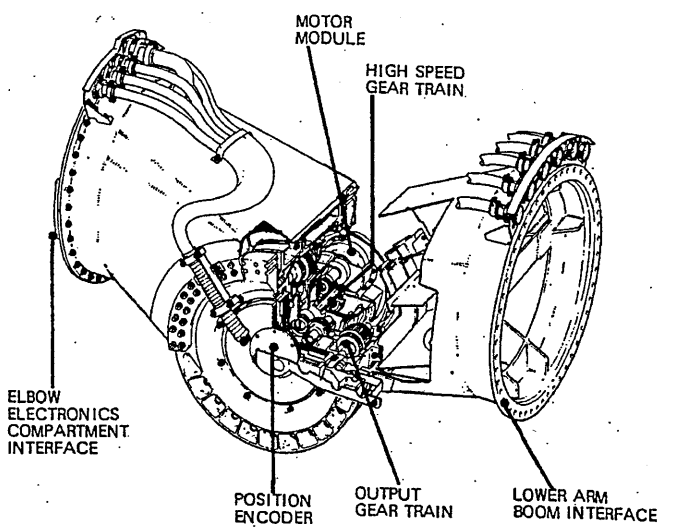

Figure 2.1: Cut away view of SRMS joint unit ([6])

As is shown for example in [1] or [52], the reduction of angular acceleration and velocity by the ratio of the gear box N_g leads in return to an increased effective inertia of the motor rotor if it is backdriven from the gear box output side.
If θ_{out} is the angular rotation of the output side and θ_{in} that of the input side (the motor rotor), we can write

$$\frac{\theta_{\text{in}}}{N_g} = \theta_{\text{out}} \Rightarrow \frac{\dot{\theta}_{\text{in}}}{N_g} = \dot{\theta}_{\text{out}} \text{ and } \frac{\ddot{\theta}_{\text{in}}}{N_g} = \ddot{\theta}_{\text{out}} \tag{2.1}$$

Let I_{in} be the moment of inertia of the input side due to the motor armature and I_{out} the total moment of inertia of the output or payload side. The acceleration of I_{in} due to the input torque T_{in} is then

$$I_{in}\,\ddot{\theta}_{in} = T_{in} - T_{inertia,\,out} \tag{2.2}$$

where $T_{inertia,\,out}$ denotes the effective reaction torque of the output side due to the acceleration of I_{out}. Using equation (2.1) and assuming negligible stiction and friction and constant gear tooth contact with zero backlash, equation (2.2) can be re-written as

$$I_{in}\,\ddot{\theta}_{in} = T_{in} - \frac{I_{out}}{N_g}\ddot{\theta}_{out} \tag{2.3}$$

If a torque is applied at the output side instead of the input side, equation (2.3) can be re-written by using equation (2.1) as

$$I_{in}\,\ddot{\theta}_{in} = \frac{T_{out}}{N_g} - \frac{I_{out}}{N_g}\ddot{\theta}_{out} \tag{2.4}$$

Multiplying both sides of equation (2.4) with N_g yields

$$I_{in}\,\ddot{\theta}_{in}\,N_g = T_{out} - I_{out}\,\ddot{\theta}_{out} \tag{2.5}$$

Using equation (2.1) again, the left-hand side can be written as

$$I_{in}\,\ddot{\theta}_{out}\,N_g^2 = T_{out} - I_{out}\,\ddot{\theta}_{out} \tag{2.6}$$

and therefore

$$T_{out} = \left(I_{out} + I_{in}\,N_g^2\right)\ddot{\theta}_{out} \tag{2.7}$$

This shows that the effective inertia on the output side has been increased by the term $I_{in}\,N_g^2$. Using the SRMS data ([7]) with N_g = 1840 and I_{in} = 3.5×10^{-4} kgm^2, this yields an effective inertia at the shoulder joint of 1188 kgm^2. Thus, if a joint is not locked, the manipulator link connected to the actual gearbox output side has the boundary conditions of a pinned-free beam with a rotational inertia at the pinned end. This will be shown to be significant in the manipulator's dynamics in the next section.

A second important aspect is flexibility within the joints. Although mentioned in many papers, for example [3], [4], [5], [10], [53] and [54], information about the cause and location of joint stiffness is sparse. It is assumed that joint flexibility occurs when it is locked with the brakes on, say at the shoulder when the elbow joint is being driven. It appears that flexibility is due to elasticity in the housing and nonlinear torsional flexibility in the meshing gear teeth. In the latter case an equivalent linear torsion spring is selected to cover the range of vibration amplitudes expected, neglecting any backlash effects. When a joint is driven, it is revolute or free to rotate,

hence torsional stiffness is absent and only the rotary inertia term, equation (2.7), exists. Very few papers (e.g. [7]) state that if a joint of the SRMS is not actively driven, its brakes are on, and that, except for the case when the manipulator performs a computer-controlled motion with all joints actively driven, only one single joint is manually driven at a time.

2.2 DETERMINATION OF NATURAL FREQUENCIES AND MODE SHAPES

Formulation of equations of motion of flexible robot manipulators requires dynamic modelling of the first few elastic mode shapes of the system. For multi-body flexible robots a literature search reveals no published work on exact dynamic modelling of such systems, but many papers ([48], [53], ...) give an analytical solution for a single flexible link with various springs. [22] gives analytical solutions for beams with offset inertial end masses in three dimensions with coupled bending/torsional vibrations. [50] considers a mass at the free end of a clamped-free planar Bernoulli beam, and [49] considers a cantilever Timoshenko beam with a mass at the free end. Due to lack of an exact analytical solution for articulated beam systems, extensive use has been made of approximate methods to represent beam vibrations in the equations of motion of flexible robots. Those approximations normally consist of arbitrary or assumed mode shapes ([20], [36], [51], etc.) or superpositions of both, but can sometimes also be simple polynomials. The following method gives the exact analytical solution for the natural frequency of a flexible link with large payload and thus allows for comparison with the different approximation methods.

2.2.1 EXACT SOLUTION FOR NATURAL FREQUENCIES

The partial differential equation of free vibration of a uniform beam with zero axial force, neglecting rotary inertia and shear force (Bernoulli beam), is given as ([47])

$$EI\, y^{\mathrm{iv}} + m_b\, \ddot{y} = 0 \tag{2.8}$$

where EI is the beam flexural stiffness, m_b its mass per unit length, y its lateral deflection, and where dashes or superscript Roman numbers denote derivations with respect to x and dots derivations with respect to time t. It is seen that in equation (2.8)

$$y = y(x,t) \tag{2.9}$$

therefore equation (2.9) is a partial differential equation. It is solved via separation of variables by letting

$$y(x,t) = W(x)\, q(t) \tag{2.10}$$

and inserting equation (2.10) into equation (2.8) we obtain

$$EI\, W^{\mathrm{iv}}(x)\, q(t) + m_b\, W(x)\, \ddot{q}(t) = 0 \tag{2.11}$$

Now since the differential equation (2.8) is linear, the solution can be expressed in terms of a homogeneous and a particular solution. From equation (2.11) it is seen that the homogeneous equation is given by

$$\frac{EI\,W^{\mathrm{iv}}(x)}{m_b\,W(x)} = -\frac{\ddot{q}(t)}{q(t)} = \omega^2 \tag{2.12}$$

with a constant ω^2, because only in this case the spatial and time dependent parts agree. Thus with equation (2.10) two normal differential equations are obtained from equation (2.8), which yields the solutions for $W(x)$ and $q(t)$ as

$$\ddot{q}(t) + \omega^2\, q(t) = 0 \tag{2.13}$$

and

$$W^{\mathrm{iv}}(x) - k^4\, W(x) = 0 \tag{2.14}$$

where

$$k^4 = \omega^2 \frac{m_b}{EI} \tag{2.15}$$

and ω is the natural frequency. The general solution for the differential equation (2.13) is given by

$$q(t) = q(0)\cos(\omega t) + \frac{\dot{q}(0)}{\omega}\sin(\omega t) \tag{2.16}$$

from which it is seen that equation (2.8) leads to a vibration problem. All values k_i of k for which equation (2.14) has non-trivial solutions $W(x) \neq 0$ are called eigenvalues, and the corresponding functions $W(x) = W_i(x)$ are called eigenfunctions or mode shapes. The general solution for equation (2.14) is given by ([41])

$$W_i(x) = A_i \sin(k_i x) + B_i \cos(k_i x) + C_i \sinh(k_i x) + D_i \cosh(k_i x) \tag{2.17}$$

and since equation (2.14) is homogeneous, all eigenfunctions $W_i(x)$ have four free parameters A_i, B_i, C_i and D_i, which are finally obtained by taking into account the boundary conditions. Thus we obtain a linear equation system, for which non-trivial solutions only exist if its determinant is zero. With this condition we obtain the characteristic equation for the computation of the eigenvalues $k = k_i$, which always has an infinite number of solutions (for example, the characteristic equation for the cantilever beam is ([41]) $\cos kL \cosh kL = -1$). Inserting these eigenvalues into equation (2.17) yields the eigenfunctions or mode shapes, and one remaining parameter can be used for scaling, for example by letting $W_i(L) = 1$. Under certain conditions it is possible to show that eigenfunctions form a complete orthogonal system ([71]). Thus a particular solution or forced response of the homogeneous partial differential equation (2.8) under a disturbance $Q(t)$

$$EI\, y^{\mathrm{iv}} + m_b\, \ddot{y} = Q(t) \tag{2.18}$$

can be expressed in terms of a superposition of the eigenfunctions in the form

$$y(x,t) = \sum_{i=1}^{\infty} W_i(x)\, q_i(t) \tag{2.19}$$

For numerical analyses, equation (2.19) is approximated by using a finite number n of eigenfunctions, thus

$$\hat{y}(x,t) = \sum_{i=1}^{n} W_i(x)\, q_i(t) \tag{2.20}$$

The above mentioned method allows for the computation of the natural frequencies of a flexible beam with arbitrary kinematic and / or dynamical boundary conditions, but the literature does not report its application to space robots with large overhanging payloads in general or the SRMS in particular.
Formulating the kinematic and dynamical boundary conditions in terms of the mode shapes $W(x)$ and / or their time / spatial derivatives yields four equations. Bringing all terms in these four equations to the left-hand side and collecting them with respect to A_i, B_i, C_i and D_i, we obtain the aforementioned linear equation system

$$\begin{bmatrix} d_{11} & d_{12} & d_{13} & d_{14} \\ d_{21} & d_{22} & d_{23} & d_{24} \\ d_{31} & d_{32} & d_{33} & d_{34} \\ d_{41} & d_{42} & d_{43} & d_{44} \end{bmatrix} \cdot \begin{bmatrix} A_i \\ B_i \\ C_i \\ D_i \end{bmatrix} = \mathbf{0} \tag{2.21}$$

where the elements d_{nm} are complex expressions depending on the trigonometric and hyperbolic functions in equation (2.17) or their derivations. As stated above, since A_i, B_i, C_i and D_i are non-zero constants, equation (2.21) can only be solved if

$$\begin{vmatrix} d_{11} & d_{12} & d_{13} & d_{14} \\ d_{21} & d_{22} & d_{23} & d_{24} \\ d_{31} & d_{32} & d_{33} & d_{34} \\ d_{41} & d_{42} & d_{43} & d_{44} \end{vmatrix} = 0 \tag{2.22}$$

Equation (2.22) can now be solved numerically to give the natural frequencies ω of the system.
Now the procedure described above is illustrated for a pinned-free beam in space with a rotational inertia I_g at the pinned end and a large mass M_p with rotary inertia I_p at the free end. This is representative of a single arm flexible robot driven about the pinned end, where the effective gear box inertia $I_{\text{in}}\, N_g^2$ from equation (2.7) is replaced by I_g. M_p is assumed to be rigidly attached to the beam end at $x = L$. It is also assumed that there are no flexible joints between the ends of the beam and that m_b and EI are continuous. Figure 2.2 sketches the configuration.

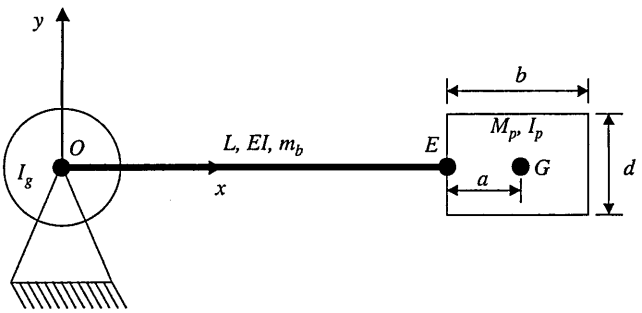

Figure 2.2: Schematic of pinned-free beam with idealised rigid, rectangular and homogeneous mass at the free end and rotary inertia at the pinned end

In figure 2.2, G denotes the centre of mass of the payload, which is at distance $a = b/2$ on the tangential extension of the free link end E at $x = L$, where the payload is rigidly attached to the link. Figure 2.3 shows the boundary conditions at $x = 0$ and $x = L$, where $\ddot{u}$ and $\ddot{\phi}$ are the translational and rotational acceleration about G, and $\ddot{\phi}_g$ the rotational acceleration of I_g at $x = 0$.

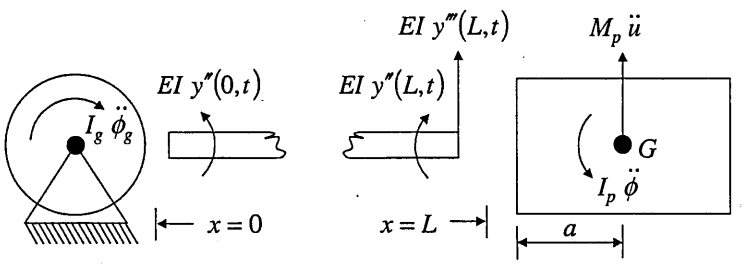

Figure 2.3: Kinematic and dynamical boundary conditions at $x = 0$ and $x = L$

In figure 2.3 the terms $EI\, y''(x,t)$ and $EI\, y'''(x,t)$ are the beam bending moment and shear force at x, respectively. Taking into account the sign conventions for the beam and considering figures 2.2 and 2.3 the boundary conditions at $x = 0$ are

$$y(0,t) = 0 \tag{2.23}$$

and

$$EI\, y''(0,t) = I_g\, \ddot{\phi}_g(t) \tag{2.24}$$

At $x = L$ the boundary conditions are

$$E\,I\, y''(L,t) = -I_p \ddot{\phi}(t) - \left(M_p\, \ddot{u}(t)\right) a \tag{2.25}$$

and

$$E\,I\, y'''(L,t) = M_p\, \ddot{u}(t) \tag{2.26}$$

From figure 2.3

$$\ddot{u}(t) = \ddot{y}(L,t) + a\, \ddot{y}'(L,t) \tag{2.27}$$

Since the beam vibrations in each mode i are harmonic oscillations with a natural frequency ω, using equation (2.10) and relation (2.13) we can write

$$\ddot{y}(x,t) = -\omega^2 W(x) q(t) \tag{2.28}$$

and similar for the d-th derivative $y^d(x,t)$ of $y(x,t)$ with respect to x

$$\ddot{y}^d(x,t) = -\omega^2 W^d(x) q(t) \tag{2.29}$$

Thus using equation (2.10) and relation (2.13) the three dynamical boundary conditions in equations (2.24) through (2.26) can be written as

$$EI W''(0) = -I_g \omega^2 W'(0) \tag{2.30}$$

$$EI W''(L) = I_p \omega^2 W'(L) + \left[M_p \omega^2 \left[W(L) + a W'(L)\right]\right] a \tag{2.31}$$

$$EI W'''(L) = -M_p \omega^2 \left[W(L) + a W'(L)\right] \tag{2.32}$$

where from figure 2.2 and assuming an idealised homogeneous and rectangular payload mass, the rotational inertia I_p of mass M_p about G is given as

$$I_p = M_p \frac{b^2 + d^2}{12} \tag{2.33}$$

From the kinematic boundary equation (2.23) it is seen that in equation (2.17)

$$D_i = -B_i \tag{2.34}$$

Bringing all terms in equations (2.30), (2.31) and (2.32) to the left-hand side and collecting them with respect to A_i, B_i and C_i, equation (2.21) reduces to

$$\begin{bmatrix} d_{11} & d_{12} & d_{13} \\ d_{21} & d_{22} & d_{23} \\ d_{31} & d_{32} & d_{33} \end{bmatrix} \begin{bmatrix} A_i \\ B_i \\ C_i \end{bmatrix} = \mathbf{0} \tag{2.35}$$

Note that the matrix elements in equation (2.35) have nothing to do with those in equation (2.21). Using the notation C = cos (kL), S = sin (kL), Ch = cosh (kL) and Sh = sinh (kL), the elements d_{nm} are given by

$$\begin{aligned}
d_{11} &= d_{13} = I_g k \omega^2 \\
d_{12} &= -2 EI k^2 \\
d_{21} &= k\left(I_p + a^2 M_p\right)\omega^2 C + \left(EI k^2 + a M_p \omega^2\right) S \\
d_{22} &= EI k^2 \left(C + Ch\right) - I_p k \omega^2 \left(S + Sh\right) - \\
&\quad a M_p \omega^2 \left(-C + Ch + a k S + a k Sh\right)
\end{aligned} \tag{2.36}$$

$$
\begin{aligned}
d_{23} &= k\left(I_p + a^2 M_p\right)\omega^2 Ch + \left(-EI\,k^2 + a M_p\,\omega^2\right)Sh \\
d_{31} &= -EI\,k^3\,C + M_p\,\omega^2\left(a\,k\,C + S\right) \\
d_{32} &= EI\,k^3\left(S - Sh\right) - M_p\,\omega^2\left(-C + Ch + a\,k\,S + a\,k\,Sh\right) \\
d_{33} &= EI\,k^3\,Ch + M_p\,\omega^2\left(a\,k\,Ch + Sh\right)
\end{aligned}
\tag{2.36}
$$

In elements d_{11}, d_{12} and d_{13}, one common factor k can be ignored and is only given for completeness. Equation (2.36) can only be solved if

$$
\left|d_{nm}(k)\right| = \begin{vmatrix} d_{11} & d_{12} & d_{13} \\ d_{21} & d_{22} & d_{23} \\ d_{31} & d_{32} & d_{33} \end{vmatrix} = 0 \tag{2.37}
$$

which using equation (2.15) can be solved numerically for the natural frequencies ω_i. When the drive motor joint is locked with brakes on, say for Shuttle manoeuvring, the gear drive cannot rotate so that the inertia term is replaced by the joint torsional stiffness, which is assumed to completely replace the gear box, so that the spring acts directly between the base and the flexible link at x = 0. Hence equation (2.30) becomes $EI\,W''(0) = \lambda W'(0)$, where λ denotes the linearised joint torsional stiffness ([53], [54]). Then the elements d_{11} and d_{13} in equation (2.36) become

$$
d_{11} = d_{13} = -k\lambda \tag{2.38}
$$

Note that the first row of the matrix in equations (2.35) and (2.37) represents the first dynamical boundary condition, equation (2.30), the second row the second dynamical boundary condition, equation (2.31), and the third row the third dynamical boundary condition, equation (2.32).

For reasons of comparison, we introduce a reference configuration (A) with beam properties L = 14 m, m_b = 3.9786 kg/m and EI = 3×10^6 Nm^2, payload mass properties b = 3 m, d = 6 m, M_p = 10000 kg and I_p = 37500 kgm^2 (about G), and λ = 10^6 Nm/rad for a locked joint or I_g = 1188 kgm^2 if the joint is unlocked or free to rotate. For these data, the first 5 natural frequencies ω_i of the system are given in table 2.1. Note that the unlocked joint system has one rigid body mode with ω_1 = 0.

Freq. [rad/s]	Unlocked	locked
ω_1	0.00	0.39
ω_2	4.55	5.18
ω_3	25.98	81.46
ω_4	103.17	236.66
ω_5	274.76	478.56

Table 2.1: The first five natural frequencies of the example system for the case of an unlocked and a locked joint

A literature search reveals virtually no reference to natural frequencies of single or double link flexible RMS systems accounting for joint elasticity or large payloads, with brakes on or off. Such information is of utmost importance in assessing the vibration characteristics of flexible robotic arm systems.
The following figures with the mode shapes will show that for $\lambda = 0$ (shoulder joint unlocked), the mode shapes consist of pinned-free modes with the payload essentially rotating about its centre of mass G. When the gear box brakes are on, the system becomes a cantilever beam with torsional stiffness λ at $x = 0$. From table 2.1 we see that $\omega_{1,\text{unlocked}} / \omega_{1,\text{locked}} = 11.66$ for the present data.
It can be shown ([41]) that the dynamic response under step function excitation is proportional to $1/\omega_n^2$. Thus for brakes off we expect the oscillatory motion in the pinned-free mode as being very small compared to the response for a locked joint. However, for a doubly articulated RMS it will be shown that application of brakes at say one joint, for example at the shoulder, and applying a torque at the elbow or wrist joint gives a much lower natural frequency and hence larger response.
Similarly with the RMS in a straight, fully extended configuration with brakes on perpendicular to Shuttle axis, thruster firings to manoeuvre the payload will be shown to give considerable dynamic response.

2.2.2 EXACT SOLUTION FOR MODE SHAPES

Having solved equation (2.22) for the natural frequencies of a flexible beam subject to kinematic and / or dynamical boundary conditions, the frequencies ω_i can be re-inserted into equation (2.21) to give

$$\begin{bmatrix} d_{11} & d_{12} & d_{13} & d_{14} \\ d_{21} & d_{22} & d_{23} & d_{24} \\ d_{31} & d_{32} & d_{33} & d_{34} \\ d_{41} & d_{42} & d_{43} & d_{44} \end{bmatrix} \begin{bmatrix} A_i \\ B_i \\ C_i \\ D_i \end{bmatrix} = \mathbf{0} \tag{2.39}$$

where now all the matrix elements d_{nm} are known. If the determinant of the matrix is zero, as required for equation (2.22), equation (2.39) can be solved for non-trivial, that is non-zero, A_i, B_i, C_i and D_i ([57]). Re-inserting these constants together with the natural frequency into equation (2.17) gives the exact mode shape $W_i(x)$ for the natural frequency ω_i. It turns however out that due to limits in numerical accuracy, the determinant computed after re-insertion of a natural frequency ω_i, equation (2.39), is never exactly zero. In this case the following equation

$$\begin{bmatrix} d_{11} & d_{12} & d_{13} & d_{14} \\ d_{21} & d_{22} & d_{23} & d_{24} \\ d_{31} & d_{32} & d_{33} & d_{34} \\ d_{41} & d_{42} & d_{43} & d_{44} \end{bmatrix} \begin{bmatrix} A_i \\ B_i \\ C_i \\ D_i \end{bmatrix} = \begin{bmatrix} f \\ f \\ f \\ f \end{bmatrix} \tag{2.40}$$

can be solved for non-trivial A_i, B_i, C_i and D_i ([57]). As mentioned before, each row in equation (2.39) or (2.40) represents one of the boundary condition equations. It is therefore important to choose one identical value f for each element of the right-hand side vector, for convenience say 1. This is equivalent to weighting the four boundary conditions equally. Using different values in the right-hand side vector yields wrong values for A_i, B_i, C_i and D_i, and thus wrong mode shapes. The magnitude of f determines the scaling of A_i, B_i, C_i and D_i, and thus of the mode shape. Note that equation (2.40) has to be solved for each mode shape $W_i(x)$ or natural frequency ω_i.

The following figures show the mode shapes for the natural frequencies as listed in table 2.1 for the reference beam system, whose properties are listed two pages before.

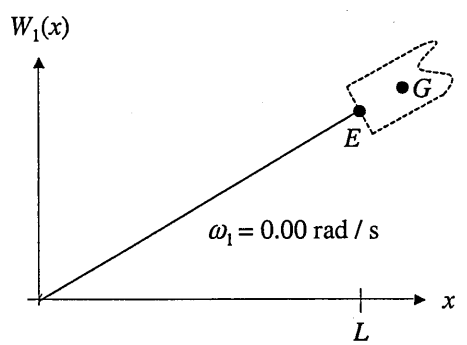

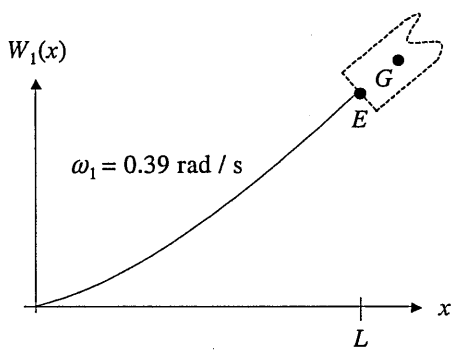

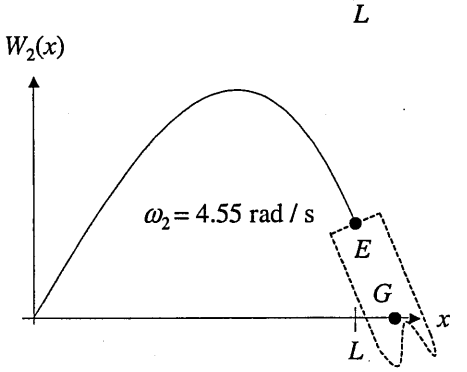

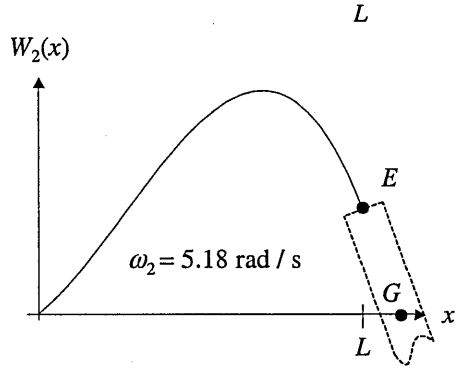

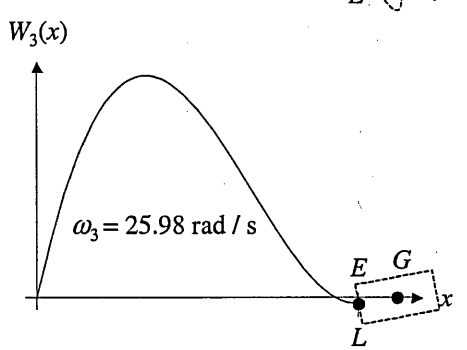

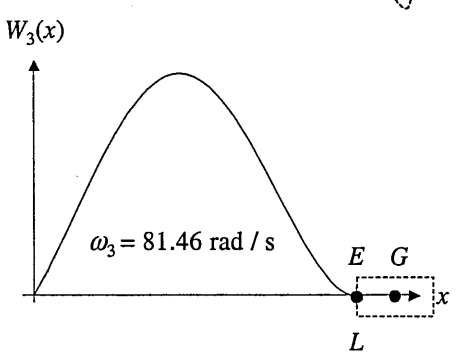

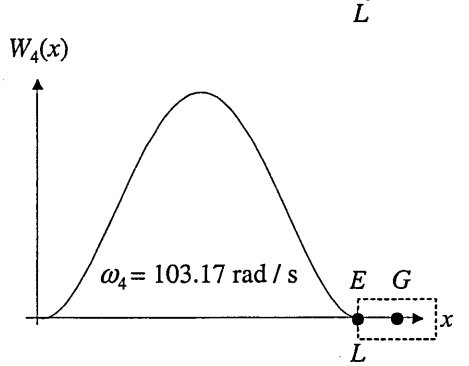

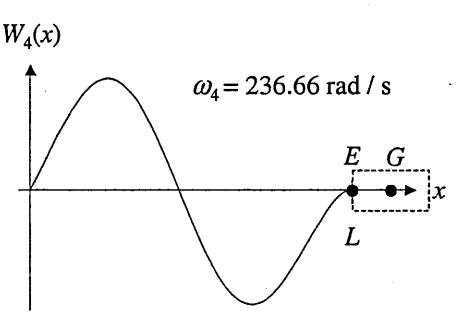

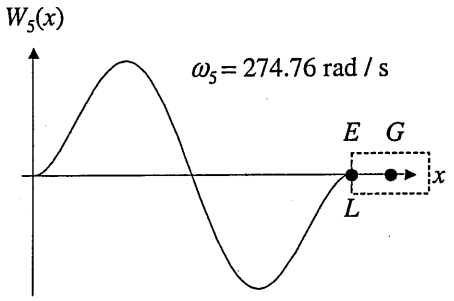

Figures 2.4 through 2.8: Mode shapes for unlocked joint with I_g

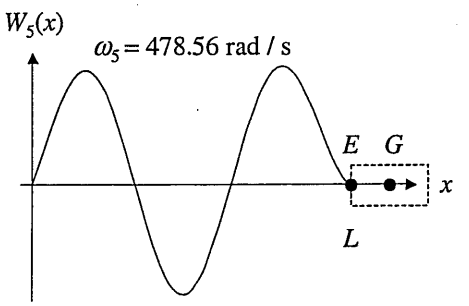

Figures 2.9 through 2.13: Mode shapes for locked joint with λ

The above figures show that for the chosen system properties, the centre of mass G of M_p is essentially a nodal point, about which the mass oscillates, except in the first mode for the locked link with joint stiffness, figure 2.9. This is found to be true for all masses in excess of say 3000 kg, and smaller masses cause negligible dynamic responses, as will be shown in the following chapters. It is further noted that the higher mode shapes rapidly approach those of a clamped-clamped beam, as the figures prove. Again, this is found to be true for the whole payload range, which in practice might reach from say from M_p = 0 kg to M_p = 30000 kg. Due to this fact we expect the dynamic response of the first mode for the locked joint case to be very much larger than of all the other modes for either the locked or unlocked joint case.
Due to lack of exact mode shapes it is almost universally common practice to use approximate mode shapes or quasicomparison functions ([8], [32], [33], [35], [36], etc.) $\hat{W}_i(x)$, which may consist of mode shapes of classical beams, say clamped-clamped, clamped-free and so on in order to represent link flexibility in the equations of motion. It can be shown ([71]) that under certain conditions, all groups of functions $\hat{W}_i(x)$ that form a complete orthogonal system and that take account of the boundary conditions, can be used in equation (2.19) to solve the partial differential equation. However, equation (2.19) suggests that the approximation of the exact solution, equation (2.20), becomes better with increasing number of mode shapes, and it is also known ([47], [66], [67], [68], [71]) that exact mode shapes $W_i(x)$ for the system under consideration lead to a faster convergence than other complete function systems, but such convergence is rarely checked out against exact mode shapes. It is therefore one of the main purposes of this thesis to obtain exact solutions for the natural frequencies and mode shapes of a single link and double link flexible robot arm, with a large payload, to provide a basis for comparison with the various approximate methods that are used. The results of this study, as outlined above, will also provide a basis for selecting mode shapes for the double articulated flexible robot. It is stressed here that the above figures prove that for an unlocked joint, the gear box inertia I_g does not effectively lead to a clamped link at the gear box output side in the lower modes, which is often claimed in the literature ([8], [69], etc.), and we also note that incorrect dynamic modelling can lead to gross errors in dynamic response calculations and to unstable control systems ([3]). In order to design closed-loop vibration control systems it is therefore essential to have accurate methods of determining the wide range of natural frequencies and mode shapes to be expected.

2.3 VALIDATION OF THE DETERMINANT RESULTS

The results of table 2.1 can be validated by Rayleigh's principle of constraints ([81]), which states that an increase in the mass of a dynamic system will cause the natural frequencies to fall and lie between the frequency of the original system and the next lower frequency of the system for infinitely increasing mass. Conversely adding constraints, such as springs, will cause the natural frequencies to increase and lie between the frequencies of the original system and the next higher value of the system for infinitely increasing stiffness.

To illustrate this principle we use equation (2.37) with the elements given in equation (2.36) for the data set (A) introduced on page 20, but let $M_p = I_p = \lambda = I_g = 0$, thus producing a pinned-free beam without any other (dynamical) boundary conditions. Increasing M_p and I_p should then lower the frequencies until for very large M_p and I_p the natural frequencies approximate those of a pinned-clamped beam.

This is shown in table 2.2, where the values in the row "pinned-clamped" are the exact analytical values ([41]) for a pinned-clamped beam with properties L = 14 m, m_b = 3.9786 kg/m and $EI = 3\times10^6$ Nm^2. Note also that in table 2.2 the second frequency of the pinned-free beam approaches zero as the payload mass increases, thus effectively producing a second mode with $\omega_1 = 0$.

The 200000 kg case in table 2.2 is given as a check of convergence for very large masses. The first line proves that for $M_p = I_p = I_g = 0$, the determinant gives the exact analytical results of a pinned-free beam with the above properties, which validates the exact eigenvalue solution of equation (2.37). Furthermore, the table shows the well known fact that the natural frequencies ω_i of a pinned-clamped beam are identical with the natural frequencies ω_{i+1} of a pinned-free beam.

It also shows that the natural frequencies ω_{i+1} approach the natural frequencies ω_i of the original system with increasing mass, as expected.

M_p [kg], b [m], d [m]	ω_1 [rad/s]	ω_2 [rad/s]	ω_3 [rad/s]	ω_4 [rad/s]	ω_5 [rad/s]
0, 0, 0	0.00	68.31	221.36	461.86	789.80
50, 1, 1	0.00	44.37	162.33	348.67	596.37
100, 1, 1	0.00	42.25	156.04	327.89	555.61
1000, 1, 1	0.00	35.88	108.05	240.84	472.94
2000, 1, 1.5	0.00	28.12	83.46	227.33	465.31
4000, 1, 2	0.00	18.72	73.38	223.32	463.02
10000, 3, 6	0.00	4.59	68.69	221.57	462.01
15000, 3, 8	0.00	2.97	68.48	221.46	461.93
20000, 3, 10	0.00	2.12	68.40	221.42	461.90
200000, 6, 20	0.00	0.38	68.31	221.37	461.86
pinned-clamped:			68.31	221.36	461.86

Table 2.2: Variation of exact natural frequencies of the beam system shown in figure 2.2 with M_p and I_p, when $I_g = 0$, $\lambda = 0$

Figure 2.14 shows the effect of Rayleigh's constraint theorem on the natural frequencies of a dynamic system and illustrates that an increase of mass in a system

will shift the natural frequencies ω_i of the new system somewhere between ω_{i-1} and ω_i of the original system, where the lower limit is ω_{i-1} for infinite additional mass and the upper limit is ω_i for zero additional mass.

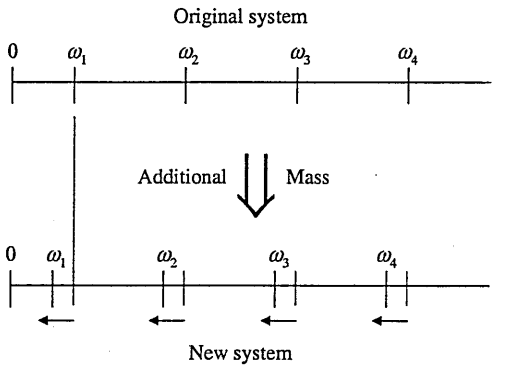

Figure 2.14: Effect of Rayleigh's constraint theorem on natural frequencies

As a second example we produce again a pinned-free beam by letting $M_p = I_p = \lambda = I_g = 0$. Increasing I_g should then lower the frequencies until for very large I_g the frequencies approach those of a clamped-free beam. Table 2.3 shows the results, where the row "clamped-free" gives the exact analytical values ([41]) for a pinned-clamped beam with the actual beam properties.

I_g [kgm^2]	ω_1 [rad/s]	ω_2 [rad/s]	ω_3 [rad/s]	ω_4 [rad/s]	ω_5 [rad/s]
0	0.00	68.31	221.36	461.86	789.80
1000	0.00	31.78	102.21	274.93	536.45
2000	0.00	25.46	99.87	274.13	536.04
5000	0.00	20.26	98.51	273.66	535.80
10000	0.00	18.10	98.06	273.50	535.72
20000	0.00	16.89	97.84	273.42	535.68
30000	0.00	16.47	97.77	273.39	535.67
40000	0.00	16.25	97.73	273.38	535.66
50000	0.00	16.12	97.71	273.37	535.66
10^6	0.00	15.60	97.63	273.34	535.64
clamped-free:		15.58	97.62	273.34	535.64

Table 2.3: Variation of natural frequencies the beam system shown in figure 2.2 with inertia I_g for $M_p = I_p = \lambda = 0$

For a third example we take again the pinned-free beam by choosing $M_p = I_p = \lambda = I_g = 0$. Instead of the rotational inertia, we now take the case of a locked joint with torsional stiffness λ. An increase of λ should then raise the natural frequencies towards those of a clamped-free or cantilever beam as $\lambda \rightarrow \infty$. Table 2.4 shows the results and also shows that the ω_i are related to λ in a nonlinear manner.

λ [Nm/rad]	ω_1 [rad/s]	ω_2 [rad/s]	ω_3 [rad/s]	ω_4 [rad/s]
0	0.00	68.31	221.36	461.86
10^2	0.17	68.31	221.37	461.86
10^4	1.65	68.50	221.57	462.06
10^6	11.39	80.17	236.52	478.41
10^8	15.51	97.21	272.19	533.40
clamped-free:	15.58	97.62	273.34	535.64

Table 2.4: Variation of natural frequencies the beam system shown in figure 2.2 with joint torsional stiffness λ for $I_g = M_p = I_p = 0$

The given examples show that the determinant method works correctly for all the presented test cases.
Figure 2.15 shows the variation of the first two natural frequencies of data set (A) with an unlocked joint when the rotational inertia I_g = 1188 kgm^2 is constant and λ = 0 and M_p and I_p are increased (see also figure 2.2).
It also shows that for a constant I_g at $x = 0$, an additional mass at $x = L$ changes the natural frequencies in relation of its ratio to the mass of the whole system. This result agrees with Rayleigh's principle and its implications mentioned before. In figure 2.15, the convergence of the natural frequencies is already very close to the converged values for $M_p \geq 10000$ kg.

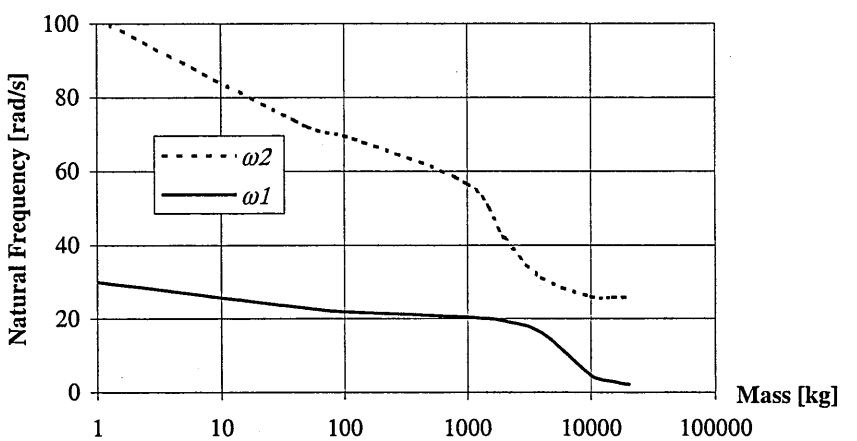

Figure 2.15: Variation of first two natural frequencies of unlocked joint beam (I_g = 1188 kgm^2, $\lambda = 0$) with M_p and I_p

Figure 2.16 shows the variation of ω_1 and ω_2 for the locked joint with M_p and I_p, λ = 10^6 Nm/rad and $I_g = 0$.
Like the previous tables, figures 2.15 and 2.16 show that the eigenfrequencies are a non-linear function of the payload properties. Especially in the payload range 2000 to 4000 kg the eigenfrequencies drop rapidly, approaching their final values as M_p and I_p approach infinity. It thus appears that for payload masses in excess of say, 3000 kg, the distributed beam mass is practically negligible compared to the payload.

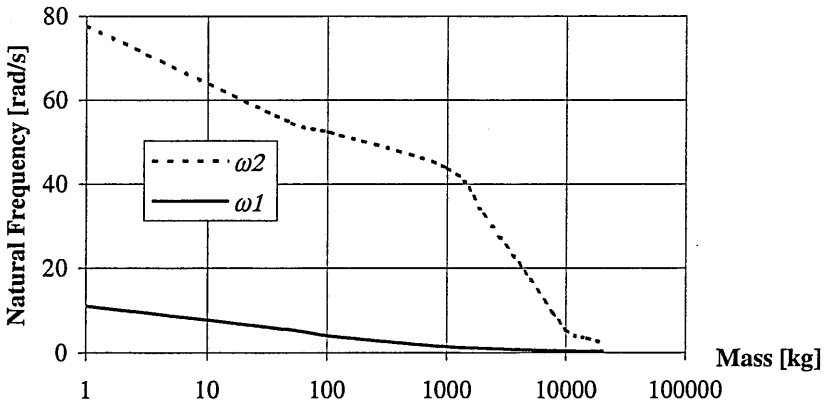

Figure 2.16: Variation of first two natural frequencies of locked joint beam ($\lambda = 10^6$ Nm/rad and $I_g = 0$) with M_p and I_p

2.4 INFLUENCE OF CENTRIFUGAL FORCES

A tensile axial force on a beam increases its natural frequencies and changes its mode shapes, and the partial differential equation of free vibration of a uniform beam with constant tensile axial force N, neglecting rotary inertia and shear force (Bernoulli beam), is [41]

$$EI\, y^{iv} + N(x)\, y'' + m_b\, \ddot{y} = 0 \tag{2.41}$$

The centrifugal acceleration a_c due to an angular velocity ω at a distance L from the pivot is given as

$$a_c = \omega^2 L \tag{2.42}$$

Thus the centrifugal or tensile axial force F_c on a link rotating with the angular velocity ω and holding a payload of mass M_p at a distance L is given as

$$F_c = \omega^2 L M_p \tag{2.43}$$

In order to obtain a sensible value for F_c due to centrifugal forces, we consider the case of a payload mass M_p = 30000 kg, the straight SRMS with L = 15.3 m and the maximum angular velocity ([7]) of the loaded SRMS, ω = 0.004 rad/s. Assuming a homogeneous payload with length b = 3 m, the total distance of the payload centre of mass is $L_{tot} = L + b/2$ = 16.8 m. Inserting these data into equation (2.43) yields an axial force F_c = 8.064 N, which is neglectibly small. Since this is the worst case calculation, for a large payload, the centrifugal forces in general can be neglected.

2.5 DYNAMIC MODELLING

In general, equations of motion are derived by consideration of the kinetic and potential energies in a given system or by the principles of virtual work and power

respectively. Here the equations are derived using the most common Lagrangian approach, which provides a systematic method of formulating the equations of motion also for nonlinear systems. As an extension of Hamilton's principle Lagrange's equation requires the kinetic and potential energy of the system. In order to find the expressions for the kinetic and potential energy, we consider figure 2.17, which sketches the unlocked joint system and its various velocity components relative to the body reference frame. It is assumed that elastic deflections are small and that geometric stiffening effects are negligible.

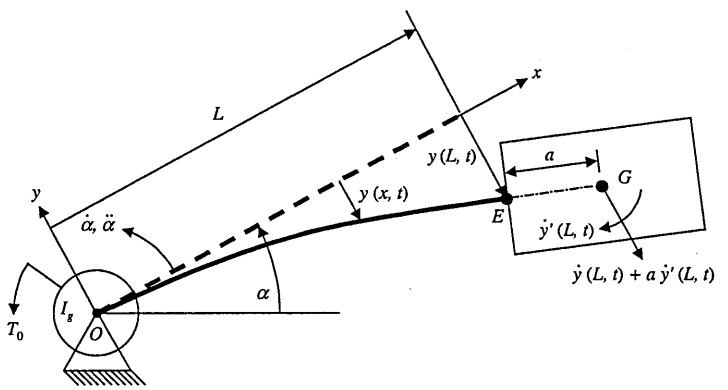

Figure 2.17: Velocity components of unlocked joint system relative to body frame

In figure 2.17 the revolute joint O is assumed to be inertially fixed. The motion y of the flexible link is a function of x and t, thus $y = y(x,t)$. Note that dashes or superscript Roman numbers denote derivations with respect to x and dots derivations with respect to time t. G is the payload centre of mass which is at distance a on the tangential extension of the link at E, where the payload is rigidly attached to the link. The payload is defined by its mass M_p and its rotary inertia I_p about G. Since the joint at O is not mechanically locked, the flexible deformations of the link experience the presence of a rotary inertia I_g at $x = 0$ due to the joint gear box.

Application of a torque $T_0(t)$ will produce a reaction force at O which in the case of a free Shuttle will give rigid body translational and rotational motion of the Shuttle if thrusters or other devices do not maintain attitude. This complex interactive motion between the Shuttle and the manoeuvring flexible RMS will lead to extremely complicated equations of motion. The authors of [8] have solved the interaction problem for surge, heave, pitch motion of the Shuttle and planar motion of the RMS, but the importance of Shuttle motion was not evaluated. This thesis will show Shuttle motion effects in 2D analyses.

If the Shuttle is not attitude controlled while operating the RMS the initial Shuttle attitude would need to be recovered by thruster firings which would themselves excite further RMS vibration. This is a subject which requires detailed investigation as the literature contains little or no reference to this problem.

For the unlocked joint the total kinetic energy T of the system is given as the sum of the kinetic energies of the payload, the beam and the gear box inertia I_g, thus

$$T = \tfrac{1}{2}M_p\left[\dot{y}(L,t) + a\dot{y}'(L,t) + \dot{\alpha}(L+a)\right]^2 + \tfrac{1}{2}I_p\left[\dot{y}'(L,t) + \dot{\alpha}\right]^2 + \tfrac{1}{2}I_g\left[\dot{y}'(0,t)\right]^2 + \tfrac{1}{2}m_b\int_0^L\left[\dot{y}(x,t)\right]^2 dx \tag{2.44}$$

Considering only strain energy of bending and assuming constant flexural stiffness EI over length L, the total potential energy V_U for the unlocked joint case is given as

$$V_U = \tfrac{1}{2} EI \int_0^L [y''(x,t)]^2 \, dx \tag{2.45}$$

It is noted that in equations (2.44) and (2.45) the beam deflection $y(x,t)$ is not known. However the exact solution for the mode shapes can be obtained from equation (2.40), and $y(x,t)$ is then approximated by a finite series of exact or assumed mode shapes, $W(x)$ or $\hat{W}(x)$, according to equation (2.20). Note that if only elastic motions are of interest, a rigid body mode does not have to be included in equation (2.20).
Figure 2.18 shows the system chosen to study the dynamical behaviour of the locked joint system, where the rotary inertia I_0 is connected to an inertial frame by a revolute joint at O, and the flexible link is connected to I_0 also by a revolute joint at O. The torsional spring with stiffness λ acts between I_0 and the flexible link at $x = 0$, and the torque $T_0(t)$ drives I_0 about its joint to the inertia frame. Note that I_0 is independent from I_g for the unlocked joint case.

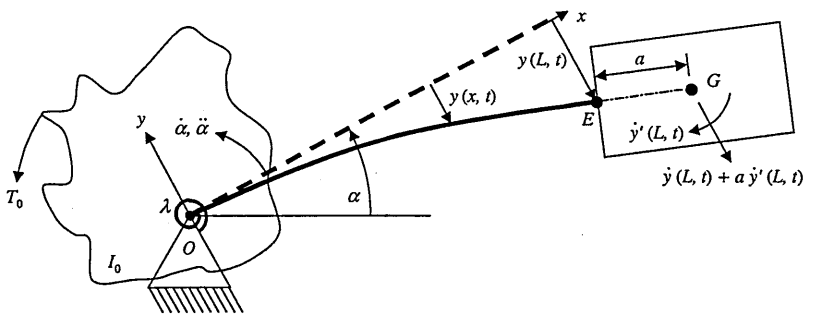

Figure 2.18: Velocity components of locked joint system relative to body frame

The reason for the introduction of the rotary inertia I_0 is that if the RMS base were fixed, as is assumed for the computation of the mode shapes for the locked joint case, the application of a joint drive torque $T_0(t)$ at the locked joint would make no sense. Note that the system shown in figure 2.18 is different from that for which the locked joint modes are computed, but if I_0 is chosen very large (say 10^{20} kgm^2) it effectively represents a fixed base for the link vibrations, and thus the natural frequencies and mode shapes given in table 2.1 and figures 2.9 through 2.13 for the locked joint case are not affected. This might be approximately true for example for a single link system on the International Space Station, where the station mass and rotary inertia are very much larger than those of the link and payload. By choosing $T_0(t)$, any arbitrary angular acceleration $\ddot{\alpha}(t)$ of the complete system including the flexible link and payload can be produced, and the results can be checked against analytically.
The total energy of the locked joint system is given as

$$\begin{aligned} T = {} & \tfrac{1}{2} M_p [\dot{y}(L,t) + a\dot{y}'(L,t) + \dot{\alpha}(L+a)]^2 + \tfrac{1}{2} I_p [\dot{y}'(L,t) + \dot{\alpha}]^2 + \\ & \tfrac{1}{2} I_0 \dot{\alpha}^2 + \tfrac{1}{2} m_b \int_0^L [\dot{y}(x,t)]^2 \, dx \end{aligned} \tag{2.46}$$

Instead of using $T_0(t)$ and I_0 one can take the rigid body motion $\alpha(t)$ of the system to be a prescribed motion, which means that $\ddot{\alpha}(t)$ is known. Assuming that $\alpha(t)$ is the first system degree of freedom, applying Lagrange's equation (2.48) to the kinetic energy expression (2.44) or (2.46) will give the off-diagonal or coupling elements M_{12}, M_{13}, ... in the equations of motion (2.49) below. Now since $\ddot{\alpha}(t)$ is known we strike the first row in equation (2.49) and bring the terms $\ddot{\alpha}(t)M_{12}, \ddot{\alpha}(t)M_{13}, \ldots$ in the remaining equations to the right hand side of equation (2.49) as the generalised forces $P_2(t)$, $P_3(t)$, and so on. Now the M_{12}, M_{13}, ... are called exciting force coefficients.
If the joint is locked account must be taken of the torsional stiffness λ at $x = 0$, and thus the potential energy V_L for the locked joint system then becomes

$$V_L = \tfrac{1}{2}EI\int_0^L [y''(x,t)]^2\,\mathrm{d}x + \tfrac{1}{2}\lambda[y'(0,t)]^2 \tag{2.47}$$

For both the unlocked and locked joint case Lagrange's equation is then applied to each of the generalised coordinates $p_j(t)$, thus

$$\frac{\mathrm{d}}{\mathrm{dt}}\left(\frac{\partial T}{\partial \dot{p}_j(t)}\right) - \frac{\partial T}{\partial p_j(t)} + \frac{\partial V}{\partial p_j(t)} = P_j(t) \tag{2.48}$$

where the $P_j(t)$ are the generalised forces. Here the generalised coordinates vector is $\mathbf{p}(t) = [\alpha(t), q_1(t), q_2(t), \ldots, q_n(t)]^{\mathrm{T}}$. Note that we introduced the $p_j(t)$ to avoid confusion with the $q_i(t)$, which are used for flexible coordinates or degrees of freedom only.
In the present case the term $\partial T/\partial p_j(t)$, representing centrifugal and Coriolis forces, is zero, but will always be neglected from here on due to the very low angular velocities involved (except for some simulations in chapter 2.10). This practice was proven to be justified in chapter 2.4. Thus the equations of motion obtained with equation (2.48) are written in matrix form as

$$\begin{bmatrix} M_{11} & M_{12} & \cdots & M_{1n} \\ M_{21} & M_{22} & \cdots & M_{2n} \\ \vdots & \vdots & \ddots & \vdots \\ M_{n1} & M_{n2} & \cdots & M_{nn} \end{bmatrix} \begin{bmatrix} \ddot{p}_1 \\ \ddot{p}_2 \\ \vdots \\ \ddot{p}_n \end{bmatrix} + \begin{bmatrix} K_{11} & K_{12} & \cdots & K_{1n} \\ K_{21} & K_{22} & \cdots & K_{2n} \\ \vdots & \vdots & \ddots & \vdots \\ K_{n1} & K_{n2} & \cdots & K_{nn} \end{bmatrix} \begin{bmatrix} p_1 \\ p_2 \\ \vdots \\ p_n \end{bmatrix} = \begin{bmatrix} P_1 \\ P_2 \\ \vdots \\ P_n \end{bmatrix} \tag{2.49}$$

or $\mathbf{M}\ddot{\mathbf{p}} + \mathbf{K}\mathbf{p} = \mathbf{P}$ with symmetric mass and stiffness matrices $\mathbf{M}$ and $\mathbf{K}$ respectively.
If only exact and thus orthogonal mode shapes $W_i(x)$ for a system under consideration are inserted into equation (2.20), $\mathbf{M}$ and $\mathbf{K}$ in equation (2.49) will be diagonal matrices, except for very small off-diagonal terms due to limits in numerical accuracy. The magnitude of these off-diagonal terms is a measure for the numerical accuracy of the mode shapes computed with the method described previously.
The eigenvalue problem of the discretised system represented by equation (2.49) is

$$\left|\mathbf{K} - \omega^2\mathbf{M}\right| = 0 \tag{2.50}$$

which yields n eigenfrequencies ω_j and eigenvectors $\mathbf{ev}_j$. Note that in general the ω_j are not identical to the ω_i of the flexible link as computed in sections 2.2 and 2.3.
Using exact mode shapes in the equations of motion the generalised forces $P_j(t)$ in equation (2.49) are given by

$$P_j(t) = \sum_n \left[F_n(x,t)\, W_j(x)\right] + \sum_m \left[M_m(x,t)\, W_j'(x)\right] \tag{2.51}$$

where F_n and M_m are all real forces and moments acting on body j. Using the $W_j(x)$ and their derivatives computed before, equation (2.51) suggests that body j is flexible, but if it is rigid, its exact mode shapes are simply the rigid body modes or $W_r(x) = x$.
If instead of exact mode shapes assumed mode shapes are used for flexible bodies, the $W_j(x)$ and $W_j'(x)$ in equation (2.51) are replaced by $\hat{W}_j(x)$ and $\hat{W}_j'(x)$.

2.6 EXACT MODE SHAPES IN THE EQUATIONS OF MOTION

Inserting the first two exact (non-rigid) mode shapes $W_2(x)$ and $W_3(x)$ as computed and shown in chapter 2.2.2 for data set (A) with unlocked joint (λ = 0, I_g = 1188 kgm^2) into the equations of motion (2.49) and calculating the eigenfrequencies with equation (2.50) yields the figures given in table 2.5 for the first two (non-zero) eigenfrequencies ω_2 and ω_3 for various M_p and I_p, where I_p is calculated according to equation (2.33) for the payload physical dimensions as given in table 2.5.
Note that if the exact mode shapes are used for vibration analyses, the rigid body mode with $\omega_1 = 0$ does not have to be taken into account, since it is one of the exact mode shapes and thus orthogonal to all the other mode shapes. The errors in table 2.5 are given in comparison to the exact natural frequencies obtained by the determinant method, equation (2.37), and they occur mainly due to rounding, since the exact natural frequencies to compute the exact mode shapes are re-inserted into equation (2.35) to only two decimal places. Also errors can occur due to numerical inaccuracies during the calculation of equation (2.50). Neglecting these deviations however, table 2.5 proves clearly that the mode shapes obtained by the presented method describe the system exactly in the equations of motion.

M_p [kg], b [m], d [m]	ω_2 [rad/s]	error [%]	ω_3 [rad/s]	error [%]
0, 0, 0	30.00	0.0	101.46	0.0
50, 1, 1	22.76	0.0	72.32	0.5
1000, 1, 1	21.84	0.0	57.14	1.0
4000, 1, 2	16.14	0.0	31.16	0.1
10000, 3, 6	4.56	0.2	25.98	0.0
15000, 3, 8	2.96	0.0	25.82	0.0
20000, 3, 10	2.12	0.5	25.76	0.0
200000, 6, 20	0.38	0.0	25.70	0.0

Table 2.5: ω_2 and ω_3 for data set (A) with unlocked joint ($\lambda = 0$, I_g = 1188 kgm^2) computed by equation (2.50) when using the exact mode shapes $W_2(x)$ and $W_3(x)$

2.7 ASSUMED MODE SHAPES IN THE EQUATIONS OF MOTION

2.7.1 UNLOCKED JOINT CASE

To check the natural frequencies using assumed mode shapes in the equations of motion (2.49) against those of the exact solution, the various assumed mode shapes $\hat{W}(x)$ usually used by the various researchers ([8], [32], [33], [35], [36], etc.) are inserted into the discretised equations of motion, equation (2.49), for data set (A) with unlocked joint ($\lambda = 0$, $I_g = 1188$ kgm^2).

The following table 2.6 shows the results of using assumed mode shapes $\hat{W}_i(x)$ for a pinned-pinned beam ([41]). The number of mode shapes is increased, and the order of the mode shapes is their natural order in an eigenmode analysis, i.e. mode number 1 is the first mode shape, mode number 2 the second mode and so on. Note that in all the following eigenfrequency analyses the rigid body rotation of the beam is taken account of, quasi as the 0th mode shape $\hat{W}_0(x) = x$, which in the present case allows for the translatory motion of the payload, as the pinned-pinned mode shapes alone do not provide this freedom of motion ($\hat{W}_i(L) = 0$). The rigid body natural frequency with $\omega_1 = 0$ is not listed in the following tables. Again, the errors are given in comparison with the exact analytical frequencies as given in table 2.1 for the unlocked joint case.

nr. of shapes	ω_2 **[rad/s]**	ω_3 **[rad/s]**	ω_4 **[rad/s]**	ω_5 **[rad/s]**	ω_6 **[rad/s]**
1	5.71				
error [%]	25.5				
2	5.19	31.44			
error [%]	14.1	21.0			
3	4.95	31.36	132.38		
error [%]	8.8	20.7	28.3		
4	4.83	28.20	132.37	329.45	
error [%]	6.2	8.5	28.3	19.9	
5	4.70	28.15	117.54	324.56	675.39
error [%]	3.3	8.4	13.9	18.1	13.2

Table 2.6: Natural frequencies of reference beam configuration for unlocked joint, using approximate mode shapes of a pinned-pinned beam and one rigid body mode

It is seen from table 2.6 that the frequencies and thus the errors decrease with an increasing number of mode shapes, as expected from Rayleigh's theory ([81]).

Now the same analysis is performed with mode shapes of a free-free beam ([41]). Note that these mode shapes do not satisfy the boundary condition $y(0) = 0$, but they can be modified to do so, as shown for example in [72] or [73]. In the present case the

modification is performed by simply subtracting the value of every approximate mode shape at $x = 0$ from that mode shape, thus $\hat{W}_{i,\text{modified}} = \hat{W}_i - \hat{W}_i(0)$ to take account of the kinematic constraint at $x = 0$. Note that the performance of such manipulations can affect the original orthogonality of the modes. The results are given in table 2.7. As before, one rigid body mode is also inserted.

nr. of shapes	ω_2 [rad/s]	ω_3 [rad/s]	ω_4 [rad/s]	ω_5[rad/s]	ω_6 [rad/s]
1	6.16				
error [%]	35.4				
2	5.66	35.49			
error [%]	24.4	36.6			
3	5.20	35.31	147.99		
error [%]	14.3	35.9	43.4		
4	5.00	29.45	147.97	355.34	
error [%]	9.9	13.4	43.4	29.3	
5	4.81	29.33	117.15	355.34	677.37
error [%]	5.7	12.9	13.6	29.3	26.3

Table 2.7: Natural frequencies of the reference beam configuration for unlocked joint, using modified mode shapes of a free-free beam and one rigid body mode

Table 2.8 shows the results if clamped-free beam mode shapes and the rigid body mode are inserted into the equations of motions (2.49).

nr. of shapes	ω_2 [rad/s]	ω_3 [rad/s]	ω_4 [rad/s]	ω_5[rad/s]	ω_6 [rad/s]
1	10.72				
error [%]	135.6				
2	6.32	31.25			
error [%]	38.9	20.3			
3	5.61	28.92	146.87		
error [%]	23.3	11.3	42.3		
4	5.32	28.35	129.70	382.68	
error [%]	16.9	9.1	25.7	39.3	
5	5.12	27.47	123.90	335.05	687.28
error [%]	12.5	5.7	20.1	21.9	15.2

Table 2.8: Natural frequencies of the reference beam configuration for unlocked joint, using mode shapes of a clamped-free beam and one rigid body mode

As can be seen from table 2.8, the errors are relatively large for a small number of mode shapes used to approximate the exact mode shapes. The convergence of the fundamental frequency towards the exact value is slow, which makes it necessary to use a large number of mode approximate shapes.
Finally table 2.9 shows the results if pinned-free beam mode shapes together with the rigid body mode are used in the equations of motion (2.49).

nr. of shapes	ω_2 [rad/s]	ω_3 [rad/s]	ω_4 [rad/s]	ω_5[rad/s]	ω_6 [rad/s]
1	6.66				
error [%]	46.4				
2	5.71	32.56			
error [%]	25.5	25.3			
3	5.29	32.55	141.87		
error [%]	16.3	25.3	37.5		
4	5.14	29.78	141.81	402.03	
error [%]	13.0	15.0	37.4	46.3	
5	4.91	29.47	123.83	376.12	701.23
error [%]	7.9	13.4	20.0	36.9	17.6

Table 2.9: Natural frequencies of the reference beam configuration for unlocked joint, using mode shapes of a pinned-free beam and one rigid body mode

As in table 2.8, table 2.9 shows that the convergence of the fundamental frequency is relatively slow using mode shapes of a pinned-free beam.
In view of the results for the natural frequencies obtained by the formulation of Lagrange's discretised equations of motion, if various approximate mode shapes as used by other researchers ([8], [32], [33], [35], [36], etc.) are inserted, it is recommended to use only exact mode shapes, which would drastically reduce the computational burden as the number of mode shapes can be kept small.

2.7.2 LOCKED JOINT CASE

As one example for the locked joint case, table 2.10 gives the results of using pinned-pinned beam mode shapes together with the rigid body mode shape $\hat{W}_0(x) = x$ for data set (A) for with a locked joint ($I_g = 0$, $\lambda = 10^6$ Nm/rad).
Table 2.10 shows good agreement of the natural frequencies with the exact values. The use of mode shapes obtained for other boundary conditions, as in the previous tables, gives similar results. This is mainly due to the fact that in all the cases the rigid body mode shape allows for the rigid body motion due to the joint stiffness, which in the present case is an important part of the total beam motion. It is stressed that not taking into account the rigid body mode when using assumed mode shapes leads to incorrect results, see table 2.13.

nr. of shapes	ω_1 [rad/s]	ω_2 [rad/s]	ω_3 [rad/s]	ω_4 [rad/s]	ω_5 [rad/s]
1	0.43				
error [%]	10.3				
2	0.42	6.07			
error [%]	7.7	17.2			
3	0.41	5.95	95.34		
error [%]	5.1	14.9	17.0		
4	0.40	5.57	93.75	264.36	
error [%]	2.6	7.5	15.1	11.7	
5	0.39	5.52	86.87	258.04	511.28
error [%]	0.0	6.6	6.6	9.0	6.8

Table 2.10: Natural frequencies of the reference beam configuration for locked joint, using mode shapes of a pinned-pinned beam and one rigid body mode

In view of the above analyses it thus appears that the use of assumed multi-mode expansions based on uniform Bernoulli beams, by previous researchers can only be justified if the number of mode shapes is relatively large to get a good approximation of the fundamental frequency. It is also clear that the alternative use of polynomials for say the lowest mode should be based on static deflection curves of a cantilever beam with static end force and moment applied at $x = L$, together with a rigid body deflection shape to allow for the rigid body motions in case of either a locked or unlocked joint. The respective static forces and moments should be equivalent to the translatory and rotatory inertia forces of the payload.
Thus it is essential that approximate mode shapes should satisfy the boundary conditions at $x = 0$ and $x = L$.

2.8 DYNAMIC RESPONSE ANALYSES

The exact analytical mode shapes are clearly complex trigonometric and hyperbolic functions, which are therefore unsatisfactory for general dynamic analysis of flexible robot systems, when deriving the equations of motion for simulations and dynamic response analyses.
Thus a polynomial approximation of the exact mode shape functions can be obtained by a standard interpolation fit in the form $W_{app}(x) = \sum_{n=1}^{N} a_n x^n$. Prior to any computations it is ensured that the approximate polynomials deviate only with a maximum relative magnitude of 10^{-3} from the original functions. A test case proves that the dynamic responses using polynomials is identical to the response using the original functions within the boundaries of a sensible accuracy, say 0.1%. To avoid confusion, the polynomials are also called "exact" mode shapes from here on.

2.8.1 UNLOCKED JOINT CASE

For the dynamic behaviour of the single link system the consequences of the gear train backdriveability of the joints are considerable. At the SRMS, joint backdriveability should avoid overloads of the gear trains due to vibrations and accidental impact reaction forces.
Inserting the first two exact (non-rigid) mode shapes $W_2(x)$ and $W_3(x)$ as computed and shown in chapter 2.2.2 for data set (A) with unlocked joint (λ = 0, I_g = 1188 kgm^2) into the equations of motion (2.49) and applying a torque to the reference beam system with unlocked joint yields relatively small deflections, as was expected from the figures, tables and explanations in sections 2.2.1 and 2.2.2.
For example, choosing a step function torque at x = 0 so that the rigid body angular acceleration of the link is $\ddot{\alpha}(t) = 0.004$ rad/s^2 = const. yields a maximum elastic deflection of only 0.023 mm of the free beam end E at $x = L$ and an angular rotation at x = 0 of 0.002°, which can cause wear and fatigue of the gear teeth and bearings ([1]). These small figures may appear to be unlikely, hence as a check an approximate calculation is performed, assuming that in the first mode the payload oscillates about G at $x = L + b/2 = L + a$ as shown in figure 2.19.

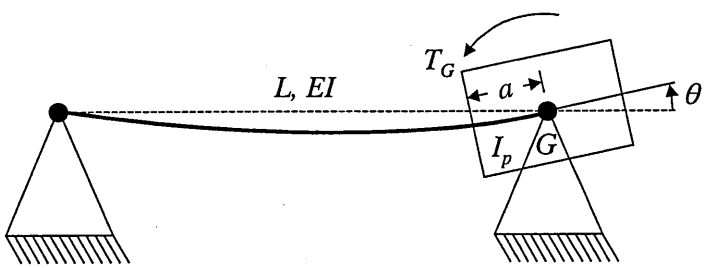

Figure 2.19: Simplified model of unlocked joint system for check calculation

Assuming a pinned-pinned beam of length $L + a$ and flexural stiffness EI with an applied moment T_G about G at $x = L + a$, the angular displacement θ is given as [45]

$$\theta = \frac{T_G (L+a)}{3EI} \tag{2.52}$$

hence the angular stiffness k is $$k = \frac{T_G}{\theta} = \frac{3EI}{L+a} \tag{2.53}$$

Let I_p be the rotational inertia of mass M_p about the attachment point G at $x = L + a$. From equation (2.53) the equations of motion the first mode of the simplified system is

$$I_p \ddot{\theta} + k\theta = T_G \tag{2.54}$$

where T_G is the exciting torque, or

$$\ddot{\theta} + \omega_1^2 \theta = \frac{T_G}{I_p} \tag{2.55}$$

and thus the square of the only natural frequency is

$$\omega_1^2 = \frac{3EI}{I_p(L+a)} \tag{2.56}$$

The exciting torque T_G about G due to angular acceleration $\ddot{\alpha}$ is

$$T_G = I_p \ddot{\alpha} \tag{2.57}$$

The solution of equation (2.55) for a step function torque input is then

$$\theta = \frac{T_G}{I_p \omega_1^2}(1-\cos\omega_1 t) = \frac{\ddot{\alpha}}{\omega_1^2}(1-\cos\omega_1 t) \tag{2.58}$$

and therefore the maximum angular rotation about the mass centre G is

$$\theta_{\max} = \frac{2T_G}{I_p \omega_1^2} = \frac{2\ddot{\alpha}}{\omega_1^2} \tag{2.59}$$

and hence the amplitude of vibration about G is

$$\theta_{\text{amp}} = \frac{T_G}{I_p \omega_1^2} = \frac{\ddot{\alpha}}{\omega_1^2} \tag{2.60}$$

Inserting the reference data into the above equations and again letting the rigid body angular acceleration of the link be $\ddot{\alpha}(t) = 0.004$ rad/s^2 = const., equation (2.59) yields $\theta_{\max} = 0.0148^{\circ}$ and equation (2.56) gives $\omega_1 = 3.93$ rad/s. Considering the fact that this is only an approximate calculation neglecting distributed beam mass and the second rotational inertia at the other beam end due to the gear box and assuming pinned-pinned boundary conditions for a link length $L + a$, the result confirms the small magnitude of the rotations for a pinned joint at $x = 0$.

Having checked on the results obtained when using exact mode shapes in the equations of motion we can make a variation. To this end we compute the exact mode shapes $W_2(x)$ and $W_3(x)$ for data identical to data set (A) except that $M_p = 0$. Repeating the simulations with a ten-fold increased angular acceleration $\ddot{\alpha}(t) = 0.04$ rad/s^2 = const. then yields translational and angular deflections of the free beam end at $x = L$ of 0.0009 mm and 0.00002° respectively. This shows that the deflections are also very small for small or zero payload masses.

Examining the figures above it becomes obvious that an increase in the number of mode shapes used in the equations of motion (2.49) will not change the dynamic response magnitude drastically. This shows that if a manipulator arm is rotated about a free joint, the elastic deflections are practically zero for the whole range of payload masses and can therefore be neglected. Thus a driven single link with the given properties can be assumed to behave as a rigid body.

2.8.2 LOCKED JOINT CASE

As shown in the previous section, the backdriveability of the joint gear trains yields practically zero elastic link deflection if a link is not locked with brakes on and if the manipulator has properties similar to those of the SRMS. On the other hand, if the joint is locked the link will show greater elastic deflections due to the presence of joint stiffness, which create a cantilever beam system with a much lower natural frequency.
To check the following results of dynamic response analyses of the locked joint system using various sets of mode shapes, we first calculate the analytical solution.
Taking data set (A) for the locked joint system (I_g = 0, λ = 10^6 Nm/rad) shown in figure 2.18, letting I_0= 10^{20} kgm^2 and neglecting the distributed beam mass, the translational acceleration a_G of the payload centre of mass G, caused by an angular acceleration $\ddot{\alpha}(t)$ of I_0 and thus of the whole system (for example a space station angular acceleration) due to a torque $T_0(t)$, is given by

$$a_G = \ddot{\alpha}(L+a) \tag{2.61}$$

where L is the length of the link and a the tangential distance of the payload centre of mass G from the link end E at $x = L$. The inertia force F_i and moment M_i about the payload centre of mass G due to its mass M_p and its rotational inertia I_p are given as

$$F_i = M_p\, a_G \tag{2.62}$$

and

$$M_i = I_p\, \ddot{\alpha} \tag{2.63}$$

Inserting the above data and $\ddot{\alpha}(t) = 0.004$ rad/s^2 = const., equations (2.62) and (2.63) yield F_i = 620 N and M_i = 150 Nm. Due to the offset a of the payload centre of mass G from the end of the link, the effective inertia moment M_{iL} about the link end E is given by

$$M_{iL} = M_i + F_i\, a \tag{2.64}$$

which, for the given values, yields M_{iL} = 1080 Nm. The (linearised) rigid body deflection y_J of the link end due to the angle β against the joint stiffness λ is given as

$$y_J = \beta L = \left(\frac{F_i L + M_{iL}}{\lambda} \right) L \tag{2.65}$$

The deflections y_F and y_M of the free end of a cantilever or clamped-free beam due to F_i and M_{iL} are ([45])

$$y_F = \frac{F_i L^3}{3EI} \tag{2.66}$$

and $$y_M = \frac{M_{iL} L^2}{2EI} \tag{2.67}$$

The total deflection y_L of the link end E at $x = L$ is the sum of all the deflections of equations (2.65), (2.66) and (2.67), thus

$$y_L = y_J + y_F + y_M \tag{2.68}$$

Inserting all data into equations (2.61) through (2.67), equation (2.68) yields y_L = 36.10 cm. Inserting F_i and M_{iL} into a FE programme (© S. Wiedemann, 2000) yields also y_L = 36.10 cm.

Inserting a number of exact mode shapes for data set (A) with a locked joint ($I_g = 0$, $\lambda = 10^6$ Nm/rad) as shown in figures 2.9 through 2.13 into the equations of motion (2.49) should yield results in close agreement with the analytical figures above if we choose $T_0(t)$ so that $\ddot{\alpha}(t) = 0.004$ rad/s^2 = const.

It is stressed again that although the system to validate the locked joint mode shapes, see figure 2.18 and text, is different from that for which the mode shapes were computed due to the additional I_0, the very high value for I_0 effectively produces a fixed base for the link during vibrations, and the natural frequencies as computed with equation (2.50) prove that the original frequencies listed in table 2.1 for the locked joint case are not affected by the additional degree of freedom represented by I_0.

Solving the equations of motion (2.49) leads to maximum amplitudes of vibrations of the free link end E at $x = L$ as given in table 2.11, when an increasing number of exact mode shapes is inserted into the equations of motion.

nr. of shapes	vibration amplitude
1	36.24 cm
2	36.15 cm
3	36.14 cm

Table 2.11: Dynamic response, when an increasing number of exact mode shapes is inserted into the equations of motion

Table 2.11 shows that the amplitude of vibration converges to ≈ 36.14 cm with an increasing number of exact mode shapes, which is in very close agreement to the figures obtained by the analytical calculation above, all the more since in the simulations the distributed beam mass is taken into account. Also, table 2.11 shows that the share of the second and third mode shape in the total elastic deflection of the link is very small with less than 0.3 %, which was expected from the figures of the mode shapes for the locked joint system, figures 2.9 through 2.13. This fact allows for the use of only the first mode shape in dynamic response analyses.

Note that since in the present case there is no rigid body mode of the flexible link due to the joint stiffness λ at $x = 0$, no rigid body mode is used in the equations of motion with the exact mode shapes.

Table 2.12 gives the results of the simulation, when various assumed mode shapes as listed in section 2.7 are inserted into the equations of motion (2.49). It was mentioned

before that all the mode shapes lead to natural frequency agreements similar to those given in table 2.10. It is noted that in all the cases two elastic mode shapes from beams with the listed boundary conditions are inserted, whereas the third mode shape is a rigid body deflection ($\hat{W}_3(x) = x$) to allow for the rigid body motion due to the joint stiffness. Note that the free-free mode shapes are modified as described in 2.7.1.

mode shapes	vibration amplitude
pinned-pinned	30.98 cm
free-free	34.01 cm
pinned-free	31.03 cm
clamped-free	35.94 cm
clamped-clamped	13.69 cm

Table 2.12: Dynamic response, when two assumed elastic modes shapes and one rigid body mode shape are inserted into the equations of motion

The last row in table 2.12 is given for a check, thus mode shapes of clamped-clamped boundary conditions have no effect on the displacements of the payload, since they do not allow for rotation or translation at the beam ends. Therefore the deflections should only appear due to the rigid body motion against the joint stiffness λ at $x = 0$. Neglecting the distributed beam mass, the rigid body motion due to the joint stiffness can be calculated with equations (2.61) through (2.65), which on insertion of the given data yields 13.66 cm. This value is in almost exact agreement with row 5 in table 2.12, and the deviation is only due to the distributed beam mass. Table 2.12 shows that although the natural frequencies obtained by the equations of motion may be in good agreement with the exact values, see table 2.10 and text, the deflections can differ considerably from the deflections obtained by using the exact mode shapes. It is stressed here that from experimental work ([47], [66], [67], [68] and others) it is known that even though the frequencies using assumed mode shapes may already be in close agreement with the exact values, the translatory deflections can still be in gross error to analytical values, and the convergence of the rotatory deflections against exact numbers is usually the slowest.
If a third elastic mode shape is inserted instead of the rigid body deflection shape, thus not allowing for the rigid body motion due to the joint stiffness, the results of the simulations as above are given in table 2.13.

mode shapes	vibration amplitude
free-free	0.68 cm
pinned-free	0.93 cm
clamped-free	22.37 cm
pinned-pinned	0.00 cm

Table 2.13: Dynamic response for three elastic modes shapes for various boundary conditions without a rigid body mode shape

Table 2.13 shows that the errors are large if the rigid body mode is not taken into

account and is only given as a reminder for all researchers using assumed modes.
As one example for the use of simple polynomials in the equations of motion we finally consider the following approximate fundamental mode shape

$$\hat{W}(x) = 3\left(\frac{x}{L}\right)^2 - \left(\frac{x}{L}\right)^3 \tag{2.69}$$

for the static deflection of a clamped-free beam with a point mass ([45]). Using this mode shape together with a rigid body mode shape to allow for the rotation due to the joint stiffness in the equations of motion (2.49) yields a vibration amplitude of 36.14 cm, which is in exact agreement when using the first three exact mode shapes.
For M_p = 20000 kg and M_p = 50 kg (and corresponding I_p), using equation (2.69) and a rigid body mode shape in the equations of motion also yields results that are in almost exact agreement with the results obtained using the first three exact mode shapes for the actual cases. The deviations are 0.02 mm and 0.07 mm respectively, thus allowing for the use of the mode shape given by equation (2.69) for the whole range of payloads for the single flexible link system with locked joint.
From all the previous analyses it is concluded that if the joint is unlocked, the link can be assumed to be rigid, and if the joint is locked, the elastic deflection can be described with very high accuracy as a cantilever beam with end mass, equation (2.69), together with a rigid body rotation due to the joint stiffness, $\hat{W}(x) = x$.

2.9 FEASIBILITY OF REACTION WHEEL DAMPING

The use of reaction wheels is common practice in three-axis control of spacecraft to provide stiffness and damping about the principal axes. The reaction wheel operates by feeding a signal to its direct current drive motor, proportional to the spacecraft angular velocities and displacements. From Newton's third law there is then an equal but opposite reaction torque on the spacecraft, which provides the required control damping and stiffness torque.
In space operations, such as transferring payloads from the SRMS to the Space Station, damping of residual (post slew) vibrations is necessary if accurate positioning is to be achieved. Structural damping is usually small, β = 0.01 ([1]), hence time for decay of vibration can be excessive and some form of active damping augmentation is required. Active damping will also reduce vibratory forces applied to the SRMS gear trains and minimise vibration effects on sensitive payload equipment.
The reaction wheel can also be used for damping out structural vibrations ([51], [64]), providing the frequencies are not too high, say for the first one or two modes of vibration. In that case sensors, such as accelerometers or rate gyros measure the modal velocities, which are then fed back to collocated or non-collocated torque controllers (reaction wheels) to damp out vibration.
The limiting factors in adding reaction wheels to a RMS are their mass, which may be large, compared to the links but much smaller than most payloads, and their power consumption, which may exceed the resources of the Shuttle or the Space Station.
For the single flexible link with payload, the reaction wheel would be mounted at or

near to the position of the greatest angular rotation, which is near to the payload.
To show the feasibility of reaction wheel damping and to give an idea of the dimensions of the wheel size and power requirement, the following simple single degree of freedom manipulator equation of motion is used.
Consider a system as shown in figure 2.18 with one elastic degree of freedom $q_1(t)W_1(x)$, where $W_1(x)$ is the first exact mode shape for a locked joint as shown in figure 2.9 for data set (A). The equations of motion (2.49) are obtained by applying equation (2.48) to the kinetic energy expression, equation (2.44) or (2.46), giving a system with two degrees of freedom $\mathbf{p} = [\alpha(t),\ q_1(t)]^T$. Then the off-diagonal or coupling elements are $M_{12} = M_{21} = (L+a)W(L)M_p + W'(L)[(L+a)M_p + I_p]$ in the mass matrix **M**. As outlined in section 2.5, we assume the rigid body motion $\alpha(t)$ of the system due to $T_0(t)$ to be prescribed, so that $\ddot{\alpha}(t)$ is known. Thus we can strike the first row in the equations of motion and bring the $\ddot{\alpha}(t)M_{21}$ term to the right hand side. Now M_{21} is called the exciting force coefficient. Adding a damping term $C\dot{q}$ as a generalised non-conservative force, this finally gives one equation of motion

$$M_{22}\ddot{q} + C\dot{q} + K_{22}q = M_{21}\ddot{\alpha} \qquad (q = q_1 = p_2) \tag{2.70}$$

where M_{22} is now the modal mass. The reaction wheel damping torque M_w is

$$M_w(t) = g_w\ \dot{q}(t) \tag{2.71}$$

where g_w is the feedback gain. The modal damping force is obtained by considering the virtual work done on an infinitesimal beam rotation $\delta\Phi(L_w)$, where L_w denotes the location of the reaction wheel, measured from the joint. The virtual work is then

$$\delta W = M_w(t)\delta\Phi \tag{2.72}$$

where $W'(L_w)$ is the elastic slope of the link at L_w. Then equations (2.71) and (2.72) give

$$\delta W = g_w\,\dot{q}(t)W'(L_w)\delta q \tag{2.73}$$

and thus the modal damping force is

$$F_d(t) = -\frac{\delta W}{\delta q} = -g_w\,\dot{q}(t)W'(L_w) = -C\dot{q}(t) \tag{2.74}$$

where

$$C = g_w W'(L_w) \tag{2.75}$$

Also, C in equation (2.70) is given by

$$C = 2\beta\omega_1 M_{22} \tag{2.76}$$

where ω_1 is the fundamental natural frequency and β the damping ratio. The solution of equation (2.70) for a step torque input, which gives the greatest elastic response, is

$$q(t) = -\frac{M_{21}\,\ddot{\alpha}}{M_{22}\,\omega_1^2}\left(1 - e^{-\beta\omega_1 t}\left(\cos\omega_d t - \frac{\beta}{\sqrt{1-\beta^2}}\sin\omega_d t\right)\right) \tag{2.77}$$

where $\omega_d = \omega_1\sqrt{1-\beta^2}$ is the damped natural frequency. For small β, equation (2.77) gives the maximum amplitude of vibration for the step function $\ddot{\alpha}$ as

$$q_{\max} \approx \frac{M_{21}\,\ddot{\alpha}}{M_{22}\,\omega_1^2} \tag{2.78}$$

and

$$\dot{q}_{\max} \approx \omega_1\, q_{\max} \tag{2.79}$$

Then the maximum modal damping force from equations (2.74), (2.76) and (2.79) is

$$\delta F_d = 2\beta\omega_1^2\, M_{22}\, q_{\max} \tag{2.80}$$

and the gain constant g_w for a specified damping ratio β can be obtained from equations (2.75) and (2.76) as

$$g_w = \frac{2\beta\omega_1 M_{22}}{W'(L_w)} \tag{2.81}$$

where M_{22} denotes the modal mass in the equation of motion, as mentioned.

Calculation of wheel size: The wheel executes harmonic motion, thus the maximum damping torque is equal to the maximum inertia torque, and therefore equation (2.71) yields

$$M_{w,\max} = I_w\,\omega_1^2\,\alpha_0 = g_w\,\dot{q}_{\max} \tag{2.82}$$

where I_w is the moment of inertia of the reaction wheel, α_0 is the amplitude of the oscillatory wheel motion in [rad] and $W'(L_w)$ the mode shape slope at L_w. Inserting the reference data for the locked joint case L = 14 m, m_b = 3.9786 kg/m, $EI = 3\times10^6$ Nm^2, M_p = 10000 kg, I_p = 37500 kgm^2 (about G), $a = b/2$ = 1.5 m, $\lambda = 10^6$ Nm/rad, and ω_1 = 0.39 rad/s, and choosing $\ddot{\alpha}(t)$ = 0.004 rad/s^2 = const. and say β = 0.01, equation (2.82) yields $M_{w,\max}$ = 59.6 Nm, assuming that $L_w \approx L$. Note that although the first mode shape for the locked joint system is computed without damping, a small damping ratio β does not change the mode shape, as confirmed by a test with BEAM. Another proof of this statement is given in section 9.
The rotational inertia I_w of a solid wheel of diameter d_w and mass m_w is given as

$$I_w = \tfrac{1}{8} m_w\, d_w^2 \tag{2.83}$$

Selecting a solid wheel of mass m_w = 100 kg and diameter d_w = 0.7 m, equation (2.83) yields I_w = 6.125 kgm^2. Using a dense material like iron (density $\rho \approx 8$ g/cm^3), the wheel thickness t_w is given as

$$t_w = \frac{4 m_w}{\pi d_w^2 \rho} \tag{2.84}$$

For the given data, equation (2.84) yields t_w = 3.25 cm. Finally, inserting the known data into equation (2.82) yields α_0 = 65.1 rad (10.4 revolutions). If the exciting angular acceleration $\ddot{\alpha}(t)$ is increased for example two-fold, then to maintain the same damping ratio, α_0 also has to increase two-fold.

Calculation of power requirement: Let $\alpha(t) = \alpha_0 \sin \omega_1 t$, $\dot{\alpha}(t) = \omega_1 \alpha_0 \cos \omega_1 t$ and $M_w = M_{w,\max} \cos \omega_1 t$, then the work done per second is given as

$$\frac{\mathrm{d}W}{\mathrm{d}t} = M_w(t)\dot{\alpha}(t) = M_{w,\max}\, \alpha_0\, \omega_1 \cos^2 \omega_1 t \tag{2.85}$$

which is a maximum when $\omega_1 t = 0, \pi, 2\pi, \ldots$ Thus the maximum power consumption is

$$\frac{\mathrm{d}W}{\mathrm{d}t}(\max) = M_{w,\max}\, \alpha_0\, \omega_1 \tag{2.86}$$

Inserting $M_{w,\max}$ from equation (2.82), equation (2.86) yields dW/dt (max) = 1500 Watts. Using a wheel of mass m_w = 100 kg, but diameter d_w = 1 m leads to dW/dt (max) = 735 Watts. The achievable damping ratio and therefore the energy consumption depends on the reaction wheel inertia I_w, and thus on the size of the wheel and its shape. The major problems in adding reaction wheels to the RMS are the mass and size of the system and the associated sensors and electronics. Also since out of plane oscillation would require an additional orthogonal wheel, the use of reaction wheels as active damping actuators appears to be not easily realisable.

2.10 SHUTTLE / RMS INTERACTION

The purpose of this section is to analyse the interaction between an RMS and the Shuttle. Therefore some simple example calculations are used to give an idea of the magnitude of the interactions. Only this section applies a 3D model for analysing the effect of bang-bang torques applied to the rigid RMS / payload on the Shuttle (cases 1, 2 and 3). The effects of Shuttle thruster firing on a flexible RMS (case 4) are analysed using the usual planar model.

In the previous analysis of the RMS vibration it is assumed that the shoulder pivot point is inertially fixed, implying that the effect of Shuttle motion on the RMS vibration is negligible. In reality however the RMS shoulder pivot O is positioned offset from the Shuttle longitudinal axis at the cockpit end of the payload bay. This point is some considerable distance from the Shuttle mass centre which lies at about the ¼ chord point of the delta wing.

A possible sequence of payload manoeuvre is shown in figure 2.20.

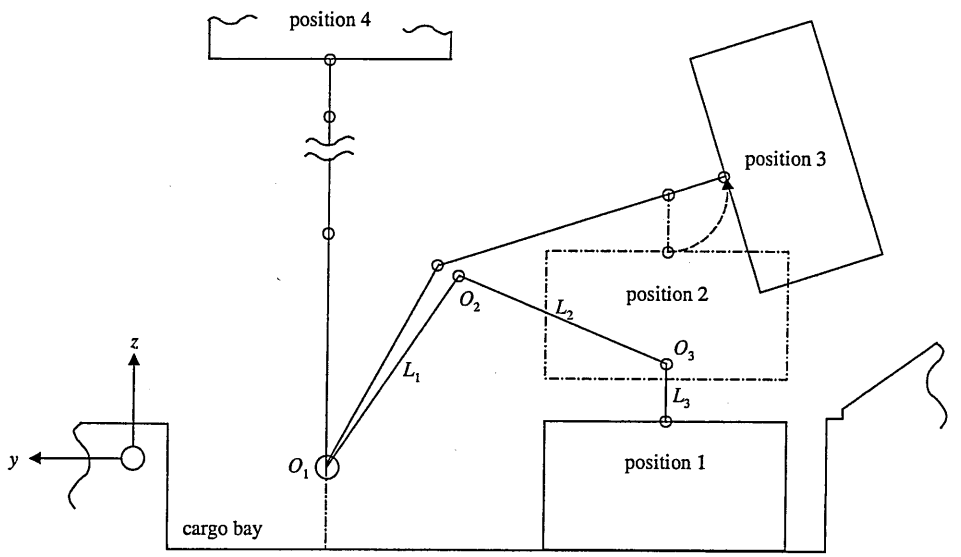

Figure 2.20: Example planar manoeuvre of payload deployment

In this section however only a straight single rigid RMS system is considered for simplicity, and the RMS axis is assumed to be parallel to one axis of symmetry of the payload.
The following simplified analysis assumes a hypothetical situation where the payload is grappled with the RMS straight and lifted clear of the payload bay through 90°. The degrees of freedom of the Shuttle are limited to roll motion only, neglecting surge, pitch, heave and yaw.
Clearly the Shuttle rigid body motion is produced by the RMS shoulder joint reaction caused by angular acceleration and deceleration of the payload. In case 1, the Shuttle is assumed to have only roll motion γ about the y axis with the other degrees of freedom restrained. The analysis yields the variation of roll angle γ, velocity $\dot{\gamma}$ and acceleration $\ddot{\gamma}$. Angle γ indicates how much the payload deviates from its desired inertial position due to the Shuttle motion. Acceleration $\ddot{\gamma}$ indicates how much lateral inertial excitation force will act on the slewing RMS.

Case 1

At first, we consider the configuration of figure 2.21: the single link RMS is initially parallel to the Shuttle main axis, and a bang-bang torque $\pm T_0(t)$ is applied. The simplified simulation yields the roll motion γ of the Shuttle about the y-axis.
Figure 2.21 shows that application of $T_0(t)$ to the RMS at the pivot O causes a centrifugal force F_C and a reaction force F_R at O due to the payload inertia force (note that the small reaction torques due to the high ratio gear trains at driven joints are neglected, see the general assumptions in chapter 1.3). Also the pivot O is offset from the Shuttle centre of mass CM_S by Δx.
The forces together with the offset cause a roll moment on the Shuttle about the y-axis. It is noted that the angle α of the RMS relative to the Shuttle is measured from the negative Shuttle y-axis. Also note the payload local reference frame x', y' and z'.

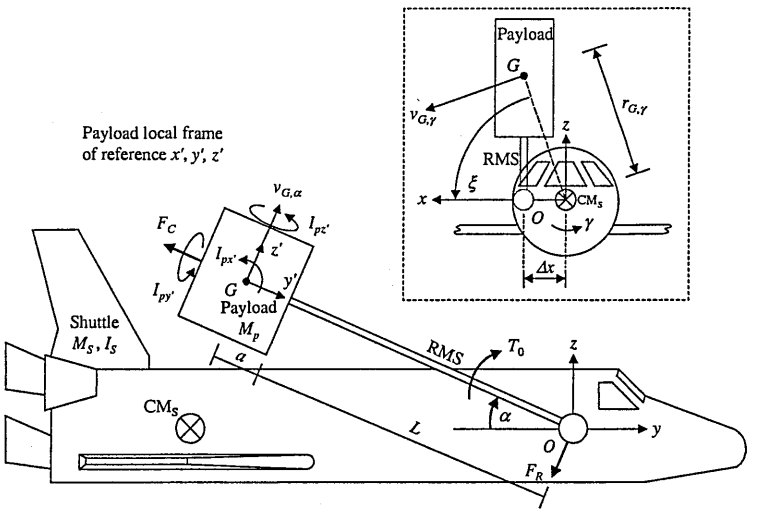

Figure 2.21: Analysis of effects of bang-bang torque applied to RMS on the Shuttle

The following simulations are performed using the equations of motion as obtained from Lagrange's equation computed with MATHEMATICA and, for comparison, with SIMPACK.

To derive the system kinetic energy T for the Lagrangian, we consider figure 2.21. The velocity $v_{G,\alpha}$ of the payload centre of mass G at distance $(L+a)$ from O due to the RMS rotation about O is

$$v_{G,\alpha} = \dot{\alpha}(L+a) \tag{2.87}$$

The velocity $v_{G,\gamma}$ of G due to the Shuttle rotation about its y-axis is

$$v_{G,\gamma} = \dot{\gamma} r_{G,\gamma} \tag{2.88}$$

where

$$r_{G,\gamma} = \sqrt{\Delta x^2 + [(L+a)\sin\alpha]^2} \tag{2.89}$$

Taking the components of $v_{G,\alpha}$ and $v_{G,\gamma}$ in x, y, and z, the total translational velocity v_G of G is

$$v_G = \sqrt{\underbrace{\left(v_{G,\gamma}\sin\xi\right)^2}_{(x)} + \underbrace{\left(v_{G,\alpha}\sin\alpha\right)^2}_{(y)} + \underbrace{\left(v_{G,\alpha}\cos\alpha - v_{G,\gamma}\cos\xi\right)^2}_{(z)}} \tag{2.90}$$

where ξ in figure 2.21 is

$$\xi = \arctan\left(\frac{(L+a)\sin\alpha}{\Delta x}\right) \tag{2.91}$$

The payload rotational kinetic energy is $\frac{1}{2}I_{px'}\dot{\alpha}^2 + \frac{1}{2}I_{py'}(\dot{\gamma}\cos\alpha)^2 + \frac{1}{2}I_{pz'}(\dot{\gamma}\sin\alpha)^2$, where the three moments of inertia $I_{px'}$, $I_{py'}$ and $I_{pz'}$ are indicated in figure 2.21. Assuming that $I_{px'} = I_{py'} = I_{pz'} = I_p$, the total kinetic energy T is

$$T = \tfrac{1}{2} M_p v_G^2 + \tfrac{1}{2} I_{Sy} \dot{\gamma}^2 + \tfrac{1}{2} I_p \left(\dot{\gamma}^2 + \dot{\alpha}^2 \right) \tag{2.92}$$

where M_p is the payload mass and I_{Sy} the Shuttle rotary inertia about its y-axis.
Applying Lagrange's equation (2.48) to the generalised coordinates $\mathbf{p}(t) = [\gamma(t), \alpha(t)]^T$ yields the equations of motion with a 2×2 mass matrix **M**, where the elements M_{nm} are given as

$$\begin{aligned} M_{11} &= I_p + I_{Sy} + \Delta x^2 M_p + (L+a)^2 M_p \sin\alpha^2 \\ M_{12} &= M_{21} = -\frac{(L+a)^2 M_p \cos\alpha \sqrt{\Delta x^2 + [(L+a)\sin\alpha]^2}}{\sqrt{1 + \dfrac{[(L+a)\sin\alpha]^2}{\Delta x^2}}} \\ M_{22} &= I_p + (L+a)^2 M_p \end{aligned} \tag{2.93}$$

As mentioned in chapter 2.5, only in this section the term $\partial T/\partial p_j(t)$ in Lagrange's equation (2.48) is not neglected to get results that should be identical to those of SIMPACK. Thus vector **c** due to Coriolis and other effects has elements c_j given as

$$\begin{aligned} c_1 &= \frac{(L+a) M_p \alpha \sin\alpha \left(2(L+a)\dot{\gamma}\cos\alpha \sqrt{\Delta x^2 + [(L+a)\sin\alpha]^2} + \Delta x^2 \alpha \sqrt{1 + \dfrac{[(L+a)\sin\alpha]^2}{\Delta x^2}} \right)}{\sqrt{\Delta x^2 + [(L+a)\sin\alpha]^2}} \\ c_2 &= -\tfrac{1}{2}(L+a)^2 M_p \dot{\gamma}^2 \sin(2\alpha) \end{aligned} \tag{2.94}$$

Since the only generalised force is $T_0(t)$ at O the equations of motion for the present case are written in matrix form as

$$\mathbf{M} \begin{bmatrix} \ddot{\gamma} \\ \ddot{\alpha} \end{bmatrix} + \mathbf{c} = \begin{bmatrix} 0 \\ T_0 \end{bmatrix} \tag{2.95}$$

The data are chosen as L = 14 m, M_p = 10000 kg, a = $b/2$ = 1.5 m, d = 6 m, I_p = 37500 kgm^2, $T_0(t)$ = 100 Nm = const. and, due to the available information ([60]), the Shuttle mass is estimated to be M_S = 70000 kg, the moment of inertia to be $I_{Sy} = 10^6$ kgm^2, and the offset of O from CM_S in x to be Δx = 2 m.
Figure 2.22 shows the time history of angle α using MATHEMATICA and SIMPACK. The reasons for the deviations of the two results in figures 2.22 and 2.23 could not be found out but are assumed to be mainly due to different solving algorithms for the differential equations and due to different settings for the solvers.
Figure 2.23 shows the simulation results for the roll angle γ of the Shuttle, and it is seen that again the MATHEMATICA and SIMPACK results are almost identical. Thus the comparison of figures 2.22 and 2.23 also prove that the elements of the system matrices in equation (2.95) are correct.
Note that figure 22 does not apply in reality, since the work range of the RMS shoulder joint in reality is ([3]) -2°...145° or -0.035...2.531 rad.

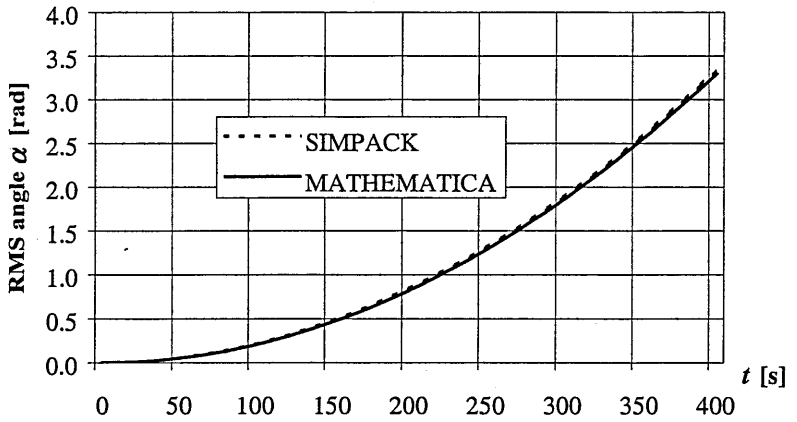

Figure 2.22: Angle α of RMS relative to Shuttle for simulation using MATHEMATICA and SIMPACK

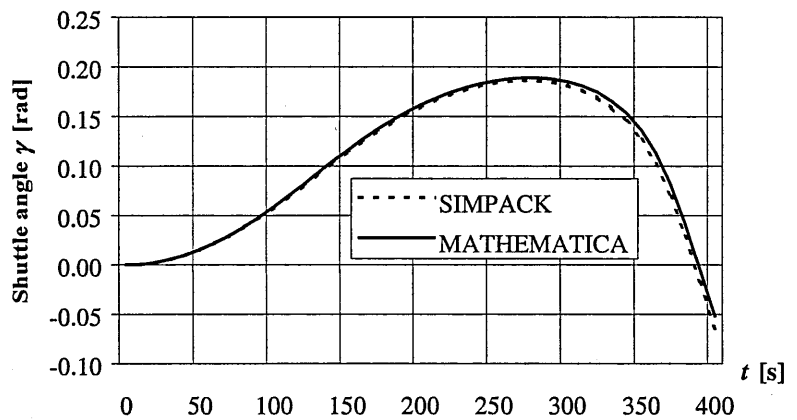

Figure 2.23: Shuttle roll angle γ about y-axis for simulation using MATHEMATICA and SIMPACK

Next consider three examples of a bang-bang acceleration/deceleration for the data given above. The three cases are a 45° slew of the RMS relative to the Shuttle, a 90° slew and a slew with randomly chosen point of time for the deceleration. The decelerating bang-bang torque is chosen so that $\dot{\alpha} = 0$ at the end of the slew manoeuvres. For the first two cases $T_0(t)$ = 1298 Nm, which is the maximum torque at the SRMS shoulder joint ([3]), and for the third case $T_0(t)$ = 1000 Nm. In all cases the maximum allowed shoulder joint velocity of the SRMS, $\dot{\alpha}_{s,\max}$ = 0.004 rad/s, is taken account of. Figure 2.24 shows the results, where for the 90° slew the Shuttle roll acceleration $\ddot{\gamma}$ is also given. Note that these values are multiplied by 500 for better vision and that in the diagram the three cases are $\gamma(45)$, $\gamma(90)$ and $\gamma()$, and $\gamma.. = \ddot{\gamma}$. Figure 2.24 proves that although the directions of the forces F_C and F_R in figure 2.16 change with α, the accelerating and decelerating torque cancel almost exactly. The residual angular velocity $\dot{\gamma}$ is of magnitude of 10^{-6} rad/s. The maximum Shuttle roll acceleration $\ddot{\gamma}$, which in reality excites out of plane motion of the flexible RMS, is $\ddot{\gamma}_{\max} = 1.59\times10^{-4}$ rad/s^2, which is about $0.3\,\ddot{\alpha}$. Thus the effect of a torque applied by the RMS on the Shuttle roll motion is clearly obvious.

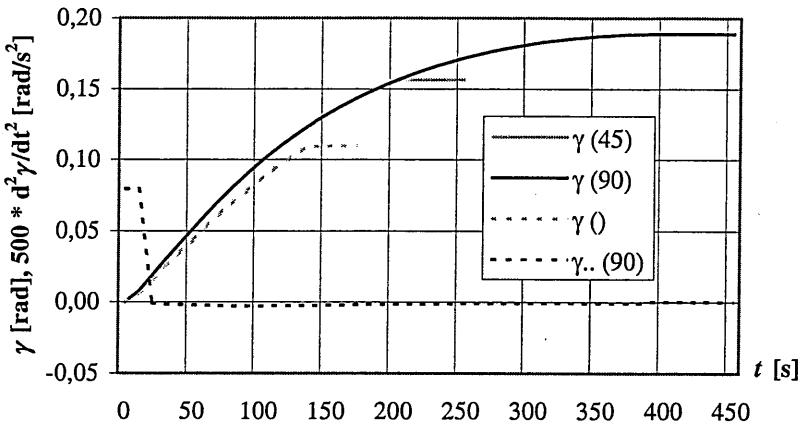

Figure 2.24: Effect of bang-bang torque for various RMS slew angles on γ and $\ddot{\gamma} = \gamma..$

Case 2

We next study only the Shuttle surge motion in y direction due to a torque applied to the RMS. Thus the simplification here is to assume zero roll, pitch, heave and yaw motion. In this case, the position of the Shuttle centre of mass relative to the pivot O is irrelevant. The initial configuration is shown in figure 2.25. By contrast to figure 2.21 the Shuttle is now only free to move in y. The angle α of the RMS relative to the Shuttle is again measured from the negative Shuttle y-axis but now α is 90° in the initial state, so that the RMS is parallel to the Shuttle z-axis.

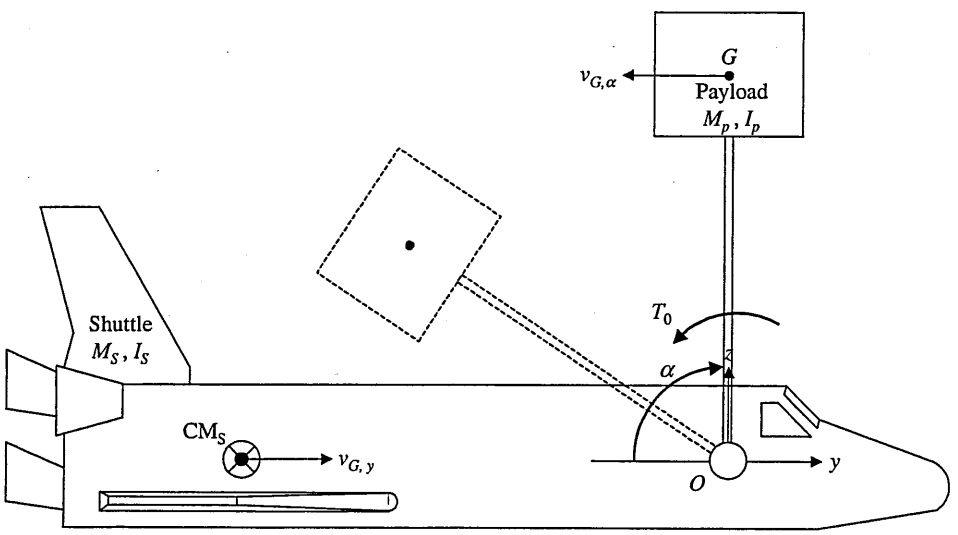

Figure 2.25: Schematic of case 2 simulation

In figure 2.25 the velocity $v_{G,\alpha}$ of G due to rotation about O is given by equation (2.87), and the velocity $v_{G,y}$ of G due to the Shuttle motion in y is

$$v_{G,y} = \dot{y} \tag{2.96}$$

Using the cosine rule, the square of the total velocity v_G of the payload centre of mass G due to $v_{G,\alpha}$ and $v_{G,y}$ is

$$v_G^2 = v_{G,\alpha}^2 + v_{G,y}^2 + 2v_{G,\alpha}\, v_{G,y} \cos\left(\tfrac{1}{2}\pi - \alpha\right) \tag{2.97}$$

The total kinetic energy T is given by

$$T = \tfrac{1}{2} M_p\, v_G^2 + \tfrac{1}{2} I_p\, \dot{\alpha}^2 + \tfrac{1}{2} M_S\, v_{G,y}^2 \tag{2.98}$$

For the present case application of equation (2.48) to the generalised coordinates vector $\mathbf{p}(t) = [y(t),\ \alpha(t)]^T$ yields the 2×2 mass matrix $\mathbf{M}$ with elements M_{nm} given by

$$\begin{aligned} M_{11} &= M_p + M_S \\ M_{12} &= M_{21} = (L+a) M_p \sin\alpha \\ M_{22} &= I_p + (L+a)^2 M_p \end{aligned} \tag{2.99}$$

Also in the present case Lagrange's equation (2.48) again yields a vector $\mathbf{c}$ due to Coriolis, gyroscopic and centrifugal effects. Its elements c_j are given as

$$\begin{aligned} c_1 &= \dot{\alpha}\, \dot{y} (L+a) M_p \cos\alpha \\ c_2 &= 0 \end{aligned} \tag{2.100}$$

Thus the equations of motion are

$$\mathbf{M} \begin{bmatrix} \ddot{y} \\ \ddot{\alpha} \end{bmatrix} + \mathbf{c} = \begin{bmatrix} 0 \\ -T_0 \end{bmatrix} \tag{2.101}$$

where the negative sign of $T_0(t)$ indicates that its direction is opposite to α in figure 2.25. To validate the given equations of motion we first let L = 14 m, M_p = 10000 kg, a = $b/2$ = 1.5 m, d = 6 m, I_p = 37500 kgm^2, Shuttle mass M_S = 70000 kg and $T_0(t)$ = 100 Nm = constant, where the simulations are also performed with SIMPACK for a check. Figure 2.26 shows the results of the Shuttle surge motion in y due to constant T_0. Note that in figure 2.26 the two results are in exact agreement, confirming that the elements in equation (2.101) are correct.

Now we consider the same system, but choose a bang-bang acceleration / deceleration due to $T_0(t)$. The force law is chosen to be $T_0(t)$ = 100 Nm [$\sigma(t) - \sigma(t\text{-}30) - \sigma(t\text{-}100) + \sigma(t\text{-}130.836)$], where σ denotes the step function and where the decelerating torque is chosen so that $\dot{\alpha} = 0$ at the end of the RMS slew. This gives a 45° RMS slew manoeuvre. The result of this simulation is shown in figure 2.27, from which it can be seen that in the present case, the accelerating and decelerating torque cancel almost exactly. The residual values of $\dot{y}$ for various example configurations are of magnitude 10^{-4} to 10^{-7} m/s. From figure 2.27, the final displacement of the Shuttle is y_F = 1.24 m at the end of the simulation.

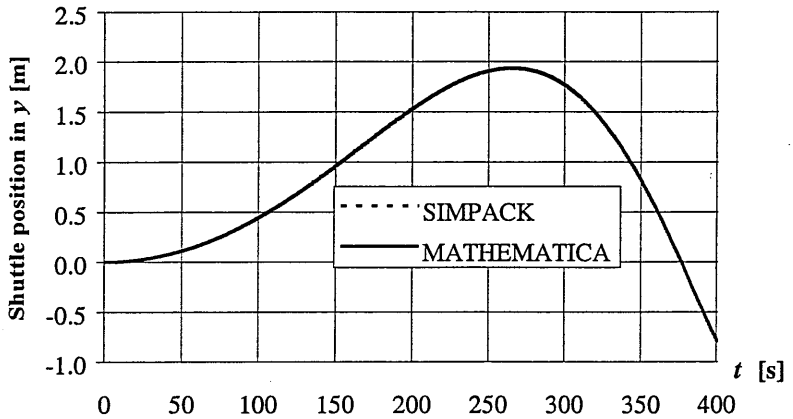

Figure 2.26: Displacement of Shuttle in y due to T_0

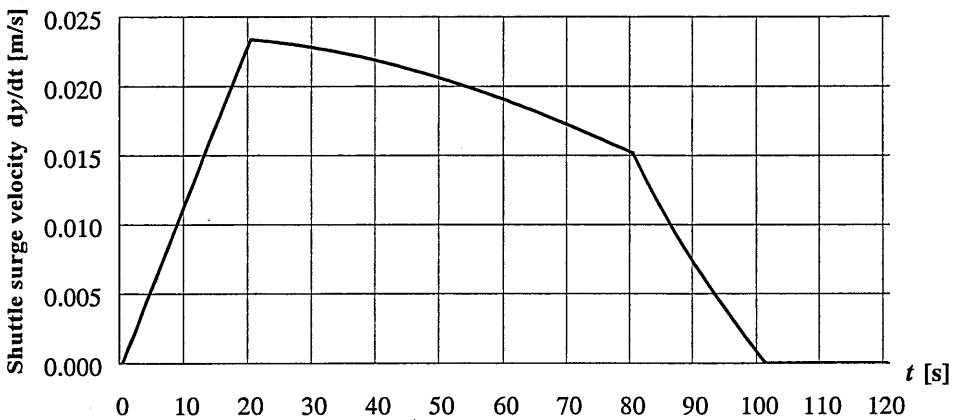

Figure 2.27: Shuttle surge velocity $\dot{y}$ due to bang-bang acceleration/deceleration $\ddot{\alpha}$

Case 3

We next study the inertial translational acceleration a of the payload centre of mass G, depending on whether the Shuttle is assumed to be fixed in space (due to active attitude control) or if it is free to move with all six degrees of freedom. Here a is measured in the plane perpendicular to the RMS axis so that it is a measure of the lateral excitation of the flexible RMS.
The configuration is similar to that shown in figure 2.21, but now the pivot O is offset in x from the Shuttle y-axis by Δx, and also in y by Δy. The data for the offsets are estimated using [60]. Thus L = 14 m, M_p = 10000 kg, a = $b/2$ = 1.5 m, d = 6 m, I_p = 37500 kgm^2, M_S = 70000 kg, I_{Sy} = 10^6 kgm^2, Δx = 2 m, Δy = 14m, and $T_0(t)$ = 1298 Nm = constant. Here a maximum joint velocity is not taken account of to reinforce the effect. In the initial state, the RMS is parallel to the Shuttle y-axis.
The present simulations are performed with SIMPACK only, since the formulation of the kinetic energy of a complex seven-degree-of-freedom three-dimensional system by hand is very tedious and prone to errors.
Figures 2.28 and 2.29 show the results for a fixed and a free Shuttle and the resulting

displacements of the free Shuttle about its y and z axes.

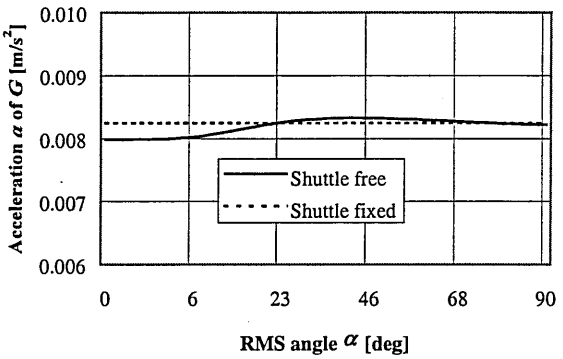

Figure 2.28: Influence of Shuttle freedoms of motion on acceleration a of G

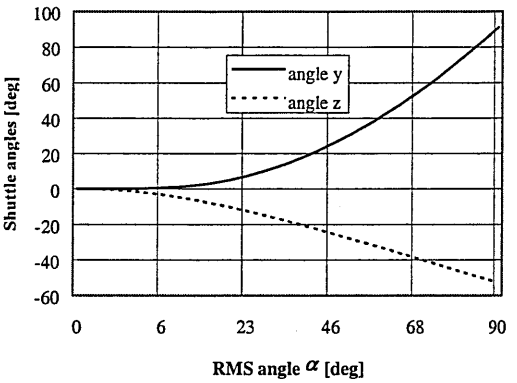

Figure 2.29:Angular displacements of free Shuttle about its y and z axes

Figure 2.28 shows that the translational acceleration a of G in the inertial frame changes only slightly when the Shuttle is free to move in space, whereas the Shuttle angular motions are large, see figure 2.29. The following chapters however will show that even if the inertial acceleration of the payload changes only slightly, the influence of the Shuttle motion on the RMS flexible dynamics is considerable and will lead to much smaller elastic responses of the RMS than with a fixed base. This aspect does not appear to be discussed to any extent in the literature. Note again that figures 2.28 and 2.29 do not apply in reality due to restricted mechanical work ranges and maximum velocities of the joints.

When the RMS angle α = 90° in figures 2.28 and 2.29, the Shuttle angular displacement about its x axis (not shown in the plots) is less than 2°, and all the Shuttle translatory displacements (also not in the plots) are less than 0.5 m. Again it is stressed that the applied torque T_0 is constant and maximum. Taking into account a maximum allowed joint velocity and choosing a smaller torque lead to smaller Shuttle motion effects.

The value of a for a fixed Shuttle in figure 2.28 can be verified as follows. The angular RMS acceleration $\ddot{\alpha}$ is

$$\ddot{\alpha} = \frac{T_0}{I_{p,O}} \tag{2.102}$$

where the effective payload inertia about the pivot O is $I_{p,O} = I_p + M_p (L+a)^2$, and

$$a = \ddot{\alpha}(L+a) \tag{2.103}$$

Inserting the actual data from above yields a = 0.00825 rad/s^2, which is identical with the value in figure 2.28. It is noted that for other values of $T_0(t)$, the results of the actual analysis are similar since the ratios of the various inertias remain the same.

Case 4

The last simulation analyses the effect of Shuttle thruster firing on a flexible RMS. Assuming that the Shuttle is free to move only in y and that joint O is locked, then the RMS will have the greatest dynamic response. This is because if the Shuttle is only free to move in y the force provided by the thrusters will be fully used to accelerate the Shuttle and the payload mass perpendicular to the RMS, which is not the case if the Shuttle is free to rotate. The system is shown in figure 2.30.

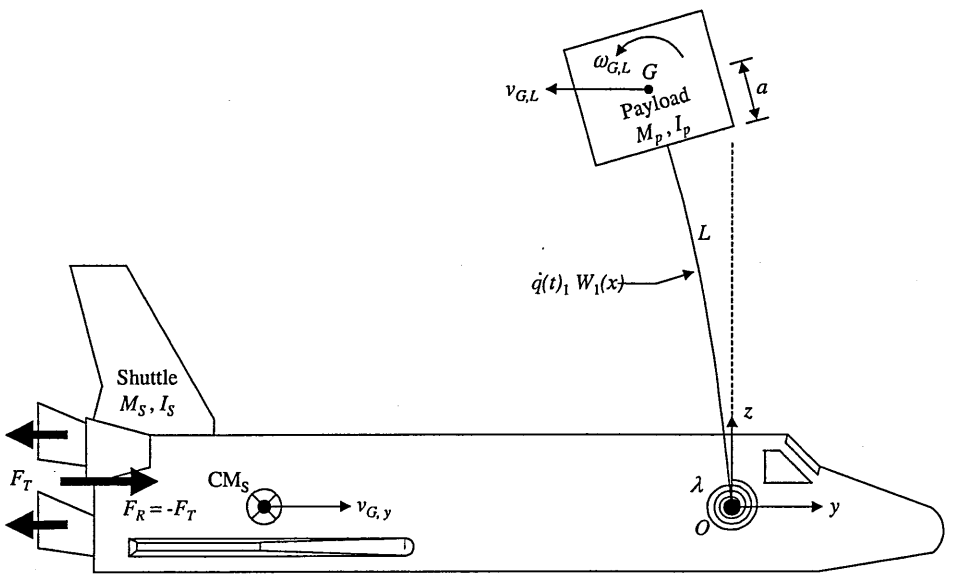

Figure 2.30: Configuration to analyse the effect of Shuttle thruster firing on RMS

Figure 2.30 shows that a thruster firing causes a reaction force F_R on the Shuttle, and the resulting acceleration causes RMS vibration. Note that since the Shuttle is free to move only in y, an offset of the extension of F_R from CM_S can cause no roll motion of the Shuttle.

To formulate the kinetic energy for the Lagrangian, we consider figure 2.30. Using the first exact mode shape $W_1(x)$ obtained by the determinant method for the locked joint case to describe the RMS flexibility, the translatory velocity $v_{G,L}$ of the payload centre of mass G relative to the Shuttle due to RMS deformation is

$$v_{G,L} = \dot{q}_1(t)W_1(L) + \dot{q}_1(t)W_1'(L)a \tag{2.104}$$

where it is assumed that the first exact mode shape $W_1(x)$ does not change if the RMS base is no longer fixed, but free to move linearly. In chapter 6 this assumption will be justified. The payload angular velocity $\omega_{G,L}$ about G is

$$\omega_{G,L} = \dot{q}_1(t)W_1'(L) \tag{2.105}$$

The velocity of the Shuttle is $v_{G,y} = \dot{y}$, and hence the total kinetic energy T is

$$T = \tfrac{1}{2} M_p \left(v_{G,y} - v_{G,L}\right)^2 + \tfrac{1}{2} I_p \, \omega_{G,L}^2 + \tfrac{1}{2} M_S \, v_{G,y}^2 \tag{2.106}$$

In the case at hand the application of equation (2.48) to the generalised coordinates vector $\mathbf{p}(t) = [y(t), q_1(t)]^T$ yields the 2×2 mass matrix $\mathbf{M}$ with elements M_{nm} given by

$$\begin{aligned} M_{11} &= M_p + M_S \\ M_{12} &= M_{21} = -M_p \left(W_1(L) + a W_1'(L)\right) \\ M_{22} &= I_p \, W_1'(L)^2 + M_p \left(W_1(L) + a W_1'(L)\right)^2 \end{aligned} \tag{2.107}$$

Since for the present example the Shuttle and RMS are non-rotating the application of Lagrange's equation (2.48) to the kinetic energy expression does not yield Coriolis, gyroscopic or centrifugal terms. The RMS flexural stiffness and the joint stiffness is taken into account in the strain energy expression, which after applying Lagrange's equation yields the 2×2 stiffness matrix $\mathbf{K}$ with elements

$$\begin{aligned} K_{11} &= K_{12} = K_{21} = 0 \\ K_{22} &= \lambda [W_1'(0)]^2 + EI \int_0^L [W_1''(x)]^2 \, dx \end{aligned} \tag{2.108}$$

where EI denotes the RMS flexural stiffness and λ the joint stiffness at O. The equations of motion are written in matrix form as

$$\mathbf{M} \begin{bmatrix} \ddot{y} \\ \ddot{q} \end{bmatrix} + \mathbf{K} \begin{bmatrix} y \\ q \end{bmatrix} = \begin{bmatrix} F_R \\ 0 \end{bmatrix} \tag{2.109}$$

where $F_R = -F_T$ is the thruster reaction force on the Shuttle.
The system data are L = 14 m, M_p = 30000 kg, a = $b/2$ = 2 m, d = 12 m, I_p = 400000 kgm^2, M_S = 70000 kg and $F_T(t)$ = 6×107 N = const. According to [60], the Shuttle attitude is controlled by at maximum six "Vernier Thrusters", each of which is able produce a thrust of 107 N. This worst case simulation for a large payload, maximum dynamic RMS response and maximum thrust yields a vibration amplitude of the RMS tip of 11.45 cm and of 13.62 cm for the payload centre of mass G.
Inserting the payload properties of data set (A), the simulation yields a vibration amplitude of the RMS tip and of G of 4.59 cm and 5.23 cm respectively.
To verify the statement above that the dynamic response of the RMS is smaller if the Shuttle is free to move in all directions, a rigid body simulation is performed with SIMPACK. For identical system properties, the dynamic response of the rigid RMS due to joint stiffness is about double if the Shuttle is free to move only in y than if the Shuttle has all six degrees of freedom.
The previous analyses show that the RMS / Shuttle interactions are not negligible and make it necessary to control the Shuttle attitude while operating the RMS or to correct it after RMS operation.

2.11 SUMMARY / CONCLUSIONS

The present analyses of the single link robot provide insight into the dynamic response of large space manipulators such as the Space Shuttle Remote Manipulator System (SRMS).
The related literature points out that the joints of the SRMS can have two states: locked and unlocked. The possibility to lock the joints provides help in precision positioning of payloads and additional security in cases of malfunction or dangerous situations. Also the literature stresses that except for a computer controlled motion with more than one joint driven and thus unlocked, the SRMS joints are normally locked, and if manually operated, only one joint is driven at a time.
Information on the SRMS shows that the locked joints have a certain flexibility, referred to as the joint stiffness, and that the driving gear trains can be backdriven from the output side, which avoids overload and damage of the gear box due to accidents, impacts and so on.
Although mentioned in many related papers, a clear investigation of the effects of joint stiffness and gear train backdriveability on the dynamical behaviour of an RMS has apparently not been published. Due to the available information it is assumed that joint stiffness is only relevant if the joints are locked, because in the unlocked state the gear train backdriveability prevents stressing of the gear system and housing.
Since it is not assumed feasible to model the nonlinearities of gear back-lash, flexible housing, deformable bearings and so on, and since the necessary information is not available, the joint stiffness is modelled as a linear revolute spring, in agreement with the related papers.
Using the presented determinant method to obtain exact analytical solutions for the natural frequencies of a Bernoulli beam, representing a RMS, with large overhanging payloads for a locked an unlocked joint it turns out that if unlocked, the free revolute joint leads to negligibly small elastic deflections of a single flexible RMS due to slew manoeuvres. This is because the joint then yields almost the boundary conditions of a pinned-free beam, and the payload centre of mass becomes a nodal point in the pinned-free vibration modes. The exact analyses also show that for an unlocked joint, the effective inertia at the output side of a gear box due to its high ratio does not effectively lead to a clamped link at the gear box side in the lower modes, which is usually claimed in papers on the SRMS. Due to this incorrect assumption it is inferred that many of the dynamic response figures given in the various papers are too large, which could be the reason why researchers usually stress the control aspect of the SRMS, whereas the previous analyses for the single link show that if the joint is unlocked, the elastic deflections are negligibly small. The following sections investigate if this is also true for a multi-link robot like the SRMS.
For a locked shoulder joint, the elastic deflections are not negligible when the Shuttle is disturbed for example by thruster firing. The dynamic analyses are performed using the equations of motion as obtained from Lagrange's equation, where the RMS flexibility is represented by exact analytical mode shapes. The results of several simulations show that for a locked joint, the fundamental vibration mode always represents more than 99.5 % of the total elastic RMS deflection, thus allowing to use only one mode shape in the equations of motion. Note however that the single link RMS with constant flexural stiffness is a simplified representation of a three-link

system, locked at the elbow and wrist with infinite joint torsional stiffness. The prime aim of the single link study is to clarify the basic dynamic behaviour of the more complex doubly and triply articulated RMS to be studied subsequently.
An active damping control of the single flexible RMS by a reaction wheel (RW) is shown to be feasible. The achievable damping coefficient is limited in practice by the wheel size, its mass and power requirement.
The last aspect that seems to be frequently overlooked in the related literature is the Shuttle / RMS interaction. Any acceleration of the Shuttle will have an effect on the RMS and vice versa. The presented example simulations prove clearly that a RMS operation will affect the attitude of the Shuttle, especially during precise positioning where the interactions can lead to incorrect payload positioning, if the Shuttle attitude is not controlled and kept fixed relative to the target.

CHAPTER 3: SINGLE LINK WITH FIXED BASE AND END EFFECTOR

To complete the single link RMS dynamic analysis with fixed base, we consider the case of an articulation of the payload through a constant angle θ about the wrist joint O_2 to study the effect on the natural frequencies of the system. In the literature ([8]) it is common to assume that the short end effector link is stiff compared to the main links of the Shuttle RMS, and that the connection between end effector and payload can be taken as rigid ([1], [3], [69]), see also chapter 10. A schematic is shown in figure 3.1, in which the angle θ denotes the rigid body attitude of the end effector and the payload relative to the flexible main link.

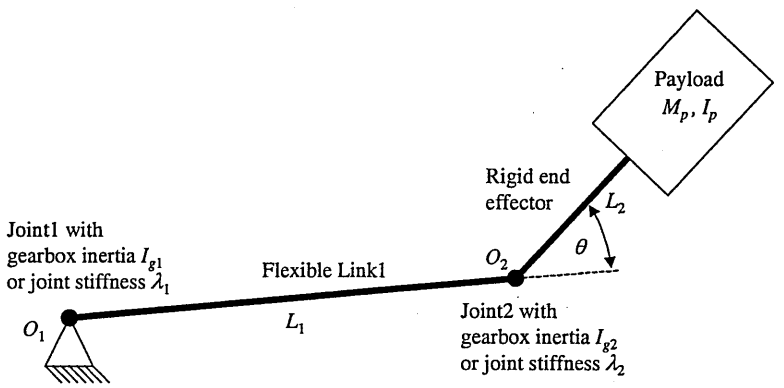

Figure 3.1: Single link system with articulated end effector/payload

3.1 DETERMINATION OF NATURAL FREQUENCIES AND MODE SHAPES

3.1.1 EXACT SOLUTION FOR NATURAL FREQUENCIES

To obtain the exact natural frequencies of the single flexible link with rigid end effector, the determinant method is applied.
In order to derive the necessary kinematic and dynamical boundary conditions of the flexible link, consider figure 3.2, where angle $\Delta\theta$ is the rotation of the end effector and the payload about O_2 due to the joint stiffness λ_2.

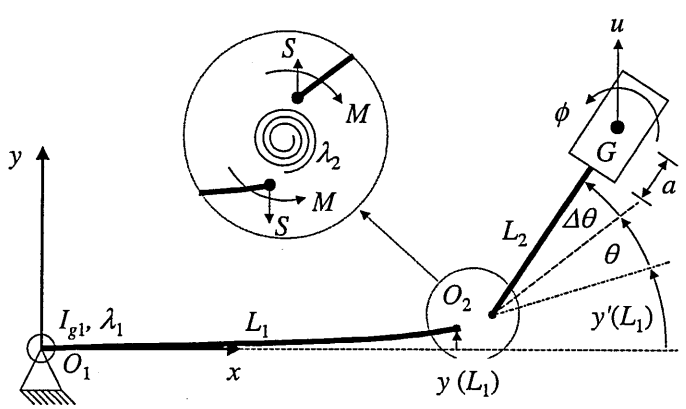

Figure 3.2: Boundary conditions of the single flexible link with rigid articulated end effector

In figure 3.2, L_1 is the length of the flexible link, L_2 is the length of the rigid end effector, S and M in the enlarged circle are the beam shear force and bending moment at $x = L_1$, respectively, and the other designations are analogous to those defined in chapter 2.2.

At $x = 0$, the boundary conditions are identical to those of the single flexible link without end effector and are given with equations (2.23) and (2.30) for the case of an unlocked joint at O_1, where I_g is now replaced by I_{g1}.

To derive the boundary conditions at $x = L_1$ for a locked joint at O_2 we assume that the angular deflections $\Delta\theta$ and $y'(L_1,t)$ are small, so that θ can be taken as constant. Then the angular acceleration $\ddot{\phi}$ of the end effector and the payload about O_2 is

$$\ddot{\phi} = \Delta\ddot{\theta} + \ddot{y}'(L_1,t) \tag{3.1}$$

where the usual system of dashes and dots is used to indicate derivations with respect to space and time, respectively.

The translatory acceleration a_{r1} of the payload centre of mass G relative to Link1 is

$$a_{r1} = \ddot{\phi}(L_2 + a) \tag{3.2}$$

where a_r is inclined to the acceleration $\ddot{y}(L_1,t)$ of Link1 at O_2 at the angle θ.

The angle $\Delta\theta$ is obtained from moment equilibrium at O_2, thus

$$\Delta\theta = \frac{EI\, y''(L_1,t)}{\lambda_2} \tag{3.3}$$

Using equations (2.10), (2.28) and (2.29) as well as relations (2.13) together with the method of separation of variables derived in chapter 2.2.1 and formulating the moment and force equilibrium at O_2 gives the two boundary conditions at $x = L_1$ as

$$\begin{aligned} EI\,W''(L_1) = {} & I_p\,\omega^2\,(EI\,W''(L_1,t)/\lambda_2 + W'(L_1)) + \\ & (L_2 + a)M_p\,\omega^2\,(W(L_1)\cos\theta + (L_2 + a)(EI\,W''(L_1,t)/\lambda_2 + W'(L_1))) \end{aligned} \tag{3.4}$$

and $$EI\,W'''(L_1) = -M_p\,\omega^2\,(W(L_1) + (L_2 + a)(EI\,W''(L_1,t)/\lambda_2 + W'(L_1))\cos\theta) \tag{3.5}$$

Equations (3.4) and (3.5) neglect the mass of Link2 and the gear box inertia of Joint2, I_{g2}, if the joint is unlocked. These can be included in the payload mass and rotary inertia, but are negligible compared to payloads in excess of say 1000 kg. Thus the four boundary conditions are given by equations (2.23), (2.30), (3.4) and (3.5). Applying the boundary conditions to the general boundary equation (2.21) yields

$$\begin{bmatrix} d_{11} & d_{12} & d_{13} \\ d_{21} & d_{22} & d_{23} \\ d_{31} & d_{32} & d_{33} \end{bmatrix} \begin{bmatrix} A_i \\ B_i \\ C_i \end{bmatrix} = \mathbf{0} \tag{3.6}$$

which can only be solved if

$$\begin{vmatrix} d_{11} & d_{12} & d_{13} \\ d_{21} & d_{22} & d_{23} \\ d_{31} & d_{32} & d_{33} \end{vmatrix} = 0 \tag{3.7}$$

where it is noted that the present matrix elements can differ from previous elements with the same designation. Using the notation $C = \cos(kL_1)$, $S = \sin(kL_1)$, $Ch = \cosh(kL_1)$ and $Sh = \sinh(kL_1)$, the elements d_{nm} are given by

$$\begin{aligned}
d_{11} &= I_{g1}\, k\, \omega^2 \\
d_{12} &= -2EI\, k^2 \\
d_{13} &= I_{g1}\, k\, \omega^2 \\
d_{21} &= k\left(I_p + (L_2+a)^2 M_p\right)\omega^2 C + \frac{EI\,k^2\left(\lambda_2 - I_p\,\omega^2 - (L_2+a)^2 M_p \omega^2\right)S}{\lambda_2} + \\
&\quad (L_2+a) M_p\, \omega^2\, S\cos\theta \\
d_{22} &= -EI\, k^2 (C+Ch) + \frac{I_p\, k\, \omega^2 (EI\,k\,C + EI\,k\,Ch + \lambda_2 S + \lambda_2 Sh)}{\lambda_2} + \\
&\quad (L_2+a) M_p\, \omega^2 \left(\cos\theta(-C+Ch) + \frac{(L_2+a)k(EI\,k\,C + EI\,k\,Ch + \lambda_2 S + \lambda_2 Sh)}{\lambda_2} \right) \\
d_{23} &= k\left(I_p + (L_2+a)^2 M_p\right)\omega^2 Ch + \frac{EI\,k^2\left(-\lambda_2 + I_p\,\omega^2 + (L_2+a)^2 M_p \omega^2\right)Sh}{\lambda_2} + \\
&\quad (L_2+a) M_p\, \omega^2\, Sh\cos\theta \\
d_{31} &= -EI\, k^3\, C + M_p\, \omega^2 \left(S + (L_2+a)k\cos\theta\left(C - \frac{EI\,k\,S}{\lambda_2}\right)\right) \\
d_{32} &= -EI\, k^3 (S - Sh) + M_p\, \omega^2 \left(-C + Ch + (L_2+a)k\cos\theta\left(S + Sh + \frac{EI\,k\,C + EI\,k\,Ch}{\lambda_2}\right)\right) \\
d_{33} &= -EI\, k^3\, Ch + M_p\, \omega^2 \left(Sh + (L_2+a)k\cos\theta\left(Ch + \frac{EI\,k\,Sh}{\lambda_2}\right)\right)
\end{aligned} \tag{3.8}$$

If joint O_1 is locked, equation (2.30) becomes

$$EI\,W''(0) = \lambda_1\, W'(0) \tag{3.9}$$

and the elements d_{11} and d_{13} in equation (3.8) then become

$$\begin{aligned} d_{11} &= -\lambda_1\, k \\ d_{13} &= -\lambda_1\, k \end{aligned} \tag{3.10}$$

If Joint2 is unlocked, λ_2 is set to a very small value, say 10^{-5} or so. Note that setting λ_2 to zero is not allowed since it appears in denominators, see equations (3.3) and (3.8).

Since the single flexible link system with articulated end effector has two joints that can either be locked or unlocked, there are four possible configurations for the joints.

Tables 3.1 through 3.4 give the variation of the natural frequencies with θ for each configuration. The system properties are always L_1 = 12.12 m, L_2 = 1.88 m, m_b = 3.9786 kg/m, EI = 3×10^6 Nm^2, M_p = 5000 kg, I_p = 5417 kgm^2, a = 1 m, I_{g1} = 1188 kgm^2 or λ_1 = 10^6 Nm/rad for Joint1 and I_{g2} = 191 kgm^2 or λ_2 = 2.4×10^5 Nm/rad for Joint2. It is mentioned above that for payloads in excess of about 1000 kg, the gearbox inertia I_{g2} is negligible, but is included here in the payload rotary inertia.
Tables 3.1 through 3.4 show that the effect of an end effector articulation about Joint2 on the natural frequencies is very small in the higher modes. Only the first or at maximum the first and the second natural vibration frequencies are changed significantly, depending on whether Joint1 and Joint2 are locked or unlocked.
It is noted that θ is varied only in the range 0...90° since the theoretical possibilities are infinite, and since in reality the work range of the joints is most likely to be limited. Also due to symmetry the natural frequencies for positive and negative θ are identical. Therefore the variations of the joint angles in all the following chapters are given only in the aforementioned range.

θ [deg]	ω_1 [rad/s]	ω_2 [rad/s]	ω_3 [rad/s]	ω_4 [rad/s]
0	0.00	0.00	23.88	96.28
10	0.00	0.00	23.84	96.20
20	0.00	0.00	23.76	96.08
30	0.00	0.00	23.71	96.00
40	0.00	0.00	23.68	95.96
50	0.00	0.00	23.67	95.93
60	0.00	0.00	23.66	95.92
70	0.00	0.00	23.65	95.91
80	0.00	0.00	23.65	95.90
90	0.00	0.00	23.65	95.90

Table 3.1: Variation of exact natural frequencies of single flexible link system with end effector with θ for both joints unlocked

θ [deg]	ω_1 [rad/s]	ω_2 [rad/s]	ω_3 [rad/s]	ω_4 [rad/s]
0	0.00	6.91	25.21	101.50
10	0.00	6.26	25.07	101.36
20	0.00	5.07	24.87	101.15
30	0.00	4.07	24.74	101.02
40	0.00	3.37	24.67	100.94
50	0.00	2.88	24.63	100.90
60	0.00	2.53	24.61	100.87
70	0.00	2.30	24.59	100.85
80	0.00	2.13	24.58	100.84
90	0.00	2.03	24.58	100.84

Table 3.2: Variation of exact natural frequencies of single flexible link system with end effector with θ for Joint1 unlocked and Joint2 locked

θ [deg]	ω_1 [rad/s]	ω_2 [rad/s]	ω_3 [rad/s]	ω_4 [rad/s]
0	0.00	2.22	72.55	251.43
10	0.00	2.00	72.47	251.34
20	0.00	1.62	72.34	251.21
30	0.00	1.31	72.26	251.12
40	0.00	1.10	72.22	251.07
50	0.00	0.95	72.19	251.04
60	0.00	0.86	72.18	251.03
70	0.00	0.80	72.17	251.02
80	0.00	0.77	72.16	251.01
90	0.00	0.76	72.16	251.01

Table 3.3: Variation of exact natural frequencies of single flexible link system with end effector with θ for Joint1 locked and Joint2 unlocked

θ [deg]	ω_1 [rad/s]	ω_2 [rad/s]	ω_3 [rad/s]	ω_4 [rad/s]
0	0.56	7.89	77.77	256.74
10	0.56	7.11	77.62	256.62
20	0.57	5.71	77.38	256.44
30	0.58	4.55	77.23	256.33
40	0.59	3.73	77.15	256.26
50	0.60	3.16	77.10	256.22
60	0.63	2.76	77.07	256.20
70	0.65	2.47	77.05	256.19
80	0.68	2.26	77.04	256.18
90	0.72	2.12	77.03	256.18

Table 3.4: Variation of exact natural frequencies of single flexible link system with end effector with θ for both joints locked

Tables 3.1 through 3.4 show that the fundamental and higher frequencies of the single link system with unlocked Joint1 are very high compared to the frequencies for a locked Joint1. These results agree with the analyses in section 2.
Also, tables 3.3 and 3.4 give a first possibility to validate the proposed determinant method: if the two links are perpendicular to each other with $\theta = 90°$ and if the angular deflections of the flexible link end at O_2 are small, it should make no significant difference whether Joint2 is locked with joint stiffness or unlocked and free to rotate. This is because the payload rotary and translatory inertia always appear at the end of Link1 at O_2 due to the joint stiffness, if Joint2 is locked. But with θ approaching 90°, the payload translatory inertia also appears at the end of Link1 at O_2, if Joint2 is not locked. For $\theta = 90°$, the payload translatory inertia appears completely at the end of Link1 at O_2, independent from Joint2 being locked or unlocked. A difference in the fundamental frequency for Joint2 locked and unlocked occurs due to the small angular deflection of the end of Link1 at O_2, which is coupled to the payload rotary inertia by the joint stiffness, if Joint2 is locked. If the effective

payload rotary inertia at O_2 is zero, the fundamental frequencies are identical for both cases.
The last lines in tables 3.3 and 3.4 for $\theta = 90°$ agree very good, thus proving that the determinant gives results that agree with the considerations above and implying that, in the given configuration, the influence of the payload rotary inertia is small compared to that of the translatory inertia because of small angular deflections of Link1 at O_2.

3.1.2 EXACT SOLUTION FOR MODE SHAPES

The exact mode shapes are obtained by the method described in chapter 2.2.2 by re-inserting the computed natural eigenfrequencies into equation (3.6), where the zeros in the right-hand side vector are replaced by always the same elements f as described in 2.2.2. This kind of normalising make the mode shapes distinguishable in the plots, since other normalisations ($W(L) = 1$) yield mode shapes that lie above each other.
Figure 3.3 shows the first mode shape for the configuration Joint1 unlocked and Joint2 locked with $\theta = 0°$, $L_1 = 12.12$ m, $L_2 = 1.88$ m, $m_b = 3.9786$ kg/m, $EI = 3\times10^6$ Nm^2, $M_p = 5000$ kg, $I_p = 5417$ kgm^2, $a = 1$ m, $I_{g1} = 1188$ kgm^2 and $\lambda_2 = 2.4\times10^5$ Nm/rad. Figure 3.4 compares the first mode shape for the present system properties for $\theta = 0°$, 50° and 90°.

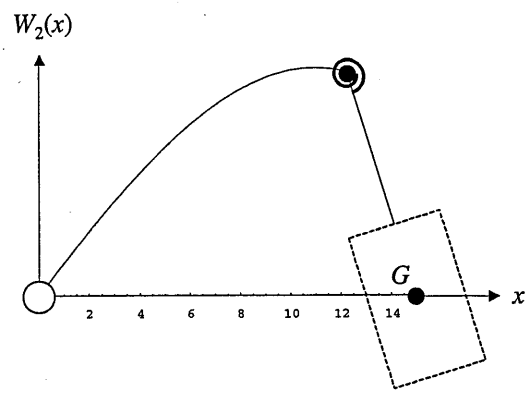

Figure 3.3: First mode shape of flexible link for configuration Joint1 unlocked and Joint2 locked for $\theta = 0°$

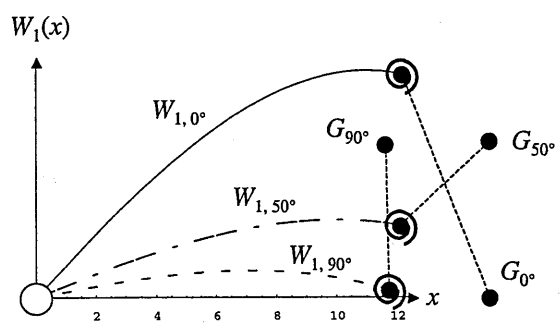

Figure 3.4: First mode shape of flexible link for configuration Joint1 unlocked and Joint2 locked for various θ

Figure 3.5 shows the first mode shape of the flexible link for $\theta = 0°$, 50° and 90° for the case Joint1 and Joint2 unlocked, when the other system parameters remain.

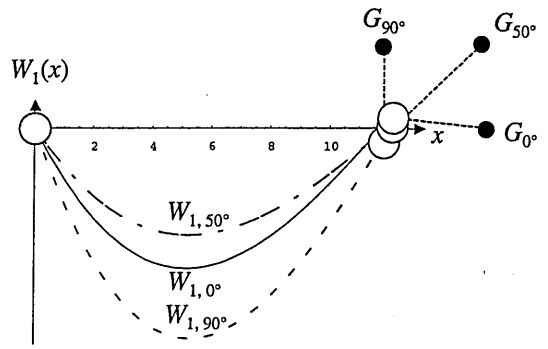

Figure 3.5: First mode shape of flexible link for configuration Joint1 and Joint2 unlocked for various θ

Using the same system properties again for the configuration Joint1 locked and Joint2 unlocked, the first mode shape of the flexible link for $\theta = 0°$, 50° and 90° is as shown in figure 3.6.

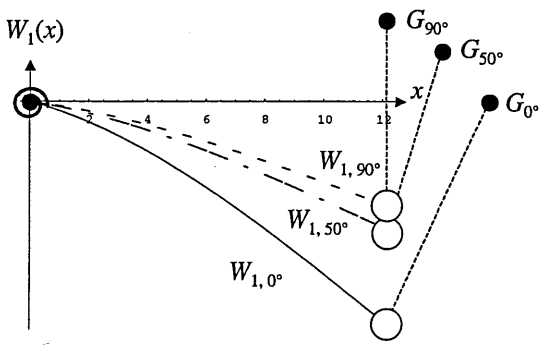

Figure 3.6: First mode shape of flexible link for configuration Joint1 locked and Joint2 unlocked for various θ

Finally, figure 3.7 gives the first mode shape of the flexible Link1 for $\theta = 0°$, 50° and 90° for the last configuration Joint1 and Joint2 locked.

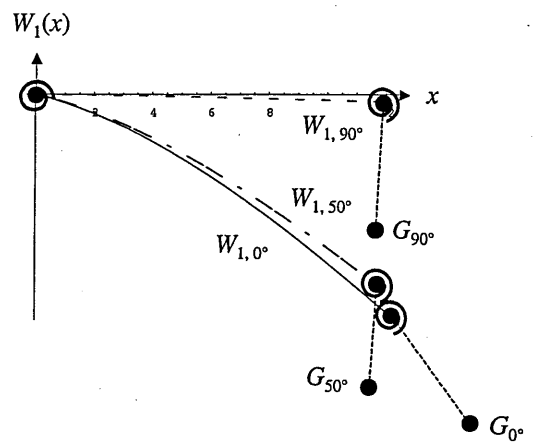

Figure 3.7: First mode shape of flexible link for configuration Joint1 and Joint2 locked for various θ

3.2 VALIDATION OF THE DETERMINANT RESULTS

Here we apply different methods to verify the results obtained with the present determinant for the single flexible link with end effector, such as reproduction of the single flexible link without end effector and imitation of a rigid double pendulum.

3.2.1 REPRODUCTION OF FLEXIBLE LINK WITHOUT END EFFECTOR

The results of the present determinant can be validated by choosing the properties so that the single link reference system from chapter 2.2 is reproduced.
Thus $\theta = 0°$, $L_1 = 14$ m, $L_2 = 0$ m, $m_b = 3.9786$ kg/m, $EI = 3\times10^6$ Nm^2, $\lambda_2 = 10^{10}$ Nm/rad, $M_p = 10000$ kg, $I_p = 37500$ kgm^2, $a = 1.5$ m, and $I_{g1} = 1188$ kgm^2 for Joint1 unlocked or $\lambda_1 = 10^6$ Nm/rad for Joint1 locked. The very high value for λ_2 should effectively clamp Joint2. The first five natural frequencies of this system for Joint1 unlocked and locked are given in table 3.5.

freq. [rad/s]	Unlocked	Locked
ω_1	0.00	0.39
ω_2	4.55	5.18
ω_3	25.98	81.45
ω_4	103.17	236.65
ω_5	274.75	478.54

Table 3.5: Natural frequencies of single flexible link with rigid end effector, with properties of the reference single link system with unlocked and locked shoulder joint O_1

The close agreement of tables 2.1 and 3.5 validates equation (3.8). The small deviations at the second decimal are due to numerical inaccuracies.

3.2.2 RIGID LINK ANALYSIS

A second means to validate equation (3.8) is to check the natural frequencies against those of a rigid double pendulum, when the flexural stiffness of the single link is chosen very high to effectively produce a rigid link. To obtain two natural frequencies for the rigid double pendulum, we consider the case of both joints locked.
The two natural frequencies are obtained using Lagrange's equation (2.48) to derive the equations of motion (2.49) with the system mass and stiffness matrices **M** and **K**. For the kinetic and potential energy, consider figure 3.8 with the various velocity components and generalised coordinates vector $\mathbf{p} = [\theta_1, \theta_2]^T$, representing motions about the joints. These motion are assumed to be small in order to allow for linearisation.

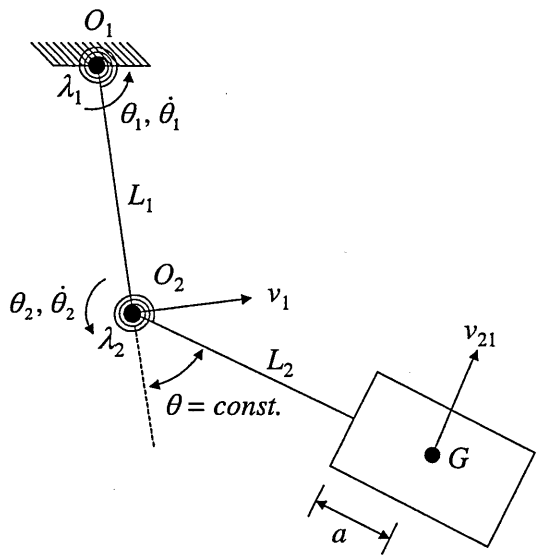

Figure 3.8: Velocity components and generalised coordinates of rigid double pendulum

From figure 3.8 and using the cosine rule, the square of the translatory velocity v_M of the payload centre of mass G is

$$v_M^2 = v_1^2 + v_{21}^2 + 2 v_1 v_{21} \cos\theta \tag{3.11}$$

where $v_1 = L_1 \dot{\theta}_1$ and $v_{21} = (L_2 + a)\left(\dot{\theta}_2 + \dot{\theta}_1\right)$. Thus the kinetic energy T, including the payload rotary inertia I_p, is

$$T = \tfrac{1}{2} M_p v_M^2 + I_p(\dot{\theta}_1 + \dot{\theta}_2)^2 + \tfrac{1}{2} M_1 v_1^2 \tag{3.12}$$

where the distributed beam mass m_b of Link1 is taken into account by the term $\frac{1}{2} M_1 v_1^2$, and where M_1 is the substitute mass of Link1 at the tip, given as ([41]) $M_1 = \frac{1}{3} L_1 m_b$. The distributed mass of Link2 can be included in M_p.
The elastic strain energy V is

$$V = \tfrac{1}{2}\lambda_1 \theta_1^2 + \tfrac{1}{2}\lambda_2 \theta_2^2 \tag{3.13}$$

Applying Lagrange's equation (2.48) to equations (3.12) and (3.13) yields the equations of motion, where the four elements of the present mass matrix **M** are

$$\begin{aligned} M_{11} &= I_p + M_p [L_1^2 + (a + L_2)^2 + 2 L_1 (a + L_2)\cos\theta] + M_1 L_1^2 \\ M_{12} &= M_{21} = I_p + M_p (a + L_2)(a + L_2 + L_1 \cos\theta) \\ M_{22} &= I_p + M_p (a + L_2)^2 \end{aligned} \tag{3.14}$$

and the stiffness matrix **K** is given by

$$\mathbf{K} = \begin{bmatrix} \lambda_1 & 0 \\ 0 & \lambda_2 \end{bmatrix} \tag{3.15}$$

Using equations (3.14) and (3.15) in equation (2.50) yields the (two) system natural frequencies. Table 3.6 gives these frequencies for the rigid double pendulum (ω_i dp) and the first two natural frequencies of the flexible single link system with articulated end effector (ω_i flee) obtained with the determinant, equation (3.7), for identical system properties. Let $\theta = 0°$, $L_1 = 12.12$ m, $L_2 = 1.88$ m, $M_p = 5000$ kg, $I_p = 5417$ kgm^2, $a = 1$, $\lambda_1 = 10^6$ Nm/rad, $\lambda_2 = 2.4\times10^5$ Nm/rad, and for the flexible system $EI = 10^{10}$ Nm^2 to effectively produce a rigid link.

θ [deg]	ω_1 dp [rad/s]	ω_1 flee [rad/s]		ω_2 dp [rad/s]	ω_2 flee [rad/s]
0	0.87	0.87		8.80	8.79
50	0.94	0.94		3.50	3.50
90	1.12	1.12		2.36	2.36

Table 3.6: Two natural frequencies of rigid double pendulum and first two natural frequencies of single flexible link system for identical properties with $EI = 10^{10}$ Nm^2

Table 3.6 verifies that the natural frequencies are in almost exact agreement. The reasons for the deviation of the second frequency for $\theta = 0°$ could not be found, but are assumed to be due to numerical inaccuracies in computing equation (2.50). Figure 3.9 gives the mode shapes of the rigid double pendulum for $\theta = 0°$ and $\theta = 90°$.

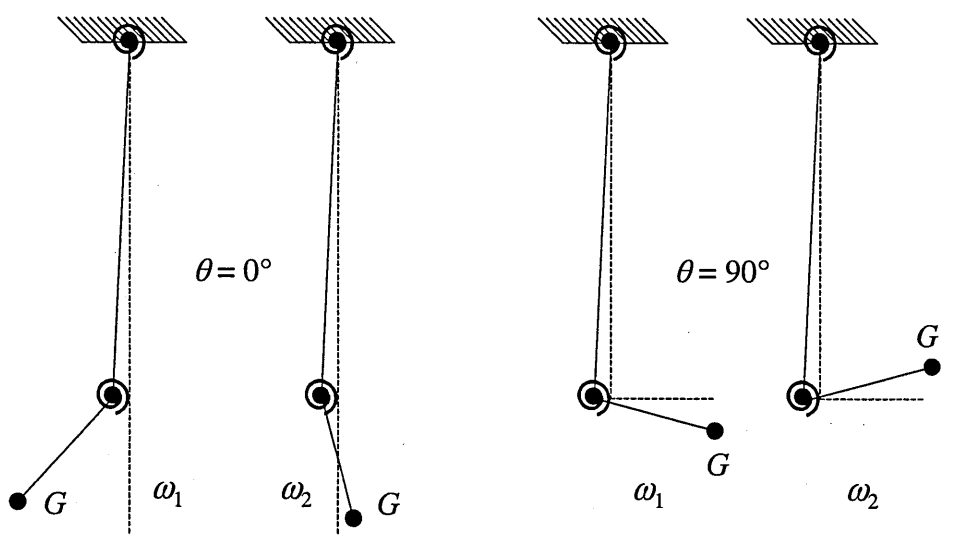

Figure 3.9: Sketch of rigid double pendulum mode shapes for $\theta = 0°$ and $\theta = 90°$

Taking a look at figure 3.9 one can easily explain that the fundamental frequency of the rigid double pendulum increases with increasing θ, since the system centre of mass, which is nearly the payload centre of mass G, gets closer to the root of the flexible link. On the other hand the second frequency decreases, because the payload mass appears more and more at the tip of the flexible link with increasing θ, thus increasing the effective inertia.

3.3 DYNAMIC RESPONSE ANALYSES

This section investigates in the dynamic responses of the double flexible link due to applied forces. Note that here and in the following chapters that develop the RMS to the full system identical to the SRMS, natural frequency comparisons using assumed mode shapes are not performed, but assumed mode shapes will again be applied to verify dynamic response results of the fully developed RMS in the later chapters, using BEAM (for more information see [83]) and SIMPACK.

3.3.1 JOINT1 UNLOCKED AND JOINT2 LOCKED

As stated in section 2, the deflection of a single link with an unlocked shoulder joint is negligibly small. To check if this holds also for a two-link system, the first exact mode shape for the configuration Joint1 unlocked and Joint2 locked is inserted into the equations of motion, which for sake of brevity are not given here.
The system properties are $\theta = 0°$, $L_1 = 12.12$ m, $L_2 = 1.88$ m, $m_b = 3.9786$ kg/m, $EI = 3\times10^6$ Nm^2, $M_p = 5000$ kg, $I_p = 5417$ kgm^2, $a = 1$ m, $I_{g1} = 1188$ kgm^2, and $\lambda_2 = 2.4\times10^5$ Nm/rad, and the driving torque of Joint1 is taken to be 1298 Nm, which is the actual maximum value for the SRMS at the shoulder joint. The total rotary inertia about Joint1 in the straight SRMS configuration is 1206667 kgm^2. Dividing the maximum torque by the rotary inertia we obtain an angular acceleration of the RMS of $\ddot{\alpha} = 0.001$ rad/s^2. For the given data, the translatory vibration amplitude of Link1 at O_2 and of the payload centre of mass G are less than 2.1 mm and 0.04 mm respectively in the fundamental mode. For a very large payload, say $M_p = 30000$ kg and $I_p = 400000$ kgm^2, the vibration amplitude of Link1 at O_2 and of G are 3.7 mm and 0.5 mm respectively, if the same torque is applied again and if the other system properties remain unchanged.

3.3.2 JOINT1 AND JOINT2 UNLOCKED

To complete the analysis of the system with Joint1 unlocked, we consider the case Joint2 also unlocked. For this configuration, a simulation as before is performed. Again, the first exact mode shape is inserted into the equations of motion. The properties are $\theta = 0°$, $L_1 = 12.12$ m, $L_2 = 1.88$ m, $m_b = 3.9786$ kg/m, $EI = 3\times10^6$ Nm^2, $M_p = 5000$ kg, $I_p = 5417$ kgm^2, $a = 1$ m, $I_{g1} = 1188$ kgm^2, $\lambda_2 = 10^{-5}$ Nm/rad and $\ddot{\alpha} = 0.001$ rad/s^2 due to the torque at Joint1. The small value for λ_2 effectively produces a revolute joint at O_2 (as stated before, λ_2 must not be set to zero since it appears in denominators in equation (3.8)). The rotational inertia due to the gear box at O_2 can be included in I_p, but is neglected here.
For these data, the elastic vibration amplitude of Link1 at O_2 is less than 0.05 mm, and the vibration amplitude of the mass centre G is less than 0.005 mm. It is noted that in all the simulation cases the share of the second, third, fourth and fifth exact mode shape together in the total defection is less than 1 %, which allows for using only the first mode shape in the equations of motion.

3.3.3 JOINT1 LOCKED AND JOINT2 UNLOCKED

As for the case of Joint1 unlocked, two system configurations for a locked Joint1 are possible, depending on whether Joint2 is also locked or unlocked. First we consider the case of Joint2 unlocked. As before, an angular acceleration $\ddot{\alpha}$ of the flexible Link1 due to a torque at Joint1 is simulated, using the first exact mode shape. Since Joint1 is locked now, it is assumed that the angular acceleration of Link1 is due to a thruster firing for example on a space station, similar to the situation shown in figure 2.18 for the single flexible link without end effector in chapter 2.5. This allows for a comparison with the results for the unlocked Joint1. The properties are $\theta = 0°$, $L_1 = 12.12$ m, $L_2 = 1.88$ m, $m_b = 3.9786$ kg/m, $EI = 3\times10^6$ Nm^2, $M_p = 5000$ kg, $I_p = 5417$ kgm^2, $a = 1$ m, $\lambda_1 = 10^6$ Nm/rad, $\lambda_2 = 10^{-5}$ Nm/rad, $I_0 = 10^{20}$ kgm^2, and the torque T_0 is chosen so to again produce an angular acceleration of $\ddot{\alpha} = 0.001$ rad/s^2 of the whole system.

For these data the vibration amplitude of Link1 at O_2 is 2.5 mm and the vibration amplitude of the payload centre of mass is less than 0.03 mm in the fundamental mode. It is noted that these results assume a stable vibration mode, but in the present configuration with Joint2 unlocked an angular acceleration of the system causes the payload and the rigid end effector to freely rotate about Joint2. The motion of the payload mass centre G is random and depends on the vibration of the flexible link and on the payload's rotation about O_2. This fact confirms again the fundamental assumption in section 2 that if a joint is not actively driven by the actual joint motor, it is locked with brakes on.

In the actual simulation, the share of the second and third mode in the total deflection is less than 0.1 %.

To obtain the results of the simulation as before for perpendicular links, the system properties are chosen as $\theta = 90°$, $L_1 = 12.12$ m, $L_2 = 1.88$ m, $m_b = 3.9786$ kg/m, $EI = 3\times10^6$ Nm^2, $M_p = 5000$ kg, $I_p = 5417$ kgm^2, $a = 1$ m, $\lambda_1 = 10^6$ Nm/rad, $\lambda_2 = 10^{-5}$ Nm/rad and again a torque so that $\ddot{\alpha} = 0.001$ rad/s^2.

For these data, the vibration amplitude of Link1 at O_2 and therefore of the payload centre of mass G is 2.24 cm in the fundamental mode.

3.3.4 JOINT1 AND JOINT2 LOCKED

Finally we consider the configuration Joint1 and Joint2 locked. As stated before, a simulation should give similar results for Joint2 unlocked and locked, if $\theta = 90°$. To confirm this we choose $\theta = 90°$, $L_1 = 12.12$ m, $L_2 = 1.88$ m, $m_b = 3.9786$ kg/m, $EI = 3\times10^6$ Nm^2, $M_p = 5000$ kg, $I_p = 5417$ kgm^2, $a = 1$ m, $\lambda_1 = 10^6$ Nm/rad, $\lambda_2 = 2.4\times10^5$ Nm/rad and let the torque produce the usual angular acceleration $\ddot{\alpha} = 0.001$ rad/s^2.

For this configuration the vibration amplitude of Link1 at O_2 and thus of G is 2.27 cm. This result is close to the figure above for Joint2 unlocked and corresponds to the close agreement of the fundamental frequencies for Joint2 unlocked and locked, if $\theta = 90°$. In the present case, the share of the second and third mode shape in the deformation is less than 0.7 %.

The last example considers the straight RMS with $\theta = 0°$, $L_1 = 12.12$ m, $L_2 = 1.88$ m, $m_b = 3.9786$ kg/m, $EI = 3\times10^6$ Nm^2, $M_p = 5000$ kg, $I_p = 5417$ kgm^2, $a = 1$ m, $\lambda_1 = 10^6$

Nm/rad, $\lambda_2 = 2.4\times10^5$ Nm/rad and as before the torque so that $\ddot{\alpha} = 0.001$ rad/s^2.
For these data, the vibration amplitude of Link1 at O_2 is 3.21 cm and the vibration amplitude of the payload centre of mass G is 4.51 cm. In the actual configuration the share of the second and third mode shape in the total deflection is less than 0.2 %.
The previous analyses show that for the actual configurations, the flexibility of Link1 can be represented sufficiently accurate in the equations of motion by using only the first mode shape. As check simulations show, this holds also true for big payloads, so that using the first mode shape only is sufficient for the whole range of payloads.

3.4 SUMMARY

The determinant method introduced in chapter 2 is applied to the single flexible link with an articulated end effector and payload. This yields exact analytical natural frequencies and mode shapes for the system. The frequency determinant is validated by comparison with the natural frequencies of the single flexible link system without end effector and with the natural frequencies of a rigid double pendulum with torsion springs, when the system properties are chosen so to imitate these comparison systems.
A dynamic response analysis for the four possible joint state configurations free-free, free-locked, locked-free and locked-locked shows that the deflections are small in general, and very small for an unlocked Joint1.
The analyses of the single flexible link system with end effector provide the basis for the investigation of the double flexible link system.

CHAPTER 4: DOUBLE LINK WITH FIXED BASE

Based on the analysis of the single flexible link with and without rigid end effector, the system is now extended to the double flexible link system without end effector shown in figure 4.1, where the dotted lines are the rigid body position of the links and the solid lines the superimposed elastic deflections. Again the base is assumed being inertially fixed, and the other designations are as introduced in the previous sections.

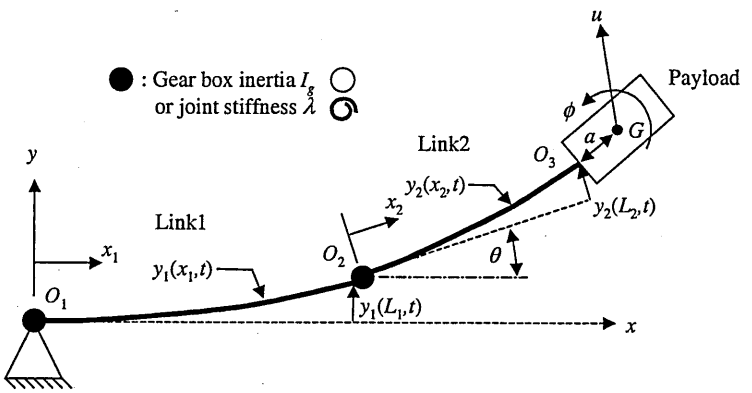

Figure 4.1: Schematic of doubly articulated flexible manipulator

Depending on whether a joint is locked or unlocked, either joint stiffness or the gear box inertia is present. As for the single flexible link system without end effector, the payload is assumed to be rigidly attached to Link2 at O_3, and the links are inclined at a fixed angle θ in the undeformed configuration.

4.1 DETERMINATION OF NATURAL FREQUENCIES AND MODE SHAPES

4.1.1 EXACT SOLUTION FOR NATURAL FREQUENCIES

To obtain the exact natural frequencies of the double flexible link system, the determinant method is applied. Although literature on the boundary conditions of single beams is vast, the boundary conditions of a two-beam-system have apparently not been analysed.
The deflection shape of each link l for a natural frequency ω_i ($i = 1..\infty$) is given as

$$W_{l,i}(x) = A_{l,i}\sin(k_{l,i}x_l) + B_{l,i}\cos(k_{l,i}x_l) + C_{l,i}\sinh(k_{l,i}x_l) + D_{l,i}\cosh(k_{l,i}x_l) \quad (4.1)$$

where
$$k_{l,i} = \sqrt{\omega_i\sqrt{\frac{m_{bl}}{EI_l}}} \qquad l = 1,2. \quad (4.2)$$

where m_{bl} = mass per unit length of link l and EI_l = flexural stiffness.
Equation (4.1) is solved for the two links using the boundary conditions at $x_l = 0$ and $x_l = L_l$. The 2×4 boundary conditions yield 8 equations, and after collecting terms $A_{l,i}$, $B_{l,i}$, $C_{l,i}$ and $D_{l,i}$, the eigenvalue equation becomes

$$\begin{bmatrix} d_{11} & d_{12} & d_{13} & d_{14} & d_{15} & d_{16} & d_{17} & d_{18} \\ d_{21} & d_{22} & d_{23} & d_{24} & d_{25} & d_{26} & d_{27} & d_{28} \\ d_{31} & d_{32} & d_{33} & d_{34} & d_{35} & d_{36} & d_{37} & d_{38} \\ d_{41} & d_{42} & d_{43} & d_{44} & d_{45} & d_{46} & d_{47} & d_{48} \\ d_{51} & d_{52} & d_{53} & d_{54} & d_{55} & d_{56} & d_{57} & d_{58} \\ d_{61} & d_{62} & d_{63} & d_{64} & d_{65} & d_{66} & d_{67} & d_{68} \\ d_{71} & d_{72} & d_{73} & d_{74} & d_{75} & d_{76} & d_{77} & d_{78} \\ d_{81} & d_{82} & d_{83} & d_{84} & d_{85} & d_{86} & d_{87} & d_{88} \end{bmatrix} \begin{bmatrix} A_{1,i} \\ B_{1,i} \\ C_{1,i} \\ D_{1,i} \\ A_{2,i} \\ B_{2,i} \\ C_{2,i} \\ D_{2,i} \end{bmatrix} = \mathbf{0} \tag{4.3}$$

which requires numerical solution of the following determinant for the natural frequencies ω_i

$$\begin{vmatrix} d_{11} & d_{12} & d_{13} & d_{14} & d_{15} & d_{16} & d_{17} & d_{18} \\ d_{21} & d_{22} & d_{23} & d_{24} & d_{25} & d_{26} & d_{27} & d_{28} \\ d_{31} & d_{32} & d_{33} & d_{34} & d_{35} & d_{36} & d_{37} & d_{38} \\ d_{41} & d_{42} & d_{43} & d_{44} & d_{45} & d_{46} & d_{47} & d_{48} \\ d_{51} & d_{52} & d_{53} & d_{54} & d_{55} & d_{56} & d_{57} & d_{58} \\ d_{61} & d_{62} & d_{63} & d_{64} & d_{65} & d_{66} & d_{67} & d_{68} \\ d_{71} & d_{72} & d_{73} & d_{74} & d_{75} & d_{76} & d_{77} & d_{78} \\ d_{81} & d_{82} & d_{83} & d_{84} & d_{85} & d_{86} & d_{87} & d_{88} \end{vmatrix} = 0 \tag{4.4}$$

For the boundary conditions of the links, consider figure 4.1. For a locked elbow joint (Joint2 at O_2) and an unlocked shoulder joint (Joint1 at O_1), the boundary conditions of Link1 at $x_1 = 0$ are (using equations (2.10), (2.28) and (2.29) as well as relations (2.13) together with the method of separation of variables derived in chapter 2.2.1)

$$W_1(0) = 0 \tag{4.5}$$

and

$$I_{g1}\,\omega^2 W_1'(0) = -E\,I_1 W_1''(0) \tag{4.6}$$

At $x_1 = L_1$, moment equilibrium of inertia forces gives

$$\begin{aligned} &E\,I_1 W_1''(L_1) = I_p\,\omega^2\left[W_1'(L_1) + W_2'(L_2)\right] + M_p\,\omega^2 W_1(L_1)\left(L_2 + a\right)\cos\theta + \\ &M_p\,\omega^2\left[W_2(L_2) + W_2'(L_2)\,a + W_1'(L_1)\left(L_2 + a\right)\right]\left(L_2 + a\right) + \\ &\int_0^{L_2} m_{b2}\,\omega^2\left[W_2(x_2) + W_1(L_1)\cos\theta + W_1'(L_1)\,x_2\right]x_2\,\mathrm{d}x_2 \end{aligned} \tag{4.7}$$

and force equilibrium gives

$$\begin{aligned} &E\,I\,W_1'''(L_1) = -M_p\,\omega^2\left[W_2(L_2) + W_2'(L_2)\,a + W_1'(L_1)\left(L_2 + a\right)\right]\cos\theta - \\ &\left(M_p + M_2\right)\omega^2 W_1(L_1) - \int_0^{L_2} m_{b2}\,\omega^2\left(W_2(x_2) + W_1'(L_1)\right)\cos\theta\,\mathrm{d}x_2 \end{aligned} \tag{4.8}$$

where M_2 is the mass of Link2. The integrals in equations (4.7) and (4.8) are negligibly small for dynamic response analyses but should be included for very small or zero payloads to get better results for the natural frequencies of an unloaded RMS. Note that due to their complexity and since they are never used (except to validate the given equations) they are not given in the elements d_{nm} in equation (4.15) below.
Also note that throughout this thesis the tangent frame formulation is used, and thus the boundary conditions for Link2 at $x_2 = 0$ are (relative to Link1!)

$$W_2(0) = 0 \tag{4.9}$$

and

$$\lambda_2 W_2'(0) = EI_2 W_2''(0) \tag{4.10}$$

At $x_2 = L_2$, moment equilibrium gives

$$\begin{aligned} &EI_2 W_2''(L_2) = I_p \omega^2 \left(W_1'(L_1) + W_2'(L_2)\right) + \\ &M_p \omega^2 \left[W_2(L_2) + W_2'(L_2)a + W_1'(L_1)\left(L_2 + a\right) + W_1(L_1)\cos\theta\right]a \end{aligned} \tag{4.11}$$

and force equilibrium gives

$$EIW_2'''(L_2) = -M_p \omega^2 \left[W_2(L_2) + W_2'(L_2)a + W_1'(L_1)\left(L_2 + a\right) + W_1(L_1)\cos\theta\right] \tag{4.12}$$

Applying the boundary conditions and collecting all terms with respect to $A_{1,i}$, $B_{1,i}$, $C_{1,i}$, $A_{2,i}$, $B_{2,i}$, and $C_{2,i}$, equation (4.3) reduces to

$$\begin{bmatrix} d_{11} & d_{12} & d_{13} & d_{14} & d_{15} & d_{16} \\ d_{21} & d_{22} & d_{23} & d_{24} & d_{25} & d_{26} \\ d_{31} & d_{32} & d_{33} & d_{34} & d_{35} & d_{36} \\ d_{41} & d_{42} & d_{43} & d_{44} & d_{45} & d_{46} \\ d_{51} & d_{52} & d_{53} & d_{54} & d_{55} & d_{56} \\ d_{61} & d_{62} & d_{63} & d_{64} & d_{65} & d_{66} \end{bmatrix} \begin{bmatrix} A_{1,i} \\ B_{1,i} \\ C_{1,i} \\ A_{2,i} \\ B_{2,i} \\ C_{2,i} \end{bmatrix} = \mathbf{0} \tag{4.13}$$

which can only be solved when

$$\begin{vmatrix} d_{11} & d_{12} & d_{13} & d_{14} & d_{15} & d_{16} \\ d_{21} & d_{22} & d_{23} & d_{24} & d_{25} & d_{26} \\ d_{31} & d_{32} & d_{33} & d_{34} & d_{35} & d_{36} \\ d_{41} & d_{42} & d_{43} & d_{44} & d_{45} & d_{46} \\ d_{51} & d_{52} & d_{53} & d_{54} & d_{55} & d_{56} \\ d_{61} & d_{62} & d_{63} & d_{64} & d_{65} & d_{66} \end{vmatrix} = 0 \tag{4.14}$$

Neglecting the integral terms in equations (4.7) and (4.8) and using the notation C_1= cos (k_1L_1), S_1 = sin (k_1L_1), Ch_1 = cosh (k_1L_1), Sh_1 = sinh (k_1L_1), C_2 = cos (k_2L_2), S_2 = sin (k_2L_2), Ch_2 = cosh (k_2L_2), Sh_2 = sinh (k_2L_2), the elements d_{nm} in equation (4.14) are given as

$$
\begin{aligned}
&d_{11} = d_{13} = I_{g1}\, k_1\, \omega^2; d_{12} = -2EI_1\, k_1^2; d_{14} = d_{15} = d_{16} = 0\\
&d_{21} = k_1\left(I_p + M_p\,(L_2+a)^2\right)\omega^2\, C_1 + S_1\left(EI_1\, k_1^2 + M_p\,(L_2+a)\omega^2\cos\theta\right)\\
&d_{22} = C_1\left(EI_1\, k_1^2 + M_p\,(L_2+a)\omega^2\cos\theta\right) + Ch_1\left(EI_1\, k_1^2 - M_p\,(L_2+a)\omega^2\cos\theta\right) -\\
&\qquad k_1\left(I_p + M_p\,(L_2+a)^2\right)\omega^2\,(S_1 + Sh_1)\\
&d_{23} = k_1\left(I_p + M_p\,(L_2+a)^2\right)\omega^2\, Ch_1 + \left(-EI_1\, k_1^2 + M_p\,(L_2+a)\omega^2\cos\theta\right)Sh_1\\
&d_{24} = \omega^2\,(L_2+a)M_p\, S_2 + \omega^2\, k_2\left(I_p + M_p\,(L_2+a)a\right)C_2\\
&d_{25} = \omega^2\,(L_2+a)M_p\,(C_2 - Ch_2) - \omega^2\, k_2\left(I_p + a(L_2+a)M_p\right)(S_2 + Sh_2)\\
&d_{26} = \omega^2\, k_2\left(I_p + M_p\,(L_2+a)a\right)Ch_2 + \omega^2\,(L_2+a)M_p\, Sh_2\\
&d_{31} = \left(M_2 + M_p\right)\omega^2\, S_1 + k_1\, C_1\left(-EI_1\, k_1^2 + M_p\,(L_2+a)\omega^2\cos\theta\right)\\
&d_{32} = \left(M_2 + M_p\right)\omega^2\,(C_1 - Ch_1) + EI_1\, k_1^3\,(S_1 - Sh_1) -\\
&\qquad k_1\,(L_2+a)M_p\,\omega^2\cos\theta\,(S_1 + Sh_1);\\
&d_{33} = \left(M_2 + M_p\right)\omega^2\, Sh_1 + k_1\, Ch_1\left(EI_1\, k_1^2 + M_p\,(L_2+a)\omega^2\cos\theta\right)\\
&d_{34} = \omega^2\cos\theta\, M_p\,(S_2 + a\,k_2\, C_2)\\
&d_{35} = \omega^2\cos\theta\, M_p\,(C_2 - Ch_2 + a\,k_2(S_2 + Sh_2))\\
&d_{36} = \omega^2\cos\theta\, M_p\,(Sh_2 + Ch_2); d_{41} = d_{42} = d_{43} = 0\\
&d_{44} = d_{46} = k_2\,\lambda_2; d_{45} = 2\,EI_2\, k_2^2\\
&d_{51} = \omega^2\cos\theta\, M_p\, a\, S_1 + \omega^2\, k_1\left(I_p + M_p\,(L_2+a)a\right)C_1\\
&d_{52} = \omega^2\cos\theta\, M_p\, a(C_1 - Ch_1) - \omega^2\, k_1\left(I_p + M_p\,(L_2+a)a\right)(S_1 + Sh_1)\\
&d_{53} = \omega^2\, k_1\left(I_p + M_p\,(L_2+a)a\right)Ch_1 + \omega^2\cos\theta\, M_p\, a\, Sh_1\\
&d_{54} = k_2\left(I_p + a^2\, M_p\right)\omega^2\, C_2 + \left(EI_2\, k_2^2 + a\,M_p\,\omega^2\right)S_2\\
&d_{55} = \left(EI_2\, k_2^2 + a\,M_p\,\omega^2\right)C_2 + \left(EI_2\, k_2^2 - a\,M_p\,\omega^2\right)Ch_2 -\\
&\qquad k_2\left(I_p + a^2\, M_p\right)\omega^2\,(S_2 + Sh_2)\\
&d_{56} = k_2\left(I_p + a^2\, M_p\right)\omega^2\, Ch_2 + \left(-EI_2\, k_2^2 + a\,M_p\,\omega^2\right)Sh_2\\
&d_{61} = M_p\,\omega^2\left(k_1\,(L_2+a)C_1 + \cos\theta\, S_1\right)\\
&d_{62} = M_p\,\omega^2\left(-k_1\,(L_2+a)(S_1 + Sh_1) + \cos\theta\,(C_1 - Ch_1)\right)\\
&d_{63} = M_p\,\omega^2\left(k_1\,(L_2+a)Ch_1 + \cos\theta\, Sh_1\right)\\
&d_{64} = -EI_2\, k_2^3\, C_2 + M_p\,\omega^2\left(a\,k_2\, C_2 + S_2\right)\\
&d_{65} = -M_p\,\omega^2\left(-C_2 + Ch_2 + a\,k_2\,(S_2 + Sh_2)\right) + EI_2\, k_2^3\,(S_2 - Sh_2)\\
&d_{66} = EI_2\, k_2^3\, Ch_2 + M_p\,\omega^2\left(a\,k_2\, Ch_2 + Sh_2\right)
\end{aligned}
\tag{4.15}
$$

For a locked Joint1, equation (4.6) becomes $\lambda W_1'(0) = E\,I_1\, W_1''(0)$, and the elements d_{11} and d_{13} in equation (4.15) are then given by

$$d_{11} = d_{13} = -k_1\,\lambda_1 \tag{4.16}$$

where λ_1 denotes the joint stiffness of Joint1.
For an unlocked Joint2, equation (4.10) becomes $I_{g2}\omega^2 W_2'(0) = -EI_2 W_2''(0)$, and in that case the elements d_{44} and d_{46} in equation (4.15) are

$$d_{44} = d_{46} = -I_{g2} k_2 \omega^2 \tag{4.17}$$

where I_{g2} is the rotary inertia due to the gear box effect at Joint2.
Tables 4.1 through 4.4 give the variation of the natural frequencies of the double flexible link system without end effector with θ. The system properties are L_1 = 6.37 m, L_2 = 8.93 m, m_{b1} = 3.9 kg/m, m_{b2} = 3.4 kg/m, EI_1 = 3.9786×10^6 Nm^2, EI_2 = 2.334×10^6 Nm^2, M_p = 20000 kg, I_p = 181667 kgm^2, a = 1.5 m, and $\lambda_1 = \lambda_2 = 10^6$ Nm/rad for locked joints or I_{g1} = 1188 kgm^2 and I_{g2} = 556 kgm^2 for unlocked joints.

θ [deg]	ω_1 [rad/s]	ω_2 [rad/s]	ω_3 [rad/s]	ω_4 [rad/s]
0	0.00	0.00	9.20	32.39
20	0.00	0.00	3.13	31.56
40	0.00	0.00	2.65	31.51
60	0.00	0.00	2.55	31.50
80	0.00	0.00	2.52	31.50
90	0.00	0.00	2.52	31.50

Table 4.1: Variation of exact natural frequencies of double flexible link system with θ for both joints unlocked

θ [deg]	ω_1 [rad/s]	ω_2 [rad/s]	ω_3 [rad/s]	ω_4 [rad/s]
0	0.00	1.72	22.93	80.95
20	0.00	1.56	5.08	41.06
40	0.00	1.21	3.36	40.75
60	0.00	0.94	3.00	40.69
80	0.00	0.77	2.88	40.68
90	0.00	0.72	2.86	40.67

Table 4.2: Variation of exact natural frequencies of double flexible link system with θ for Joint1 unlocked and Joint2 locked

θ [deg]	ω_1 [rad/s]	ω_2 [rad/s]	ω_3 [rad/s]	ω_4 [rad/s]
0	0.00	1.99	15.16	62.29
20	0.00	1.78	3.64	34.88
40	0.00	1.30	2.70	34.55
60	0.00	1.02	2.56	34.48
80	0.00	0.91	2.52	34.46
90	0.00	0.90	2.52	34.46

Table 4.3: Variation of exact natural frequencies of double flexible link system with θ for Joint1 locked and Joint2 unlocked

θ [deg]	ω_1 [rad/s]	ω_2 [rad/s]	ω_3 [rad/s]	ω_4 [rad/s]
0	0.23	2.05	5.91	554.29
20	0.24	1.96	5.91	500.62
40	0.24	1.68	3.58	499.97
60	0.25	1.39	3.07	499.84
80	0.27	1.22	2.91	499.80
90	0.28	1.17	2.87	499.78

Table 4.4: Variation of exact natural frequencies of double flexible link system with θ for both joints locked

It is seen from the previous tables that by contrast to the single flexible link system with end effector, the angle θ influences the natural frequencies at least up to the fourth, and the fundamental mode relatively varies the most. As mentioned before, this can lead to changing mode shapes throughout a slew manoeuvre. Note that a zero natural frequency indicates a rigid body mode.

4.1.2 EXACT SOLUTION FOR MODE SHAPES

The exact mode shapes for the two flexible links are obtained by applying the procedure described in chapter 2.2.2 to equation (4.13). Again, the zeros in the right-hand side vector are replaced by the scaling factor f to take account of the limits in numerical accuracy as explained in chapter 2.2.2.
Figures 4.2 through 4.4 show the first three mode shapes $W_{S1}(x)$, $W_{S2}(x)$ and $W_{S3}(x)$ of the complete system for the configuration Joint1 and Joint2 locked for the case $\theta = 0°$ for the above data set (see also first row in table 4.4 above).
From these figures it can be guessed that as in the previous chapters, only the fundamental mode for the case all joints locked gives rise to elastic deflections that are not very small or even negligible. In some example dynamic response analyses in chapter 4.3 this guess will be justified, since the elastic deflections will be shown to be of the magnitude of millimetres at maximum.

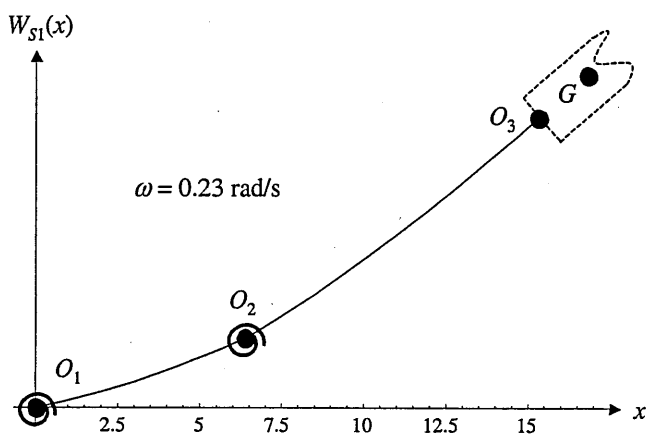

Figure 4.2: First system mode shape $W_{S1}(x)$ for configuration Joint1 and Joint2 locked for $\theta = 0°$

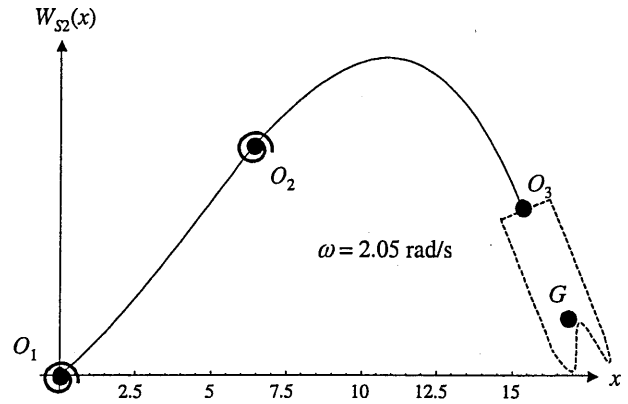

Figure 4.3: Second system mode shape $W_{S2}(x)$ for configuration Joint1 and Joint2 locked for $\theta = 0°$

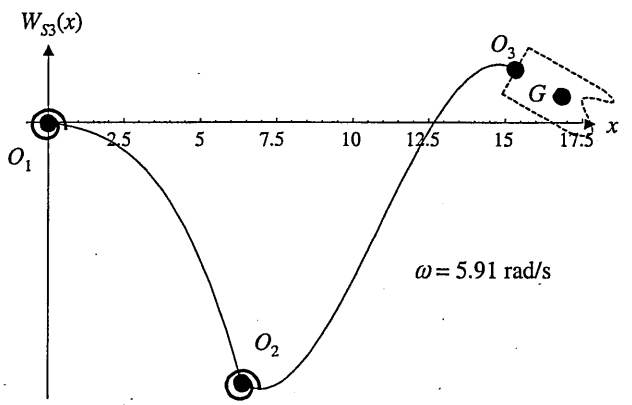

Figure 4.4: Third system mode shape $W_{S3}(x)$ for configuration Joint1 and Joint2 locked for $\theta = 0°$

Note that the mode shapes of other configurations with at least one joint unlocked are similar to figures 4.3 and 4.4 with G staying near to or on the system axis (for $\theta = 0°$).

4.2 VALIDATION OF THE DETERMINANT RESULTS

4.2.1 REPRODUCTION OF FLEXIBLE LINK WITHOUT END EFFECTOR

The determinant elements can be verified in several ways. First, the system properties are chosen so that the single link reference configuration from chapter 2 is reproduced for locked and unlocked Joint1. Thus $L_1 = L_2 = 7$ m, $m_{b1} = m_{b2} = 3.9786$ kg/m, $EI_1 = EI_2 = 3\times10^6$ Nm^2, $\lambda_2 = 10^{10}$ Nm/rad, $\theta = 0°$, $M_p = 10000$ kg, $I_p = 37500$ kgm^2, $a = 1.5$ m, and $I_{g1} = 1188$ kgm^2 for Joint1 unlocked or $\lambda_1 = 10^6$ Nm/rad for Joint1 locked. The very high value for λ_2 effectively produces a clamped Joint2 to rigidly attach Link2 to Link1. The first two natural frequencies for this system for locked and unlocked Joint1 are given in table 4.5.
Comparing tables 2.1 and 4.5 it can be seen that the determinant gives results in very close agreement to the exact results for the single link. The deviations occur due to numerical errors during the calculation of the relatively complex determinant.

freq. [rad/s]	unlocked	locked
ω_1	4.56	0.38
ω_2	25.34	5.19

Table 4.5: First two natural frequencies of double flexible link system, when the single link system is reproduced

It turns out that the proposed 6×6 determinant can produce wrong higher frequencies in certain configurations, for example when the inserted physical properties are very big or very small figures. That is the reason why the higher frequencies in table 4.1 are omitted. It is inferred that the errors are due to numerical reasons, since very great and very small figures can easily produce an ill-conditioned matrix. Due to the complexity of the determinant, one can not say where exactly the inaccuracies appear. However, by checking a series of determinant results against various results obtained by assumed multi-mode approximations and against results of BEAM, the determinant is proven to work correctly for the lower frequencies, and the previous and the following chapters show that for this work only the fundamental frequency and the corresponding mode shapes for the flexible links are of interest.
Chapter 6.4 will be dedicated to the topic of numerical problems with the proposed determinant method.

4.2.2 REPRODUCTION OF FLEXIBLE LINK WITH END EFFECTOR

Next we reproduce the single flexible link with rigid end effector from chapter 3 for one example case, say Joint1 and Joint2 locked, for various θ. Thus $L_1 = 12.12$ m, $L_2 = 1.88$ m, $m_{b1} = 3.9786$ kg/m, $m_{b2} = 10^{-5}$, $EI_1 = 3\times10^6$ Nm^2, $EI_2 = 10^{10}$ Nm^2, $\lambda_1 = 10^6$ Nm/rad, $\lambda_2 = 2.4\times10^5$ Nm/rad, $M_p = 5000$ kg, $I_p = 5417$ kgm^2, $a = 1$ m.
The results are given in Table 4.6, together with the original values from table 3.4, which are calculated with the 3×3 determinant for the single flexible link with rigid end effector. Deviations may occur due to the more complex 6×6 determinant. However, table 4.6 shows almost perfect agreement, thus verifying the elements given in equation (4.15).

θ [deg]	method	ω_1 [rad/s]	ω_2 [rad/s]	ω_3 [rad/s]	ω_4 [rad/s]
0	3×3 det.	0.56	7.89	77.77	256.74
	6×6 det.	0.56	7.89	77.77	256.73
50	3×3 det.	0.60	3.16	77.10	256.22
	6×6 det.	0.60	3.16	77.10	256.22
90	3×3 det.	0.72	2.12	77.03	256.18
	6×6 det.	0.72	2.12	77.03	256.18

Table 4.6: Verification of 6×6 determinant by comparison with results from 3×3 determinant for single flexible link with rigid end effector

4.2.3 RIGID LINK ANALYSIS

For a third verification we reproduce the rigid double pendulum from chapter 3. Therefore, $L_1 = 12.12$ m, $L_2 = 1.88$ m, $m_{b1} = 3.9786$ kg/m, $m_{b2} = 10^{-5}$, $EI_1 = EI_2 = 10^{10}$ Nm^2, $\lambda_1 = 10^6$ Nm/rad, $\lambda_2 = 2.4\times10^5$ Nm/rad, $\theta = 0°$, $M_p = 5000$ kg, $I_p = 5417$ kgm^2 and $a = 1$ m. The high value for EI_1 and EI_2 effectively produces rigid links, and the very small value for m_{b2} makes Link2 effectively massless; setting m_{b2} to zero is not allowed because if equation (4.2) gets zero, the determinant given in equation (4.14) is trivially zero for all ω. The results of this configuration are shown in Table 4.7, where "ω_i dp" and "ω_i dfl" denote the frequencies of the rigid double pendulum and the double flexible link respectively.

θ [deg]	ω_1 dp [rad/s]	ω_1 dfl [rad/s]		ω_2 dp [rad/s]	ω_2 dfl [rad/s]
0	0.87	0.87		8.80	8.80
50	0.94	0.94		3.50	3.50
90	1.12	1.12		2.36	2.36

Table 4.7: Two natural frequencies of rigid double pendulum and first two natural frequencies of double flexible link system for identical properties with $EI_i = 10^{10}$ Nm^2

Table 4.7 shows that the results obtained by the 6×6 determinant are in exact agreement with the rigid double pendulum frequencies.

4.2.4 DOUBLE FLEXIBLE LINK WITHOUT END MASS

It was mentioned in 4.2.1 that the complex determinant can produce wrong higher frequencies due to ill-conditioning. Experiments show that especially the payload mass at the end of Link2 can cause ill-conditioned matrices and determinants, probably due to its very big mass compared to the masses of all the other system members. Thus to show that the determinant does not necessarily produce wrong higher frequencies if the matrix is well conditioned, an example beam system of [47] is reproduced here. The system is shown in figure 4.5.

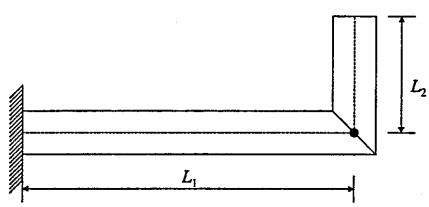

Figure 4.5: Example beam system from [47]

The system properties are $L_1 = 2$ m, $L_2 = 0.4$ m, $m_{b1} = 5.4$ kg/m, $m_{b2} = 15.0005$ kg/m, $EI_1 = 850.5$ Nm^2, $EI_2 = 3000.9$ Nm^2, and $\theta = 90°$, without payload. To create cantilever beams, the spring stiffnesses are set to a very high value, thus $\lambda_1 = \lambda_2 = 10^{10}$ Nm/rad.

Table 4.8 shows the results of [47] and of the determinant for the first four natural frequencies. It is noted that for the computation of table 4.8, the integral terms in equations (4.7) and (4.8) have been included, but are otherwise neglected.

freq. [rad/s]	[47]	determinant
ω_1	6.04	6.04
ω_2	44.36	44.36
ω_3	108.13	108.11
ω_4	216.46	216.46

Table 4.8: First four natural frequencies of example beam system of [47] in comparison with the determinant results

Table 4.8 proves clearly that the determinant is capable of reproducing also the higher frequencies of double flexible link systems correctly, if it is not ill-conditioned.

4.3 DYNAMIC RESPONSE ANALYSES

To give an idea of the magnitudes of the elastic deflections that occur during a slew of the double flexible link RMS, the following simulations are performed. It is stressed that the share of the second, third, fourth and fifth mode together in the total elastic deflection is found to be always less than 2% for some check cases. To give an idea of the influence of the higher modes: the share of a fifth mode in the total defection is typically about 10^{-5} % and thus clearly negligible. Similar to the single flexible link system with and without end effector, this proves that using only the first exact mode shape for each flexible link in the equations of motion is sufficiently accurate.

4.3.1 JOINT1 UNLOCKED AND JOINT2 LOCKED

First we consider the straight RMS with $\theta = 0°$ and Joint1 unlocked and Joint2 locked. For reasons of comparison we choose the system properties for the following analyses to be $L_1 = 6.37$ m, $L_2 = 8.93$ m, $m_{b1} = 3.9$ kg/m, $m_{b2} = 3.4$ kg/m, $EI_1 = 3.9786\times10^6$ Nm^2, $EI_2 = 2.334\times10^6$ Nm^2, $M_p = 20000$ kg, $I_p = 181667$ kgm^2 and $a = 1.5$ m. Since Joint1 is unlocked and Joint2 locked, we also have $I_{g1} = 1188$ kgm^2 and $\lambda_2 = 10^6$ Nm/rad. The RMS angular acceleration $\ddot{\alpha}$ is due to an applied torque at O_1, which is chosen identical to the SRMS maximum torque as $T_1 = 1298$ Nm. The following figures are obtained from an insertion of the first exact mode shape of each flexible link for each joint configuration into the equations of motion, which are not given here. It is noted that in the following simulations it is assumed that if a joint is unlocked, the system oscillates stable about a reference configuration, although in practice an unlocked joint may cause the actual link to rotate steadily or random about the joint.
In the present case the vibration amplitudes of Link1 at O_2 and of G are 5.7 mm and 0.7 mm respectively.

In the perpendicular case with $\theta = 90°$, Link2 and G oscillates with an amplitude of 6.5 mm perpendicular to Link1, and G also oscillates with an amplitude of 3.4 mm parallel to Link1, that is perpendicular to Link2.

4.3.2 JOINT1 AND JOINT2 UNLOCKED

Now we consider the case of a straight RMS with both joints unlocked. The system properties are as before, except that instead of $\lambda_2 = 10^6$ Nm/rad we now have $I_{g2} = 556$ kgm^2.
Here the amplitude of vibration of Link1 at O_2 is 1.78 cm, and the vibration amplitude of the payload centre of mass G is 0.07 mm.
Performing the same simulation with perpendicular links, that is with $\theta = 90°$, the elastic deflection amplitude of Link1 at O_2 and of G is less than 0.1 mm.

4.3.3 JOINT1 LOCKED AND JOINT2 UNLOCKED

The third case is the straight RMS with Joint1 locked and Joint2 unlocked. As before, an angular acceleration $\ddot{\alpha}$ of the whole RMS system is simulated, using the first exact mode shapes for both flexible links. Since Joint1 is locked now, we apply the same method described in chapters 2.5 and 3.3.3 for the single flexible link without and with end effector to allow for a comparison with the results for an unlocked Joint1. As before, all properties remain except that $I_{g1} = 1188$ kgm^2 is now replaced by $\lambda_1 = 10^6$ Nm/rad. For the given configuration the amplitudes of the elastic deflections of Link1 at O_2 and of G are 5.4 mm and 1.1 mm.
If the links are perpendicular with $\theta = 90°$, the vibration amplitudes of Link2 and of G perpendicular to Link1 are 7.7 mm, and G also vibrates with an amplitude of 1.26 cm perpendicular to Link2, that is parallel to Link1.

4.3.4 JOINT1 AND JOINT2 LOCKED

The last possible joint configuration is both joints locked, thus $I_{g2} = 556$ kgm^2 is now replaced by $\lambda_2 = 10^6$ Nm/rad.
The oscillation amplitudes of Link1 at O_2 and of G are now 9.4 mm and 4.47 cm respectively.
For perpendicular links with $\theta = 90°$, the deflection amplitudes of Link2 and of G perpendicular to Link1 are 4.1 mm, and the vibration amplitude of G perpendicular to Link2 is 8.6 mm.

4.4 VALIDATION OF DYNAMIC RESPONSE ANALYSES

From the previous analyses it is seen that the elastic deflections are relatively small in general and are determined by the maximum torques. To validate the results, the following simple calculations are performed.

Neglecting the payload rotary inertia, the inertia force F at the payload centre of mass G due to an angular acceleration $\ddot{\alpha}$ at distance $L = L_1 + L_2 + a$ from a revolute joint is

$$F = \ddot{\alpha} L M_p \tag{4.18}$$

where M_p denotes the payload translatory inertia and L_1, L_2 and a are the length of Link1 and Link2 and the distance of G from the end of Link2. But since the angular acceleration is chosen so as if a torque T was applied at (locked) Joint1, we can write

$$\ddot{\alpha} = \frac{T}{M_p L^2} \tag{4.19}$$

Inserting equation (4.19) into (4.18), F simplifies to

$$F = \frac{T}{L} \tag{4.20}$$

The (linearised) rigid body deflections y_{1r} and y_{2r} of the links at O_2 and O_3 due to the joint stiffnesses λ_1 and λ_2 (see figure 4.1) are for Link1

$$y_{1r} = \frac{F L}{\lambda_1} L_1 \tag{4.21}$$

and for Link2

$$y_{2r} = \frac{F(L_2 + a)}{\lambda_2} L_2 \tag{4.22}$$

The elastic deflections y_{1e} and y_{2e} of the links at O_2 and O_3 due to F are ([45]) for Link1

$$y_{1e} = \frac{F L_1^3}{3 E I_1} \tag{4.23}$$

and for Link2

$$y_{2e} = \frac{F L_2^3}{3 E I_2} \tag{4.24}$$

Finally, the elastic deflections y_{1M} and y_{2M} of the links due to the moment caused by F times the actual offset from the link ends are ([45]) for Link1

$$y_{1M} = \frac{F(L_2 + a) L_1^2}{2 E I_1} \tag{4.25}$$

and for Link2

$$y_{2M} = \frac{F\,a\,L_2^2}{2\,EI_2} \tag{4.26}$$

The sum y of the partial deflections is then

$$y = y_{1r} + y_{2r} + y_{1e} + y_{2e} + y_{1M} + y_{2M} \tag{4.27}$$

It is noted that the deflection of Link2 at O_3 due to the slope of Link1 at O_2 is not taken into account in the above calculations.
Inserting L_1 = 6.37 m, L_2 = 8.93 m, a = 1.5 m, T = 1298 Nm and M_p = 20000 kg yields y_2 = 2.92 cm. Taking into account that the payload rotary inertia and the deflection of Link2 due to the slope of Link1 at O_2 have been neglected and that G is offset from O_3 by a, this result confirms the previous figures, especially their dimensions.

4.5 SUMMARY

This section applies the determinant method to the double flexible link system, which yields the exact analytical natural frequencies and mode shapes. The determinant elements are derived with the assumption that the base of the RMS is fixed, which is comparable to an RMS operating on an attitude controlled Shuttle or a very large space station, or to an RMS in the ground test bed with low friction bearings. It is found that the higher frequencies obtained by the determinant can be wrong in certain configurations, which is due to the complexity of the determinant expression. It is however proven that the lower frequencies, which are of sole interest for this thesis, are always calculated correctly. Chapter 6.4 will analyse numerical problems when using the determinant method.
It is stressed that an analysis of a double flexible link system with various boundary conditions for the links can apparently not be found in the available literature.
Performing some typical dynamic response analyses shows that the most important aspect of the system is the limiting of the torques at the joints. Since the exciting force of an elastic coordinate q_i in the equations of motion is the product of inertias and accelerations, and since on the other hand the accelerations depend on the maximum torques and the inertias, the exciting force depends almost only on the maximum torques (except for the payload rotary inertia, which is different for different payload sizes).
Assuming sensible values for the maximum torques, for example the SRMS maximum torques ([3]), the elastic deflections are relatively small in general. The simulation of a space station angular acceleration so that the RMS is accelerated as if the maximum torque was applied at Joint1 yields vibration amplitudes of G of about 4.3 cm, if both joints are locked. It is noted however that in reality the space station is not capable of such an angular acceleration.

CHAPTER 5: DOUBLE LINK WITH FIXED BASED AND END EFFECTOR

This section applies the determinant method to the double flexible link system with fixed base and articulated end effector. The system represents the fully developed RMS as examined here, comparable to the Shuttle Remote Manipulator System (SRMS). Assuming system properties similar to those of the SRMS, the end effector can be taken as rigid due to its relatively stiff and short structure ([3]). The aim is to determine the variation of the natural frequencies and mode shapes for a range of θ_2 and θ_3. The system is shown in figure 5.1.

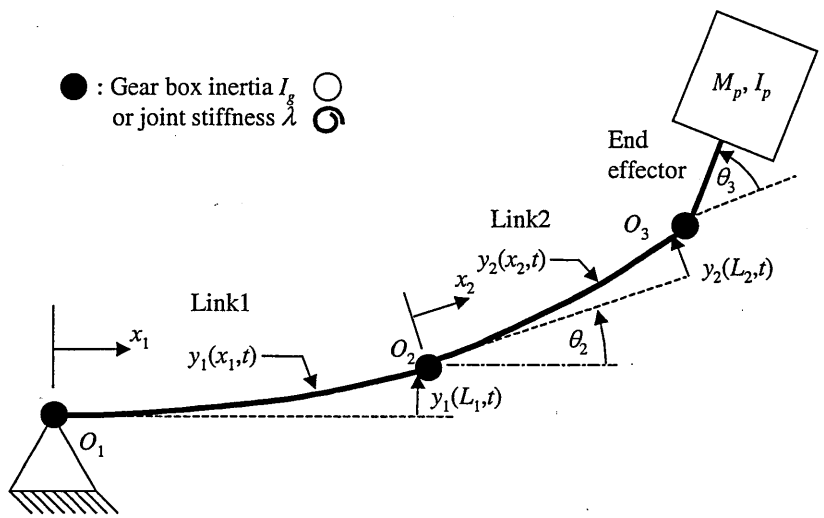

Figure 5.1: Sketch of the double flexible link system with articulated end effector

In figure 5.1, $y_1(x_1,t)$ and $y_2(x_2,t)$ denote the elastic deflections of Link1 and Link2, θ_2 is the angle of Link2 relative to Link1 at O_2, and θ_3 is the angle of the end effector relative to Link2 at O_3 in the undeformed configuration. The figure represents the ground based test set up with an inertially fixed base and low friction bearings ([3]).

5.1 DETERMINATION OF NATURAL FREQUENCIES AND MODE SHAPES

5.1.1 EXACT SOLUTION FOR NATURAL FREQUENCIES

To obtain the exact natural frequencies of the system we apply the determinant method. The mode shape of link l (l = 1, 2) is given by equations (4.1) and (4.2), and after collecting the terms with respect to $A_{l,i}$, $B_{l,i}$, $C_{l,i}$ and $D_{l,i}$, the eigenvalue equation for the general case becomes equation (4.3), and the arising determinant for the general case is given by equation (4.4).
Equation (4.1) is solved by taking into account the boundary conditions at $x_l = 0$ and $x_l = L_l$. To obtain the necessary boundary conditions for the present configuration, we consider figure 5.2, which sketches the various acceleration components of the payload centre of mass G.
In figure 5.2 a_1, a_{21} and a_{32} denote the translatory accelerations of O_2 relative to O_1, of O_3 relative to O_2 and of G relative to O_3.

The boundary conditions are derived by formulating the payload inertia forces and moments at the end of the links and by formulating the kinematic boundary conditions. The joints can be locked or unlocked, causing the presence of either joints stiffnesses or gear box inertias.

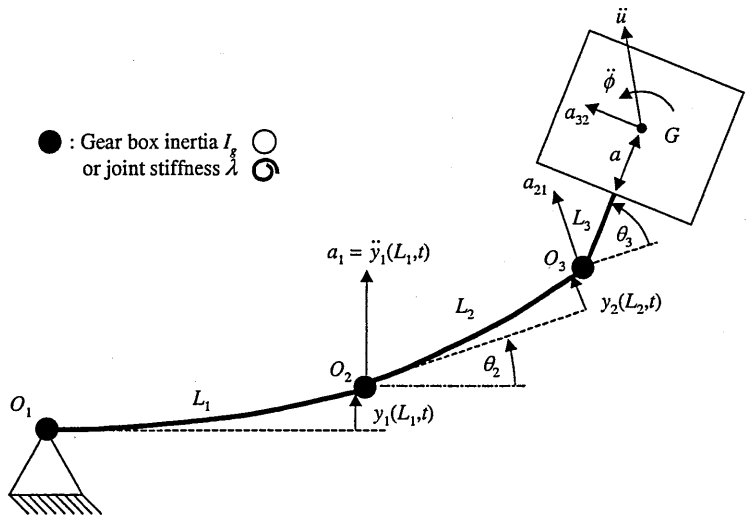

Figure 5.2: Acceleration components of the payload centre of mass G

Using again equations (2.10), (2.28) and (2.29) and the relations (2.13) together with the method of separation of variables as shown in chapter 2.2.1, the boundary conditions of Link1 at $x_1 = 0$ for a locked Joint1 are

$$W_1(0) = 0 \tag{5.1}$$

and

$$\lambda_1 W_1'(0) = E I_1 W_1''(0) \tag{5.2}$$

To obtain the boundary conditions of Link1 at $x_1 = L_1$, we calculate the total moment about O_2 and the total force perpendicular to Link1 at O_2. From figure 5.2 the total angular acceleration $\ddot{\phi}$ about the payload centre of mass G is

$$\ddot{\phi} = \ddot{y}_1'(L_1,t) + \ddot{y}_2'(L_2,t) + \Delta\ddot{\theta}_3 \tag{5.3}$$

where $\Delta\ddot{\theta}_3$ is the acceleration of the angular motion $\Delta\theta_3$ of the end effector and the payload relative to Link2 at O_3 due to the joint stiffness λ_3, which is given by

$$\Delta\theta_3 = \frac{EI_2\, y_2''(L_2,t)}{\lambda_3} = \frac{EI_2\, W_2''(L_2) q(t)}{\lambda_3} = \Delta\bar{\theta}_3\, q(t) \tag{5.4}$$

The total translatory acceleration $\ddot{u}_{1M}$ of G perpendicular to Link2 is

$$\begin{aligned}\ddot{u}_{1M} = {} & \ddot{y}_1(L_1,t)\cos\theta_2 + \ddot{y}_2(L_2,t) + \ddot{y}_1'(L_1,t)\left[L_2 + (L_3 + a)\cos\theta_3\right] + \\ & \left[\ddot{y}_2'(L_2,t) + \Delta\ddot{\theta}_3\right](L_3 + a)\cos\theta_3\end{aligned} \tag{5.5}$$

In equation (5.5) and the following equations it is assumed that the angular deflections of the links and the end effector at the joints due the joint stiffnesses is small, so that the angles θ_2 and θ_3 of the undeformed configuration can be taken as constant while applying the cosine function.
The bending moment of Link1 at O_2 must be equal to the total moment about O_2 due to the various inertias, thus using equations (5.3) and (5.5) and the usual method of separation of variables

$$\begin{aligned} &EI_1 W_1''(L_1) = I_p \omega^2 \left[W_1'(L_1) + W_2'(L_2) + \Delta\bar{\theta}_3\right] + \\ &M_p \omega^2 \left[W_2(L_2) + W_1(L_1)\cos\theta_2 + W_1'(L_1)\left(L_2 + (L_3 + a)\cos\theta_3\right) + \right. \\ &\left.\left(W_2'(L_2) + \Delta\bar{\theta}_3\right)(L_3 + a)\cos\theta_3\right]\left(L_2 + (L_3 + a)\cos\theta_3\right) + \\ &\int_0^{L_2} m_{b2}\,\omega^2 \left[W_2 + W_1(L_1)\cos\theta_2 + W_1'(L_1)\,x_2\right] x_2\,\mathrm{d}x_2 \end{aligned} \tag{5.6}$$

The integrals in equations (5.6) and (5.7) represent the inertia moment of the distributed mass of Link2 about O_2.
The shear force of Link1 at O_2 must be equal to the total force perpendicular to Link1 due to the various inertias, thus with M_2 being the mass of Link2,

$$\begin{aligned} &-EI_1 W_1'''(L_1) = \left(M_p + M_2\right)\omega^2 W_1(L_1) + \int_0^{L_2} m_{b2}\,\omega^2 \left(W_2 + W_1'(L_1)\right)\cos\theta_2\,\mathrm{d}x_2 + \\ &M_p \omega^2 \left(W_2'(L_2) + \Delta\bar{\theta}_3\right)(L_3 + a)\cos\left(\theta_2 + \theta_3\right) + \\ &M_p \omega^2 \left[W_2(L_2) + W_1'(L_1)\left(L_2 + (L_3 + a)\cos\theta_3\right)\right]\cos\theta_2 \end{aligned} \tag{5.7}$$

The boundary conditions of Link2 at $x_2 = 0$ are given by

$$W_2(0) = 0 \tag{5.8}$$

and

$$\lambda_2 W_2'(0) = E I_2 W_2''(0) \tag{5.9}$$

if Joint2 is locked with joint stiffness λ_2.
The boundary conditions at $x_2 = L_2$ are obtained by considering the various inertia forces at O_3. The translatory acceleration $\ddot{u}_{2M}$ of G perpendicular to the end effector is

$$\begin{aligned} \ddot{u}_{2M} = &\ddot{y}_1(L_1, t)\cos\left(\theta_2 + \theta_3\right) + \left(\ddot{y}_2'(L_2, t) + \Delta\ddot{\theta}_3\right)(L_3 + a) + \\ &\ddot{y}_2(L_2) + \ddot{y}_1'(L_1)\left(L_2 + (L_3 + a)\cos\theta_3\right)\cos\theta_3 \end{aligned} \tag{5.10}$$

With the usual method and equations (5.3) and (5.10), moment equilibrium at O_3 is

$$\begin{aligned} &EI_2 W_2''(L_2) = I_p \omega^2 \left[W_1'(L_1) + W_2'(L_2) + \Delta\bar{\theta}_3\right] + M_p \omega^2 \left[W_1(L_1)\cos\left(\theta_2 + \theta_3\right) + \right. \\ &\left.\left(W_2'(L_2) + \Delta\bar{\theta}_3\right)(L_3 + a) + \left[W_2(L_2) + W_1'(L_1)\left(L_2 + (L_3 + a)\cos\theta_3\right)\right]\cos\theta_3\right](L_3 + a) \end{aligned} \tag{5.11}$$

The shear force of Link2 at O_3 must be equal to all the inertia force components perpendicular to Link2 at O_3, thus

$$\begin{aligned} -EI_2 W_2'''(L_2) = M_p \omega^2 [&W_1(L_1)\cos\theta_2 + W_2(L_2) + \\ &\left(W_2'(L_2) + \Delta\bar{\theta}_3\right)(L_3 + a)\cos\theta_3 + W_1'(L_1)(L_2 + (L_3 + a)\cos\theta_3)] \end{aligned} \tag{5.12}$$

Applying the boundary conditions and collecting all terms with respect to $A_{1,i}$, $B_{1,i}$, $C_{1,i}$, $A_{2,i}$, $B_{2,i}$, and $C_{2,i}$, equation (4.3) reduces to

$$\begin{bmatrix} d_{11} & d_{12} & d_{13} & d_{14} & d_{15} & d_{16} \\ d_{21} & d_{22} & d_{23} & d_{24} & d_{25} & d_{26} \\ d_{31} & d_{32} & d_{33} & d_{34} & d_{35} & d_{36} \\ d_{41} & d_{42} & d_{43} & d_{44} & d_{45} & d_{46} \\ d_{51} & d_{52} & d_{53} & d_{54} & d_{55} & d_{56} \\ d_{61} & d_{62} & d_{63} & d_{64} & d_{65} & d_{66} \end{bmatrix} \begin{bmatrix} A_{1,i} \\ B_{1,i} \\ C_{1,i} \\ A_{2,i} \\ B_{2,i} \\ C_{2,i} \end{bmatrix} = \mathbf{0} \tag{5.13}$$

which is solved if

$$\begin{vmatrix} d_{11} & d_{12} & d_{13} & d_{14} & d_{15} & d_{16} \\ d_{21} & d_{22} & d_{23} & d_{24} & d_{25} & d_{26} \\ d_{31} & d_{32} & d_{33} & d_{34} & d_{35} & d_{36} \\ d_{41} & d_{42} & d_{43} & d_{44} & d_{45} & d_{46} \\ d_{51} & d_{52} & d_{53} & d_{54} & d_{55} & d_{56} \\ d_{61} & d_{62} & d_{63} & d_{64} & d_{65} & d_{66} \end{vmatrix} = 0 \tag{5.14}$$

With the notation $C_1 = \cos(k_1 L_1)$, $S_1 = \sin(k_1 L_1)$, $Ch_1 = \cosh(k_1 L_1)$, $Sh_1 = \sinh(k_1 L_1)$, $C_2 = \cos(k_2 L_2)$, $S_2 = \sin(k_2 L_2)$, $Ch_2 = \cosh(k_2 L_2)$, $Sh_2 = \sinh(k_2 L_2)$, and neglecting the integrals in equations (5.6) and (5.7), the elements d_{nm} in equation (5.14) are given as

$$\begin{aligned} &d_{11} = d_{13} = k_1 \lambda_1; d_{12} = 2EI_1 k_1^2; d_{14} = d_{15} = d_{16} = 0 \\ &d_{21} = k_1 \left(I_p + M_p \left(L_2 + (a + L_3)\cos\theta_3\right)^2\right)\omega^2 C_1 + \\ &\qquad S_1 \left(EI_1 k_1^2 + M_p \left(L_2 + (a + L_3)\cos\theta_3\right)\omega^2 \cos\theta_2\right) \\ &d_{22} = M_p \omega^2 \cos\theta_2 \left(L_2 + (a + L_3)\cos\theta_3\right)\left(C_1 - Ch_1 + EI_1 k_1^2 \left(C_1 + Ch_1\right)\right) - \\ &\qquad I_p k_1 \omega^2 \left(S_1 + Sh_1\right) - M_p k_1 \omega^2 \left(L_2 + (a + L_3)\cos\theta_3\right)^2 \left(S_1 + Sh_1\right) \\ &d_{23} = k_1 \left(I_p + M_p \left(L_2 + (a + L_3)\cos\theta_3\right)^2\right)\omega^2 Ch_1 - \\ &\qquad Sh_1 \left(EI_1 k_1^2 - M_p \left(L_2 + (a + L_3)\cos\theta_3\right)\omega^2 \cos\theta_2\right) \end{aligned} \tag{5.15}$$

$$d_{24} = \omega^2 \left(M_p \left(L_2 + (a+L_3)\cos\theta_3\right) S_2 + I_p\, k_2\, C_2\right) +$$
$$\omega^2 \left(-\frac{I_p\, k_2^2\, EI_2\, S_2}{\lambda_3} + k_2 (a+L_3) M_p \cos\theta_3 \left(L_2 + (a+L_3)\cos\theta_3\right)\left(C_2 - \frac{EI_2 k_2 S_2}{\lambda_3}\right)\right)$$

$$d_{25} = \omega^2 \left(M_p \left(L_2 + (a+L_3)\cos\theta_3\right)(C_2 - Ch_2)\right) +$$
$$\omega^2 \left(-I_p\, k_2 \left(S_2 + Sh_2 + \frac{EI_2\, k_2 (C_2 + Ch_2)}{\lambda_3}\right)\right) -$$
$$\omega^2 \left(M_p\, k_2 \cos\theta_3 (a+L_3)\left(L_2 + (a+L_3)\cos\theta_3\right)\left(S_2 + Sh_2 + \frac{EI_2\, k_2 (C_2 + Ch_2)}{\lambda_3}\right)\right)$$

$$d_{26} = \omega^2 \left(M_p \left(L_2 + (a+L_3)\cos\theta_3\right) Sh_2 + I_p\, k_2\, Ch_2\right) +$$
$$\omega^2 \left(\frac{I_p\, k_2^2\, EI_2\, Sh_2}{\lambda_3} + k_2 (a+L_3) M_p \cos\theta_3 \left(L_2 + (a+L_3)\cos\theta_3\right)\left(Ch_2 + \frac{EI_2 k_2 Sh_2}{\lambda_3}\right)\right)$$

$$d_{31} = k_1\, C_1 \left(-EI_1\, k_1^2 + M_p\, \omega^2 \cos\theta_2 \left(L_2 + (a+L_3)\cos\theta_3\right)\right) + \left(M_p + M_2\right)\omega^2\, S_1$$

$$d_{32} = \left(M_p + M_2\right)\omega^2 \left(C_1 - Ch_1\right) + EI_1\, k_1^3 \left(S_1 - Sh_1\right) -$$
$$k_1\, M_p\, \omega^2 \cos\theta_2 \left(L_2 + (a+L_3)\cos\theta_3\right)\left(S_1 + Sh_1\right)$$

$$d_{33} = k_1\, Ch_1 \left(EI_1\, k_1^2 + M_p\, \omega^2 \cos\theta_2 \left(L_2 + (a+L_3)\cos\theta_3\right)\right) + \left(M_p + M_2\right)\omega^2\, Sh_1$$

$$d_{34} = \frac{\omega^2}{k_2\, \lambda_3} \left(-k_2^2 (a+L_3) M_p \cos\left(\theta_2 + \theta_3\right)\left(-\lambda_3\, C_2 + EI_2\, k_2\, S_2\right)\right) +$$
$$\omega^2 \cos\theta_2\, M_p\, S_2 \qquad (5.15)$$

$$d_{35} = \omega^2\, M_p \cos\theta_2 \left(C_2 - Ch_2\right) -$$
$$\omega^2 \left(k_2 (a+L_3) M_p \cos\left(\theta_2 + \theta_3\right)\left(S_2 + Sh_2 + EI_2\, k_2 \frac{C_2 + Ch_2}{\lambda_3}\right)\right)$$

$$d_{36} = \frac{\omega^2}{k_2\, \lambda_3} \left(k_2^2 (a+L_3) M_p \cos\left(\theta_2 + \theta_3\right)\left(\lambda_3\, Ch_2 + EI_2\, k_2\, Sh_2\right)\right) +$$
$$\omega^2 \cos\theta_2\, M_p\, Sh_2$$

$$d_{41} = d_{42} = d_{43} = 0; d_{44} = d_{46} = k_2\, \lambda_2; d_{45} = 2\, EI_2\, k_2^2;$$

$$d_{51} = \omega^2 \left(I_p\, k_1\, C_1 + k_1 (a+L_3) M_p\, C_1 \cos\theta_3 \left(L_2 + (a+L_3)\cos\theta_3\right)\right) +$$
$$\omega^2 \left((a+L_3) M_p\, C_1 \cos\left(\theta_2 + \theta_3\right) S_1\right)$$

$$d_{52} = \omega^2 (a+L_3) M_p\, C_1 \cos\left(\theta_2 + \theta_3\right)\left(C_1 - Ch_1\right) - \omega^2\, I_p\, k_1 \left(S_1 + Sh_1\right) -$$
$$\omega^2\, k_1 (a+L_3) M_p \cos\theta_3 \left(L_2 + (a+L_3)\cos\theta_3\right)\left(S_1 + Sh_1\right)$$

$$d_{53} = \omega^2 \left(I_p\, k_1\, Ch_1 + k_1 (a+L_3) M_p\, Ch_1 \cos\theta_3 \left(L_2 + (a+L_3)\cos\theta_3\right)\right) +$$
$$\omega^2 \left((a+L_3) M_p\, C_1 \cos\left(\theta_2 + \theta_3\right) Sh_1\right)$$

$$d_{54} = EI_2\, k_2^2\, S_2 + \omega^2 \left(k_1 (a+L_3) M_p \cos\theta_3\, S_2 + I_p\, k_2 \left(C_2 - EI_2\, k_2 \frac{S_2}{\lambda_3}\right)\right) +$$
$$k_2 (a+L_3)^2\, M_p\, \omega^2 \left(C_2 - EI_2\, k_2 \frac{S_2}{\lambda_3}\right)$$

$$
\begin{aligned}
d_{55} &= EI_2 k_2^2 (C_2 + Ch_2) + \omega^2 k_1 (a + L_3) M_p \cos\theta_3 (C_2 - Ch_2) + \\
&\quad \omega^2 I_p k_2 \left(S_2 + Sh_2 + EI_2 k_2 \tfrac{C_2 + Ch_2}{\lambda_3}\right) + \\
&\quad k_2 (a + L_3)^2 M_p \omega^2 \left(S_2 + Sh_2 + EI_2 k_2 \tfrac{C_2 + Ch_2}{\lambda_3}\right) \\
d_{56} &= \omega^2 \left(k_1 (a + L_3) M_p \cos\theta_3 \, Sh_2 + I_p k_2 \left(Ch_2 + EI_2 k_2 \tfrac{Sh_2}{\lambda_3}\right)\right) - EI_2 k_2^2 \, Sh_2 + \\
&\quad k_2 (a + L_3)^2 M_p \omega^2 \left(Ch_2 + EI_2 k_2 \tfrac{Sh_2}{\lambda_3}\right) \\
d_{61} &= M_p \omega^2 \left(k_1 C_1 \left(L_2 + (a + L_3)\cos\theta_3\right) + \cos\theta_2 \, S_1\right) \\
d_{62} &= M_p \omega^2 \left(-k_1 (S_1 + Sh_1)\left(L_2 + (a + L_3)\cos\theta_3\right) + \cos\theta_2 (C_1 - Ch_1)\right) \\
d_{63} &= M_p \omega^2 \left(k_1 Ch_1 \left(L_2 + (a + L_3)\cos\theta_3\right) + \cos\theta_2 \, Sh_1\right) \\
d_{64} &= -EI_2 k_2^3 C_2 + M_p \omega^2 \left(S_2 + k_2 (a + L_3)\cos\theta_3 \left(C_2 - EI_2 k_2 \tfrac{S_2}{\lambda_3}\right)\right) \\
d_{65} &= EI_2 k_2 (S_2 - Sh_2) + \\
&\quad M_p \omega^2 \left(C_2 - Ch_2 + k_2 (a + L_3)\cos\theta_3 \left(S_2 + Sh_2 + EI_2 k_2 \tfrac{C_2 + Ch_2}{\lambda_3}\right)\right) \\
d_{66} &= EI_2 k_2^3 \, Ch_2 + M_p \omega^2 \left(Sh_2 + k_2 (a + L_3)\cos\theta_3 \left(Ch_2 + EI_2 k_2 \tfrac{Sh_2}{\lambda_3}\right)\right)
\end{aligned}
\tag{5.15}
$$

If Joint1 is unlocked, equation (5.2) becomes $I_{g1} \omega^2 W_1'(0) = -E I_1 W_1''(0)$, and the elements d_{11} and d_{13} in equation (5.15) are then given by

$$
d_{11} = d_{13} = -I_{g1} k_1 \omega^2 \tag{5.16}
$$

where I_{g1} is the rotary inertia due to the gear box at Joint1. Similar, for an unlocked Joint2, equation (5.9) becomes $I_{g2} \omega^2 W_2'(0) = -E I_2 W_2''(0)$, and the elements d_{44} and d_{46} in equation (5.15) are then

$$
d_{44} = d_{46} = -I_{g2} k_2 \omega^2 \tag{5.17}
$$

where I_{g2} is the rotary inertia due to the gear box at Joint2. The rotatory and translatory inertia of the end effector and the gear box inertia for unlocked Joint3 can be included in the payload, but are negligible small.

For the actual system, eight different joint states are possible. The following tables 5.1 through 5.8 show the variation of the first non-zero natural frequency with θ_2 and θ_3 for each joint configuration. It is noted that if Joint3 is unlocked, a very small figure is inserted into the determinant ($\lambda_3 = 10^{-3}$ Nm/rad). Inserting zero is not allowed since λ_3 appears in the denominators in equation (5.15). The system properties are chosen identical to the SRMS ([3]), thus $L_1 = 6.37$ m, $L_2 = 7.05$ m, $L_3 = 1.88$ m, $m_{b1} = 3.9$ kg/m, $m_{b2} = 3.4$ kg/m, $EI_1 = 3.9786 \times 10^6$ Nm^2 and $EI_2 = 2.334 \times 10^6$ Nm^2. The joints properties are $\lambda_1 = 10^6$ Nm/rad or $I_{g1} = 1188$ kgm^2, $\lambda_2 = 10^6$ Nm/rad or $I_{g2} = 556$ kgm^2 and $\lambda_3 = 2.4 \times 10^5$ Nm/rad or $I_{g3} = 191$ kgm^2 respectively if the actual joint is locked or unlocked. The payload is chosen to be $M_p = 30000$ kg, $I_p =$

400000 kgm^2 and a = 2 m. From now on this will be the standard data set (B).

$\theta_2\downarrow$ $\theta_3\rightarrow$	0°	30°	60°	90°
0°	34.04	19.49	19.29	19.26
30°	31.21	30.13	27.86	27.18
60°	31.20	30.19	29.65	29.18
90°	31.19	30.40	29.30	28.90

Table 5.1: Variation of first non-zero frequency of double flexible link with end effector with θ_2 and θ_3 for all three joints unlocked

$\theta_2\downarrow$ $\theta_3\rightarrow$	0°	30°	60°	90°
0°	6.04	1.95	1.62	1.42
30°	1.29	1.33	1.24	1.08
60°	1.15	1.17	1.07	0.91
90°	1.14	1.09	0.96	0.78

Table 5.2: Joint1 and Joint2 unlocked, Joint3 locked

$\theta_2\downarrow$ $\theta_3\rightarrow$	0°	30°	60°	90°
0°	20.44	4.37	3.08	2.69
30°	2.15	1.97	1.82	1.61
60°	1.21	1.30	1.24	1.06
90°	0.94	1.02	0.94	0.78

Table 5.3: Joint1 and Joint3 unlocked, Joint2 locked

$\theta_2\downarrow$ $\theta_3\rightarrow$	0°	30°	60°	90°
0°	0.83	0.65	0.47	0.41
30°	0.76	0.52	0.40	0.37
60°	0.61	0.43	0.35	0.35
90°	0.50	0.37	0.33	0.34

Table 5.4: Joint1 unlocked, Joint2 and Joint3 locked

$\theta_2\downarrow$ $\theta_3\rightarrow$	0°	30°	60°	90°
0°	13.33	2.06	1.44	1.34
30°	1.46	0.94	0.86	0.84
60°	0.84	0.67	0.66	0.66
90°	0.73	0.61	0.60	0.61

Table 5.5: Joint1 locked, Joint2 and Joint3 unlocked

$\theta_2\downarrow$ $\theta_3\rightarrow$	0°	30°	60°	90°
0°	1.02	0.78	0.54	0.45
30°	0.98	0.62	0.45	0.39
60°	0.82	0.53	0.41	0.38
90°	0.73	0.52	0.43	0.40

Table 5.6: Joint1 and Joint3 locked, Joint2 unlocked

$\theta_2\downarrow$ $\theta_3\rightarrow$	0°	30°	60°	90°
0°	0.40	0.33	0.27	0.27
30°	0.40	0.31	0.26	0.27
60°	0.42	0.32	0.28	0.30
90°	0.48	0.35	0.31	0.34

Table 5.7: Joint1 and Joint2 locked, Joint3 unlocked

$\theta_2\downarrow$ $\theta_3\rightarrow$	0°	30°	60°	90°
0°	0.17	0.18	0.20	0.24
30°	0.18	0.19	0.21	0.26
60°	0.19	0.20	0.23	0.28
90°	0.20	0.22	0.25	0.32

Table 5.8: All three joints locked

It is seen from the previous tables that the first non-zero frequency can change considerably with varying angles θ_2 and θ_3. It is stressed however that a very big change of the fundamental frequency does not automatically correspond to big changes in the elastic deflections or the mode shapes. Note finally that for configurations with one or more joints unlocked, there are as many zero frequency or rigid body modes as there are unlocked joints.

5.1.2 EXACT SOLUTION FOR MODE SHAPES

The exact mode shapes are computed following the method described in 2.2.2 and the previous chapters 3 and 4. The following figures 5.3 through 5.6 show the first non-rigid system mode shape $W_{S1}(x)$ for all joint configurations when at least two joints are locked. It is found that the mode shapes do practically not change with varying angles of θ_2 and θ_3 in the joint configurations that lead to non-negligible elastic deflections of the RMS and that are analysed in the following chapters in open and closed loop dynamic responses. Therefore the mode shapes computed for the straight RMS for one joint configuration can be used for simulations with time varying joint angles without loss of accuracy when using tangent frame formulation.
This statement will be proven in chapter 7.

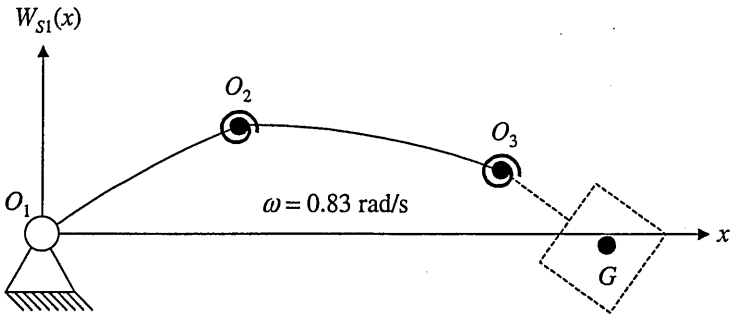

Figure 5.3: First system mode shape $W_{S1}(x)$ for configuration Joint1 unlocked, Joint2 and Joint3 locked for $\theta_2 = \theta_3 = 0°$

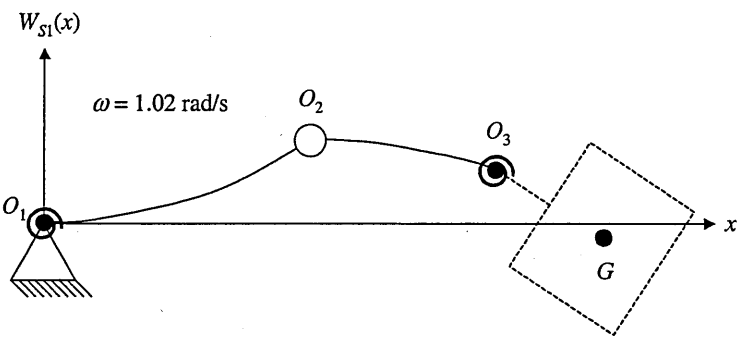

Figure 5.4: First system mode shape $W_{S1}(x)$ for configuration Joint1 and Joint3 locked, Joint2 unlocked for $\theta_2 = \theta_3 = 0°$

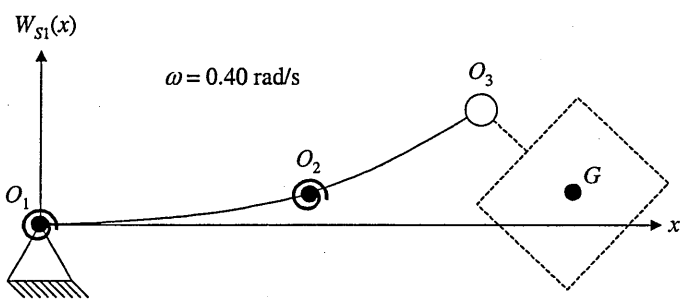

Figure 5.5: First system mode shape $W_{S1}(x)$ for configuration Joint1 and Joint2 locked, Joint3 unlocked for $\theta_2 = \theta_3 = 0°$

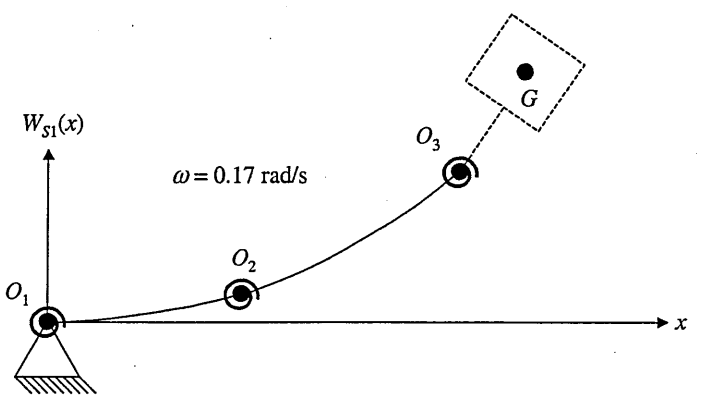

Figure 5.6: First system mode shape $W_{S1}(x)$ for configuration all three joints locked for $\theta_2 = \theta_3 = 0°$

5.2 VALIDATION OF THE DETERMINANT RESULTS

The determinant elements are verified in the way established before, that is comparison to the various natural frequencies obtained from previous determinants and from the double rigid pendulum, and by comparison with an assumed mode shape expansion using BEAM and SIMPACK.

5.2.1 REPRODUCTION OF FLEXIBLE LINK WITHOUT END EFFECTOR

At first we reproduce the standard single link system by inserting $L_1 = L_2 = 7$ m, $L_3 = 0$ m, $m_{b1} = m_{b2} = 3.9786$ kg/m, $EI_1 = EI_2 = 3\times10^6$ Nm^2, $\lambda_2 = \lambda_3 = 10^{10}$ Nm/rad, $\theta_2 = \theta_3 = 0°$, $M_p = 10000$ kg, $I_p = 37500$ kgm^2, $a = 1.5$ m, and $I_{g1} = 1188$ kgm^2 for Joint1 unlocked or $\lambda_1 = 10^6$ Nm/rad for Joint1 locked. The natural frequencies for this system are given in table 5.9.

freq. [rad/s]	unlocked	locked
ω_1	4.56	0.39
ω_2	25.34	5.19

Table 5.9: First two natural frequencies of double flexible link system with end effector, when the single link system is reproduced

The comparison of table 2.1 with 5.9 proves that the eigenvalue determinant, equation (5.14), has been verified.
Like the 6×6 determinant for the double flexible link system without end effector, the actual 6×6 determinant can produce wrong higher frequencies in certain configurations, for example if the inserted physical properties are very big or very small figures. That is the reason why, as for the previous 6×6 determinant, table 5.9 only gives the first two natural frequencies for both configurations. As stated before, it is assumed that the errors occur due to ill-conditioning of the determinant, and it is noted that the expression for the ω-dependent determinant is about 30 pages long.
It is noted that an analytical examination of beam systems with the presented degree of complexity can apparently not be found in the related literature. It is also noted that the development of the double flexible link system with rigid end effector throughout the previous sections show that the determinant system can also be applied to the multi-link or beam case, and the necessary mathematical routines may be improved devising or using stronger algorithms. With increasing determinant complexity, the results for the higher modes should be checked against with the various approximation methods. The problem of numerical limits when using the determinant method for complex beam systems will be addressed in chapter 6.4, as mentioned in the previous chapters.

5.2.2 REPRODUCTION OF FLEXIBLE LINK WITH END EFFECTOR

For the next validation, the single flexible link with rigid end effector from chapter 3

is reproduced for the case Joint1 and Joint2 locked. Thus $L_1 = 12.12$ m, $L_2 = 1.88$ m, $L_3 = 0$ m, $m_{b1} = 3.9786$ kg/m, $m_{b2} = 10^{-3}$, $EI_1 = 3\times10^6$ Nm^2, $EI_2 = 10^{10}$ Nm^2, $\lambda_1 = 10^6$ Nm/rad, $\lambda_2 = 2.4\times10^5$ Nm/rad, $\lambda_3 = 10^{10}$ Nm/rad, $M_p = 5000$ kg, $I_p = 5417$ kgm^2 and $a = 1$ m.
The results for various θ_2 (θ) are given in Table 5.10, together with the original values from table 3.4, which are calculated with the 3×3 determinant for the single flexible link with rigid end effector.

θ_2 (θ) [deg]	method	ω_1 [rad/s]	ω_2 [rad/s]	ω_3 [rad/s]	ω_4 [rad/s]
0	3×3 det.	0.56	7.89	77.77	256.74
	6×6 det.	0.56	7.89	77.77	256.72
50	3×3 det.	0.60	3.16	77.10	256.22
	6×6 det.	0.60	3.16	77.10	256.22
90	3×3 det.	0.72	2.12	77.03	256.18
	6×6 det.	0.72	2.12	77.03	256.18

Table 5.10: Verification of 6×6 determinant by comparison with results from 3×3 determinant for single flexible link with rigid end effector

Except for one deviation, table 5.10 shows perfect agreement of the various frequencies, thus validating the elements in equation (5.15).

5.2.3 RIGID LINK ANALYSIS

A reproduction of the double rigid pendulum yields the results given in table 5.11, where "dp" and "dfle" denote the natural frequencies of the original rigid double pendulum and of the actual determinant for the double flexible link system with end effector.
The properties are $L_1 = 12.12$ m, $L_2 = 1.88$ m, $L_3 = 0$ m, $m_{b1} = m_{b2} = 3.9786$ kg/m, $EI_1 = EI_2 = 10^{10}$ Nm^2, $\lambda_1 = 10^6$ Nm/rad, $\lambda_2 = 2.4\times10^5$ Nm/rad, $\lambda_3 = 10^{10}$ Nm/rad, $\theta_3 = 0°$, $M_p = 10000$ kg, $I_p = 37500$ kgm^2 and $a = 1.5$ m.

θ_2 (θ) [deg]	ω_1 dp [rad/s]	ω_1 dfle [rad/s]		ω_2 dp [rad/s]	ω_2 dfle [rad/s]
0	0.87	0.87		8.80	8.79
50	0.94	0.94		3.50	3.50
90	1.12	1.12		2.36	2.36

Table 5.11: Two natural frequencies of rigid double pendulum and first two natural frequencies of double flexible link system for identical properties with $EI_i = 10^{10}$ Nm^2

Table 5.11 shows that the results obtained by the actual determinant are in almost exact agreement with the rigid double pendulum frequencies, thus verifying the proposed determinants.

5.2.4 COMPARISON WITH BEAM AND SIMPACK

As mentioned above, the final results for the fundamental natural frequency of the triple articulated RMS with SRMS properties, which is the only one of interest for this thesis, are checked against with professional software. The pre-processor BEAM is used to create a data set for the two flexible links for implementation into SIMPACK. For each link ten mode shapes for pinned-free boundary conditions are chosen, therefore the SIMPACK solution is an approximation. Table 5.12 compares the fundamental natural frequencies from the determinant with the SIMPACK solution for the three cases a) Joint1 unlocked, b) Joint2 unlocked and c) Joint3 unlocked for the above data and for $\theta_2 = \theta_3 = 0°$ (the agreement for other joint configurations is similar).
Table 5.12 shows very good agreement between the approximate SIMPACK solution and the determinant, thus validating the presented determinant and its elements.

case	determinant	SIMPACK
a)	0.83	0.87
b)	1.02	1.06
c)	0.40	0.47

Table 5.12: Comparison of SIMPACK using assumed mode shapes and of fundamental frequencies of determinant for three joint configurations

It is noted that even with the use of ten assumed mode shapes (which is already a relatively high number) for each flexible link, the fundamental frequency does not converge to the determinant result, so that in order to achieve the convergence, still more modes are necessary. Extensive experimental work shows that the computational burden during simulations is roughly a cubical function of the number of mode shapes used ([66], [67], [68]). Thus the determinant method provides a strong tool to get exact natural frequencies and mode shapes, which can reduce the system complexity and thus the computation time enormously.

5.3 SUMMARY

This section applies the determinant method to the double flexible link system with articulated end effector. The system represents the fully developed space manipulator as examined in this thesis and is comparable to the SRMS. As usually, the determinant elements are derived assuming that the RMS base is fixed, which is true for the RMS in the ground test bed or approximately true for an RMS on a large space station.
The proposed determinant is validated in the usual way, that is comparison to the results of the previous determinants and to the natural frequencies of the double rigid pendulum. Like the determinant presented in the previous chapter for the double flexible link system without end effector, it is found that due to the increasing complexity of the determinant expression, the higher frequencies can be wrong in certain configurations. However, for the fundamental or the lower modes the results

are always checked against assumed multi-mode approximations with existing software, and the proposed determinant is proven to always work correctly for those frequencies. Again it is stressed that an analysis of a flexible beam or link system with the presented complexity can apparently not be found in the related literature. As mentioned in the previous chapters, the problem of numerical limits when using the determinant method will be addressed in chapter 6.4.
Using SRMS properties the results of the determinant show that the fundamental frequency can change extremely with changing joint angles.
The determinant is also used to compute the exact analytical mode shapes. These mode shapes are applied in the following sections for open-loop and closed-loop dynamic response analysis of the RMS, and it is found that the mode shapes do practically not vary with changing joint angles in the analysed joint configurations. This will also be shown in the following chapters.

CHAPTER 6: DOUBLE LINK WITH FREE BASE AND END EFFECTOR

The previous sections developed the determinant method for the double flexible link system with rigid end effector, assuming an inertially fixed base, which is the case in the ground test bed or if the Shuttle is attitude controlled while operating the RMS or if the RMS is operating on a space station, so that the payload mass is very much smaller than the mass of the space station.
For the general case, the free motion of the Shuttle and thus the RMS base must be taken account of. This section gives the boundary conditions of the double flexible link system with a free floating Shuttle. Note that the boundary conditions of the left hand side of the first link are similar to those of a single free-free beam with large end masses and additional torsion springs as analysed in [82].

6.1 DETERMINATION OF NATURAL FREQUENCIES AND MODE SHAPES

6.1.1 EXACT SOLUTION FOR NATURAL FREQUENCIES

The determinant method is used to calculate the natural frequencies of the double flexible link system with rigid end effector and free RMS base (= Shuttle). Again we use equations (4.1) through (4.4) for the general case of a system with two flexible links. For the derivation of the boundary conditions of the actual system, consider figure 6.1, where the usual notation is used.

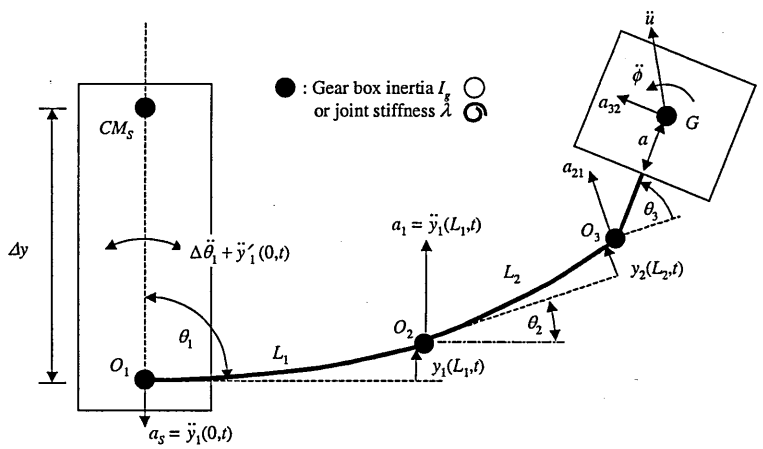

Figure 6.1: Acceleration components of the double flexible link system with end effector and free base

It is seen from figure 6.1 that the boundary conditions of Link2 and of Link1 at $x_1 = L_1$ are identical to those of the double flexible link system with end effector with fixed a base, equations (5.6), (5.7), (5.8), (5.9), (5.11) and (5.12). Only the boundary conditions of Link1 at $x_1 = 0$ change. They are analogous to the boundary conditions of the single flexible link with fixed base and articulated end effector at $x = L$.
Since the angular deflection $\Delta\theta_1 + y_1'(0,t)$ at $x_1 = 0$ due to the joint stiffness and the beam motion is small, θ_1 can be taken as constant. With the usual notations, the angular deflection $\Delta\theta_1$ due to the joint stiffness λ_1 is

$$\Delta\theta_1 = \frac{EI_1\, y_1''(0,t)}{\lambda_1} = \frac{EI_1\, W_1''(0)\, q(t)}{\lambda_1} = \Delta\bar{\theta}_1\, q(t) \tag{6.1}$$

Taking account of the sign convention the bending moment and shear force boundary conditions of Link1 at $x_1 = 0$ for a locked joint are thus (again using the method of separation of variables and equations (2.10), (2.28) and (2.29) and relations (2.13))

$$EI_1\, W_1''(0) = -I_S\, \omega^2 \left(W_1'(0) - \Delta\bar{\theta}_1\right) - \Delta y\, M_S\, \omega^2 \left[W_1(0)\cos\theta_1 + \Delta y\left(W_1'(0) - \Delta\bar{\theta}_1\right)\right] \tag{6.2}$$

and

$$EI_1\, W_1'''(0) = M_S\, \omega^2 \left[W_1(0) + \Delta y\left(W_1'(0) - \Delta\bar{\theta}_1\right)\cos\theta_1\right] \tag{6.3}$$

where Δy is the offset of the Shuttle centre of mass CM_S from the RMS base O_1 in y, and where M_S and I_S are the mass and rotary inertia of the Shuttle about its centre of mass. It is seen that by contrast to the determinants for a fixed RMS base, the above boundary conditions will lead to a determinant which is a function also of θ_1.
For the boundary conditions of Link1 at $x_1 = L_1$ and for Link2 at $x_2 = 0$ and $x_2 = L_2$, we use equations (5.6), (5.7), (5.8), (5.9), (5.11) and (5.12), as mentioned before.
Using the boundary conditions (6.2) and (6.3) for the various systems presented in the previous chapters, the respective determinant dimensions are increased by 1, since at O_1 there is no longer a revolute joint which allows for a reduction of the matrix and thus determinant. Therefore in the present case, by contrast to equation (5.13), equation (4.3) reduces only to a 7×7 system given by

$$\begin{bmatrix} d_{11} & d_{12} & d_{13} & d_{14} & d_{15} & d_{16} & d_{17} \\ d_{21} & d_{22} & d_{23} & d_{24} & d_{25} & d_{26} & d_{27} \\ d_{31} & d_{32} & d_{33} & d_{34} & d_{35} & d_{36} & d_{37} \\ d_{41} & d_{42} & d_{43} & d_{44} & d_{45} & d_{46} & d_{47} \\ d_{51} & d_{52} & d_{53} & d_{54} & d_{55} & d_{56} & d_{57} \\ d_{61} & d_{62} & d_{63} & d_{64} & d_{65} & d_{66} & d_{67} \\ d_{71} & d_{72} & d_{73} & d_{74} & d_{75} & d_{76} & d_{77} \end{bmatrix} \begin{bmatrix} A_{1,i} \\ B_{1,i} \\ C_{1,i} \\ D_{1,i} \\ A_{2,i} \\ B_{2,i} \\ C_{2,i} \end{bmatrix} = \mathbf{0} \tag{6.4}$$

and the associated determinant is

$$\begin{vmatrix} d_{11} & d_{12} & d_{13} & d_{14} & d_{15} & d_{16} & d_{17} \\ d_{21} & d_{22} & d_{23} & d_{24} & d_{25} & d_{26} & d_{27} \\ d_{31} & d_{32} & d_{33} & d_{34} & d_{35} & d_{36} & d_{37} \\ d_{41} & d_{42} & d_{43} & d_{44} & d_{45} & d_{46} & d_{47} \\ d_{51} & d_{52} & d_{53} & d_{54} & d_{55} & d_{56} & d_{57} \\ d_{61} & d_{62} & d_{63} & d_{64} & d_{65} & d_{66} & d_{67} \\ d_{71} & d_{72} & d_{73} & d_{74} & d_{75} & d_{76} & d_{77} \end{vmatrix} = 0 \tag{6.5}$$

Neglecting the integral terms in equations (5.6) and (5.7) and using the usual notations, the elements d_{nm} in equation (6.5) are

$$
\begin{aligned}
d_{11} &= d_{13} = k_1 \left(I_S + \Delta y^2 M_S\right)\omega^2 \\
d_{12} &= EI_1 k_1^2 \left(-1 + \frac{\left(I_S + \Delta y^2 M_S\right)\omega^2}{\lambda_1}\right) + \omega^2 \Delta y M_S \cos\theta_1 \\
d_{14} &= EI_1 k_1^2 \left(1 - \frac{\left(I_S + \Delta y^2 M_S\right)\omega^2}{\lambda_1}\right) + \omega^2 \Delta y M_S \cos\theta_1 \\
d_{15} &= d_{16} = d_{17} = 0 \\
d_{21} &= EI_1 k_1^3 + \omega^2 k_1 \Delta y M_S \cos\theta_1 \\
d_{22} &= \omega^2 M_S \left(1 + \frac{k_1^2 \Delta y EI_1 \cos\theta_1}{\lambda_1}\right) \\
d_{23} &= -EI_1 k_1^3 + \omega^2 k_1 \Delta y M_S \cos\theta_1 \qquad (6.6) \\
d_{24} &= \omega^2 M_S \left(1 - \frac{k_1^2 \Delta y EI_1 \cos\theta_1}{\lambda_1}\right) \\
d_{25} &= d_{26} = d_{27} = 0 \\
d_{31} &= k_1 \left(I_p + M_p \left(L_2 + (a + L_3)\cos\theta_3\right)^2\right)\omega^2 C_1 + \\
&\quad S_1 \left(EI_1 k_1^2 + M_p \left(L_2 + (a + L_3)\cos\theta_3\right)\omega^2 \cos\theta_2\right) \\
d_{32} &= C_1 \left(M_p \omega^2 \cos\theta_2 \left(L_2 + (a + L_3)\cos\theta_3\right) + EI_1 k_1^2\right) - \omega^2 I_p k_1 S_1 - \\
&\quad \omega^2 M_p k_1 \left(L_2 + (a + L_3)\cos\theta_3\right)^2 S_1 \\
d_{33} &= k_1 \left(I_p + M_p \left(L_2 + (a + L_3)\cos\theta_3\right)^2\right)\omega^2 Ch_1 - \\
&\quad Sh_1 \left(EI_1 k_1^2 - M_p \left(L_2 + (a + L_3)\cos\theta_3\right)\omega^2 \cos\theta_2\right) \\
d_{34} &= Ch_1 \left(M_p \omega^2 \cos\theta_2 \left(L_2 + (a + L_3)\cos\theta_3\right) - EI_1 k_1^2\right) + \omega^2 I_p k_1 Sh_1 + \\
&\quad \omega^2 M_p k_1 \left(L_2 + (a + L_3)\cos\theta_3\right)^2 Sh_1 \\
d_{35} &= \omega^2 \left(M_p \left(L_2 + (a + L_3)\cos\theta_3\right) S_2 + I_p k_2 C_2\right) + \\
&\quad \omega^2 \left(-\frac{I_p k_2^2 EI_2 S_2}{\lambda_3} + k_2 (a + L_3) M_p \cos\theta_3 \left(L_2 + (a + L_3)\cos\theta_3\right)\left(C_2 - \frac{EI_2 k_2 S_2}{\lambda_3}\right)\right) \\
d_{36} &= \omega^2 \left(M_p \left(L_2 + (a + L_3)\cos\theta_3\right)(C_2 - Ch_2)\right) + \\
&\quad \omega^2 \left(-I_p k_2 \left(S_2 + Sh_2 + \frac{EI_2 k_2 (C_2 + Ch_2)}{\lambda_3}\right)\right) - \\
&\quad \omega^2 \left(M_p k_2 \cos\theta_3 (a + L_3)\left(L_2 + (a + L_3)\cos\theta_3\right)\left(S_2 + Sh_2 + \frac{EI_2 k_2 (C_2 + Ch_2)}{\lambda_3}\right)\right) \\
d_{37} &= \omega^2 \left(M_p \left(L_2 + (a + L_3)\cos\theta_3\right) Sh_2 + I_p k_2 Ch_2\right) + \\
&\quad \omega^2 \left(\frac{I_p k_2^2 EI_2 Sh_2}{\lambda_3} + k_2 (a + L_3) M_p \cos\theta_3 \left(L_2 + (a + L_3)\cos\theta_3\right)\left(Ch_2 + \frac{EI_2 k_2 Sh_2}{\lambda_3}\right)\right)
\end{aligned}
$$

$$
\begin{aligned}
d_{41} &= k_1 C_1 \left(-EI_1 k_1^2 + M_p \omega^2 \cos\theta_2 \left(L_2 + (a+L_3)\cos\theta_3\right)\right) + \left(M_p + M_2\right)\omega^2 S_1 \\
d_{42} &= \omega^2 \left(M_p + M_2\right) C_1 + EI_1 k_1^3 S_1 - k_1 M_p \omega^2 \cos\theta_2 \left(L_2 + (a+L_3)\cos\theta_3\right) S_1 \\
d_{43} &= k_1 Ch_1 \left(EI_1 k_1^2 + M_p \omega^2 \cos\theta_2 \left(L_2 + (a+L_3)\cos\theta_3\right)\right) + \left(M_p + M_2\right)\omega^2 Sh_1 \\
d_{44} &= \omega^2 \left(M_p + M_2\right) Ch_1 + EI_1 k_1^3 Sh_1 + k_1 M_p \omega^2 \cos\theta_2 \left(L_2 + (a+L_3)\cos\theta_3\right) Sh_1 \\
d_{45} &= \frac{\omega^2}{k_2 \lambda_3} \left(-k_2^2 (a+L_3) M_p \cos(\theta_2+\theta_3)\left(-\lambda_3 C_2 + EI_2 k_2 S_2\right)\right) + \\
&\quad \omega^2 \cos\theta_2 M_p S_2 \\
d_{46} &= \omega^2 M_p \cos\theta_2 \left(C_2 - Ch_2\right) - \\
&\quad \omega^2 \left(k_2 (a+L_3) M_p \cos(\theta_2+\theta_3)\left(S_2 + Sh_2 + EI_2 k_2 \frac{C_2+Ch_2}{\lambda_3}\right)\right) \\
d_{47} &= \frac{\omega^2}{k_2 \lambda_3} \left(k_2^2 (a+L_3) M_p \cos(\theta_2+\theta_3)\left(\lambda_3 Ch_2 + EI_2 k_2 Sh_2\right)\right) + \\
&\quad \omega^2 \cos\theta_2 M_p Sh_2 \\
d_{51} &= d_{52} = d_{53} = d_{54} = 0 \\
d_{55} &= d_{57} = k_2 \lambda_2 \\
d_{56} &= 2 EI_2 k_2^2 \\
d_{61} &= \omega^2 \left(I_p k_1 C_1 + k_1 (a+L_3) M_p C_1 \cos\theta_3 \left(L_2 + (a+L_3)\cos\theta_3\right)\right) + \\
&\quad \omega^2 \left((a+L_3) M_p C_1 \cos(\theta_2+\theta_3) S_1\right) \\
d_{62} &= \omega^2 \left((a+L_3) M_p C_1 \cos(\theta_2+\theta_3) - I_p k_1 S_1\right) - \\
&\quad \omega^2 k_1 (a+L_3) M_p \cos\theta_3 \left(L_2 + (a+L_3)\cos\theta_3\right) S_1 \\
d_{63} &= \omega^2 \left(I_p k_1 Ch_1 + k_1 (a+L_3) M_p Ch_1 \cos\theta_3 \left(L_2 + (a+L_3)\cos\theta_3\right)\right) + \\
&\quad \omega^2 \left((a+L_3) M_p C_1 \cos(\theta_2+\theta_3) Sh_1\right) \\
d_{64} &= \omega^2 \left((a+L_3) M_p C_1 \cos(\theta_2+\theta_3) + I_p k_1 Sh_1\right) + \\
&\quad \omega^2 k_1 (a+L_3) M_p \cos\theta_3 \left(L_2 + (a+L_3)\cos\theta_3\right) Sh_1 \\
d_{65} &= EI_2 k_2^2 S_2 + \omega^2 \left((a+L_3) M_p \cos\theta_3 S_2 + I_p k_2 \left(C_2 - EI_2 k_2 \frac{S_2}{\lambda_3}\right)\right) + \\
&\quad k_2 (a+L_3)^2 M_p \omega^2 \left(C_2 - EI_2 k_2 \frac{S_2}{\lambda_3}\right) \\
d_{66} &= EI_2 k_2^2 (C_2 + Ch_2) + \omega^2 (a+L_3) M_p \cos\theta_3 \left(C_2 - Ch_2\right) + \\
&\quad \omega^2 I_p k_2 \left(S_2 + Sh_2 + EI_2 k_2 \frac{C_2+Ch_2}{\lambda_3}\right) + \\
&\quad k_2 (a+L_3)^2 M_p \omega^2 \left(S_2 + Sh_2 + EI_2 k_2 \frac{C_2+Ch_2}{\lambda_3}\right) \\
d_{67} &= \omega^2 \left((a+L_3) M_p \cos\theta_3 Sh_2 + I_p k_2 \left(Ch_2 + EI_2 k_2 \frac{Sh_2}{\lambda_3}\right)\right) - EI_2 k_2^2 Sh_2 + \\
&\quad k_2 (a+L_3)^2 M_p \omega^2 \left(Ch_2 + EI_2 k_2 \frac{Sh_2}{\lambda_3}\right)
\end{aligned}
\tag{6.6}
$$

$$
\begin{aligned}
d_{71} &= M_p\,\omega^2\left(k_1 C_1\left(L_2+(a+L_3)\cos\theta_3\right)+\cos\theta_2\, S_1\right)\\
d_{72} &= M_p\,\omega^2\left(-k_1\left(L_2+(a+L_3)\cos\theta_3\right)S_1+\cos\theta_2\, C_1\right)\\
d_{73} &= M_p\,\omega^2\left(k_1 C_1\left(L_2+(a+L_3)\cos\theta_3\right)+\cos\theta_2\, Sh_1\right)\\
d_{74} &= M_p\,\omega^2\left(k_1\left(L_2+(a+L_3)\cos\theta_3\right)Sh_1+\cos\theta_2\, Ch_1\right)\\
d_{75} &= -EI_2\,k_2^3\,C_2+M_p\,\omega^2\left(S_2+k_2(a+L_3)\cos\theta_3\left(C_2-EI_2\,k_2\,\frac{S_2}{\lambda_3}\right)\right)\\
d_{76} &= EI_2\,k_2^3\left(S_2-Sh_2\right)+\\
&\quad M_p\,\omega^2\left(C_2-Ch_2-k_2(a+L_3)\cos\theta_3\left(S_2+Sh_2+EI_2\,k_2\,\frac{C_2+Ch_2}{\lambda_3}\right)\right)\\
d_{77} &= EI_2\,k_2^3\,Ch_2+M_p\,\omega^2\left(Sh_2+k_2(a+L_3)\cos\theta_3\left(Ch_2+EI_2\,k_2\,\frac{Sh_2}{\lambda_3}\right)\right)
\end{aligned}
\tag{6.6}
$$

For an unlocked Joint1, λ_1 is set to a very small value (zero is not allowed, since it appears in denominators), and equation (6.2) becomes

$$
-EI_1 W_1''(0) = I_{g1}\,\omega^2 W_1'(0) \tag{6.7}
$$

Then the elements d_{11}, d_{12}, d_{13} and d_{14} in equation (6.6) become

$$
\begin{aligned}
d_{11} &= d_{13} = I_{g1}\,k_1\,\omega^2\\
d_{14} &= -d_{12} = EI_1\,k_1^2
\end{aligned}
\tag{6.8}
$$

For an unlocked Joint2, λ_2 is set to a very small value, and equation (5.9) becomes

$$
-EI_2 W_2''(0) = I_{g2}\,\omega^2 W_2'(0) \tag{6.9}
$$

and the elements d_{55} and d_{57} in equation (6.6) become

$$
d_{55} = d_{57} = -I_{g2}\,k_2\,\omega^2 \tag{6.10}
$$

It is seen that the present system can have eight different joint configurations depending on whether the three joints are locked or unlocked, like the double flexible link system with fixed base and end effector. In the previous sections the variation of the first non-zero frequency with varying joint angles is always given, but in the present case due to the huge number of possibilities even for joint angle steps of say 30°, we only consider the straight RMS for each joint configuration, which will give the very lowest frequency possible for the case all joints locked.
Table 6.1 gives the first non-zero frequency in rad/s of the double flexible RMS with end effector in the straight configuration ($\theta_2 = \theta_3 = 0°$) for the free base determinant with M_p = 30000 kg, $I_p = 4\times10^5$ kgm^2, $\theta_1 = 90°$, Δy = 14 m, M_S = 70000 kg and $I_S = 10^6$ kgm^2 for various joint configuration, which are indicated using 1 for a locked joint and 0 for a free joint. Thus 1-0-1 for example means Joint1 and Joint3 locked and Joint2 unlocked. Note that from now on this will be the standard data set (C).

joint config.	free base
0 – 0 – 0	30.94
0 – 0 – 1	5.11
0 – 1 – 0	18.37
1 – 0 – 0	10.59
0 – 1 – 1	0.84
1 – 0 – 1	1.05
1 – 1 – 0	0.46
1 – 1 – 1	0.25

Table 6.1: First non-zero frequency in [rad/s] of double flexible link system with end effector and free base

6.1.2 EXACT SOLUTION FOR MODE SHAPES

We apply the usual procedure described in the previous chapters to obtain the exact mode shapes for the two flexible links. The following figures 6.2 through 6.5 show the first non-rigid system mode shape $W_{S1}(x)$ for all joint configurations when at least two joints are locked, that is 0 – 1 – 1, 1 – 0 – 1, 1 – 1 – 0 and 1 – 1 – 1 when $\theta_1 = 90°$ and $\theta_2 = \theta_3 = 0°$ (see table 6.1 above).
Note that figures 6.2 through 6.5 correspond to the respective system mode shapes for the fixed base system with otherwise identical data, figures 5.3 through 5.6. From a visual comparison it can be seen that the mode shapes of each individual flexible link do hardly change when the manipulator base is free to float instead of being fixed. This will be proven to be true with table 6.2 further down.

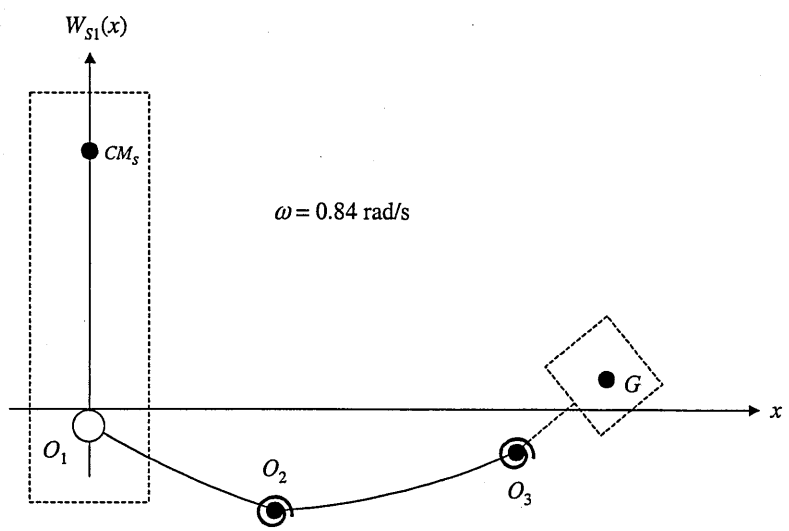

Figure 6.2: First system mode shape $W_{S1}(x)$ for configuration Joint1 unlocked, Joint2 and Joint3 locked (0 – 1 – 1) for $\theta_1 = 90°$ and $\theta_2 = \theta_3 = 0°$

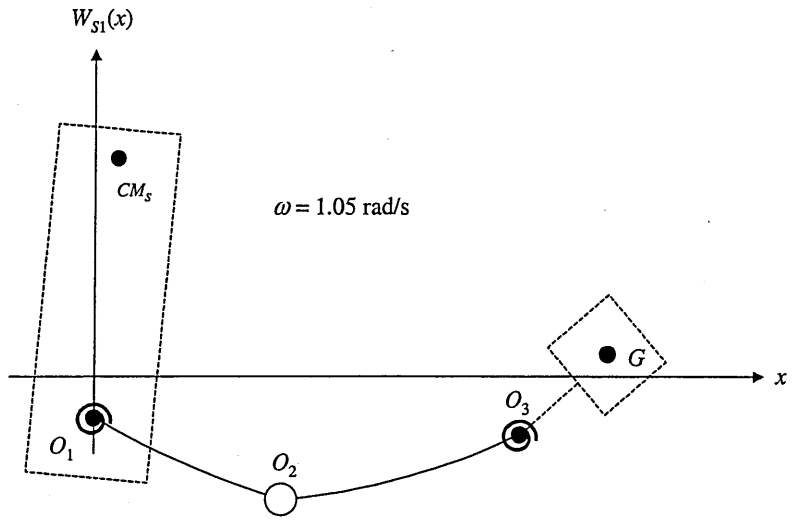

Figure 6.3: First system mode shape $W_{S1}(x)$ for configuration Joint1 and Joint3 locked, Joint2 unlocked (1 – 0 – 1) for $\theta_1 = 90°$ and $\theta_2 = \theta_3 = 0°$

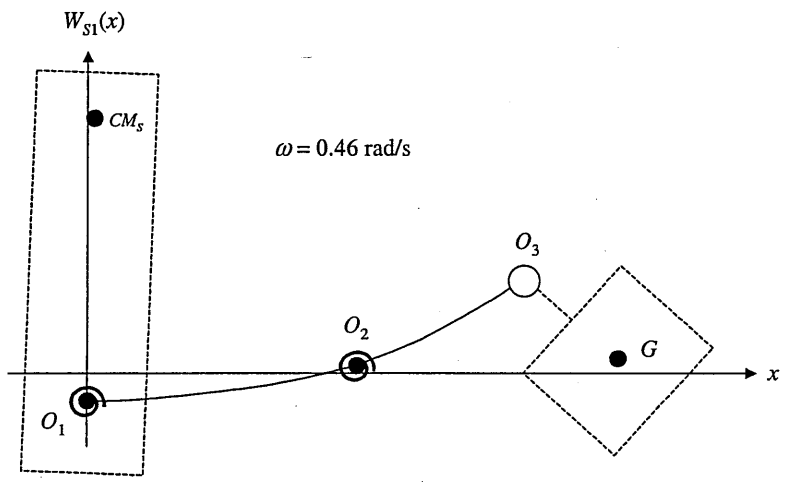

Figure 6.4: First system mode shape $W_{S1}(x)$ for configuration Joint1 and Joint2 locked, Joint3 unlocked (1 – 1 – 0) for $\theta_1 = 90°$ and $\theta_2 = \theta_3 = 0°$

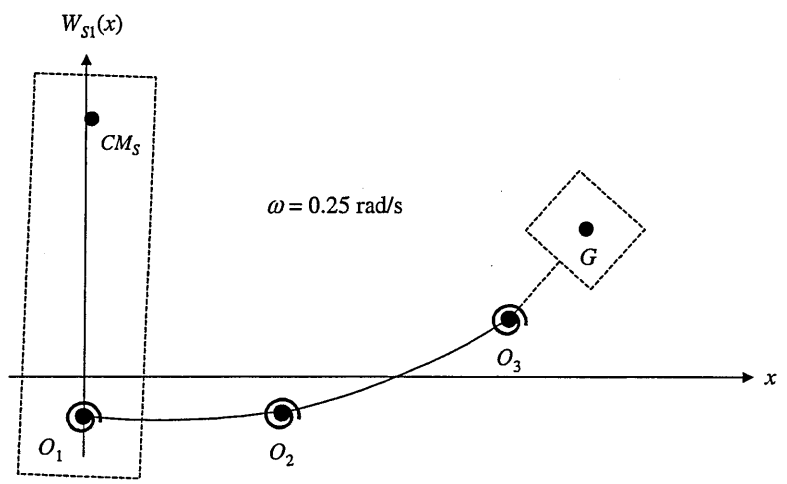

Figure 6.5: First system mode shape $W_{S1}(x)$ for configuration all three joints locked (1 – 1 – 1) for $\theta_1 = 90°$ and $\theta_2 = \theta_3 = 0°$

To analyse the influence of a free RMS base on the mode shapes, we insert the mode shapes for the fixed (figures 5.3 through 5.6) and the free RMS base (figures 6.2 through 6.5) for the configurations with at least two joints locked for the straight RMS ($\theta_1 = 90°$, $\theta_2 = \theta_3 = 0°$) into equations of motion that allow for the Shuttle motion (free base). We then compute the first non-zero eigenfrequency using equation (2.50) and compare it with the first non-zero frequency obtained with the determinant. The results are given in table 6.2, where "eom (fix)" and "eom (free)" denote the results obtained with the equations of motion using equation (2.50) on inserting the mode shapes for the fixed or free base, and where "det" indicate the determinant results. All results are given in [rad/s].

joint config.	eom (fix)	eom (free)	det
0 – 1 – 1	0.84	0.84	0.84
1 – 0 – 1	1.10	1.05	1.05
1 – 1 – 0	0.46	0.47	0.46
1 – 1 – 1	0.31	0.30	0.25

Table 6.2: First non-zero frequencies in [rad/s] for RMS with free base, using the exact mode shapes for fixed and free base in free base equations of motion, compared with the exact values obtained from the free base determinant

Table 6.2 shows that all the results are in very good agreement, verifying equation (6.6). It is noted that only for the joint configuration 1 – 1 – 1, the determinant gives a slightly different result than equation (2.50) on inserting the exact mode shapes for the links. Comparing the various results, it is therefore assumed that although the mode shapes are obviously computed correctly on re-inserting 0.25 rad/s into equation (6.4) to compute the mode shapes, the determinant results are wrong by about 0.05 rad/s. Chapter 6.4 addresses the problem of numerical limits when using the determinant method.
Comparing the results obtained by using mode shapes for the fixed case with results obtained by using mode shapes for the free case in table 6.2, it becomes obvious that the mode shapes change only slightly or not at all when changing from the fixed to the free base. It is however noted that small changes in the mode shapes do not automatically allow for the assumption of small changes in the elastic deflections in dynamic response analyses, when the system itself changes ([47], [66], [67], [68]).

6.2 VALIDATION OF THE DETERMINANT RESULTS

6.2.1 REPRODUCTION OF PREVIOUS RESULTS

For very large values of M_S and I_S, the results obtained by the various determinants should be identical to the results of the corresponding determinants with fixed base.
This is found to be true for the single flexible link system and the single flexible link with articulated end effector, whereas for the double flexible link system without end effector, only frequencies below 10 rad/s are reproduced correctly. This is by far sufficient to compute the frequencies and mode shapes of interest.

However, applying the above boundary conditions to the double flexible link system with end effector it turns out that only those low frequencies are exactly reproduced, which lead to elastic deflections that are not negligibly small. As mentioned before it is inferred that the reason is ill-conditioning of the determinant, and to give an idea of the complexity it is noted that the expression of the determinant is about 50 pages long, involving hundreds of trigonometric and hyperbolic functions.
Table 6.3 gives the first non-zero frequencies in rad/s of the double flexible RMS with end effector in the straight configuration for the fixed and the free base determinant with M_p = 30000 kg, $I_p = 4\times10^5$ kgm^2, $\theta_1 = 90°$, Δy = 14 m, $M_S = 10^{10}$ kg and $I_S = 10^{10}$ kgm^2 for various joint configuration, which are indicated using the system introduced in table 6.2 above. The very large values for M_S and I_S effectively yield a fixed RMS base for comparison.

joint config.	free base	fixed base
0 – 0 – 0	30.65	34.04
0 – 0 – 1	5.11	6.04
0 – 1 – 0	18.38	20.44
1 – 0 – 0	10.59	13.33
0 – 1 – 1	0.83	0.83
1 – 0 – 1	1.02	1.02
1 – 1 – 0	0.40	0.40
1 – 1 – 1	0.17	0.17

Table 6.3: First non-zero frequency in rad/s of double flexible link system with end effector for fixed and free base using $M_S = 10^{10}$ kg and $I_S = 10^{10}$ kgm^2 for the free base to represent a fixed base

Table 6.3 shows the aforementioned deviation of the results for a fixed and a free base with $M_S = 10^{10}$ kg and $I_S = 10^{10}$ kgm^2 to reproduce a fixed base for frequencies in excess of about 5 rad/s. For the computation of higher frequencies with the proposed determinant it is therefore better to compute the changes in the frequencies when changing from M_S, $I_S \rightarrow \infty$ to the real values, and adding these differences to the frequencies obtained from the determinant for a fixed base for the actual joint configuration.
However, various simulations and the figures given in the previous chapters show that only those joint configurations with at least two joints locked yield non-negligible elastic RMS deflections in dynamic response analyses, which will also be proven in the following chapters. Table 6.3 shows that for these configurations the first non-zero frequencies are reproduced correctly.

6.2.2 COMPARISON WITH BEAM AND SIMPACK

The following table 6.4 compares the first non-zero frequency obtained from the determinant for the free base inserting the real values for M_S and I_S (70000 kg and 10^6 kgm^2) and the SIMPACK results, using three assumed mode shapes of a cantilever

beam for each flexible link created with BEAM, for the joint configurations with at least two joints locked. The results are given in [rad/s].

joint config.	determinant	SIMPACK
0 – 1 – 1	0.84	0.87
1 – 0 – 1	1.05	1.08
1 – 1 – 0	0.46	0.52
1 – 1 – 1	0.25	0.31

Table 6.4: First non-zero frequency in [rad/s] of the free base determinant and SIMPACK, using the real values for M_S and I_S (70000 kg and 10^6 kgm^2)

Table 6.4 shows that although there is reasonable agreement between the approximate SIMPACK and the determinant results, inserting one exact mode shape for each link still yields better results than inserting three mode shapes of a cantilever beam. Again it is stressed that the exact mode shapes, in securing instant agreement with the exact natural frequencies, can reduce the computational burden drastically.
With table 6.2 it was proven that the mode shapes change only slightly when changing form a fixed to a free RMS base. Comparing the first non-zero frequency for the configurations with at least two joints locked for the free base in table 6.4 with the corresponding first non-zero frequency for the fixed base as given in tables 5.4, 5.6, 5.7 and 5.8 for the case $\theta_2 = \theta_3 = 0°$, it can also be seen that the first non-zero frequency changes only slightly when changing from a fixed to a free RMS base. Note that in the present case these changes are worst, since the change is still smaller for payloads smaller than the maximum of 30000 kg. However, note also that small changes in the natural frequencies do not automatically correspond to small changes in the elastic deflections in dynamic responses, if the dynamic system itself is changing from a fixed to a free base. This will be shown in the following chapter 7.

6.2.3 SIMPLIFIED CHECK CALCULATION

The reason for the small changes of the first non-zero frequency when changing from a fixed to a free base is the offset Δy, producing a very large effective inertia (1.472×10^7 kgm^2) about O_1, which only allows for very small rotations of the Shuttle and the big Shuttle mass. For a verification, we examine the change of the first non-zero frequency of a simple single flexible link RMS with payload, once with a fixed base and once with a base that is free to move perpendicular to the RMS, see figure 6.6. Using the usual notation and taking the same assumed mode shape $\hat{W}(x)$ (for example the mode shape given by equation (2.69)) for the fixed and the free base (a practice justified with table 6.4), the natural frequencies obtained with equation (2.50) are

$$\omega_{\text{free}}^2 = \frac{(M_p + M_S)(\lambda + \frac{1}{2}EI\int_0^L [\hat{W}''(x)]^2\,dx)}{M_S M_p \hat{W}(L)^2 + 2aM_S M_p \hat{W}(L)\hat{W}'(L) + [I_p(M_p + M_S) + a^2 M_S M_p]\hat{W}'(L)^2} \qquad (6.11)$$

and
$$\omega_{\text{fixed}}^2 = \frac{\lambda + \frac{1}{2}EI\int_0^L [\hat{W}''(x)]^2\,dx}{M_p\hat{W}(L)^2 + 2aM_p\hat{W}(L)\hat{W}'(L) + (I_p + a^2M_p)\hat{W}'(L)^2} \tag{6.12}$$

from which we obtain the ratio R of the frequencies as

$$R = \frac{\omega_{\text{fixed}}}{\omega_{\text{free}}} \tag{6.13}$$

It is sufficient now to insert values for M_p and M_S into equation (6.13) to obtain the ratio R.

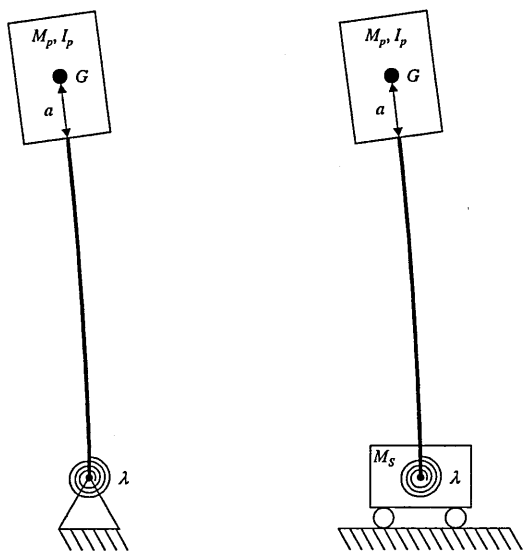

Figure 6.6: Single flexible link with payload
and joint stiffness with fixed and free base

For the worst case with M_S = 70000 kg and M_p = 30000 kg, equation (6.13) yields R = 0.853 (the ratio of the exact determinant values for the first non-zero frequency for this case is 0.775). It is noted that for $M_S = M_p$ = 30000 kg, the ratio is still R = 0.740. This simple calculation verifies the small changes in the natural frequencies for the double flexible link with end effector, since the effective inertia of the Shuttle about the base of the RMS is very large also for small Shuttle masses, due to the aforementioned offset Δy. Note that the ratio approaches 1 when the payload gets smaller.

6.3 INFLUENCE OF ANGLE OF JOINT1

To give an idea of the influence of θ_1 on the first non-zero frequency, table 6.5 shows the change for the straight RMS ($\theta_2 = \theta_3 = 0°$) in [rad/s] for data set (C) , if θ_1 changes from 90° to 0°.

joint config.	change
0 – 1 – 1	+ 0.10
1 – 0 – 1	- 0.15
1 – 1 – 0	- 0.10
1 – 1 – 1	- 0.01

Table 6.5: Change of first non-zero frequency in [rad/s] for θ_1 changing from 90° to 0°

Table 6.5 shows that the relative changes are generally small, but not negligible. However, it is noted that a reasonable mechanical work range of Joint1 would most probably not allow for handling a maximum payload up to 90°, and that for smaller payloads, the changes are smaller.

6.4 NUMERICAL PROBLEMS WHEN USING THE DETERMINANT METHOD

At this point the problem of numerical limits imposed on the determinant method should be analysed. To this end recall chapter 2.5 where it was mentioned that the magnitude of the off-diagonal elements in the mass matrix **M** in equation (2.49) are an indicator for the numerical accuracy when using exact mode shapes. To show the power of the determinant method for the single flexible link as presented in chapter 2, table 6.6 gives the mass matrix **M** when 10 exact mode shapes in the form of equation (2.17) of the unlocked joint system for data set (A) are inserted into the equations of motion. Note that the off-diagonal elements are only given by their respective exponent when the factor has one place left of the decimal point (example: 5.6453×10^{-7} => mass matrix entry 10^{-7}), a method used for the rest of this section.

1	10^{-16}	10^{-15}	10^{-13}	10^{-12}	10^{-10}	10^{-9}	10^{-8}	10^{-6}	10^{-6}
10^{-16}	1	10^{-15}	10^{-13}	10^{-12}	10^{-10}	10^{-10}	10^{-8}	10^{-7}	10^{-4}
10^{-15}	10^{-15}	1	10^{-13}	10^{-13}	10^{-10}	10^{-10}	10^{-8}	10^{-6}	10^{-4}
10^{-13}	10^{-13}	10^{-13}	1	10^{-13}	10^{-11}	10^{-10}	10^{-8}	10^{-7}	10^{-5}
10^{-12}	10^{-12}	10^{-13}	10^{-13}	1	10^{-11}	10^{-11}	10^{-9}	10^{-7}	10^{-5}
10^{-10}	10^{-10}	10^{-10}	10^{-11}	10^{-11}	1	10^{-11}	10^{-9}	10^{-7}	10^{-6}
10^{-9}	10^{-10}	10^{-10}	10^{-10}	10^{-11}	10^{-11}	1	10^{-9}	10^{-8}	10^{-6}
10^{-8}	10^{-8}	10^{-8}	10^{-8}	10^{-9}	10^{-9}	10^{-9}	1	10^{-7}	10^{-7}
10^{-6}	10^{-7}	10^{-6}	10^{-7}	10^{-7}	10^{-7}	10^{-8}	10^{-7}	1	10^{-6}
10^{-6}	10^{-4}	10^{-4}	10^{-5}	10^{-5}	10^{-6}	10^{-6}	10^{-7}	10^{-6}	1

Table 6.6: Mass matrix **M** for unlocked single flexible link, data set (A), when using 10 exact mode shapes (off-diagonal elements only given by their exponents)

From table 6.6 it can be seen that using the exact mode shapes in the form of equation (2.17), the off-diagonal elements of the corresponding mass matrix are very small even for 10 inserted mode shapes, thus indicating a very high numerical accuracy when using the proposed determinant method. Note that the accuracy is the same for other payload properties and is also comparable for the locked joint and the single

flexible link with end effector for the various joints locked or unlocked.

When using the standard polynomial fit $W_{app}(x) = \sum_{n=1}^{N} a_n x^n$ as proposed in chapter 2.8 instead of the exact mode shapes in the form of equation (2.17) to reduce computational burden, the mass matrix **M** looks as shown in table 6.7 for 5 mode shapes of the unlocked single flexible link for data set (A).

1	10^{-8}	10^{-5}	10^{-1}	10^{-1}
10^{-8}	1	10^{-5}	10^{-2}	10^{-1}
10^{-5}	10^{-5}	1	10^{-4}	10^{-1}
10^{-1}	10^{-2}	10^{-4}	1	10^{-2}
10^{-1}	10^{-1}	10^{-1}	10^{-2}	1

Table 6.7: Mass matrix **M** for unlocked single flexible link, data set (A), using 5 approximate mode shapes as proposed in chapter 2.8 to reduce computational burden

Table 6.7 shows that although the errors are enormous when using a certain number of polynomial approximations for the exact mode shapes, the first three modes can be reproduced very exactly, allowing for their use in dynamic response analyses. The reader is reminded of the fact that due to al the previous analyses, only the first non-zero mode for configurations with all joints locked was found to give rise to flexible deformations that are significant.

An increase of the system complexity will however have a negative influence on numerical accuracy, and to show this table 6.8 gives the mass matrix **M** for the double flexible link system with free base and end effector for data set (C).

1	10^{-5}	10^{-3}
10^{-5}	1	10^{-2}
10^{-3}	10^{-2}	1

Table 6.8: Mass matrix **M** for double flexible link system with free base and end effector, data set (C), using 3 exact mode shapes

From table 6.8 it can be seen that the numerical accuracy is bad when using more than say, 3 mode shapes in dynamical simulations. Note however that only the fundamental mode was found to be relevant for dynamic response analyses when the focus is on the magnitude of elastic deformations. Note also that formulation of the equations of motion using the tangent frame as proposed in this thesis and setting up the equations of motion using Lagrange's equation (2.48) can, to a certain degree, smoothen out numerical errors as shown here. This is because the system frequencies and system mode shapes can be computed not only with the determinant but also with equation (2.50), as mentioned several times before, if the inserted mode shapes for the flexible links are exact or very close to the exact ones. But a deviation of the determinant results from the exact frequency value by say 5% does practically not change the mode shapes computed by re-insertion of that frequency into the respective equation systems as shown before. Thus although the computed frequency might be out for example by 5%, this would practically not change the computed

mode shapes, and if they are very accurate, equation (2.50) can be used to compute maybe more accurate system frequencies and mode shapes. Note that this happened in table 6.2 above, where although the determinant would give a result of 0.25 rad/s for the first non-zero frequency of the double flexible link system with free base and end effector for data set (C), insertion of the computed mode shapes for each flexible link and using equation (2.50) yields 0.30 rad/s, in very good agreement with the corresponding SIMPACK result in table 6.4. Note that due to these explanations it is from now on assumed that for the case at hand the correct frequency is 0.30 rad/s, as mentioned before.
Thus it is finally concluded that the determinant can be used to compute the first few natural frequencies and mode shapes of quite complex systems, when careful checking and validation of the results are applied as done in this thesis.

6.5 SUMMARY

The present chapter gives the analytical determinant solution for the double flexible link RMS with rigid end effector and free base (= Shuttle). It is found that the very large effective rotary inertia of the Shuttle (1.472×10^7 kgm^2) about the RMS shoulder joint due to the distance of the RMS base from the Shuttle centre of mass (14 m) only allows for very small rotations of the Shuttle in the vibration modes. However, this small Shuttle rotation must be taken account of, especially when computing the exact mode shapes and the natural frequencies.
It is also found that due to the considerable complexity of the determinant expression, which is about 50 pages long and contains hundreds of trigonometric and hyperbolic functions, the first non-zero frequencies, being the only ones of interest for this thesis, computed with the presented determinant for the various joint configurations do not always agree perfectly with the results obtained from the determinant with fixed RMS base on inserting a very large value for the Shuttle mass to imitate a fixed base, when the frequencies are higher than about 5 rad/s.
In order to get the best results for frequencies in excess of 5 rad/s, the difference between the first non-zero frequencies obtained by inserting a very large value for the Shuttle mass to reproduce a fixed base and the frequencies obtained by inserting the real Shuttle mass into the proposed determinant are computed. Those differences are generally found to be very small, and they are in very close agreement with the differences of a fixed and free base computed with SIMPACK, using ten mode shapes of a pinned-free beam or three mode shapes of a cantilever beam for each flexible link.
It is inferred that the exact analytical values for those higher first non-zero frequencies are the sum of the first non-zero frequencies obtained by the determinant for the fixed base plus the aforementioned differences computed with the determinant for the free base.
Due to the very small changes in the first non-zero frequencies, the mode shapes are also found to change only slightly when changing form a fixed to a free base. For typical joint configurations, mode shapes for the fixed and the free base are inserted into Lagrange's equation of motion that allow for the Shuttle motion. Computing the

first non-zero frequencies with equation (2.50) when inserting the two different sets of mode shapes gives close agreement with each other and with the exact values.
Since the boundary conditions of Link1 at Joint1 depend also on the position of the Shuttle centre of mass relative to the undeformed axis of Link1, the presented determinant is also a function of the angle θ_1 of Joint1, unlike all the previous determinants. Assuming a reasonable mechanical work range for Joint1 of 45°, the changes of the natural frequencies are very small with typical values of 0.09 rad/s.
Finally this chapter addresses the problem of numerical limits when using the determinant method. By analysing the off-diagonal elements of the mass matrix for the single flexible link and the double flexible link with free base and end effector when using exact mode shapes in the equations of motion, it is found that the determinant can be used to compute the first few natural frequencies and mode shapes of quite complex systems, but careful checking of the results should be applied.

CHAPTER 7: RMS OPEN-LOOP DYNAMIC RESPONSE ANALYSIS

Eight configurations of joint states are possible for the triple articulated RMS. This section gives some example simulations of the open-loop system to provide estimates of the worst case elastic deflections. The examples compare the results for a free RMS base with the results for a fixed RMS base (computed with Mathematica), and with SIMPACK results. As mentioned before, the fixed base case apply for the attitude controlled Shuttle, for the space station whose mass is much larger than the payload mass, and for the ground test bed.

In SIMPACK always three mode shapes of a cantilever beam for each elastic link are used. In Mathematica, all mode shapes up to the first non-rigid mode shape are used for each flexible link l (l = 1, 2), that is $W_{l,1}(x_l)$ for a locked joint at O_l, or $W_{l,1}(x_l)$ = x (rigid-body mode) plus $W_{l,2}(x_l)$ for an unlocked joint at O_l.

Note that for the following simulations the tangent frame formulation is used to set up the kinetic energy expressions with Mathematica. In this approach the kinematics of any body within the chain of bodies of the dynamical system are always formulated relative to the previous body in the chain. Therefore a correction has to be made to the non-rigid mode shapes of the first flexible link due to the following reason. The functions $W_{1,i}(x_1)$ in their present form contain also the rotatory and translatory motion of the Shuttle in the actual vibration mode. But for further use in the following dynamic response analyses, the functions must only represent the deflection of Link1 relative to the Shuttle. Therefore, since all deflections are linearised, the corrected mode shape for Link1 is obtained by letting $W_{1,i\ \mathrm{correct}}(x_1) = W_{1,i}(x_1) - W_{1,i}(0) + \Delta\bar{\theta}_1\, x_1$, where $\Delta\bar{\theta}_1$ is given by equation (6.1) and is known after applying the aforementioned method of re-inserting a known ω_i into the respective equation systems to obtain the mode shapes. For an unlocked Joint1, the $\Delta\bar{\theta}_1$ term in the above equation is waived, since in that case rotational motions are not transmitted through Joint1.

The advantage of using the tangent frame formulation is the following. Since the kinematics of any body are expressed relative to the previous body, a motion for example of the end effector about O3 changes nothing in the formulation of all previous bodies in the chain, that is of the whole rest of the system. Another example is the step from a fixed RMS base in chapter 5 to a free base in chapter 6. As the tangent frame was also used to set up the boundary conditions for the flexible links when using the determinant method, only the boundary conditions of Link1 at $x_1 = 0$ had to be modified to allow for a free floating Shuttle, whereas all the other equations representing the other boundary conditions could remain unchanged. Now since the mode shapes of the two flexible links are always computed for only one moment in time, they could basically not be used for dynamic simulations with time-varying states. Using the tangent frame however, dynamic simulations can be carried out by always using the same mode shapes for the whole simulation, provided that in reality the mode shapes do not change significantly with a changing configuration. The following table 7.1 is given for a proof. The table gives the first non-zero frequency computed with the determinant for data set (B) for the double flexible link system with fixed base and end effector as presented in chapter 5 for the configuration Joint1 and Joint3 locked and Joint2 unlocked with $\theta_3 = 0°$ (see also table 5.6) for various θ_2, and compares this frequency with the first non-zero frequency computed with

equation (2.50) for varying θ_2 when for Link1 only the first exact mode shape computed with the determinant for $\theta_2 = \theta_3 = 0°$ and for Link2 the rigid-body and the first exact flexible mode shape computed with the determinant for $\theta_2 = \theta_3 = 0°$ are inserted into Lagrange's equation (2.48). The respective frequencies are denoted ω_{det} and ω_{Lag}.

θ_2	0°	30°	60°	90°
ω_{det} [rad/s]	1.02	0.98	0.82	0.73
ω_{Lag} [rad/s]	1.02	0.98	0.82	0.73

Table 7.1: First non-zero frequency ω_{det} of determinant for chapter 5 system and ω_{Lag} of equation (2.50) for one fixed set of mode shapes for the links

Table 7.1 clearly proves the aforementioned benefit of using the tangent frame, since the mode shapes do practically not change with changing θ_2. Thus only one set of mode shapes is sufficient for dynamic analyses with time varying configurations.
The following table 7.2 makes the same comparison for the configuration Joint1 and Joint2 locked and Joint3 unlocked (see also table 5.7). Again, for Lagrange's equation the mode shapes of the flexible links were computed for $\theta_2 = \theta_3 = 0°$.

θ_3	0°	30°	60°	90°
ω_{det} [rad/s]	0.40	0.33	0.27	0.27
ω_{Lag} [rad/s]	0.40	0.34	0.29	0.27

Table 7.2: First non-zero frequency ω_{det} of determinant for chapter 5 system and ω_{Lag} of equation (2.50) for one fixed set of mode shapes for the links

Like table 7.1, table 7.2 proves the power of the tangent frame formulation.
One side effect when using the tangent frame formulation must however be noted. Since a modal decomposition due to time varying configurations is not possible, the system obtained with Lagrange's equation (2.48) will have more than only the one natural frequency for which the inserted mode shapes were computed. Consider the following example. One mode shape for each flexible link for the configuration all joints locked is computed with the determinant method and inserted into equations of motion obtained with the tangent frame formulation. Now if the system has an end effector and a fixed base, equation (2.50) will give three natural frequencies and thus three mode shapes due to three degrees of freedom: a rigid body rotation of the end effector, a flexible motion of Link2 and a flexible motion of Link1. Originally however, the mode shapes belonged to only one system mode. The influence of these additional modes arising from the tangent frame formulation must be carefully checked to make sure that they do not significantly change the results. In the following simulations however this problem does not arise since for worst case analyses of the elastic deflections only one moment in time must be considered and thus a modal decomposition is possible again. Note that a modal decomposition for the very first mode of a system set up with the tangent frame formulation as described must give the original mode again for which the inserted mode shapes of the flexible

links were originally computed. However, due to numerical inaccuracies adding up through the various stages of computation the results for example of the first frequency after modal decomposition can slightly differ from the original frequency for which the inserted mode shapes were computed. This will be the case a few times in the following simulations.
Note finally that for simplicity, the first exact non-rigid mode shapes of Link1 and Link2 computed with the free or fixed base determinant for the various configurations are denoted $W_1(x_1)$ and $W_2(x_2)$ in the following dynamic response analyses. They always have the generalised coordinates $q_1(t)$ and $q_2(t)$, and for rigid-body modes of the end effector and the flexible links if their joints are unlocked the generalised coordinates $p_3(t)$, $p_4(t)$ and so on are used. The Shuttle rigid body modes are the generalised coordinates $p_5(t)$, $p_6(t)$ and so on.

7.1 SHUTTLE THRUSTER FIRING

We first consider the case of all joints locked and a payload exciting force due to Shuttle acceleration / deceleration from thruster firings. In space construction as with the Shuttle following payload slewing say with the RMS perpendicular to the Shuttle bay, thruster firing is used to translate the payload to the vicinity of the target area. This will be a bang-bang manoeuvre using the longitudinal Vernier thrusters and all RMS joints will obviously be locked with brakes applied. Clearly this procedure will cause transients oscillations of the payload / Shuttle system. Figure 7.1 shows the system velocity components.

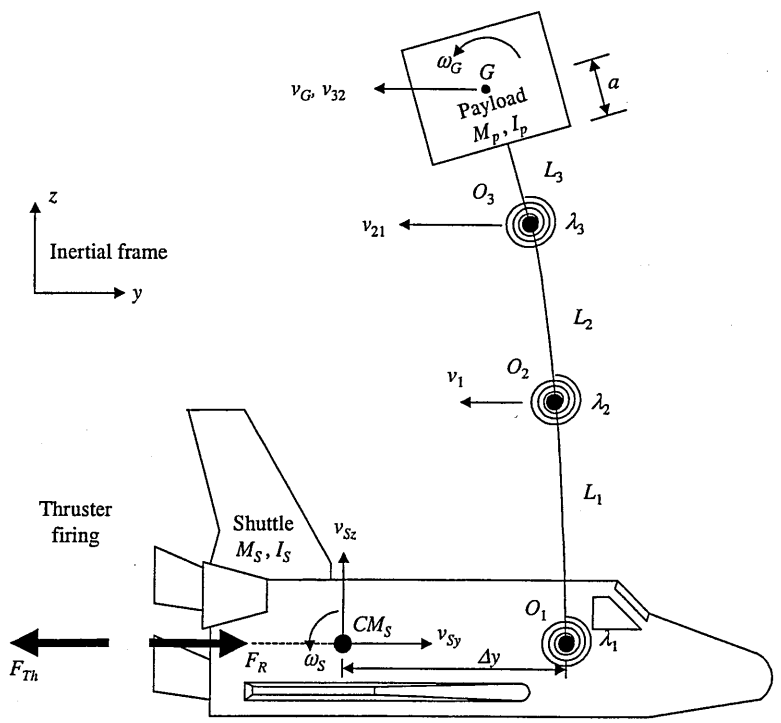

Figure 7.1: Velocity components for RMS dynamic response to Shuttle thruster firing

From figure 7.1 the translatory velocity v_G of the payload centre of mass G relative to the RMS base at O_1 is the sum of the velocities v_1, v_{21} and v_{32} of Link1 relative to the

Shuttle, Link2 relative to Link1 and the payload centre of mass G relative to Link2. The RMS base is offset from the Shuttle centre of mass CM_S in y by Δy. Note that the line of action of F_R in figure 7.1 is assumed to go through CM_S (dashed line).
The 6 generalised coordinates are q_1, q_2 for elastic deflections of Link1, Link2, p_3 for rigid body rotation of Link3 against λ_3, and p_4, p_5, p_6 for Shuttle linear motion in y, z and rotation about x (= α_S). Thus in the present case the generalised coordinates vector is $\mathbf{p}(t) = [q_1(t), q_2(t), p_3(t), p_4(t), p_5(t), p_6(t)]^T$. The velocities v_1 and v_{21} are

$$v_1 = \dot{q}_1 W_1(L_1) \tag{7.1}$$

$$v_{21} = \dot{q}_2 W_2(L_2) + \dot{q}_1 W_1'(L_1) L_2 \tag{7.2}$$

Since the end effector is rigid, its deflection shape is simply $W_3(x_3) = x$, thus v_{32} is

$$v_{32} = [\dot{p}_3 + \dot{q}_2 W_2'(L_2) + \dot{q}_1 W_1'(L_1)](L_3 + a) \tag{7.3}$$

The shuttle velocity components are

$$v_{Sy} = \dot{p}_4, \; v_{Sz} = \dot{p}_5, \; \omega_S = \dot{p}_6 \tag{7.4}$$

Thus the payload translatory and angular velocities v_G and ω_G are given by

$$\omega_G = \dot{p}_6 + \dot{q}_1 W_1'(L_1) + \dot{q}_2 W_2'(L_2) + \dot{p}_3 \tag{7.5}$$

and

$$v_G = \dot{q}_1 [W_1(L_1) + W_1'(L_1)(L_2 + L_3 + a)] + \dot{q}_2 W_2(L_2) + [\dot{p}_3 + \dot{q}_2 W_2'(L_2)](L_3 + a) \tag{7.6}$$

As in previous chapters the distributed masses m_{bl} of the two flexible links l are replaced by M_l, given by ([41]) $M_l = \frac{1}{3} m_{bl} L_l$, and the joint masses, negligibly small for the present case of maximum payload, can be included in M_1 and M_2.
In the inertia frame y and z components, the kinetic system energy is thus

$$\begin{aligned}
T = {} & \tfrac{1}{2} M_p [\dot{p}_4 - \dot{p}_6 \Delta y \sin p_6 - \dot{p}_6 (L_1 + L_2 + L_3 + a) \cos p_6 - \\
& \quad (v_1 + v_{21} + v_{32}) \cos p_6]^2 + \\
& \tfrac{1}{2} M_p [\dot{p}_5 + \dot{p}_6 \Delta y \cos p_6 - \dot{p}_6 (L_1 + L_2 + L_3 + a) \sin p_6 - \\
& \quad (v_1 + v_{21} + v_{32}) \sin p_6]^2 + \\
& \tfrac{1}{2} M_2 [\dot{p}_4 - \dot{p}_6 \Delta y \sin p_6 - \dot{p}_6 (L_1 + L_2) \cos p_6 - (v_1 + v_{21}) \cos p_6]^2 + \\
& \tfrac{1}{2} M_2 [\dot{p}_5 + \dot{p}_6 \Delta y \cos p_6 - \dot{p}_6 (L_1 + L_2) \sin p_6 - (v_1 + v_{21}) \sin p_6]^2 + \\
& \tfrac{1}{2} M_1 [\dot{p}_4 - \dot{p}_6 \Delta y \sin p_6 - \dot{p}_6 L_1 \cos p_6 - v_1 \cos p_6]^2 + \\
& \tfrac{1}{2} M_1 [\dot{p}_5 + \dot{p}_6 \Delta y \cos p_6 - \dot{p}_6 L_1 \sin p_6 - v_1 \sin p_6]^2 + \\
& \tfrac{1}{2} M_S [\dot{p}_4^2 + \dot{p}_5^2] + \tfrac{1}{2} I_p \omega_G^2 + \tfrac{1}{2} I_S \dot{p}_6^2
\end{aligned} \tag{7.7}$$

Applying Lagrange's equation yields the equations of motion with the 6×6 mass matrix **M** containing the elements M_{nm}

$$
\begin{aligned}
M_{11} = {} & M_1 W_1(L_1)^2 + I_p W_1'(L_1)^2 + M_p\left[(L_2+L_3+a)W_1'(L_1)+W_1(L_1)\right]^2 + \\
& M_2\left[L_2 W_1'(L_1)+W_1(L_1)\right]^2 \\
M_{12} = M_{21} = {} & M_2 W_2(L_2)\left[L_2 W_1'(L_1)+W_1(L_1)\right]+I_p W_1'(L_1)W_2'(L_2)+ \\
& M_p\left[(L_2+L_3+a)W_1'(L_1)+W_1(L_1)\right]\left[(L_3+a)W_2'(L_2)+W_2(L_2)\right] \\
M_{13} = M_{31} = {} & M_p(L_3+a)W_1(L_1)+W_1'(L_1)\left[I_p+(L_3+a)(L_2+L_3+a)M_p\right] \\
M_{14} = M_{41} = {} & -\left[(M_p+M_2+M_1)W_1(L_1)+\left[(L_2+L_3+a)M_p+L_2 M_2\right]W_1'(L_1)\right]\cos\alpha_S \\
M_{15} = M_{51} = {} & -\left[(M_p+M_2+M_1)W_1(L_1)+\left[(L_2+L_3+a)M_p+L_2 M_2\right]W_1'(L_1)\right]\sin\alpha_S \\
M_{16} = M_{61} = {} & \left[(L_2+L_3+a)M_p+L_2 M_2+L_1\left(M_1+M_2+M_p\right)\right]W_1(L_1)+ \\
& \left[I_p+L_2^2 M_2+(L_2+L_3+a)^2 M_p+L_1\left(L_2 M_2+(L_2+L_3+a)M_p\right)\right]W_1'(L_1) \\
M_{22} = {} & M_2 W_2(L_2)^2 + I_p W_2'(L_2)^2 + M_p\left[(L_3+a)W_2'(L_2)+W_2(L_2)\right]^2 \\
M_{23} = M_{32} = {} & M_p(L_3+a)W_2(L_2)+W_2'(L_2)\left[I_p+(L_3+a)^2 M_p\right] \\
M_{24} = M_{42} = {} & -\left[(M_p+M_2)W_2(L_2)+(L_3+a)M_p W_2'(L_2)\right]\cos\alpha_S \\
M_{25} = M_{52} = {} & -\left[(M_p+M_2)W_2(L_2)+(L_3+a)M_p W_2'(L_2)\right]\sin\alpha_S \\
M_{26} = M_{62} = {} & \left[(L_1+L_2)M_2+(L_1+L_2+L_3+a)M_p\right]W_2(L_2)+ \\
& \left[I_p+\left(a^2+L_3(L_1+L_2+L_3)+a(L_1+L_2+2L_3)\right)M_p\right]W_2(L_2) \\
M_{33} = {} & I_p+(L_3+a)^2 M_p \\
M_{34} = M_{43} = {} & -\cos\alpha_S(L_3+a)M_p \\
M_{35} = M_{53} = {} & -\sin\alpha_S(L_3+a)M_p \\
M_{36} = M_{63} = {} & I_p+\left[a^2+L_3(L_1+L_2+L_3)+a(L_1+L_2+2L_3)\right]M_p \\
M_{44} = {} & M_p+M_S+M_2+M_1 \\
M_{45} = M_{54} = {} & 0 \\
M_{46} = M_{64} = {} & \left[L_2 M_2+(a+L_2+L_3)M_p+L_1\left(M_1+M_2+M_p\right)\right]\cos\alpha_S - \\
& \Delta y\left(M_1+M_2+M_p\right)\sin\alpha_S \\
M_{55} = {} & M_p+M_S+M_2+M_1 \\
M_{56} = M_{65} = {} & \Delta y\left(M_1+M_2+M_p\right)\cos\alpha_S - \\
& \left[L_2 M_2+(a+L_2+L_3)M_p+L_1\left(M_1+M_2+M_p\right)\right]\sin\alpha_S \\
M_{66} = {} & I_p+I_S+\left(\Delta y^2+L_1^2\right)(M_1+M_2)+2L_1 L_2 M_2+L_2^2 M_2+ \\
& \left[\Delta y^2+(L_1+L_2+L_3+a)\right]M_p
\end{aligned}
\tag{7.8}
$$

The elements of the 6×6 stiffness matrix **K** due to joint stiffnesses λ_b (b = 1, 2, 3) and flexural stiffnesses EI_l are

$$
\begin{aligned}
K_{11} &= EI_1 \int_0^{L_1} [W_1''(x_1)]^2 \, dx + \lambda_1 [W_1'(0)]^2 \\
K_{22} &= EI_2 \int_0^{L_2} [W_2''(x_2)]^2 \, dx + \lambda_2 [W_2'(0)]^2 \\
K_{33} &= \lambda_3 \\
K_{nm} &= 0 \quad \text{else}
\end{aligned}
\tag{7.9}
$$

With $F_R = -F_{Th}$, see figure 7.1, the 6×1 generalised force vector **P** is

$$
\mathbf{P} = \{0, 0, 0, F_R \cos p_6, F_R \sin p_6, 0\}^{\mathrm{T}} \tag{7.10}
$$

where F_R is the accelerating or decelerating reaction force from the Vernier thrusters. The six natural frequencies ω_{jL} of the system, of which three are zero (representing the rigid body motion of the Shuttle / RMS system in y, z, and about x), are calculated by solving equation (2.50).
The first non-zero natural frequency is the fundamental frequency as computed with the determinant for this system configuration, and the other two vibration frequencies arising from using the tangent frame formulation do not have to be identical to the second and third exact natural frequency from the determinant for this case, as mentioned in the introduction to this chapter. Since the worst case analyses only consider one point in time, a modal decomposition for the first mode is performed.
If ω_j is the frequency of mode j and if $\mathbf{ev}_j$ is the 6×1 corresponding eigenvector, the modal decomposition gives

$$
\begin{aligned}
m_j &= \mathbf{ev}_j^{\mathrm{T}} \mathbf{M} \, \mathbf{ev}_j \\
k_j &= \mathbf{ev}_j^{\mathrm{T}} \mathbf{K} \, \mathbf{ev}_j \\
f_j &= \mathbf{ev}_j^{\mathrm{T}} \mathbf{P}
\end{aligned}
\tag{7.11}
$$

where m_j, k_j and f_j are the j-th modal mass, stiffness and exciting force. Note that since in the present simulations the response in the higher modes is negligibly small, as was shown in the previous chapters, steps (7.1) through (7.11) are only performed for the first exact (in this case non-rigid) mode shapes of Link1 and Link2.
The RMS excitation does not only depend on the thruster force, but also on the payload mass since it is the acceleration of M_p which produces the exciting force. We therefore consider the worst case with M_p = 30000 kg, I_p = 400000 kgm^2 and $a = b/2$ = 2 m, according to data sets (B) or (C) respectively for a fixed or free RMS base. Since the RMS is straight, $\theta_1 = \theta_2 = \theta_3 = 0°$. The longitudinal Vernier control thrusters produce a maximum force of ([60]) F_{Th} = 6×107 N = 642 N. Figure 7.2 shows the time history of $F_R = -F_{Th}$.

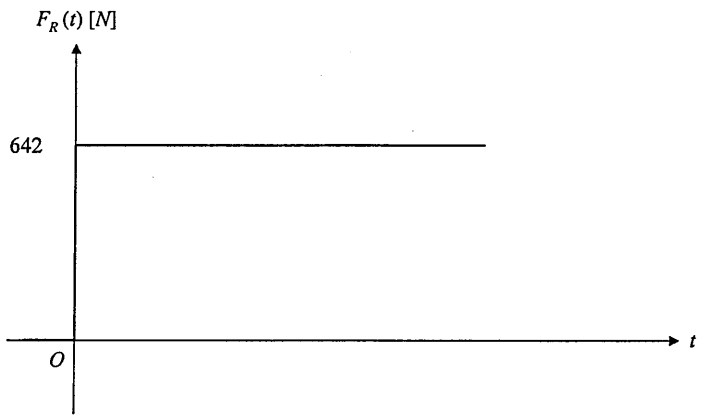

Figure 7.2: Time history of F_R

Free base results

Setting up the mass and stiffness matrix according to equations (7.8) and (7.9) and computing the natural frequencies and eigenvectors with equation (2.50) the first non-zero frequency should be identical to the exact fundamental frequency of the determinant solution for this case, $\omega_{det} = 0.25$ rad/s, but from table 6.4 $\omega_{Lag} = 0.31$ rad/s. As mentioned in chapter 6, it is assumed that for this single case the determinant results are too low by about 0.05 rad/s.
Figure 7.3 shows the time history of the deflection y_G of the payload centre of mass G relative to the Shuttle for an F_R as shown in figure 7.2. The system mode shape is shown in figure 6.5.

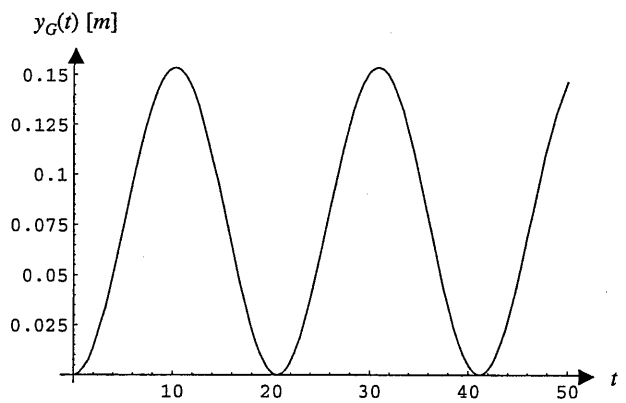

Figure 7.3: Time history of y_G

From figure 7.3 the vibration amplitude of y_G is 7.68 cm. The SIMPACK result for the present case is 7.81 cm.

Results for linearly driven base

For the worst case we assume a non-rotating base accelerated perpendicularly to the straight RMS. This situation applies to ground bed testing, where the RMS shoulder

joint at O_1 could be attached to a trolley construction having the mass of the Shuttle to be driven along a track to simulate thruster induced acceleration / deceleration. Also the situation applies to a RMS base that is attached to a frame driven along a track on a large space station to extend the work range of the RMS, or to an attitude controlled Shuttle.

To get the correct mode shapes for this case, the determinant for the free base is used, setting $I_S = 10^{20}$ kgm^2 in equation (6.6) so as to approach infinity and to allow only for translatory motion of the RMS base. However it is found that due to the immense effective rotary inertia of $1{,}472\times10^7$ kgm^2 of the Shuttle about O_1 due the offset Δy, the mode shapes remain practically unchanged, so that the mode shapes for the fixed base or the free base with the real I_S value could also be used.

The equations of motion for this case are given by deleting the fifth and sixth column and row in the mass and stiffness matrices **M** and **K**, equations (7.8) and (7.9), and the fifth and sixth element of the generalised force vector **P**, equation (7.10). Finally the Shuttle rotation α_S about x is set to zero.

Whichever mode shapes are chosen, the fundamental frequency obtained with equation (2.50) is $\omega_{Lag} = 0.20$ rad/s, which is in exact agreement with the free base determinant result for the case $I_S = 10^{20}$ kgm^2, $\omega_{det} = 0.20$ rad/s. Figure 7.4 shows the time history of y_G for the present case for F_R as shown in figure 7.2. The corresponding first system mode shape $W_{S1}(x)$ is shown in figure 7.5.

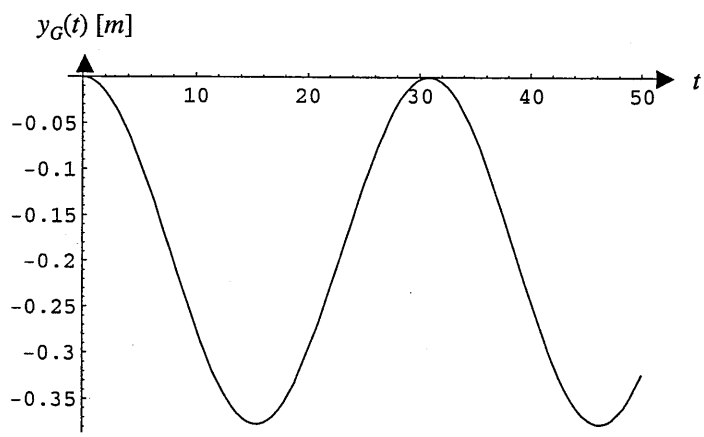

Figure 7.4: Time history of y_G

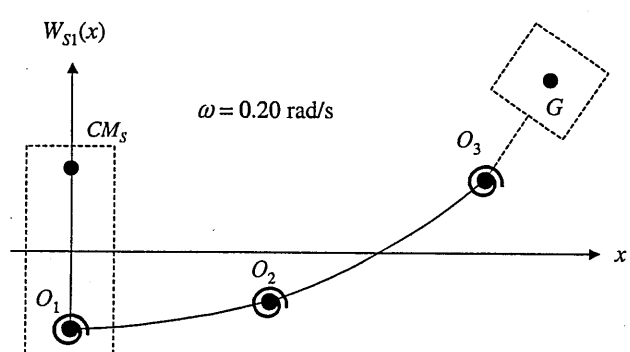

Figure 7.5: First system mode shape $W_{S1}(x)$ for linearly moving base (= Shuttle)

In figure 7.4 the vibration amplitude of the payload centre of mass G relative to the Shuttle is 18.84 cm. In SIMPACK, this deflection is computed to be 18.38 cm.
This result is verified using a quasi-static deflection as follows. The Shuttle acceleration a_s creates an inertia force F_p at the payload centre of mass G (and at the links due to the distributed beam mass, but these forces are negligible). Then F_p is given by

$$F_p = a_s M_p = \frac{F_R}{M_s + M_p} M_p \tag{7.12}$$

F_p creates shear forces F_b and moments Mo_b at the joints O_b (b = 1, 2, 3). They are

$$F_b = F_p \tag{7.13}$$

$$Mo_1 = F_p \left(L_1 + L_2 + L_3 + a\right) \tag{7.14}$$

$$Mo_2 = F_p \left(L_2 + L_3 + a\right) \tag{7.15}$$

$$Mo_3 = F_p \left(L_3 + a\right) \tag{7.16}$$

The deflections y_{Fl} and y_{Ml} of the two flexible links with length L_l and flexural stiffness EI_l (l = 1, 2) due to F_{l+1} and Mo_{l+1} at the tip are ([45])

$$y_{Fl} = \frac{F_{l+1} L_l^3}{3 E I_l} \tag{7.17}$$

and

$$y_{Ml} = \frac{Mo_{l+1} L_l^2}{2 E I_l} \tag{7.18}$$

The rigid body deflection θ_{Jl} of the two flexible links due to joint stiffness λ_l is

$$\theta_{Jl} = \frac{Mo_l}{\lambda_l} \tag{7.19}$$

The rotations θ_{Fl} and θ_{Ml} of Link l at its tip due to F_{l+1} and Mo_{l+1} at the tip are ([45])

$$\theta_{Fl} = \frac{F_{l+1} L_l^2}{2 E I_l} \tag{7.20}$$

and

$$\theta_{Ml} = \frac{Mo_{l+1} L_l}{E I_l} \tag{7.21}$$

The deflections y_1, y_2 and y_3 of G due to the various elasticities of Link1, Link2 and the end effector are

$$y_1 = y_{F1} + y_{M1} + \theta_{J1} L_1 + (\theta_{F1} + \theta_{M1} + \theta_{J1})(L_2 + L_3 + a) \quad (7.22)$$

$$y_2 = y_{F2} + y_{M2} + \theta_{J2} L_2 + (\theta_{F2} + \theta_{M2} + \theta_{J2})(L_3 + a) \quad (7.23)$$

$$y_3 = y_{J3} = \frac{F_p}{\lambda_3}(L_3 + a)^2 \quad (7.24)$$

and the static deflection y_G of G is

$$y_G = y_1 + y_2 + y_3 \quad (7.25)$$

Inserting the data into equations (7.12) through (7.25) yields a static deflection y_G = 18.95 cm, which is in very close agreement to the dynamic result. The deviations can occur due to numerical inaccuracies and the fact that for the simulation only the fundamental mode shape is used. This also proves that the influence of all modes higher than the fundamental in the deflection of G is very small.
It is noted that the present configuration yields a maximum RMS response, since all joints are locked and the excitation of the RMS due to Shuttle acceleration is maximum.
For comparison, the analytical solution above yields a vibration amplitude of 3.49 cm for a payload with M_p = 5000 kg, I_p = 3333 kgm^2 and $a = b/2$ = 1 m, which shows that the payload size has to be relatively large to give non-negligible dynamic responses.

7.2 RMS SLEW MANOEUVRES

This section gives some examples of worst case RMS responses to slew manoeuvres due to joint torques. For most of the simulations the results for the free and the fixed RMS base are compared with each other and the SIMPACK results.

7.2.1 SLEW ABOUT ALL JOINTS

For this case and the following case only the fixed base result is given because the fixed base results must always be larger than the free base results, and the fixed base figures are already negligibly small. Note that in practice for manual RMS slewing by an astronaut it is expected that only one joint is as actuated at a time with the other two locked. Automatic slew however may actuate two or all joints simultaneously. The actual system is shown in figure 7.6, where the T_b (b = 1, 2, 3) are the driving torques at the joints O_b.
With $\mathbf{p}(t) = [q_1(t), q_2(t), p_3(t), p_4(t), p_5(t)]^T$, the velocities v_1, v_{21} and v_{32} of O_2 relative to O_1, of O_3 relative to O_2 and of G relative to O_3 are for a fixed base

$$v_1 = \dot{q}_1 W_1(L_1) + \dot{p}_3 L_1 \quad (7.26)$$

$$v_{21} = \dot{q}_2 W_2(L_2) + \dot{p}_4 L_2 + [\dot{q}_1 W_1'(L_1) + \dot{p}_3] L_2 \quad (7.27)$$

$$v_{32} = \dot{p}_5 (L_3 + a) + [\dot{q}_2 W_2'(L_2) + \dot{p}_4 + \dot{q}_1 W_1'(L_1) + \dot{p}_3](L_3 + a) \quad (7.28)$$

where $\dot{p}_3 = \dot{\theta}_1$, $\dot{p}_4 = \dot{\theta}_2$ and $\dot{p}_5 = \dot{\theta}_3$.

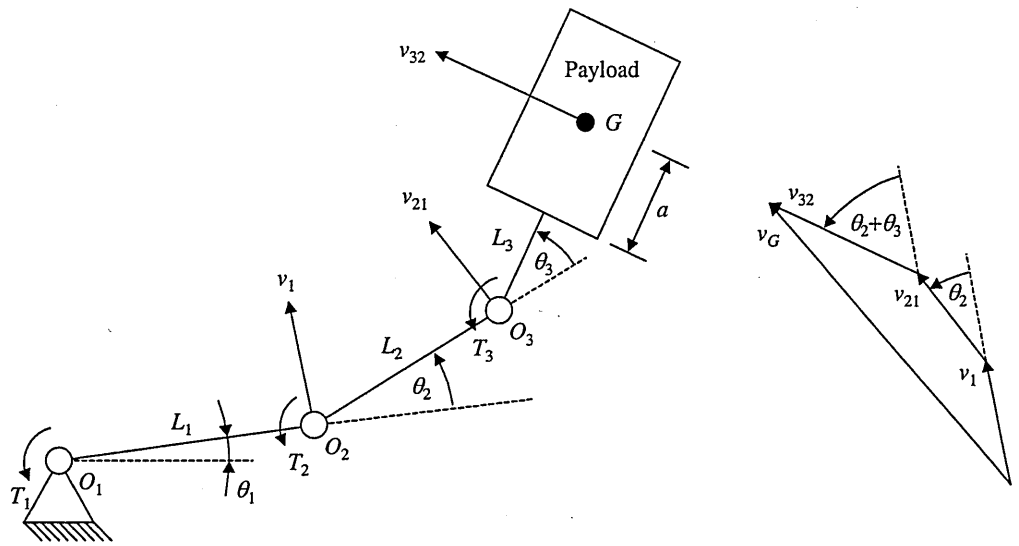

Figure 7.6: Double flexible link system with articulated end effector and fixed base

Since all joints are unlocked and thus free to drive, the rigid body coordinates p_3 and p_4 have to be included in Lagrange's equation. The kinetic energy T is obtained from figure 7.6, and using the Pythagoras theorem (see right hand side in figure 7.6) is given by

$$\begin{aligned} T = {} & \tfrac{1}{2}M_p\left(v_1^2 + v_{21}^2 + v_{32}^2 + 2v_1 v_{21}\cos\theta_2 + 2v_1 v_{32}\cos(\theta_2+\theta_3) + 2v_{21} v_{32}\cos\theta_3\right) + \\ & \tfrac{1}{2}M_1 v_1^2 + \tfrac{1}{2}M_2\left(v_1^2 + v_{21}^2 + 2v_1 v_{21}\cos\theta_2\right) + \tfrac{1}{2}I_{g1}\left[\dot{q}_1 W_1'(0) + \dot{p}_3\right]^2 + \\ & \tfrac{1}{2}I_{g2}\left[\dot{p}_4 + \dot{q}_2 W_2'(0)\right]^2 + \tfrac{1}{2}I_p\left(W_2'(L_2) + \dot{p}_4 + W_1'(L_1) + \dot{p}_3 + \dot{p}_5\right)^2 \end{aligned} \tag{7.29}$$

The equations of motion are derived with Lagrange's equation, yielding the 5×5 time-varying mass matrix **M** with elements M_{nn}

$$\begin{aligned} M_{11} = {} & \left(M_1 + M_2 + M_p\right)\left[W_1(L_1)\right]^2 + I_{g1}\left[W_1'(0)\right]^2 + 2\left[L_2\left(M_2 + M_p\right)\cos\theta_2 + \right. \\ & (L_3 + a)M_p\cos(\theta_2+\theta_3)\left]W_1(L_1)W_1'(L_1) + \left[W_1'(L_1)\right]^2\right(I_p + L_2^2 M_p + \\ & a^2 M_p + L_2^2 M_2 + 2aL_3 M_p + L_3^2 M_p + 2aL_2 M_p\cos\theta_3 + \\ & \left.2L_2 L_3 M_p\cos\theta_3\right) \\ M_{12} = M_{21} = {} & M_2 W_2(L_2)\left[\cos\theta_2 W_1(L_1) + L_2 W_1'(L_1)\right] + W_1'(L_1)W_2'(L_2)I_p + \\ & M_p W_1'(L_1)\left[\left[L_2 + (a+L_3)\cos\theta_3\right]W_2(L_2) + \right. \\ & \left.W_2'(L_2)(L_3+a)(\cos\theta_3 L_2 + L_3 + a)\right] + M_p W_1(L_1)\left[\cos\theta_2 W_2(L_2) + \right. \\ & \left.(L_3+a)\cos(\theta_2+\theta_3)W_2'(L_2)\right] \end{aligned} \tag{7.30}$$

$$
\begin{aligned}
M_{13} = M_{31} &= W_1(L_1)\left[L_1(M_1 + M_2 + M_p) + L_2(M_2 + M_p)\cos\theta_2 + \right. \\
&\quad \left. M_p\cos(\theta_2 + \theta_3)(L_3 + a)\right] + I_{g1}W_1'(0) + W_1'(L_1)\left[I_p + L_2^2(M_2 + M_p) + \right. \\
&\quad \left. a^2 M_p + 2aL_3 M_p + L_3^2 M_p + L_1 L_2\cos\theta_2(M_2 + M_p) + \right. \\
&\quad \left. 2L_2 M_p\cos\theta_3(L_3 + a) + L_1 M_p\cos(\theta_2 + \theta_3)(L_3 + a)\right] \\
M_{14} = M_{41} &= W_1(L_1)\left[L_2(M_2 + M_p)\cos\theta_2 + M_p\cos(\theta_2 + \theta_3)(L_3 + a)\right] + \\
&\quad W_1'(L_1)\left[I_p + L_2^2(M_2 + M_p) + a^2 M_p + 2aL_3 M_p + L_3^2 M_p + \right. \\
&\quad \left. 2L_2 M_p\cos\theta_3(L_3 + a)\right] \qquad (7.30) \\
M_{15} = M_{51} &= W_1'(L_1)I_p + (L_3 + a)M_p\left[W_1(L_1)\cos(\theta_2 + \theta_3) + \right. \\
&\quad \left. (\cos\theta_3 L_2 + L_3 + a)W_1'(L_1)\right] \\
M_{22} = &\quad (M_2 + M_p)[W_2(L_2)]^2 + I_{g2}[W_2'(0)]^2 + [W_2'(L_2)]^2\left[I_p + a^2 M_p + \right. \\
&\quad \left. 2aL_3 M_p + L_3^2 M_p\right] + W_2(L_2)W_2'(L_2)(L_3 + a)2M_p\cos\theta_3 \\
M_{23} = M_{32} &= M_2(\cos\theta_2 L_1 + L_2)W_2(L_2) + I_p W_2'(L_2) + M_p W_2(L_2)\left[\cos\theta_2 L_1 + L_2 + \right. \\
&\quad \left. (L_3 + a)\cos\theta_3\right] + \\
&\quad M_p W_2'(L_2)(L_3 + a)(L_1\cos(\theta_2 + \theta_3) + L_2\cos\theta_3 + L_3 + a) \\
M_{24} = M_{42} &= M_2 L_2 W_2(L_2) + I_{g2}W_2'(0) + I_p W_2'(L_2) + \\
&\quad M_p\left[W_2(L_2)(L_2 + \cos\theta_3(L_3 + a)) + W_2'(L_2)(L_3 + a)(L_2\cos\theta_3 + L_3 + a)\right] \\
M_{25} = M_{52} &= M_p(L_3 + a)W_2(L_2)\cos\theta_3 + W_2'(L_2)\left[I_p + (L_3 + a)^2 M_p\right] \\
M_{33} = &\quad I_{g1} + I_p + L_1^2 M_1 + M_2(L_1^2 + L_2^2 + 2L_1 L_2\cos\theta_2) + M_p\left[L_1^2 + L_2^2 + \right. \\
&\quad \left. (L_3 + a)^2 + 2L_1 L_2\cos\theta_2 + 2L_2(L_3 + a)\cos\theta_3 + \right. \\
&\quad \left. 2L_1(L_3 + a)\cos(\theta_2 + \theta_3)\right] \\
M_{34} = M_{43} &= I_p + M_2 L_2(\cos\theta_2 L_1 + L_2) + M_p\left[L_2^2 + (L_3 + a)^2 + \cos\theta_2 L_1 L_2 + \right. \\
&\quad \left. 2L_2(L_3 + a)\cos\theta_3 + L_1(L_3 + a)\cos(\theta_2 + \theta_3)\right] \\
M_{35} = M_{53} &= I_p + M_p\left[(L_3 + a)(\cos(\theta_2 + \theta_3)L_1 + \cos\theta_3 L_2 + L_3 + a)\right] \\
M_{44} = &\quad I_{g2} + I_p + L_2^2 M_2 + M_p\left[L_2^2 + (L_3 + a)^2 + 2L_2(L_3 + a)\cos\theta_3\right] \\
M_{45} = M_{54} &= I_p + M_p(L_3 + a)(\cos\theta_3 L_2 + L_3 + a) \\
M_{55} = &\quad I_p + M_p(L_3 + a)^2
\end{aligned}
$$

The gear box inertia at Joint3 can be included in the payload rotary inertia. The two flexible beams yield the 5×5 stiffness matrix **K** with elements K_{nm}

$$
\begin{aligned}
K_{11} &= EI_1\int_0^{L_1}[W_1''(x_1)]^2\,dx \\
K_{22} &= EI_2\int_0^{L_2}[W_2''(x_2)]^2\,dx \qquad (7.31) \\
K_{nm} &= 0 \quad \text{else}
\end{aligned}
$$

Since torques are not backcoupled through joints, the 5×1 vector of the generalised forces **P** is

$$\mathbf{P} = \{T_1 W_1'(0) + (T_2 + T_3) W_1'(L_1), T_2 W_2'(0) + T_3 W_2'(L_2), T_1 + T_3 + T_2, T_2 + T_3, T_3\}^T \quad (7.32)$$

For the straight RMS with $\theta_2 = \theta_3 = 0°$ the first non-zero natural frequency obtained from equation (2.50) is $\omega_{Lag} = 33.14$ rad/s, the exact fundamental frequency for this system is $\omega_{det} = 34.04$ rad/s. The deviation is due to ill-conditioned matrices as explained in the introduction to this chapter. The decomposition for the first mode is performed using equation (7.11).
For the simulation data set (B) is used, and the maximum torques T_b of the SRMS at all three joints, T_1 = 1298 Nm, T_2 = 888 Nm and T_3 = 389 Nm, are applied simultaneously at all three joints. Figure 7.7 shows the time history of T_1, T_2 and T_3, and figure 7.8 shows the corresponding time history of y_G.

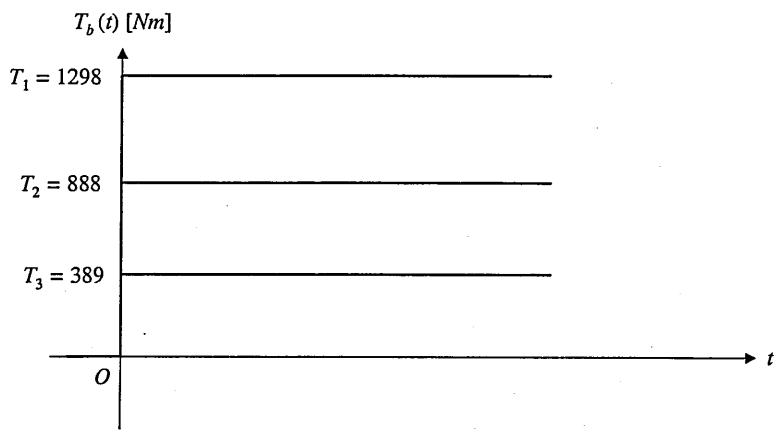

Figure 7.7: Time history of of T_1, T_2 and T_3

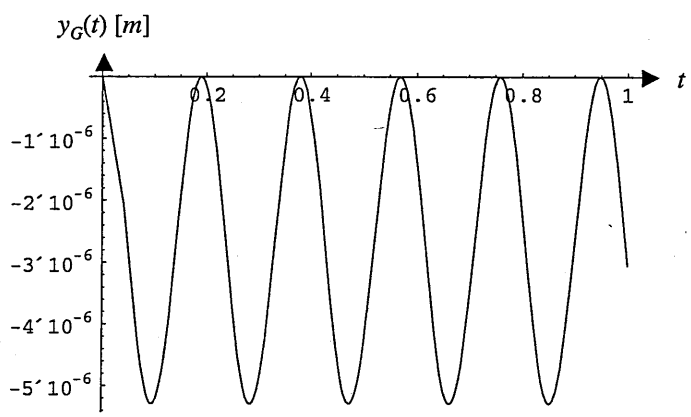

Figure 7.8: Time history of y_G

In figure 7.8 the amplitude of vibration of y_G relative to the base is less than 1/100 mm. The deflections of the tips of the two flexible links, which are not shown in the figures, are less than 4 mm in the fundamental mode. The basic reason for these small elastic responses is that the unlocked links have very high pinned-pinned natural frequencies.
These figures prove that if all joints are unlocked, the deflections are negligibly small

and allow for the assumption of rigid bodies. This finding gives rise to another aspect: for an active damping control using the joint motors, the joints must obviously be unlocked, a configuration which yields, as can be seen here, negligibly small deflections. For RMS designed similarly to the SRMS the control methods proposed for example in [5] and [9] therefore appear to be unnecessary.

7.2.2 SLEW ABOUT TWO JOINTS

For a simultaneous slew about two RMS joints, as before, only the result for a fixed RMS base is used. For the worst case scenario we choose a slew about Joint1 and Joint2 applying the maximum torques and maximum payload.
Since the only difference to the previous case is the fact that in the present case no torque T_3 is applied at O_3, the equations for the velocity components are identical, as well as the kinetic energy expression and the equations for the mass matrix elements. Thus the velocity components are given with equations (7.26) through (7.28), the kinetic energy expression is given by equation (7.29), and the elements of the 5×5 mass matrix **M** are given with equations (7.30). Note that the mode shape functions $W_1(x_1)$ and $W_2(x_2)$ used in the present case differ from those used in the previous simulation (and hence also their derivatives), since in the previous case the exact first non-rigid mode shapes for the configuration all joints unlocked were used, whereas now the exact first non-rigid mode shapes for the case only Joint3 locked are used.
Since Joint3 is locked, the 5×5 stiffness matrix **K** with elements K_{nm} differs from the stiffness matrix of the previous simulation and is given by

$$\begin{aligned} K_{11} &= EI_1 \int_0^{L_1} [W_1''(x_1)]^2 \, dx \\ K_{22} &= EI_2 \int_0^{L_2} [W_2''(x_2)]^2 \, dx \\ K_{55} &= \lambda_3 \\ K_{nm} &= 0 \quad \text{else} \end{aligned} \tag{7.33}$$

The 5×1 generalised force vector **P** is

$$\mathbf{P} = \{T_1 W_1'(0) + T_2 W_1'(L_1), T_2 W_2'(0), T_1 + T_2, T_2, 0\}^T \tag{7.34}$$

Using equation (7.11), a modal decomposition for the fundamental mode is performed for the straight RMS with $\theta_2 = \theta_3 = 0°$. With equation (2.50), the fundamental frequency obtained with equation (2.50) yields $\omega_{Lag} = 6.54$ rad/s, the exact fundamental frequency from the determinant for the fixed base is $\omega_{det} = 6.05$ rad/s. The difference is again due to ill-conditioned matrices as explained.
For the time history of T_1 and T_2 consider figure 7.7, where in the present case T_3 is zero for all time t. For this force input, figure 7.9 shows the vibration y_G of G relative to the base, whose amplitude is less than 1/30 mm. Note that for other joint configurations, a slew about two joints gives similar results.

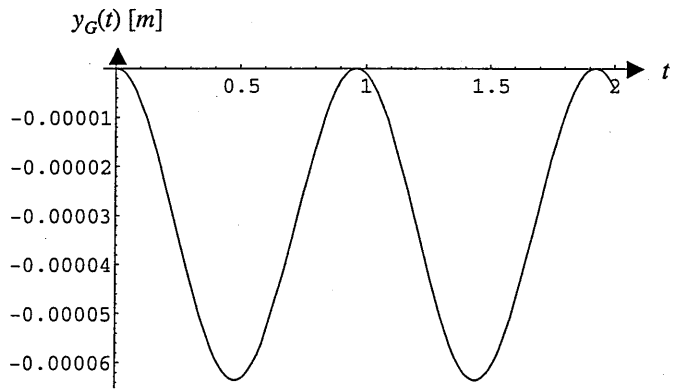

Figure 7.9: Time history of y_G

7.2.3 SLEW ABOUT JOINT1

Consider a slew of the straight ($\theta_2 = \theta_3 = 0°$) RMS about an unlocked Joint1 as shown in figure 7.10. For this and the following simulations also the RMS with free base (= Shuttle) is considered. This leads to system with seven degrees of freedom.

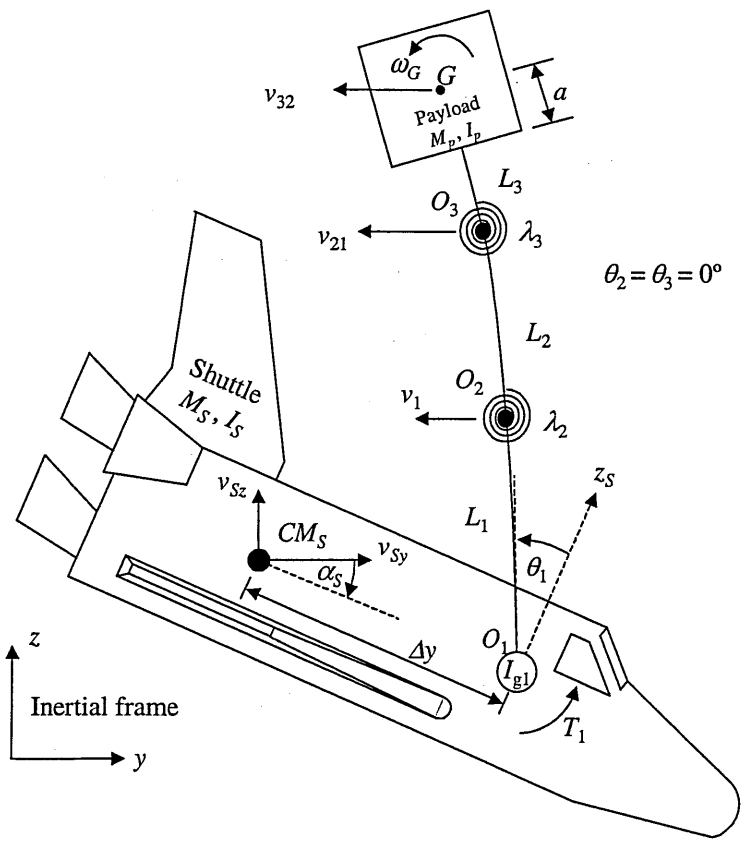

Figure 7.10: Slew of straight RMS about Joint1 with free base (= Shuttle)

In figure 7.10, $\theta_1 = p_4$ is the rigid body rotation of Link1 relative the Shuttle z axis z_S due to T_1. The generalised coordinates are q_1, q_2 for the elastic deflections of Link1

and Link2, p_3 and p_4 for the rigid body deflection of Link3 and Link1, and p_5, p_6, p_7 for the Shuttle rigid body motions in y, z and about x (= α_S), thus $\mathbf{p}(t) = [q_1(t), q_2(t), p_3(t), p_4(t), p_5(t), p_6(t), p_7(t)]^T$. The velocities v_1, v_{21} and v_{32} relative to the Shuttle are

$$v_1 = \dot{q}_1 W_1(L_1) + \dot{p}_4 L_1 \tag{7.35}$$

$$v_{21} = \dot{q}_2 W_2(L_2) + [\dot{q}_1 W_1'(L_1) + \dot{p}_4] L_2 \tag{7.36}$$

$$v_{32} = [\dot{p}_3 + \dot{q}_2 W_2'(L_2) + \dot{q}_1 W_1'(L_1) + \dot{p}_4](L_3 + a) \tag{7.37}$$

The payload angular velocity ω_G for a fixed base is

$$\omega_G = \dot{q}_1 W_1'(L_1) + \dot{q}_2 W_2'(L_2) + \dot{p}_3 + \dot{p}_4 \tag{7.38}$$

With figure 7.10 and the Shuttle rigid body motions $v_{Sy} = \dot{p}_5$, $v_{Sz} = \dot{p}_6$, $\omega_S = \dot{p}_7$, the system kinetic energy in y and z components of the inertia frame is thus

$$\begin{aligned}
T = {} & \tfrac{1}{2} M_p [\dot{p}_5 - \dot{p}_7 \Delta y \sin \alpha_S - \\
& \quad [v_1 + v_{21} + v_{32} + \dot{p}_7 (L_1 + L_2 + L_3 + a)] \cos(p_4 + p_7)]^2 + \\
& \tfrac{1}{2} M_p [\dot{p}_6 + \dot{p}_7 \Delta y \cos p_7 - \\
& \quad [v_1 + v_{21} + v_{32} + \dot{p}_7 (L_1 + L_2 + L_3 + a)] \sin(p_4 + p_7)]^2 + \\
& \tfrac{1}{2} M_2 [\dot{p}_5 - \dot{p}_7 \Delta y \sin p_7 - [v_1 + v_{21} + \dot{p}_7 (L_1 + L_2)] \cos(p_4 + p_7)]^2 + \\
& \tfrac{1}{2} M_2 [\dot{p}_6 + \dot{p}_7 \Delta y \cos p_7 - [v_1 + v_{21} + \dot{p}_7 (L_1 + L_2)] \sin(p_4 + p_7)]^2 + \\
& \tfrac{1}{2} M_1 [\dot{p}_5 - \dot{p}_7 \Delta y \sin p_7 - (v_1 + \dot{p}_7 L_1) \cos(p_4 + p_7)]^2 + \\
& \tfrac{1}{2} M_1 [\dot{p}_6 + \dot{p}_7 \Delta y \cos p_7 - (v_1 + \dot{p}_7 L_1) \sin(p_4 + p_7)]^2 + \\
& \tfrac{1}{2} M_S [\dot{p}_5^2 + \dot{p}_6^2] + \tfrac{1}{2} I_p (\omega_G + \dot{p}_7)^2 + \tfrac{1}{2} I_S \dot{p}_7^2 + \tfrac{1}{2} I_{g1} [\dot{q}_1 W_1'(0) + \dot{p}_4]^2
\end{aligned} \tag{7.39}$$

The equations of motion yield a 7×7 time-varying mass matrix $\mathbf{M}$ with elements M_{nm}

$$\begin{aligned}
M_{11} = {} & M_1 [W_1(L_1)]^2 + I_{g1} [W_1'(0)]^2 + I_p [W_1'(L_1)]^2 + M_2 [W_1(L_1) + L_2 W_1'(L_1)]^2 + \\
& M_p [W_1(L_1) + (L_2 + L_3 + a) W_1'(L_1)]^2 \\
M_{12} = M_{21} = {} & M_2 W_2(L_2) [W_1(L_1) + L_2 W_1'(L_1)] + W_1'(L_1) W_2'(L_2) I_p + \\
& M_p [W_1(L_1) + (L_2 + L_3 + a) W_1'(L_1)][W_2(L_2) + (L_3 + a) W_2'(L_2)] \\
M_{13} = M_{31} = {} & M_p (L_3 + a) W_1(L_1) + W_1'(L_1) [I_p + M_p (L_3 + a)(L_2 + L_3 + a)] \\
M_{14} = M_{41} = {} & W_1(L_1) [L_2 (M_2 + M_p) + M_p (L_3 + a) + L_1 (M_1 + M_2 + M_p)] + \\
& W_1'(0) I_{g1} + W_1'(L_1) [I_p + L_2^2 (M_2 + M_p) + L_1 L_2 (M_2 + M_p) + a^2 M_p + \\
& a L_1 M_p + 2 a M_p (L_2 + L_3) + L_1 L_3 M_p + 2 L_2 L_3 M_p + L_3^2 M_p]
\end{aligned} \tag{7.40}$$

$$
\begin{aligned}
M_{15} &= M_{51} = -\cos(\theta_1+\alpha_S)\left[(M_1+M_2+M_p)W_1(L_1)+(L_2M_2+(L_2+L_3+a)M_p)W_1'(L_1)\right]\\
M_{16} &= M_{61} = -\sin(\theta_1+\alpha_S)\left[(M_1+M_2+M_p)W_1(L_1)+(L_2M_2+(L_2+L_3+a)M_p)W_1'(L_1)\right]\\
M_{17} &= M_{71} = W_1(L_1)\left[L_1(M_1+M_2+M_p)+L_2(M_2+M_p)+(L_3+a)M_p-\right.\\
&\qquad \left.\Delta y\sin\theta_1(M_1+M_2+M_p)\right]+W_1'(L_1)\left[I_p+M_2L_2(L_1+L_2)+\right.\\
&\qquad M_p(L_2+L_3+a)^2+M_pL_1(L_2+L_3+a)-\\
&\qquad \left.\Delta y\sin\theta_1(M_p(L_2+L_3+a)+M_2L_2)\right]\\
M_{22} &= [W_2(L_2)]^2(M_2+M_p)+2M_p(L_3+a)W_2(L_2)W_2'(L_2)+\\
&\qquad (I_p+(L_3+a)^2M_p)[W_2'(L_2)]^2\\
M_{23} &= M_{32} = M_pW_2(L_2)(L_3+a)+W_2'(L_2)\left[I_p+(L_3+a)^2M_p\right]\\
M_{24} &= M_{42} = (L_1+L_2)M_2W_2(L_2)+W_2'(L_2)I_p+\\
&\qquad (L_1+L_2+L_3+a)M_p[W_2(L_2)+(L_3+a)W_2'(L_2)]\\
M_{25} &= M_{52} = -\cos(\theta_1+\alpha_S)\left[(M_2+M_p)W_2(L_2)+(L_3+a)M_pW_2'(L_2)\right]\\
M_{26} &= M_{62} = -\sin(\theta_1+\alpha_S)\left[(M_2+M_p)W_2(L_2)+(L_3+a)M_pW_2'(L_2)\right]\\
M_{27} &= M_{72} = W_2(L_2)\left[M_p(L_1+L_2+L_3+a)+M_2(L_1+L_2)-\Delta y\sin\theta_1(M_2+M_p)\right]+\\
&\qquad W_2'(L_2)\left[M_p(L_3+a)^2+M_p(L_3+a)(L_1+L_2)-\Delta y\sin\theta_1(L_3+a)M_p\right]\\
M_{33} &= I_p+M_p(L_3+a)^2\\
M_{34} &= M_{43} = I_p+M_p(L_3+a)(L_1+L_2+L_3+a) \qquad (7.40)\\
M_{35} &= M_{53} = -\cos(\theta_1+\alpha_S)M_p(L_3+a)\\
M_{36} &= M_{63} = -\sin(\theta_1+\alpha_S)M_p(L_3+a)\\
M_{37} &= M_{73} = I_p+M_p(L_3+a)(L_1+L_2+L_3+a)-\Delta y\sin\theta_1M_p(L_3+a)\\
M_{44} &= I_{g1}+I_p+M_2(L_1+L_2)^2+L_1^2M_1+(L_1+L_2+L_3+a)^2M_p\\
M_{45} &= M_{54} = -\cos(\theta_1+\alpha_S)\left[L_1M_1+(L_1+L_2+L_3+a)M_p+M_2(L_1+L_2)\right]\\
M_{46} &= M_{64} = -\sin(\theta_1+\alpha_S)\left[L_1M_1+(L_1+L_2+L_3+a)M_p+M_2(L_1+L_2)\right]\\
M_{47} &= M_{74} = I_p+L_1^2M_1+M_p(L_1+L_2+L_3+a)^2-\\
&\qquad \Delta y\sin\theta_1\left[L_1M_1+(L_1+L_2+L_3+a)M_p+M_2(L_1+L_2)\right]\\
M_{55} &= M_1+M_2+M_p+M_S\\
M_{56} &= M_{65} = 0\\
M_{57} &= M_{75} = -\Delta y\cos(\theta_1+\alpha_S)\left[L_1M_1+(L_1+L_2+L_3+a)M_p+M_2(L_1+L_2)\right]-\\
&\qquad \Delta y\sin\alpha_S(M_1+M_2+M_p)\\
M_{66} &= M_1+M_2+M_p+M_S\\
M_{67} &= M_{76} = -\Delta y\sin(\theta_1+\alpha_S)\left[L_1M_1+(L_1+L_2+L_3+a)M_p+M_2(L_1+L_2)\right]+\\
&\qquad \Delta y\cos\alpha_S(M_1+M_2+M_p)
\end{aligned}
$$

$$M_{77} = I_S + I_p + M_1\left[\Delta y^2 + L_1^2 - 2\Delta y L_1 \sin\theta_1\right] + M_2\left[\Delta y^2 + (L_1 + L_2)^2 - \right.$$
$$\left. - 2\Delta y(L_1 + L_2)\sin\theta_1\right] + M_p\left[(L_1 + L_2 + L_3 + a)\cos(\theta_1 + \alpha_S) + \right. \quad (7.40)$$
$$\left. \Delta y \sin\alpha_S\right]^2 + M_p\left[-(L_1 + L_2 + L_3 + a)\sin(\theta_1 + \alpha_S) + \Delta y \cos\alpha_S\right]^2$$

Note that this seven-degrees-of-freedom modelling allows for coupling between the RMS rigid and flexible motion and the Shuttle rigid body motion. The elements of the 7×7 stiffness matrix **K** due to joint stiffnesses λ_b (b = 1, 2, 3) and flexural stiffnesses EI_l (l = 1, 2) are

$$K_{11} = EI_1 \int_0^{L_1} [W_1''(x_1)]^2 \, dx$$
$$K_{22} = EI_2 \int_0^{L_2} [W_2''(x_2)]^2 \, dx + \lambda_2 [W_2'(0)]^2 \quad (7.41)$$
$$K_{33} = \lambda_3$$
$$K_{nm} = 0 \quad \text{else}$$

Since no joint torque backcoupling exists the generalised force vector **P** is now

$$\mathbf{P} = \{T_1\, W_1'(0), 0, 0, T_1, 0, 0, T_1\}^T \quad (7.42)$$

We use the standard data sets (B) and (C) for the fixed and free base case, and choose the torque T_1 to be a step function input with 1298 Nm as shown in figure 7.11.

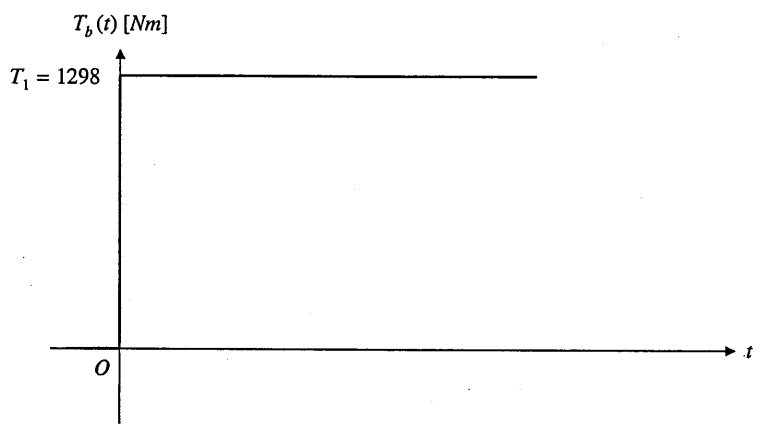

Figure 7.11: Time history of of T_1

Free base results

The fundamental frequency calculated with equation (2.50) for $\theta_1 = 0°$ is $\omega_{Lag} = 0.84$ rad/s, which is in exact agreement with the free base determinant result. Figure 7.12 shows the vibration y_G of G relative to the Shuttle. The system mode shape is shown in figure 6.2.

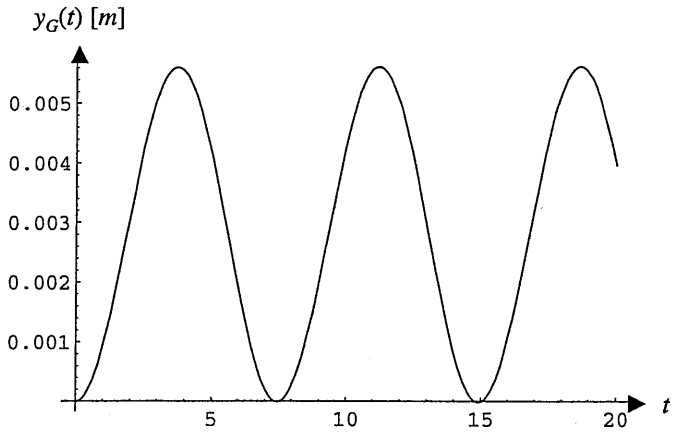

Figure 7.12: Time history of y_G

From figure 7.12 the amplitude of vibration of y_G is 2.8 mm. The corresponding SIMPACK result is 1.8 mm.

Fixed base results

To obtain the equations of motion for the fixed base, the fifth, sixth and seventh row and column in the system matrices **M** and **K**, equations (7.45) and (7.46) are deleted with the fifth, sixth and seventh element of the force vector **P**, equation (7.47). The generalised coordinates of the Shuttle, q_5, q_6 and q_7, are set to zero, together with their time derivatives.
The fundamental frequency for the fixed base using (2.50) for $\theta_1 = 0°$ is $\omega_{Lag} = 0.84$ rad/s and thus in very close agreement with the exact frequency from the fixed base determinant, which is $\omega_{det} = 0.83$ rad/s. Figure 7.13 shows the time history of the vibration y_G of G.

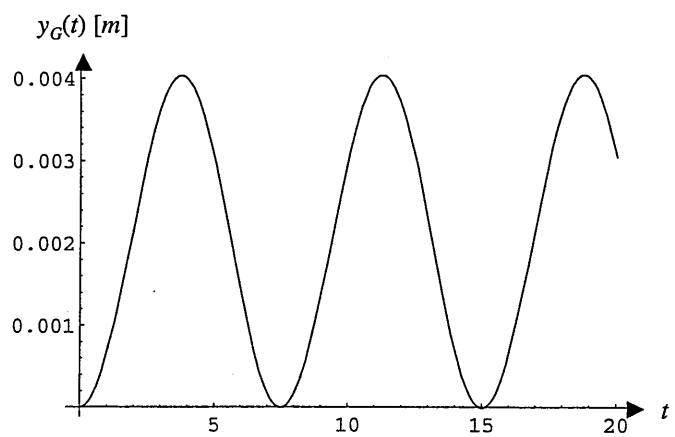

Figure 7.13: Time history of y_G

From figure 7.13 the amplitude of vibration y_G of G relative to the base is 2.0 mm. For the present case the corresponding SIMPACK result is 1.8 mm and thus in very good agreement. The system mode shape for the present case is shown in figure 5.3.

7.2.4 SLEW ABOUT JOINT2

Next we consider a slew about Joint2 for the straight RMS perpendicular to the Shuttle longitudinal axis with Joint1 and Joint3 locked. The situation is similar to that shown in figure 7.9, but now Joint1 is locked in the direction of the Shuttle z axis z_S. $\theta_2 = p_4$ is measured against the extension of Link1 at its tip. The generalised coordinates are q_1 and q_2 for the elastic deflection of Link1 and Link2, p_3 and p_4 for the rigid body deflection of Link3 and Link2, and p_5, p_6, p_7 for Shuttle rigid body motion in y, z and about x (= α_S), or $\mathbf{p}(t) = [q_1(t), q_2(t), p_3(t), p_4(t), p_5(t), p_6(t), p_7(t)]^T$. Using the usual notation, the various velocities relative to the Shuttle are

$$v_1 = \dot{q}_1 W_1(L_1) \tag{7.43}$$

$$v_{21} = \dot{q}_2 W_2(L_2) + \dot{p}_4 L_2 + \dot{q}_1 W_1'(L_1) L_2 \tag{7.44}$$

$$v_{32} = \dot{p}_3 (L_3 + a) + [\dot{q}_2 W_2'(L_2) + \dot{p}_4 + \dot{q}_1 W_1'(L_1)](L_3 + a) \tag{7.45}$$

where $\dot{p}_4 L_2$ allows for the rigid body rotation at Joint2. The payload angular velocity relative to the Shuttle is

$$\omega_G = \dot{q}_1 W_1'(L_1) + \dot{q}_2 W_2'(L_2) + \dot{p}_3 + \dot{p}_4 \tag{7.46}$$

Taking the Shuttle motion into account, the total kinetic energy expression is

$$\begin{aligned}
T = {} & \tfrac{1}{2} M_p [\dot{p}_5 - \dot{p}_7 \Delta y \sin p_7 - (\dot{p}_7 L_1 + v_1)\cos p_7 - \\
& (v_{21} + v_{32} + \dot{p}_7 [L_2 + L_3 + a])\cos(p_4 + p_7)]^2 + \\
& \tfrac{1}{2} M_p [\dot{p}_6 + \dot{p}_7 \Delta y \cos p_7 - (\dot{p}_7 L_1 + v_1)\sin p_7 - \\
& (v_{21} + v_{32} + \dot{p}_7 [L_2 + L_3 + a])\sin(p_4 + p_7)]^2 + \\
& \tfrac{1}{2} M_2 [\dot{p}_5 - \dot{p}_7 \Delta y \sin p_7 - (\dot{p}_7 L_1 + v_1)\cos p_7 - \\
& (v_{21} + \dot{p}_7 L_2)\cos(p_4 + p_7)]^2 + \\
& \tfrac{1}{2} M_2 [\dot{p}_6 + \dot{p}_7 \Delta y \cos p_7 - (\dot{p}_7 L_1 + v_1)\sin p_7 - \\
& (v_{21} + \dot{p}_7 L_2)\sin(p_4 + p_7)]^2 + \\
& \tfrac{1}{2} M_1 [\dot{p}_5 - \dot{p}_7 \Delta y \sin p_7 - (\dot{p}_7 L_1 + v_1)\cos p_7]^2 + \\
& \tfrac{1}{2} M_1 [\dot{p}_6 + \dot{p}_7 \Delta y \cos p_7 - (\dot{p}_7 L_1 + v_1)\sin p_7]^2 + \\
& \tfrac{1}{2} M_S [\dot{p}_5^2 + \dot{p}_6^2] + \tfrac{1}{2} I_p (\omega_G + \dot{p}_7)^2 + \tfrac{1}{2} I_S \dot{p}_7^2 + \tfrac{1}{2} I_{g2} [\dot{q}_2 W_2'(0) + \dot{p}_4]^2
\end{aligned} \tag{7.47}$$

In the present case the equations of motion yield a 7×7 mass matrix $\mathbf{M}$ with elements M_{nm} given by

$$\begin{aligned}
M_{11} = {} & (M_1 + M_2 + M_p)[W_1(L_1)]^2 + 2[L_2(M_2 + M_p) + \\
& (L_3 + a) M_p]\cos\theta_2 W_1(L_1) W_1'(L_1) + [W_1'(L_1)]^2 [I_p + L_2^2 M_p + \\
& (L_2 + L_3 + a)^2 M_p]
\end{aligned} \tag{7.48}$$

$$
\begin{aligned}
M_{12} = M_{21} &= \cos\theta_2\, W_1(L_1)\left[W_2(L_2)(M_2+M_p)+W_2'(L_2)M_p(L_3+a)\right]+\\
&\quad W_1'(L_1)\left[L_2 M_2+(L_2+L_3+a)M_p\right]W_2(L_2)+\\
&\quad W_1'(L_1)\left[I_p+(L_3+a)(L_2+L_3+a)M_p\right]W_2'(L_2)\\
M_{13} = M_{31} &= \cos\theta_2\, W_1(L_1)M_p(L_3+a)+\left[I_p+(L_3+a)(L_2+L_3+a)M_p\right]W_1'(L_1)\\
M_{14} = M_{41} &= W_1(L_1)\cos\theta_2\left[L_2(M_2+M_p)+M_p(L_3+a)\right]+\\
&\quad W_1'(L_1)\left[I_p+L_2^2(M_2+M_p)+a^2 M_p+2aL_3M_p+L_3^2M_p+\right.\\
&\quad \left.2L_2M_p(L_3+a)\right]\\
M_{15} = M_{51} &= -\cos\alpha_S\, W_1(L_1)(M_1+M_2+M_p)-\\
&\quad \cos(\theta_2+\alpha_S)W_1'(L_1)\left[(L_3+a)M_p+(M_2+M_p)L_2\right]\\
M_{16} = M_{61} &= -\sin\alpha_S\, W_1(L_1)(M_1+M_2+M_p)-\\
&\quad \sin(\theta_2+\alpha_S)W_1'(L_1)\left[(L_3+a)M_p+(M_2+M_p)L_2\right]\\
M_{17} = M_{71} &= W_1(L_1)\left[L_1(M_1+M_2+M_p)+\left[M_p(L_2+L_3+a)+L_2M_2\right]\cos\theta_2\right]+\\
&\quad W_1'(L_1)\left[I_p+L_2^2M_2+M_p(L_2+L_3+a)^2-\Delta y\sin\theta_2\left[M_p(L_2+L_3+a)+\right.\right.\\
&\quad \left.\left.L_2M_2\right]+L_1\left[M_p(L_2+L_3+a)+L_2M_2\right]\cos\theta_2\right]\\
M_{22} = &\quad (M_2+M_p)[W_2(L_2)]^2+[W_2'(L_2)]^2\left[I_p+(L_3+a)^2M_p\right]+\\
&\quad W_2(L_2)W_2'(L_2)(L_3+a)2M_p+I_{g2}[W_2'(0)]^2\\
M_{23} = M_{32} &= W_2(L_2)M_p(L_3+a)+W_2'(L_2)\left[I_p+(L_3+a)^2M_p\right]\\
M_{24} = M_{42} &= W_2(L_2)\left[M_p(L_3+a)+L_2(M_2+M_p)\right]+\\
&\quad W_2'(L_2)\left[I_p+(L_3+a)(L_2+L_3+a)M_p\right]+I_{g2}W_2'(0)\\
M_{25} = M_{52} &= -\cos(\theta_2+\alpha_S)\left[W_2(L_2)(M_2+M_p)+W_2'(L_2)(L_3+a)M_p\right] \qquad (7.48)\\
M_{26} = M_{62} &= -\sin(\theta_2+\alpha_S)\left[W_2(L_2)(M_2+M_p)+W_2'(L_2)(L_3+a)M_p\right]\\
M_{27} = M_{72} &= W_2(L_2)\left[M_p(L_2+L_3+a)+L_2M_2+L_1(M_2+M_p)\cos\theta_2-\right.\\
&\quad \left.\Delta y\sin\theta_2(M_2+M_p)\right]+W_2'(L_2)\left[I_p+M_p(L_3+a)^2+\right.\\
&\quad \left.M_p(L_3+a)(\cos\theta_2 L_1+L_2)-\Delta y\sin\theta_2 M_p(L_3+a)\right]\\
M_{33} = &\quad I_p+M_p(L_3+a)^2\\
M_{34} = M_{43} &= I_p+M_p\left[(L_3+a)^2+(L_3+a)L_2\right]\\
M_{35} = M_{53} &= -\cos(\theta_2+\alpha_S)M_p(L_3+a)\\
M_{36} = M_{63} &= -\sin(\theta_2+\alpha_S)M_p(L_3+a)\\
M_{37} = M_{73} &= I_p+M_p\left[(L_3+a)^2+(L_3+a)(\cos\theta_2 L_1+L_2)\right]-\sin\theta_2\,\Delta y\,M_p(L_3+a)\\
M_{44} = &\quad I_{g2}+I_p+M_2L_2^2+(L_2+L_3+a)^2M_p\\
M_{45} = M_{54} &= -\cos(\theta_2+\alpha_S)\left[L_2M_2+(L_2+L_3+a)M_p\right]\\
M_{46} = M_{64} &= -\sin(\theta_2+\alpha_S)\left[L_2M_2+(L_2+L_3+a)M_p\right]
\end{aligned}
$$

$$
\begin{aligned}
M_{47} = M_{74} &= I_p + L_2^2 M_2 + (L_2 + L_3 + a)^2 M_p + \\
&\quad [L_2 M_2 + (L_2 + L_3 + a) M_p](\cos\theta_2 L_1 - \sin\theta_2 \Delta y) \\
M_{55} &= M_1 + M_2 + M_p + M_S \\
M_{56} = M_{65} &= 0 \\
M_{57} = M_{75} &= (M_1 + M_2 + M_p)(-\cos\alpha_S L_1 - \sin\alpha_S \Delta y) - \\
&\quad [L_2 M_2 + (L_2 + L_3 + a) M_p]\cos(\theta_2 + \alpha_S) \\
M_{66} &= M_1 + M_2 + M_p + M_S \\
M_{67} = M_{76} &= (M_1 + M_2 + M_p)(\cos\alpha_S \Delta y - \sin\alpha_S L_1) - \\
&\quad [L_2 M_2 + (L_2 + L_3 + a) M_p]\sin(\theta_2 + \alpha_S) \\
M_{77} &= I_p + I_S + (M_1 + M_2 + M_p)(\Delta y^2 + L_1^2) + L_2^2 M_2 + (L_2 + L_3 + a)^2 M_p + \\
&\quad 2[L_2 M_2 + (L_2 + L_3 + a) M_p](\cos\theta_2 L_1 - \sin\theta_2 \Delta y)
\end{aligned}
\tag{7.48}
$$

The elements K_{nm} of the 7×7 stiffness matrix **K** are

$$
\begin{aligned}
K_{11} &= EI_1 \int_0^{L_1} [W_1''(x_1)]^2 \, dx + \lambda_1 [W_1'(0)]^2 \\
K_{22} &= EI_2 \int_0^{L_2} [W_2''(x_2)]^2 \, dx \\
K_{33} &= \lambda_3 \\
K_{nm} &= 0 \quad \text{else}
\end{aligned}
\tag{7.49}
$$

and the 7×1 generalised force vector **P** is

$$
\mathbf{P} = \{T_2 W_1'(L_1), T_2 W_2'(0), 0, T_2, 0, 0, T_2\}^{\mathrm{T}} \tag{7.50}
$$

The usual data sets (B) and (C) are applied. T_2 is chosen to be 888 Nm according to figure 7.14.

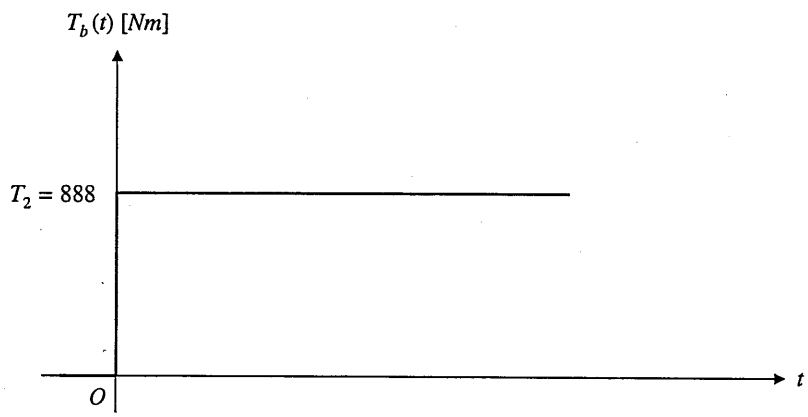

Figure 7.14: Time history of T_2

Free base results

The first non-zero natural frequency calculated with equation (2.50) is ω_{Lag} = 1.06 rad/s, which is in very close agreement with the exact fundamental frequency for the actual system ω_{det} = 1.05 rad/s. Figure 7.15 shows the time history of the vibration y_G of G. The corresponding system mode shape is shown in figure 6.3.

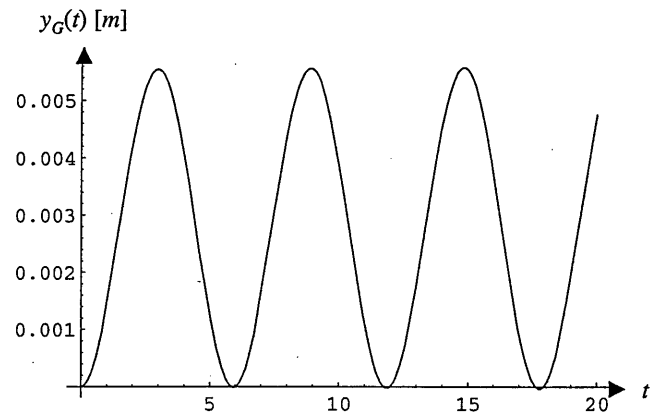

Figure 7.15: Time history of y_G

In figure 7.15 the amplitude of the vibration y_G is 2.8 mm. The SIMPACK result for this case is 1.1 mm.

Fixed base results

As before, the equations of motion for a fixed RMS base are obtained from the free base equations by cancelling the Shuttle degrees of freedom in the system matrices and vectors and by setting them to zero if they appear in the remaining terms.
For the fixed base, the fundamental frequency computed with equation (2.50) is also in perfect agreement with the analytical value, ω_{Lag} = 1.02 rad/s. For this case figure 7.16 shows the time history of y_G. Figure 5.4 shows the actual system mode shape.

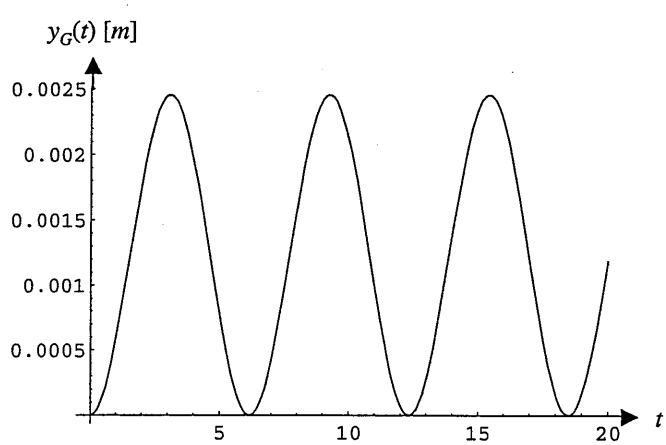

Figure 7.16: Time history of y_G

In figure 7.16 the amplitude of vibration of y_G is 1.2 mm and thus in perfect agreement with the corresponding SIMPACK result.

7.2.5 SLEW ABOUT JOINT3

As the last example of open-loop RMS slew manoeuvres we consider an articulation of the rigid end effector about Joint3 with Joint1 and Joint2 locked. Again the RMS is straight and perpendicular to the Shuttle longitudinal axis, and $\theta_3 = p_3$ is measured relative to the extension of Link2 at its tip. The generalised coordinates are q_1 and q_2 for the elastic deflections of Link1 and Link2, p_3 for the rigid body motion of Link3, and p_4, p_5, p_6 for the Shuttle rigid body motions in y, z and about x (= α_S), and thus the vector of generalised coordinates is $\mathbf{p}(t) = [q_1(t), q_2(t), p_3(t), p_4(t), p_5(t), p_6(t)]^T$. Using the usual notations, the velocities v_1, v_{21} and v_{32} relative to the Shuttle are

$$v_1 = \dot{q}_1 W_1(L_1) \tag{7.51}$$

$$v_{21} = \dot{q}_2 W_2(L_2) + \dot{q}_1 W_1'(L_1) L_2 \tag{7.52}$$

$$v_{32} = [\dot{p}_3 + \dot{q}_1 W_1'(L_1) + \dot{q}_2 W_2'(L_2)](L_3 + a) \tag{7.53}$$

and the payload angular velocity relative to the Shuttle is

$$\omega_G = \dot{q}_1 W_1'(L_1) + \dot{q}_2 W_2'(L_2) + \dot{p}_3 \tag{7.54}$$

With the Shuttle motions, the total kinetic energy is

$$\begin{aligned} T = {} & \tfrac{1}{2} M_p [\dot{p}_4 - \dot{p}_6 \Delta y \sin p_6 - (\dot{p}_6 (L_1 + L_2) + v_1 + v_{21}) \cos p_6 - \\ & [v_{32} + \dot{p}_6 (L_3 + a)] \cos (p_3 + p_6)]^2 + \\ & \tfrac{1}{2} M_p [\dot{p}_5 + \dot{p}_6 \Delta y \cos p_6 - (\dot{p}_6 (L_1 + L_2) + v_1 + v_{21}) \sin p_6 - \\ & [v_{32} + \dot{p}_6 (L_3 + a)] \sin (p_3 + p_6)]^2 + \\ & \tfrac{1}{2} M_2 [\dot{p}_4 - \dot{p}_6 \Delta y \sin p_6 - (\dot{p}_6 (L_1 + L_2) + v_1 + v_{21}) \cos p_6]^2 + \\ & \tfrac{1}{2} M_2 [\dot{p}_5 + \dot{p}_6 \Delta y \cos p_6 - (\dot{p}_6 (L_1 + L_2) + v_1 + v_{21}) \sin p_6]^2 + \\ & \tfrac{1}{2} M_1 [\dot{p}_4 - \dot{p}_6 \Delta y \sin p_6 - (\dot{p}_6 L_1 + v_1) \cos p_6]^2 + \\ & \tfrac{1}{2} M_1 [\dot{p}_5 + \dot{p}_6 \Delta y \cos p_6 - (\dot{p}_6 L_1 + v_1) \sin p_6]^2 + \\ & \tfrac{1}{2} M_S [\dot{p}_4^2 + \dot{p}_5^2] + \tfrac{1}{2} I_p (\omega_G + \dot{p}_6)^2 + \tfrac{1}{2} I_S \dot{p}_6^2 \end{aligned} \tag{7.55}$$

In the present case this yields a 6×6 mass matrix $\mathbf{M}$ with elements M_{nm}

$$\begin{aligned} M_{11} = {} & [W_1(L_1)]^2 M_1 + [W_1'(L_1)]^2 I_p + M_2 [W_1(L_1) + W_1'(L_1) L_2] + \\ & M_p [\cos \alpha_S W_1(L_1) + [\cos \alpha_S L_2 + (L_3 + a) \cos (\alpha_S + \theta_2)] W_1'(L_1)]^2 + \\ & M_p [\sin \alpha_S W_1(L_1) + [\sin \alpha_S L_2 + (L_3 + a) \sin (\alpha_S + \theta_2)] W_1'(L_1)]^2 \end{aligned} \tag{7.56}$$

$$
\begin{aligned}
M_{12} = M_{21} &= W_1(L_1)\left[W_2(L_2)(M_2+M_p)+W_2'(L_2)M_p(L_3+a)\cos\theta_3\right]+\\
&\quad W_1'(L_1)\left[L_2(M_2+M_p)+(L_3+a)M_p\cos\theta_3\right]W_2(L_2)+\\
&\quad W_1'(L_1)\left[I_p+(L_3+a)^2M_p+L_2(L_3+a)M_p\cos\theta_3\right]W_2'(L_2)\\
M_{13} = M_{31} &= \cos\theta_3\,W_1(L_1)M_p(L_3+a)+I_p+W_1'(L_1)(L_3+a)^2M_p+\\
&\quad W_1'(L_1)L_2(L_3+a)M_p\cos\theta_3\\
M_{14} = M_{41} &= -\cos\alpha_S\,W_1(L_1)(M_1+M_2+M_p)-W_1'(L_1)(M_2+M_p)L_2\cos\alpha_S-\\
&\quad W_1'(L_1)(L_3+a)M_p\cos(\theta_3+\alpha_S)\\
M_{15} = M_{51} &= -\sin\alpha_S\,W_1(L_1)(M_1+M_2+M_p)-W_1'(L_1)(M_2+M_p)L_2\sin\alpha_S-\\
&\quad W_1'(L_1)(L_3+a)M_p\sin(\theta_3+\alpha_S)\\
M_{16} = M_{61} &= W_1(L_1)\left[L_1(M_1+M_2+M_p)+L_2(M_2+M_p)+M_p(L_3+a)\cos\theta_3\right]+\\
&\quad W_1'(L_1)\left[I_p+M_p(L_3+a)^2+L_2(M_2+M_p)(L_1+L_2)\right]+\\
&\quad W_1'(L_1)\left[M_p(L_3+a)(L_1+2L_2)\cos\theta_3-\Delta y\sin\theta_3\,M_p(L_3+a)\right]\\
M_{22} = &\quad (M_2+M_p)[W_2(L_2)]^2+[W_2'(L_2)]^2\left[I_p+(L_3+a)^2M_p\right]+\\
&\quad W_2(L_2)W_2'(L_2)(L_3+a)2M_p\cos\theta_3\\
M_{23} = M_{32} &= W_2(L_2)M_p(L_3+a)\cos\theta_3+W_2'(L_2)\left[I_p+(L_3+a)^2M_p\right]\\
M_{24} = M_{42} &= -W_2(L_2)(M_2+M_p)\cos\alpha_S-W_2'(L_2)(L_3+a)M_p\cos(\theta_3+\alpha_S)\\
M_{25} = M_{52} &= -W_2(L_2)(M_2+M_p)\sin\alpha_S-W_2'(L_2)(L_3+a)M_p\sin(\theta_3+\alpha_S)\\
M_{26} = M_{62} &= W_2(L_2)\left[(M_2+M_p)(L_1+L_2)+M_p(L_3+a)\cos\theta_3\right]+\\
&\quad W_2'(L_2)\left[I_p+M_p(L_3+a)^2+M_p(L_3+a)(L_1+L_2)\cos\theta_3\right]-\\
&\quad W_2'(L_2)\Delta y\sin\theta_3\,M_p(L_3+a)
\end{aligned}
\qquad (7.56)
$$

$$
\begin{aligned}
M_{33} = &\quad I_p+M_p(L_3+a)^2\\
M_{34} = M_{43} &= -\cos(\theta_3+\alpha_S)M_p(L_3+a)\\
M_{35} = M_{53} &= -\sin(\theta_2+\alpha_S)M_p(L_3+a)\\
M_{36} = M_{63} &= I_p+M_p(L_3+a)^2+M_p(L_3+a)(L_1+L_2)\cos\theta_3-\sin\theta_3\,\Delta y\,M_p(L_3+a)\\
M_{44} = &\quad M_1+M_2+M_p+M_S\\
M_{45} = M_{54} &= 0\\
M_{46} = M_{64} &= -\cos\alpha_S\left[L_2(M_2+M_p)+L_1(M_1+M_2+M_p)\right]-\\
&\quad (L_3+a)M_p\cos(\theta_3+\alpha_S)-\sin\alpha_S\,\Delta y(M_1+M_2+M_p)\\
M_{55} = &\quad M_1+M_2+M_p+M_S\\
M_{56} = M_{65} &= (M_1+M_2+M_p)\cos\alpha_S\,\Delta y-\sin\alpha_S\left[L_1M_1+(L_1+L_2)(M_2+M_p)\right]-\\
&\quad \sin(\theta_3+\alpha_S)(L_3+a)M_p\\
M_{66} = &\quad I_p+I_S+(M_1+M_2+M_p)(\Delta y^2+L_1^2)+L_2^2(M_2+M_p)+\\
&\quad 2(L_1+L_2)(M_2+M_p)+(L_3+a)M_p\left[(L_3+a)+2(L_1+L_2)\cos\theta_3\right]-\\
&\quad 2\sin\theta_3\,\Delta y(L_3+a)M_p
\end{aligned}
$$

and the 6×6 stiffness matrix **K** with elements K_{nm}

$$K_{11} = EI_1 \int_0^{L_1} [W_1''(x_1)]^2 \, dx + \lambda_1 [W_1'(0)]^2$$

$$K_{22} = EI_2 \int_0^{L_2} [W_2''(x_2)]^2 \, dx + \lambda_2 [W_2'(0)]^2 \qquad (7.57)$$

$$K_{nm} = 0 \quad \text{else}$$

The 6×1 generalised force vector **P** is

$$\mathbf{P} = \{T_3 W_1'(L_1), T_3 W_2'(L_2), T_3, 0, 0, T_3\}^T \qquad (7.58)$$

The system is described with data sets (B) and (C) for the fixed and free RMS base, and the time history of T_3 is shown in figure 7.17.

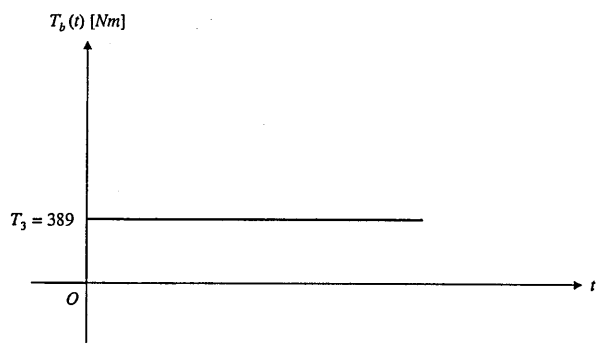

Figure 7.17: Time history of T_3

Free base results

For the free base, the fundamental frequency obtained from equation (2.50) is ω_{Lag} = 0.53 rad/s, which is in close agreement with the exact frequency computed with the free base determinant, ω_{det} = 0.46 rad/s. Figure 7.18 shows the time history of the vibration y_G of G. The corresponding system mode shape is shown in figure 6.4.

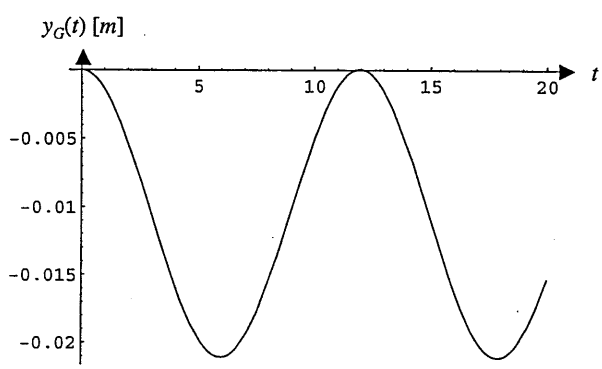

Figure 7.18: Time history of y_G

From figure 7.18 the amplitude of y_G is 10.5 mm. The SIMPACK result for this case is 3.5 mm. This is the only case where the Mathematica and the SIMPACK results are not in close agreement, and the reason for this deviation of the two results could not be established. However, in view of the fact that the difference between the free and the fixed base results for the various simulations are always very small, it is inferred that Mathematica is more accurate than SIMPACK in this case.

Fixed base results

As usual, the equations of motion for the fixed base are obtained by cancelling the Shuttle degrees of freedom in the system matrices and vectors and by setting the Shuttle states to zero in the remaining equations. Applying equation (2.50) yields ω_{Lag} = 0.40 rad/s and is identical with the exact first frequency of the fixed base determinant. The system mode shape is shown in figure 5.5, and figure 7.19 shows the time history of y_G.

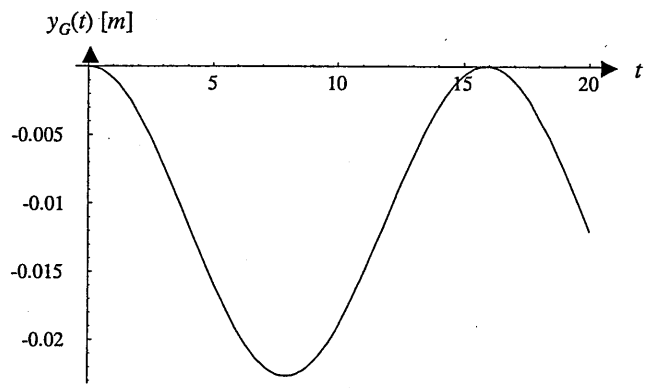

Figure 7.19: Time history of y_G

In figure 7.19 the amplitude of y_G is 11.3 mm in the fundamental mode and is thus in very good agreement with the SIMPACK result of 12.0 mm.

7.3 BUCKLING LOAD ESTIMATION FOR FLEXIBLE LINKS

Finally we consider a payload deployment from the Shuttle. It is assumed that payload deployments are performed with computer calculated RMS motions. We consider the general case of all joints driven and thus unlocked. As was shown before, the elastic deflections are negligibly small for this case, and the RMS can be taken as rigid. However, a typical deployment manoeuvre will load the links not only laterally, but also axially, and the magnitude of these forces should be examined.
Figure 7.20 shows a typical deployment manoeuvre as described in [3] where the T_b (b = 1, 2, 3) are the driving torques at the joints O_b. Although T_3 is necessary to keep the payload upright, it will not be used for the analyses. Note that for simplification, we assume that Link1 has the same length L as Link2, thus $L_1 = L_2 = L$, where L is the average of the lengths of the two links.

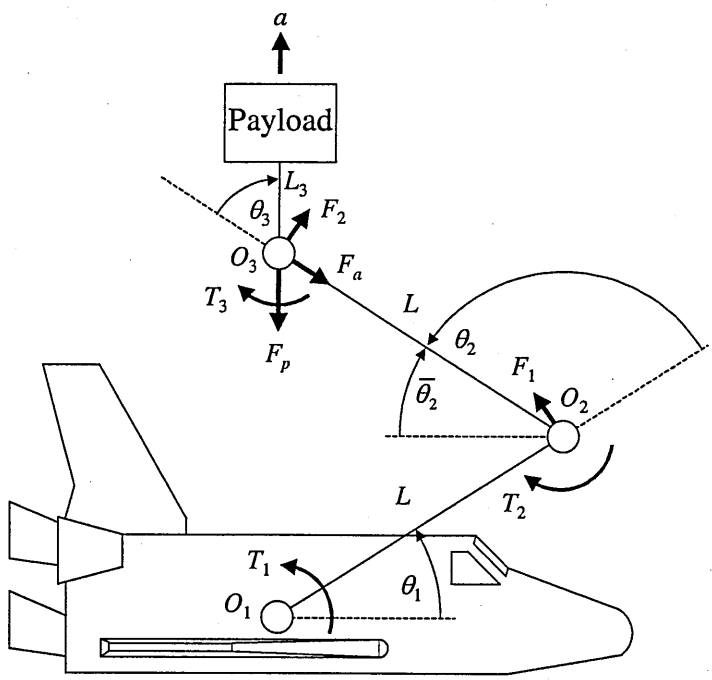

Figure 7.20:Typical payload deployment RMS manoeuvre

Figure 7.20 shows that the acceleration of the payload along a vertical line causes the inertia force F_p. This force produces an axial force F_a in Link1 and Link2. The following calculations give the maximum magnitude of F_a.
The maximum acceleration a depends on the maximum torques T_1 and T_2 at Joint1 and Joint2. The forces F_1 and F_2 at O_2 and O_3 due to the torques at O_1 and O_2 are

$$F_1 = \frac{T_1}{L} \tag{7.59}$$

$$F_2 = \frac{T_2}{L} \tag{7.60}$$

and to produce a vertical acceleration a

$$F_2 \overset{!}{=} F_1 \tag{7.61}$$

and

$$\bar{\theta}_2 \overset{!}{=} \theta_1 \tag{7.62}$$

It is seen that the smaller of the two torques determines the maximum acceleration a. Let the smaller torque be T, thus $T = T_1 = T_2$. Then from figure 7.20 it is seen that

$$F_p = F_1 \cos\theta + F_2 \cos\theta = \frac{2T}{L}\cos\theta \tag{7.63}$$

and the axial force F_a in both links is

$$F_a = F_p \sin\theta = \frac{2T}{L}\cos\theta \sin\theta \tag{7.64}$$

which is maximum for $\theta = \frac{\pi}{4}(1 \pm 2n) \qquad n = 0,1,2,3... \tag{7.65}$

Thus $$F_{a,\max} = \frac{T}{L} \tag{7.66}$$

With the SRMS properties T is the smaller of the two torques T_1 and T_2, thus T = 888 Nm, and the average length of the two SRMS links is L = 6.71 m. Thus equation (7.66) yields $F_{a,\max}$ = 132 N.
To check if this force significantly changes the flexural stiffness of the beams, we consider the partial differential equation of free vibration of a Bernoulli beam with time constant axial force N, which is [41]

$$EI\, y^{iv} + N(x)\, y'' + m\, \ddot{y} = 0 \tag{7.67}$$

In the present case, the boundary conditions of the links are pinned-pinned. The natural frequencies of a pinned-pinned Bernoulli beam without axial forces ($N(x)$ = 0) are

$$\omega_i = \sqrt{\frac{EI\,(i\pi/L)^4}{m}} \tag{7.68}$$

where EI is the flexural stiffness of the link, m its mass per unit length and L its length. The natural frequencies for the case $N(x) > 0$ (compression) and $N(x)$ = const. Are

$$\omega_i = \sqrt{\frac{EI\,(i\pi/L)^4}{m}}\left[1 - \frac{N L^2}{EI\pi^2}\frac{1}{i^2}\right] \tag{7.69}$$

From equations (7.68) and (7.69) it is seen that the compressive axial force N lowers the natural frequencies of the link by the factor f, which is

$$f = \frac{N L^2}{EI\pi^2}\frac{1}{i^2} \tag{7.70}$$

and f is maximum for the first mode with i = 1. Inserting the above data into equation (7.70) and the smaller EI value of the SRMS, $EI_2 = 2.334 \times 10^6$ Nm^2, yields f = 0.026% for the first mode. This shows that the flexural stiffness of the links is practically not affected by the expected axial forces and thus the danger of buckling does not exist.

7.4 RMS TORSION

The effects of RMS longitudinal torsion with an out-of-plane motion of the payload is examined here to get an idea of the magnitude of deflections.
A full analysis of coupled beam bending and torsion is not performed, but a simplified calculation yields the fundamental torsion frequency for the worst case of a straight RMS, holding the maximum payload. This system is modeled by taking the two flexible links of the RMS as two revolute springs with constant spring stiffness as shown in figure 7.21.

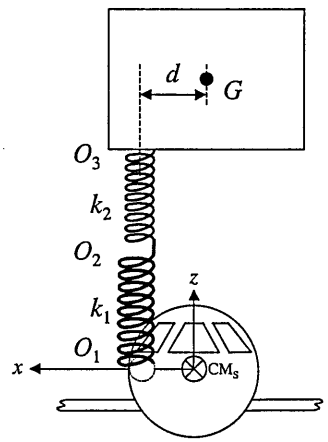

Figure 7.21: Model for RMS torsion analysis

Since the related literature about the SRMS does not report torsional joint stiffness, the whole system consists of only two revolute springs and the payload inertia about the straight RMS axis. The torsional stiffness k_l of link l (l = 1, 2) is given by

$$k_l = \frac{G_l J_l}{L_l} \tag{7.71}$$

where G_l denotes the shear modulus, J_l the area polar moment of inertia and L_l the length of link l. The two torsional stiffnesses of the flexible RMS links are in series, thus the total torsional stiffness K of the RMS with fixed base is

$$K = \frac{k_1 k_2}{k_1 + k_2} \tag{7.72}$$

It is noted that vibrations only occur if the payload centre of mass G does not coincide with the RMS axis. The effective payload inertia I_{eff} about the RMS axis is

$$I_{eff} = I_p + M_p d^2 \tag{7.73}$$

where I_p and M_p are the payload rotatory and translatory inertia and where d is the offset of the RMS axis from G.
The fundamental frequency ω of torsional vibration of the RMS is then

$$\omega = \sqrt{\frac{K}{I_{eff}}} \tag{7.74}$$

According to [2], the torsional stiffnesses GJ_l for the two SRMS links are GJ_1 = 2.067×10^6 Nm^2 and GJ_2 = 1.522×10^6 Nm^2. The lengths of the SRMS links are L_1 = 6.37 m and L_2 = 7.05 m.
For a worst case configuration we assume M_p = 30000 kg, I_p = 400000 kgm^2 and d = 1 m. Inserting these data into equations (9.35) through (9.38) yields ω = 0.55 rad/s.
The angular deflection α of the payload due to a moment M about the RMS axis is

$$\alpha = \frac{M}{K} \tag{7.75}$$

To further develop the worst case scenario we let M = 196.2 Nm. This is the moment that would occur if the Shuttle thrusters are fired perpendicular to the straight RMS, causing an inertia force F_p = 192.6 N at the payload centre of mass G (see equation (7.12)), and if d = 1 m.
Inserting this M into equation (7.75) yields a quasi static angular rotation α = 1.51345×10^{-3} rad. Assuming that the edge of the payload is 5 m offset from the end effector, this yields a maximum out-of plane deflection of the payload of 7.567 mm.
The presented examples are checked using the finite element method programme NASTRAN, and the results for the fundamental frequency and the angular deflection are in perfect agreement with the figures above.
Due to this worst case analyses it is assumed that the torsional RMS vibrations are generally negligibly small. The SRMS related literature does not report analyses of torsional vibrations, and it is therefore inferred that the torsional effects are non-significant, which agrees with the results above.

7.5 SUMMARY

This section shows the results for some representative example simulations of RMS dynamic response analysis for the double flexible link system with end effector. For all configurations the according system mass and stiffness matrices are derived. The simulations are set up by using Lagrange's equation to obtain the equations of motion and by inserting the exact mode shapes for the fundamental frequency for the two flexible links for each configuration and a rigid body mode shape for links connected to an unlocked joint. This is because for the kinematics the tangent frame formulation is used. All simulations are performed using SRMS properties and assuming worst case configurations to give estimates of the maximum elastic deflections of the RMS, and the results are checked against with SIMPACK simulations, using three mode shapes of a cantilever beam for each flexible link.
The results are mostly in very close agreement, and all the simulations confirm that the magnitude of elastic deflections in dynamic response analyses is very small with typical values in the dimension of millimetres or less. The maximum dynamic response with typical values in the dimension of centimetres occurs if the Shuttle

thrusters are fired, assuming that all joints are locked. This is also stated in [5], but without any justification or explanation. Since it is very likely that the Shuttle is able to produce more acceleration along its longitudinal (roll) axis than about it, it is assumed that the introduction of a spatial 3d formulation of the equations of motion does not yield dynamic responses bigger than those presented here. If one or more joints are unlocked the elastic deflections due to torques at the RMS joints are proven to be negligibly small, allowing for the assumption of rigid bodies.
Due to the present results it is therefore assumed that only if all RMS joints are locked and if the Shuttle thrusters are fired, the deflections make an active damping control necessary. For manipulators with properties similar to the SRMS it is inferred that damping control schemes using the joint motors themselves as actuators, as for example proposed in [5], [9] and [69], are superfluous because they can only be applied to unlocked joints, and joint configurations with unlocked joints yield elastic deflections that are much smaller than the positioning accuracy of the SRMS, which is $\pm$ 5.08 cm ([3]). It is believed that the result of the study referred to in [9], stating that the time waiting for SRMS tip motions to damp down to a sensible magnitude are about 10 hours over 15 space station assembly missions, is mainly due to Shuttle thruster firings and not due to SRMS slew manoeuvres. It is noted that even without active damping control, an overall structural damping coefficient of about 1% can be assumed for the SRMS ([1]). Together with the typical natural frequencies this seems to be sufficient to deal with the deflections due to SRMS slew manoeuvres.
This chapter also examines the effects of axial loads during a typical payload deployment manoeuvre on the flexible links. For a worst case scenario the effects are negligibly small, so that axial loads do not have to be taken account of in further simulations.
Finally the effects of RMS torsion are estimated using a simplified model. For a worst case scenario this model yields torsional deformations of the two flexible links that are negligibly small, thus confirming that RMS torsion does not have to be taken into account with complex coupled beam bending and torsion equations when setting up flexible RMS models.

CHAPTER 8: RIGID BODY RMS CONTROL

This section develops the equations of motion of the triple articulated rigid body RMS with free and fixed base and possible control algorithms. Although motion control of the RMS is not a main purpose of this thesis, a control scheme using Lyapunov stability theory will be developed. The proposed control schemes compute the forces necessary to produce a desired RMS motion, and if the resulting elastic deflections are desired, the computed control forces can be re-inserted into equations of motion that account for the link flexibility, given in the previous chapter. However, the elastic deflections due to RMS slew manoeuvres were shown to be very small.

8.1 EQUATIONS OF MOTION

In this sections we only consider the general case of a slew manoeuvre with all three links driven. For other joint configurations the equations of motion are given in the previous chapter. To derive the Shuttle / rigid RMS equations of motion using Lagrange's equation, we consider figure 8.1, where apart from the usual notations of chapter 7, F_{Sy}, F_{Sz} and T_S are the Shuttle control forces and torques (M_1 and M_2 are the substitute point masses for the distributed beam masses m_{b1} and m_{b2} from chapter 7).

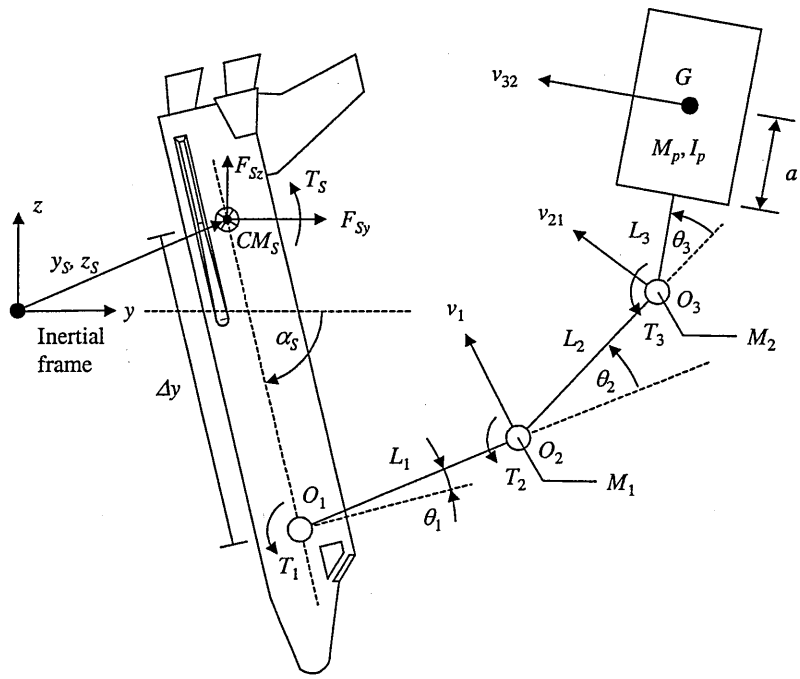

Figure 8.1: Shuttle / rigid RMS velocity components

Again using the notation of chapter 7 for the generalised coordinates, they are $\theta_1 = p_1$, $\theta_2 = p_2$ and $\theta_3 = p_3$ for the rigid body rotations of Link1 , Link2 and Link3, and p_4, p_5 and p_6 for Shuttle linear motion in y, z and rotation about x (= α_S). Thus the generalised coordinates vector is $\mathbf{p}(t) = [p_1(t), p_2(t), p_3(t), p_4(t), p_5(t), p_6(t)]^T$. Note that since the RMS is rigid here, no gear box effects arise and thus $I_{gb} = 0$ ($b = 1, 2, 3$). With figure 8.1, the usual velocities v_1, v_{21} and v_{32} relative to the Shuttle are

$$v_1 = \dot{p}_1 L_1 \tag{8.1}$$

$$v_{21} = (\dot{p}_2 + \dot{p}_1) L_2 \tag{8.2}$$

$$v_{32} = (\dot{p}_3 + \dot{p}_2 + \dot{p}_1)(L_3 + a) \tag{8.3}$$

where the velocity of G relative to the Shuttle is $v_G = v_1 + v_{21} + v_{32}$.
The shuttle velocity components are

$$v_{Sy} = \dot{p}_4, \; v_{Sz} = \dot{p}_5, \; \omega_S = \dot{p}_6 \tag{8.4}$$

The payload angular velocity ω_G relative to the Shuttle is

$$\omega_G = \dot{p}_1 + \dot{p}_2 + \dot{p}_3 \tag{8.5}$$

With the Shuttle rigid body motions the system kinetic energy in y and z components of the inertia frame is

$$\begin{aligned}
T = {} & \tfrac{1}{2} M_p [\dot{p}_4 - \dot{p}_6 \Delta y \sin p_6 - (v_1 + \dot{p}_6 L_1)\cos(p_1 + p_6) - \\
& (v_{21} + \dot{p}_6 L_2)\cos(p_1 + p_2 + p_6) - \\
& (v_{32} + p_6(L_3 + a))\cos(p_1 + p_2 + p_3 + p_6)]^2 + \\
& \tfrac{1}{2} M_p [\dot{p}_5 + \dot{p}_6 \Delta y \cos p_6 - (v_1 + \dot{p}_6 L_1)\sin(p_1 + p_6) - \\
& (v_{21} + \dot{p}_6 L_2)\sin(p_1 + p_2 + p_6) - \\
& (v_{32} + p_6(L_3 + a))\sin(p_1 + p_2 + p_3 + p_6)]^2 + \\
& \tfrac{1}{2} M_2 [\dot{p}_4 - \dot{p}_6 \Delta y \sin p_6 - (v_1 + \dot{p}_6 L_1)\cos(p_1 + p_6) - \\
& (v_{21} + \dot{p}_6 L_2)\cos(p_1 + p_2 + p_6)]^2 + \\
& \tfrac{1}{2} M_2 [\dot{p}_5 + \dot{p}_6 \Delta y \cos p_6 - (v_1 + \dot{p}_6 L_1)\sin(p_1 + p_6)\dot{p}_1 - \\
& (v_{21} + \dot{p}_6 L_2)\sin(p_1 + p_2 + p_6)]^2 + \\
& \tfrac{1}{2} M_1 [\dot{p}_4 - \dot{p}_6 \Delta y \sin p_6 - (v_1 + \dot{p}_6 L_1)\cos(p_1 + p_6)]^2 + \\
& \tfrac{1}{2} M_1 [\dot{p}_5 + \dot{p}_6 \Delta y \cos p_6 - (v_1 + \dot{p}_6 L_1)\sin(p_1 + p_6)]^2 + \\
& \tfrac{1}{2} M_S [\dot{p}_4^2 + \dot{p}_5^2] + \tfrac{1}{2} I_p [\omega_G + \dot{p}_6]^2 + \tfrac{1}{2} I_S \dot{p}_6^2
\end{aligned} \tag{8.6}$$

Neglecting Coriolis and centrifugal effects as usually, the application of Lagrange's equation (2.48) to $\mathbf{p}(t) = [p_1(t), p_2(t), p_3(t), p_4(t), p_5(t), p_6(t)]^T$ in equation (8.6) yields a 6×6 symmetric mass matrix $\mathbf{M}$ with elements M_{nm} given by

$$\begin{aligned}
M_{11} = {} & M_p \left[L_1^2 + L_2^2 + (L_3 + a)^2\right] + L_1^2 (M_1 + M_2) + L_2^2 M_2 + \\
& 2 L_1 L_2 (M_2 + M_p)\cos\theta_2 + 2 L_2 (L_3 + a) M_p \cos\theta_3 + \\
& 2(L_3 + a) L_1 M_p \cos(\theta_2 + \theta_3)
\end{aligned} \tag{8.7}$$

$$
\begin{aligned}
M_{12} = M_{21} &= M_p\left[L_2^2 + (L_3 + a)^2\right] + L_2^2 M_2 + L_1 L_2 (M_2 + M_p)\cos\theta_2 + \\
&\quad 2L_2 (L_3 + a) M_p \cos\theta_3 + (L_3 + a) L_1 M_p \cos(\theta_2 + \theta_3) \\
M_{13} = M_{31} &= M_p (L_3 + a)^2 + L_2 (L_3 + a) M_p \cos\theta_3 + L_1 (L_3 + a) M_p \cos(\theta_2 + \theta_3) \\
M_{14} = M_{41} &= -L_1 (M_1 + M_2 + M_p)\cos(\theta_1 + \alpha_S) - L_2 (M_2 + M_p)\cos(\theta_1 + \theta_2 + \alpha_S) - \\
&\quad (L_3 + a) M_p \cos(\theta_1 + \theta_2 + \theta_3 + \alpha_S) \\
M_{15} = M_{51} &= -L_1 (M_1 + M_2 + M_p)\sin(\theta_1 + \alpha_S) - L_2 (M_2 + M_p)\sin(\theta_1 + \theta_2 + \alpha_S) - \\
&\quad (L_3 + a) M_p \sin(\theta_1 + \theta_2 + \theta_3 + \alpha_S) \\
M_{16} = M_{61} &= M_p\left[L_1^2 + L_2^2 + (L_3 + a)^2\right] + L_1^2 (M_1 + M_2) + L_2^2 M_2 + \\
&\quad 2L_1 L_2 (M_2 + M_p)\cos\theta_2 + 2L_2 (L_3 + a) M_p \cos\theta_3 + \\
&\quad 2(L_3 + a) L_1 M_p \cos(\theta_2 + \theta_3) - \Delta y\, L_1 (M_1 + M_2 + M_p)\sin\theta_1 - \\
&\quad \Delta y\, L_2 (M_2 + M_p)\sin(\theta_1 + \theta_2) - \Delta y (L_3 + a) M_p \sin(\theta_1 + \theta_2 + \theta_3) \\
M_{22} &= M_p\left[L_2^2 + (L_3 + a)^2\right] + L_2^2 M_2 + 2L_2 (L_3 + a) M_p \cos\theta_3 \\
M_{23} = M_{32} &= M_p (L_3 + a)^2 + L_2 (L_3 + a) M_p \cos\theta_3 \\
M_{24} = M_{42} &= -L_2 (M_2 + M_p)\cos(\theta_1 + \theta_2 + \alpha_S) - (L_3 + a) M_p \cos(\theta_1 + \theta_2 + \theta_3 + \alpha_S) \\
M_{25} = M_{52} &= -L_2 (M_2 + M_p)\sin(\theta_1 + \theta_2 + \alpha_S) - (L_3 + a) M_p \sin(\theta_1 + \theta_2 + \theta_3 + \alpha_S) \\
M_{26} = M_{62} &= M_p\left[L_2^2 + (L_3 + a)^2\right] + L_2^2 M_2 + L_1 L_2 (M_2 + M_p)\cos\theta_2 + \\
&\quad 2L_2 (L_3 + a) M_p \cos\theta_3 + (L_3 + a) L_1 M_p \cos(\theta_2 + \theta_3) - \\
&\quad \Delta y\, L_2 (M_2 + M_p)\sin(\theta_1 + \theta_2) - \Delta y (L_3 + a) M_p \sin(\theta_1 + \theta_2 + \theta_3) \\
M_{33} &= I_p + (L_3 + a)^2 M_p \qquad (8.7) \\
M_{34} = M_{43} &= -(L_3 + a) M_p \cos(\theta_1 + \theta_2 + \theta_3 + \alpha_S) \\
M_{35} = M_{53} &= -(L_3 + a) M_p \sin(\theta_1 + \theta_2 + \theta_3 + \alpha_S) \\
M_{36} = M_{63} &= I_p + M_p (L_3 + a)^2 + L_2 (L_3 + a) M_p \cos\theta_3 + \\
&\quad (L_3 + a) L_1 M_p \cos(\theta_2 + \theta_3) - \Delta y (L_3 + a) M_p \sin(\theta_1 + \theta_2 + \theta_3) \\
M_{44} &= M_1 + M_2 + M_p + M_S \\
M_{45} = M_{54} &= 0 \\
M_{46} = M_{64} &= -L_1 (M_1 + M_2 + M_p)\cos(\theta_1 + \alpha_S) - L_2 (M_2 + M_p)\cos(\theta_1 + \theta_2 + \alpha_S) - \\
&\quad (L_3 + a) M_p \cos(\theta_1 + \theta_2 + \theta_3 + \alpha_S) - \Delta y (M_1 + M_2 + M_p)\sin\alpha_S \\
M_{55} &= M_1 + M_2 + M_p + M_S \\
M_{56} = M_{65} &= -L_1 (M_1 + M_2 + M_p)\sin(\theta_1 + \alpha_S) - L_2 (M_2 + M_p)\sin(\theta_1 + \theta_2 + \alpha_S) - \\
&\quad (L_3 + a) M_p \sin(\theta_1 + \theta_2 + \theta_3 + \alpha_S) + \Delta y (M_1 + M_2 + M_p)\cos\alpha_S \\
M_{66} &= I_S + (L_1^2 + \Delta y^2)(M_1 + M_2 + M_p) + L_2^2 (M_2 + M_p) + (L_3 + a)^2 M_p + \\
&\quad 2L_1 L_2 (M_2 + M_p)\cos\theta_2 + 2L_2 (L_3 + a) M_p \cos\theta_3 + \\
&\quad 2(L_3 + a) L_1 M_p \cos(\theta_2 + \theta_3) - 2\Delta y\, L_1 (M_1 + M_2 + M_p)\sin\theta_1 - \\
&\quad 2\Delta y\, L_2 (M_2 + M_p)\sin(\theta_1 + \theta_2) - 2\Delta y (L_3 + a) M_p \sin(\theta_1 + \theta_2 + \theta_3)
\end{aligned}
$$

Note that although the Coriolis and centrifugal terms are always neglected in this thesis due to the very small angular velocities involved and due to the analysis in chapter 2.4, the following control methods could also be applied if these effects are taken account of.
Since the system is without potential restrictions ($V = 0$), no stiffness matrix arises and the equations of motion of the triple articulated rigid RMS are thus

$$\mathbf{M(p)}\,\ddot{\mathbf{p}} = \mathbf{P} \tag{8.8}$$

with $\mathbf{P} = [T_1 + T_2 + T_3, T_2 + T_3, T_3, F_{Sy}, F_{Sz}, T_S + T_1 + T_2 + T_3]^T$ since there is no torque backcoupling due the high ratio gear trains.

8.2 INVERSE DYNAMICS METHOD

The control of the RMS system expressed by equation (8.8) is an interesting task since the mass matrix is clearly state-variant due to variation of configuration, or $\mathbf{M} = \mathbf{M(p)}$. Therefore the desired torques to move the RMS from an arbitrary initial to an arbitrary final state are non-symmetric in the general case, which means that the accelerating and the decelerating torque profiles differ.
The first possibility to create the necessary torques for a desired RMS motion is to use the common method of inverse dynamics, which makes use of the fact that the equations of motion are already explicitly solved in equation (8.8). It is now possible to give any desired acceleration profile, and inserting this profile will automatically yield the required torques, or $\mathbf{P} = \mathbf{M}\ddot{\mathbf{p}}$. But although the theory is simple, realisation requires practical considerations.
First it can be seen from the above equation that depending on the inserted $\ddot{\mathbf{p}}$, the generalised forces $\mathbf{P}$ can grow arbitrarily large. But since in reality the maximum torques are restricted, they must be taken account of.
This is essentially a problem of scaling. Restricting the desired accelerations in a proper way will make sure that the real maximum control torques will not be exceeded. In order to do so one has to find the global worst case of desired control torques, which is shown in figure 8.2.

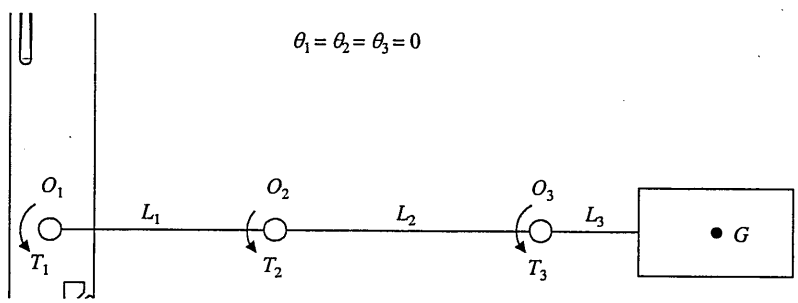

Figure 8.2: Global worst case of desired control torques

From figure 8.2 it is seen that the worst case for the RMS control torques arises when all links are driven or accelerated into the same direction, starting from the straight

position with $\theta_1 = \theta_2 = \theta_3 = 0°$. This is because in that case the reaction forces at the tip of link l (l = 1, 2) due to a torque T_{l+1} are maximum so that the reaction forces drive link l to the opposite of the desired direction. In other words, the off-diagonal coupling elements in the mass matrix **M** are maximum for this situation.
Thus inserting $p_1 = p_2 = p_3 = 0$ (that is $\theta_1 = \theta_2 = \theta_3 = 0°$) and any initial position of the Shuttle p_4, p_5 and p_6 (for simplicity also let $p_4 = p_5 = p_6 = 0$) into **M** will give $\mathbf{M}_0$ for the worst case of RMS control torques. This however does not solve the problem of restricted control torques completely, since we still have to choose the vector $\ddot{\mathbf{p}}$. Note that in the present case we are only concerned with RMS slew manoeuvres and thus want the Shuttle to keep its position in space. Therefore in all the following simulations $\ddot{p}_4 = \ddot{p}_5 = \ddot{p}_6 = 0$.
As was said, once $\ddot{\mathbf{p}}$ is known it can always be scaled to give the **P** smaller than or equal to the maximum joint torques. But the ratios of the elements of $\ddot{\mathbf{p}}$ must be defined beforehand. Since the possibilities are infinite, we let the ratios of the accelerations equal the ratios of the maximum joint velocities. This will lead to the effect that all joints will reach their maximum joint velocity at the same time, if the maximum joint velocities are taken account of. Thus we first calculate some initial values $\mathbf{P}_0$ of the generalised forces **P** by letting

$$\mathbf{P}_0 = \mathbf{M}_0 \ddot{\mathbf{p}}_0 \tag{8.9}$$

where $\ddot{\mathbf{p}}_0 = \frac{1}{s}[\dot{\theta}_{1,\max}, \dot{\theta}_{2,\max}, \dot{\theta}_{3,\max}, 0, 0, 0]^T$. The factor $\frac{1}{s}$ adapts the velocities to the accelerations, and the $\dot{\theta}_{b,\max}$ (b = 1, 2, 3) denote the maximum allowed joint velocities of the RMS.
Now the $\mathbf{P}_0$ must be scaled to fit the maximum allowed torques $T_{b,\max}$ (b = 1, 2 , 3) of the RMS. This is done by multplying $\ddot{\mathbf{p}}_0$ with a scaling factor f, thus $\ddot{\mathbf{p}}_{\max} = \ddot{\mathbf{p}}_0 f$. This scaling factor must be equal to the smallest of the ratios $T_{b,\max} / T_{b,0}$ or

$$f = \min\left(T_{b,\max} / T_{b,0}\right) \qquad (b = 1,2,3) \tag{8.10}$$

where the $T_{b,0}$ are computed from $\mathbf{P}_0$ by recalling the generalised forces vector above, thus $T_{3,0} = P_{3,0}$, $T_{2,0} = P_{2,0} - T_{3,0}$, $T_{1,0} = P_{1,0} - T_{3,0} - T_{2,0}$ and so on.
It is noted that the above procedure has to be performed for every individual payload, but this can be done with a computer yielding the result practically immediately.
The fact that the maximum torques may not be fully utilised in any situations other than the worst case situation shown in figure 8.2 if we insert the global worst case accelerations $\ddot{\mathbf{p}}_{\max}$ obtained with the above method does not significantly lower the performance of the RMS, since the maximum angular velocities are so small that, compared to the time of a typical slew manoeuvre, it makes little difference if the angular velocity is reached some seconds sooner or later.
If the maximum angular accelerations are known, the time history of the accelerations of a desired slew has to be created. The symmetric acceleration/deceleration profile for the rigid link b (b = 1, 2 , 3) is shown in figure 8.3, where $\ddot{\theta}_{b,\max} = \ddot{p}_{b,\max}$ For the present case we only consider bang-bang accelerations.

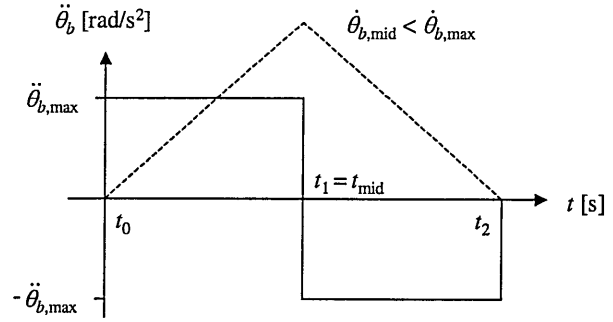

Figure 8.3: First possibility of symmetric acceleration/deceleration profile

There are in principal two possibilities for the acceleration/deceleration profile, if the maximum allowed joint velocities $\dot{\theta}_{b,\max}$ (b = 1, 2, 3) are taken into account. The first possibility is shown in figure 8.3, where $\dot{\theta}_{b,\max}$ is not exceeded if the maximum joint acceleration $\ddot{\theta}_{b,\max} = \ddot{p}_{b,\max}$ as calculated above is applied until $t_1 = t_{\mathrm{mid}}$.
The second possibility is shown in figure 8.4. Here the joint velocity $\dot{\theta}'_{b,\mathrm{mid}}$ would be larger than the allowed maximum joint velocity $\dot{\theta}_{b,\max}$, if $\ddot{\theta}_{b,\max} = \ddot{p}_{b,\max}$ were applied until t_{mid}. Therefore in that case $\ddot{\theta}_{b,\max} = \ddot{p}_{b,\max}$ must be switched off before t_{mid}, as shown in the figure.

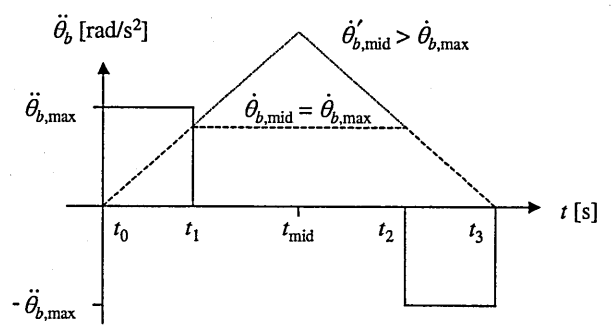

Figure 8.4: Second possibility of symmetric acceleration/deceleration profile

In order to find out which one of the two cases applies, we first check if the maximum angular velocity would be exceeded if the acceleration switching occurs at t_{mid}.
For a constant angular acceleration $\ddot{\theta}_{b,\max}$ of Joint b, the velocity $\dot{\theta}_{b,\mathrm{mid}}$ at t_{mid} is

$$\dot{\theta}_{b,\mathrm{mid}} = \ddot{\theta}_{b,\max}\, t_{\mathrm{mid}} \tag{8.11}$$

where t_{mid} is the time at mid-slew. The angle $\theta_{b,\mathrm{mid}}$ at mid-slew due to the constant acceleration is

$$\theta_{b,\mathrm{mid}} = \tfrac{1}{2}\ddot{\theta}_{b,\max}\, t_{\mathrm{mid}}^2 \tag{8.12}$$

where $\theta_{b,\mathrm{mid}}$ is

$$\theta_{b,\text{mid}} = \tfrac{1}{2}\theta_{b,\text{des}} \tag{8.13}$$

where $\theta_{b,\text{des}}$ is the desired relative angular motion. Solving equations (8.11) and (8.12) for t_{mid} and inserting one equation into the other we can write

$$\frac{\dot{\theta}_{b,\text{mid}}}{\ddot{\theta}_{b,\max}} = \sqrt{\frac{2\theta_{b,\text{mid}}}{\ddot{\theta}_{b,\max}}} = \sqrt{\frac{\theta_{b,\text{des}}}{\ddot{\theta}_{b,\max}}} \tag{8.14}$$

Then the velocity $\dot{\theta}_{b,\text{mid}}$ at mid-slew is

$$\dot{\theta}_{b,\text{mid}} = \sqrt{\theta_{b,\text{des}}\,\ddot{\theta}_{b,\max}} \tag{8.15}$$

If $\dot{\theta}_{b,\text{mid}} < \dot{\theta}_{b,\max}$, see figure 8.3, the acceleration switching times are

$$t_1 = t_{\text{mid}} = \sqrt{\frac{\theta_{b,\text{des}}}{\ddot{\theta}_{b,\max}}} \tag{8.16}$$

and

$$t_2 = 2\sqrt{\frac{\theta_{b,\text{des}}}{\ddot{\theta}_{b,\max}}} = 2t_1 = 2t_{\text{mid}} \tag{8.17}$$

The acceleration/deceleration profile is then given by

$$\ddot{\theta}_b = \ddot{\theta}_{b,\max}\left[\sigma(t) - 2\sigma(t-t_1) + \sigma(t-t_2)\right] \tag{8.18}$$

where σ denotes the unit-step function, see figure 8.3.
If $\dot{\theta}'_{b,\text{mid}} > \dot{\theta}_{b,\max}$, see figure 8.4, the switching times have to be calculated accordingly. Time t_1 is given by

$$t_1 = \frac{\dot{\theta}_{b,\max}}{\ddot{\theta}_{b,\max}} \tag{8.19}$$

The angle $\theta_{b,\text{acc}}$ that the actual robot link rotates through during the acceleration phase between $t = 0$ and t_1 is given by

$$\theta_{b,\text{acc}} = \tfrac{1}{2}\ddot{\theta}_{b,\max}\, t_1^2 \tag{8.20}$$

The angle $\theta_{b,0}$ through which the actual robot link rotates without acceleration, that is the rotation between t_1 and t_2 (see figure 8.4), is

$$\theta_{b,0} = \theta_{b,\text{des}} - 2\theta_{b,\text{acc}} = \theta_{b,\text{des}} - \ddot{\theta}_{b,\max} t_1^2 \tag{8.21}$$

Since we know that the actual robot link rotates through angle $\theta_{b,0}$ with $\dot{\theta}_{b,\max}$, the time $t_{b,0}$ between the accelerating and decelerating phase, that is the time between t_1 and t_2, is

$$t_{b,0} = \frac{\theta_{b,0}}{\dot{\theta}_{b,\max}} \tag{8.22}$$

Then t_2 and t_3 are given by

$$t_2 = t_1 + t_{b,0} \tag{8.23}$$

and

$$t_3 = t_2 + t_1 \tag{8.24}$$

The acceleration profile for Link b is now given by

$$\ddot{\theta}_b = \ddot{\theta}_{b,\max} \left[\sigma(t) - \sigma(t - t_1) - \sigma(t - t_2) + \sigma(t - t_3)\right] \tag{8.25}$$

as shown in figure 8.4.
Performing the previous calculations for each link gives the necessary acceleration profiles. The profiles are now integrated twice to give the time-history of the angles. With the known time-history for every link, the time-history of the mass matrix **M** in equation (8.8) is also known. Using equation (8.8) with the known accelerations and mass matrix yields the time-history of the necessary torques.
To validate the method, the calculated torques can be re-inserted into the original equation (8.8), thus

$$\ddot{\mathbf{p}} = \mathbf{M}^{-1}\,\mathbf{P} \tag{8.26}$$

Solving the differential equations (8.26) must give the same results as the procedure leading to the equation. This was checked for one example RMS slew manoeuvre.

8.3 LYAPUNOV'S DIRECT METHOD

The second control scheme uses Lyapunov stability theory to control the RMS motions. A brief summary of Lyapunov's direct method is given subsequently. More detailed information is given in [61] and [62].
To illustrate the basic idea in Lyapunov's direct method, we first define the term of neighbourhood B_δ. The state vector $\mathbf{x} = [\mathbf{p}, \dot{\mathbf{p}}]^T$ is in the neighbourhood B_δ ($\mathbf{x}_r(t)$) of the reference state $\mathbf{x}_r(t)$ if

$$\left\|\mathbf{x}(t) - \mathbf{x}_r(t)\right\|_2 < \delta \tag{8.27}$$

It is noted that the norm used in equation (8.27) is the Euclidian norm. Therefore a certain neighbourhood can be visualised as a three-dimensional spherical region of

radius δ around the state $\mathbf{x}_r(t)$.
The next step is to formulate a positive (negative) definite function. A function $L(\mathbf{x})$ is said to be locally positive (negative) definite about a reference state $\mathbf{x}_r$ if for

$$\mathbf{x} = \mathbf{x}_r \Rightarrow L(\mathbf{x}) = 0 \tag{8.28}$$

and if there exists a region $\delta > 0$ so that

$$\forall \mathbf{x} \in B_\delta(\mathbf{x}_r) \Rightarrow L(\mathbf{x}) > 0 \quad (L(\mathbf{x}) < 0) \tag{8.29}$$

excluding $\mathbf{x} = \mathbf{x}_r$. If equation (8.28) holds true for any state vector $\mathbf{x}$, that is if $\delta = \infty$, then $L(\mathbf{x})$ is globally positive (negative) definite.
Equations (8.28) and (8.29) guarantee that $L(\mathbf{x})$ has a unique local or global minimum (maximum) at $\mathbf{x}_r$. Since it is known that dynamical systems tend to a state of minimum total energy, the concept becomes clear. In the case of a negative definite function $L(\mathbf{x})$, one simply changes the sign, so that $-L(\mathbf{x})$ is positive definite.
Similarly, positive (negative) semi-definite functions are defined. A function $L(\mathbf{x})$ is said to be locally positive (negative) semi-definite about a reference state $\mathbf{x}_r$ if

$$\mathbf{x} = \mathbf{x}_r \Rightarrow L(\mathbf{x}) = 0 \tag{8.30}$$

and if there exists a $\delta > 0$ so that

$$\forall \mathbf{x} \in B_\delta(\mathbf{x}_r) \Rightarrow L(\mathbf{x}) \geq 0 \quad (L(\mathbf{x}) \leq 0) \tag{8.31}$$

excluding $\mathbf{x} = \mathbf{x}_r$. If equation (8.31) holds true for any state vector $\mathbf{x}$, that is if $\delta = \infty$, then $L(\mathbf{x})$ is globally positive (negative) semi-definite.
We see that a semi-definite function can have extremas other than the desired target state.
Following the concept above, a matrix $\mathbf{A}$ is positive or negative (semi-) definite if for every $\mathbf{x}$ excluding $\mathbf{x} = \mathbf{x}_r$

$$\mathbf{x}^T \mathbf{A} \mathbf{x} = \begin{cases} > 0 \Rightarrow \text{positive definite} \\ \geq 0 \Rightarrow \text{positive semi - definite} \\ < 0 \Rightarrow \text{negative definite} \\ \leq 0 \Rightarrow \text{negative semi - definite} \end{cases} \tag{8.32}$$

To prove a dynamical system to be stable, Lyapunov functions are created.
A function $L(\mathbf{x})$ is a Lyapunov function if it is continuous and there exists a $\delta > 0$ so that for any $\mathbf{x} \in B_\delta(\mathbf{x}_r)$

1. $L(\mathbf{x})$ is a positive definite function
2. $L(\mathbf{x})$ has continuous partial derivatives (8.33)
3. $\dot{L}(\mathbf{x})$ is negative semi-definite

It is noted that although $L(\mathbf{x})$ explicitly only depends on $\mathbf{x}$, the Lyapunov function is time varying since $\mathbf{x}$ is time varying.
Writing the dynamical system in state space form as

$$\dot{\mathbf{x}} = \mathbf{f}(\mathbf{x}) \tag{8.34}$$

the time derivative of $L(\mathbf{x})$ is found to be

$$\dot{L} = \left(\frac{\partial L}{\partial \mathbf{x}}\right)^{\mathrm{T}} \dot{\mathbf{x}} = \left(\frac{\partial L}{\partial \mathbf{x}}\right)^{\mathrm{T}} \mathbf{f}(\mathbf{x}) \tag{8.35}$$

Hence with all the previous definitions we can define Lyapunov stability.

Lyapunov Stability:
If a Lyapunov function $L(\mathbf{x})$ exists for the dynamical system $\dot{\mathbf{x}} = \mathbf{f}(\mathbf{x})$, then this system is stable about the origin.
Note that if this condition is not fulfilled, we cannot conclude that the system is unstable. Another theorem or Lyapunov function may be found to prove stability or instability for this case.

Asymptotic stability:
If $L(\mathbf{x})$ is a Lyapunov function for the dynamical system $\dot{\mathbf{x}} = \mathbf{f}(\mathbf{x})$, then this system is asymptotically stable if

1. *the system is stable*
2. *$\dot{L}(\mathbf{x})$ is negative definite*

Exponential stability:
If $L(\mathbf{x})$ is a Lyapunov function for the dynamical system $\dot{\mathbf{x}} = \mathbf{f}(\mathbf{x})$, and if this system is asymptotically stable, then the system is exponentially stable if there exist scalar constants $c_2 \geq c_1 > 0$ and $\lambda > 0$, $k > 0$ so that

1. $\dot{L} \leq -\lambda L$
2. $c_1 \|\mathbf{x}\|^k \leq L(\mathbf{x}) \leq c_2 \|\mathbf{x}\|^k$

To illustrate the method, we examine the stability of a simple spring-mass system in the sense of Lyapunov as follows,

$$m\ddot{p} + k\,p = 0 \tag{8.36}$$

To obtain a convenient Lyapunov function we take the sum of the system total kinetic

and potential energy about the states $\dot{p}=0$ and $p=0$. Therefore the proposed Lyapunov function is

$$L(\mathbf{x})=L(p,\dot{p})=\tfrac{1}{2}m\dot{p}^2+\tfrac{1}{2}kp^2 \tag{8.37}$$

It is seen that $L(\mathbf{x})=L(p,\dot{p})$ satisfies all three criteria of the definition (8.33). In the present case $\delta=\infty$, so that any stability will be global.
The derivative of L is given by

$$\dot{L}(p,\dot{p})=(m\ddot{p}+kp)\dot{p} \tag{8.38}$$

where the dynamical system can be substituted, so that

$$\dot{L}(p,\dot{p})=0 \tag{8.39}$$

and thus in equation (8.32) the fourth case applies. In the present example $\dot{L}$ is only negative semi-definite, therefore the system is only stable in Lyapunov's sense, but not asymptotically stable. Indeed, we know that the undamped oscillator is stable about its equilibrium state $p=\dot{p}=0$, but will never reach it from a disturbed state.
Applying Lyapunov's direct method to the triple link rigid RMS, we have to define a proper Lyapunov function, which has to take account of both the orientation of the links and their velocities, so that a desired state should be reached and the velocities become zero. Therefore we have to formulate a Lyapunov function in terms of the states $\mathbf{x}$ and $\dot{\mathbf{x}}$. [62] states that Lyapunov functions can be linearly combined, so that it is possible to define a position-based function and a velocity-based one.
Prior to the following analyses it is however noted that for a given dynamical system there may exist an infinite number of possible Lyapunov functions, and finding an optimal Lyapunov control law can be a very challenging task ([62]).
The RMS equations of motion are given in equation (8.8). A possible velocity-based Lyapunov-function for any dynamical system is the total kinetic energy ([62]). Since in the present case the target velocities are zero, we define

$$L(\dot{\mathbf{p}})=\tfrac{1}{2}\dot{\mathbf{p}}^{\mathrm{T}}\mathbf{M}\dot{\mathbf{p}} \tag{8.40}$$

where $\mathbf{M}=\mathbf{M}(\mathbf{p})$. The time derivative of L is

$$\dot{L}=\tfrac{1}{2}\ddot{\mathbf{p}}^{\mathrm{T}}\mathbf{M}\dot{\mathbf{p}}+\tfrac{1}{2}\dot{\mathbf{p}}^{\mathrm{T}}\dot{\mathbf{M}}\dot{\mathbf{p}}+\tfrac{1}{2}\dot{\mathbf{p}}^{\mathrm{T}}\mathbf{M}\ddot{\mathbf{p}} \tag{8.41}$$

Since $\mathbf{M}$ is symmetric, we can write

$$\dot{L}=\dot{\mathbf{p}}^{\mathrm{T}}\mathbf{M}\ddot{\mathbf{p}}+\tfrac{1}{2}\dot{\mathbf{p}}^{\mathrm{T}}\dot{\mathbf{M}}\dot{\mathbf{p}}=\dot{\mathbf{p}}^{\mathrm{T}}\left(\mathbf{M}\ddot{\mathbf{p}}+\tfrac{1}{2}\dot{\mathbf{M}}\dot{\mathbf{p}}\right) \tag{8.42}$$

Substituting the equations of motion (8.8), equation (8.42) yields

$$\dot{L} = \dot{\mathbf{p}}^{\mathrm{T}} \left(\mathbf{P} + \tfrac{1}{2} \dot{\mathbf{M}}\, \dot{\mathbf{p}} \right) \tag{8.43}$$

We use the identity ([62])

$$\dot{\mathbf{p}}^{\mathrm{T}}\, \dot{\mathbf{M}}\, \dot{\mathbf{p}} = \sum_{j=1}^{J} \dot{p}_j \left(\dot{\mathbf{p}}^{\mathrm{T}}\, \mathbf{M}_{p_j}\, \dot{\mathbf{p}} \right) = \dot{\mathbf{p}}^{\mathrm{T}} \left(\dot{\mathbf{p}}^{\mathrm{T}}\, \mathbf{M}_{p}\, \dot{\mathbf{p}} \right) \tag{8.44}$$

where $\mathbf{M}_{p_j}$ and $\mathbf{M}_{p}$ denote the partial derivatives of $\mathbf{M}$ with respect to p_j and $\mathbf{p}$. Since Coriolis and centrifugal effects are neglected, equation (8.44) is zero in the present case. Thus equation (8.43) simplifies to

$$\dot{L} = \dot{\mathbf{p}}^{\mathrm{T}}\, \mathbf{P} \tag{8.45}$$

To guarantee that $\dot{L}$ is negative definite, we define the control torque

$$\mathbf{P} = -c\, \dot{\mathbf{p}} \tag{8.46}$$

where c is a positive scalar feedback gain. The control law (8.46) is well-known from standard control analysis, leading to an asymptotically stable system.
It is shown in [62] that another control law can be obtained by making the feedback gains time dependent. This is achieved with

$$\mathbf{P} = -c\, \mathbf{M} \dot{\mathbf{p}} \tag{8.47}$$

with c being a positive scalar feedback gain. The configuration dependent matrix $\mathbf{M} = \mathbf{M}(\mathbf{p})$ in control law (8.47) acts as variable feedback gains, which improve the performance.
One of the benefits of control law (8.47) over (8.46) is its exponential stability, which is proven in [61].
The position dependent Lyapunov function is found in a similar way. We formulate L as

$$L(\mathbf{p}) = \tfrac{1}{2} \Delta^{\mathrm{T}}\, \mathbf{B}\, \Delta \tag{8.48}$$

where Δ denotes the position error vector $\mathbf{p}_{\text{actual}}$ - $\mathbf{p}_{\text{desired}}$, and where $\mathbf{B}$ is a matrix of position feedback gains similar to imaginary springs. In the present case $\mathbf{B}$ is a diagonal matrix, since the position error of one of the joints must not influence the desired target position of the other joints.
Performing the analyses given in equations (8.40) through (8.47) for the attitude dependent Lyapunov function L finally yields the control law

$$\mathbf{P} = -c\, \Delta \tag{8.49}$$

or, similar to the velocity control law, the improved form

$$\mathbf{P} = -c\,\mathbf{M}\,\boldsymbol{\Delta} \tag{8.50}$$

where c is again a positive feedback scalar. The velocity and position based control laws, equations (8.47) and (8.50), can now be linearly combined to give

$$\mathbf{P} = -c_1\,\mathbf{M}\,\dot{\mathbf{p}} - c_2\,\mathbf{M}\,\boldsymbol{\Delta} \tag{8.51}$$

where c_1 and c_2 are the velocity and position feedback gains respectively. Equation (8.51) is further simplified to

$$\mathbf{P} = -\mathbf{M}\left(c_1\,\dot{\mathbf{p}} + c_2\,\boldsymbol{\Delta}\right) = -\mathbf{M}\,\mathbf{C} \tag{8.52}$$

It is seen from equation (8.52) that depending on the position error $\boldsymbol{\Delta}$, the feedback gains can theoretically grow arbitrarily large, whereas the maximum velocity errors are identical to the actual maximum allowed velocities. However, in practice the position errors of the RMS joints can only be π since the motions are rotations. Inserting the maximum possible position errors and the maximum velocity errors into equation (8.52) together with the worst case configuration $\mathbf{M}_0$ of the mass matrix $\mathbf{M}$, see figure 8.2 and text, yields the maximum magnitudes of the control vector elements. This allows for computation of c_1 and c_2 so that the maximum allowed torques are never exceeded.
Similar to the inverse dynamics method, the feedback gains have to be computed for each payload and can be optimised by computation for each individual slew manoeuvre.
As mentioned before, we only consider RMS slew manoeuvres here and therefore wish the Shuttle to keep its position in space. Thus taking into account the maximum allowed joint velocities, the elements C_i of the control vector $\mathbf{C}$ in equation (8.52) finally become

$$C_j = \begin{cases} c_1\,\dot{p}_j + c_2\left(p_j - p_{j,\mathrm{des}}\right), \text{ if } \left|\dot{p}_j\right| < \dot{p}_{j,\max} \\ c_1\,\dot{p}_j + c_2\left(p_j - p_{j,\mathrm{des}}\right), \text{ if } \operatorname{sign}\left[c_1\,\dot{p}_j + c_2\left(p_j - p_{j,\mathrm{des}}\right)\right] \neq -\operatorname{sign}\left[\dot{p}_j\right] \\ 0, \text{for any other case} \end{cases} \tag{8.53}$$

for $j = b = 1,2,3$ and $C_j = 0$ for $j = 4,5,6$.

The second condition in equation (8.53) checks if the velocity would be decelerated or still accelerated, if the unrestricted control law (8.52) is fed back.
If the control law allows the joint torque motors to become saturated, it is said to be Lyapunov optimal.
A Lyapunov optimal control law is not desirable here due to the following reason. If we assume SRMS properties and allow the maximum joint torques to be fully utilised, it is possible to create configurations where one joint torque is completely overridden by the reaction forces of another joint torque, so that although the maximum torque is already applied, the joint is actually driven in the opposite direction. This is clearly not desired for SRMS manoeuvres. Therefore the method of restricted feedback gains is preferred.

8.4 EXAMPLE RMS SLEW MANOEUVRE

With the described inverse dynamics and Lyapunov's direct methods we wish to obtain the torques to perform the following rigid triple articulated RMS manoeuvre. From the straight configuration $\theta_1 = \theta_2 = \theta_3 = 0°$, we require the first, the second and the third link to rotate through relative angles $\theta_{1des} = \theta_{2des} = \theta_{3des} = 30°$, when the RMS is carrying a payload. Figure 8.5 shows the desired manoeuvre.
The SRMS system properties are $T_{1,max} = 1298$ Nm, $T_{2,max} = 888$ Nm, $T_{3,max} = 389$ Nm, $\dot{\theta}_{1,max} = 0.004$ rad/s, $\dot{\theta}_{2,max} = 0.0056$ rad/s, $\dot{\theta}_{3,max} = 0.0083$ rad/s, $L_1 = 6.37$ m, $L_2 = 7.05$ m, $L_1 = 1.88$ m, $M_1 = 25.48$ kg, $M_2 = 28.2$ kg, and since the joints are rigid and unlocked, also $I_{g1} = I_{g2} = I_{g3} = 0$ and $\lambda_1 = \lambda_2 = \lambda_3 = 0$. The payload is chosen $M_p = 10000$ kg, $I_p = 37500$ kgm^2, and $a = b/2 = 1.5$ m.

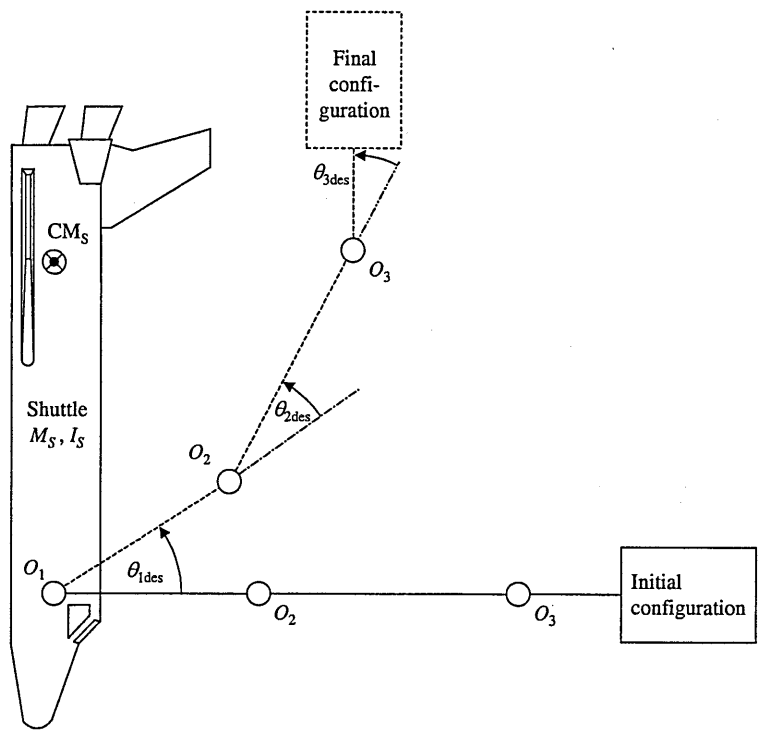

Figure 8.5: Example of a desired RMS manoeuvre

8.4.1 RESULTS WITH INVERSE DYNAMICS METHOD

Fixed RMS base

As before, the equations of motion for the fixed base are obtained from the equations of motion for the free Shuttle, equations (8.7) and (8.8), by striking the Shuttle degrees of freedom in the system matrices and vectors and by setting them to zero.
For the present case f is calculated with equations (8.9) and (8.10) to be $f = 0.066325$, giving the maximum necessary torques $T_1 = 650$ Nm, $T_2 = 719$ Nm and $T_3 = 389$ Nm for the worst case (straight RMS and all links accelerated in the same direction).
The necessary torques for the desired manoeuvre are computed with equation (8.8) after the accelerations are computed with equations (8.11) through (8.25) and

integrated twice to give the time histories of the velocities and angles, as described. The torques are given in figures 8.6 through 8.8, and the joint angles, velocities and accelerations are shown in figures 8.9 through 8.11.

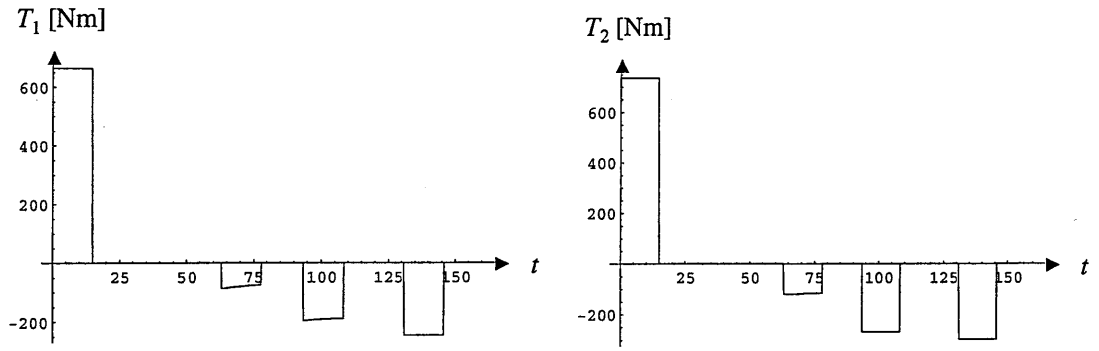

Figures 8.6 and 8.7: Computed torques T_1 and T_2

It is noted that the worst case torques are only utilised if all links are accelerated in the same direction from the straight configuration. Figure 8.6 shows that a desired bang-bang acceleration does not automatically require a bang-bang torque due to the time-varying mass matrix.

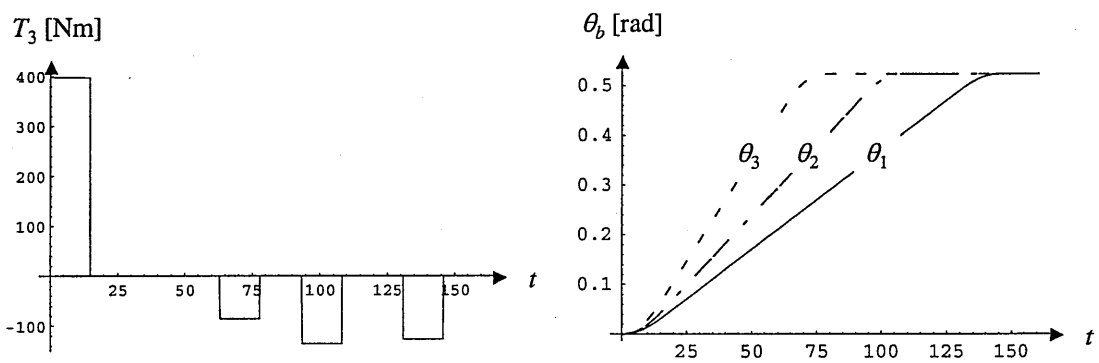

Figures 8.8 and 8.9: Computed torque T_3 and time-history of joint angles

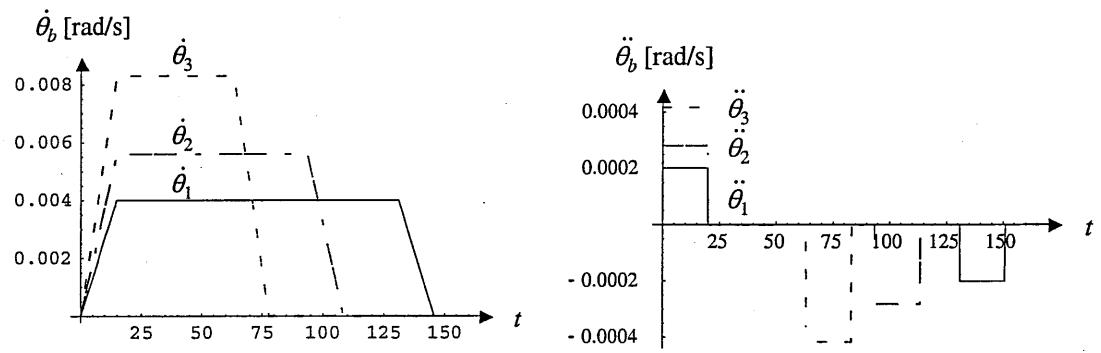

Figures 8.10 and 8.11: Time-history of joint velocities and accelerations

As can be seen from figures 8.9 and 8.10, the desired angular motions are performed accurately, while the maximum angular velocities are not exceeded.

Free RMS base

As mentioned before, we want the Shuttle to keep its position in space while operating the RMS. This effectively yields a fixed base, so that the time history of the RMS joint torques, angles and velocities is identical to the respective time histories for the fixed base, figures 8.6 through 8.11.
However, using the equations of motion for the free base yields the necessary control forces to perform the desired motion, here to keep position. Figures 8.12 through 8.14 show the necessary Shuttle control forces F_{Sy} and F_{Sz} in y and z and the control moment T_S about x.

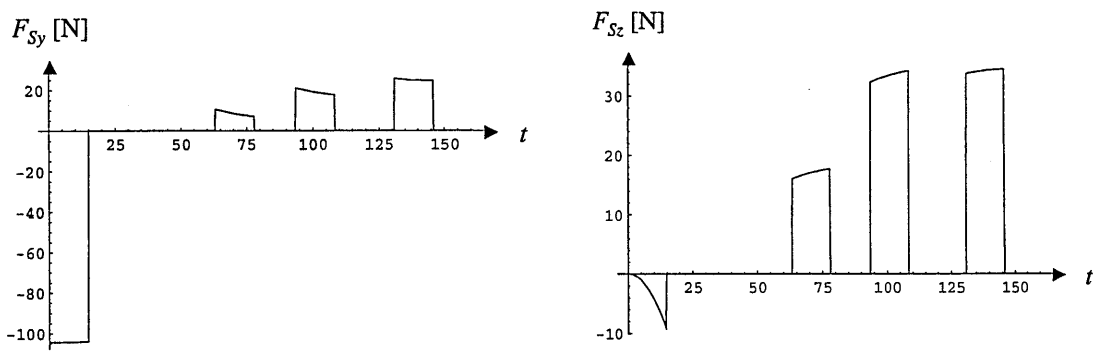

Figures 8.12 and 8.13: Shuttle control forces F_{Sy} and F_{Sz}

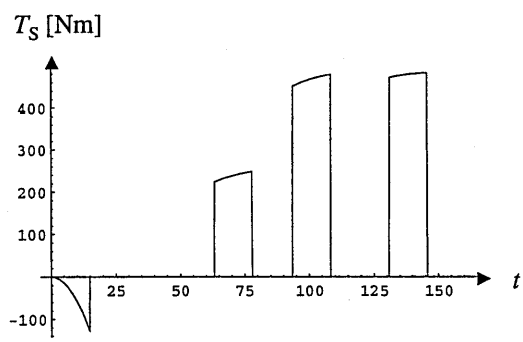

Figure 8.14: Shuttle control moment T_S

It is noted here that due to lack of information it is not known whether the Shuttle is capable of producing the desired control forces as indicated in figures 8.12 through 8.14, and if not, the factor f has to be re-computed with the described procedure to yield results that do not exceed the maximum Shuttle control forces.

8.4.2 RESULTS WITH LYAPUNOV'S DIRECT METHOD

Fixed and free RMS base

Analogue to the results obtained from the inverse dynamics method, the joint torques, angles and velocities are identical for the free and fixed RMS base case, when the

Shuttle is desired to keep its position in space, thus effectively producing a fixed base. c_2 is computed analogous to the scaling factor f from the inverse dynamics method by inserting some initial value $c_{2,0}$ of c_2 into the worst case configuration $\mathbf{M}_0$ of $\mathbf{M}$ and then finding the smallest of the ratios $T_{b,\max} / T_{b,0}$, see equations (8.9) and (8.10) and text. This procedure yields $c_2 = 6.47831 \times 10^{-4}$ and gives T_3 identical to the worst case torque T_3 for the inverse dynamics method, that is 389 Nm. To be able to compare the different control methods c_1 is chosen so that no overshoot occurs at the target state, which by experiment gives $c_1 = 0.045$.
To illustrate the different results using the two different control schemes, figures 8.15 and 8.16 show the time history of torque T_1 and the joint angles, and figures 8.17 and 8.18 show the joint velocities and accelerations. From these figures it is seen that the desired motions are performed accurately, while the maximum joint velocities are not exceeded, like when using the inverse dynamics method.

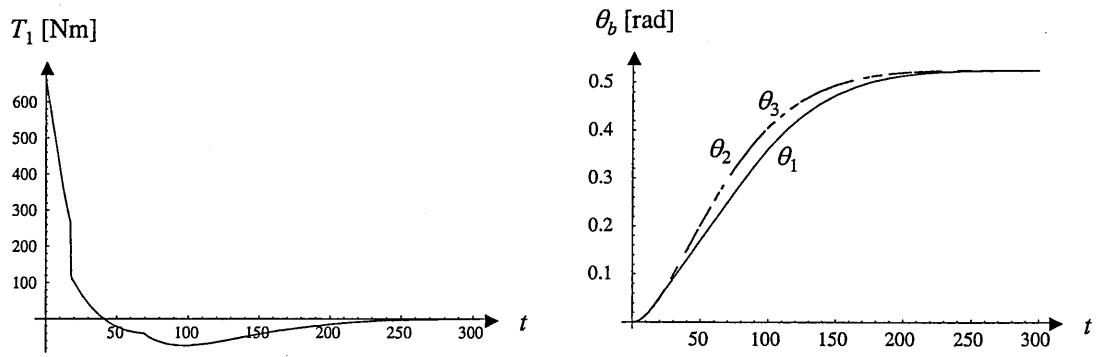

Figures 8.15 and 8.16: Computed torque T_1 and time-history of joint angles

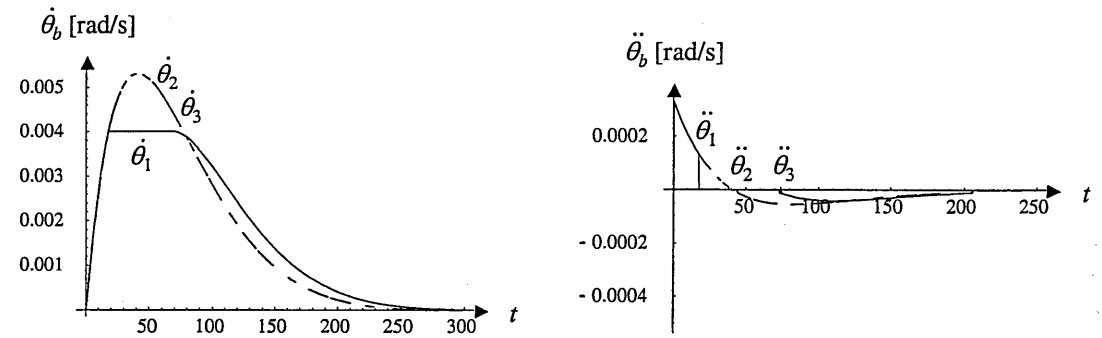

Figures 8.17 and 8.18: Time-history of joint velocities and accelerations

8.4.3 COMPARISON OF INVERSE DYNAMICS AND LYAPUNOV METHOD

The following figures 8.19 and 8.20 show the comparison of the results obtained from the two different methods for the joint angle θ_1 and the associated joint torque T_1.
The figures reveal that the performance of the Lyapunov method is poor compared to the inverse dynamics method. This is due to the fact that the time history of the mass matrix and the angles is known a priori with the inverse dynamics method, while the Lyapunov control law has to adopt to the actual states and cannot look into the future.

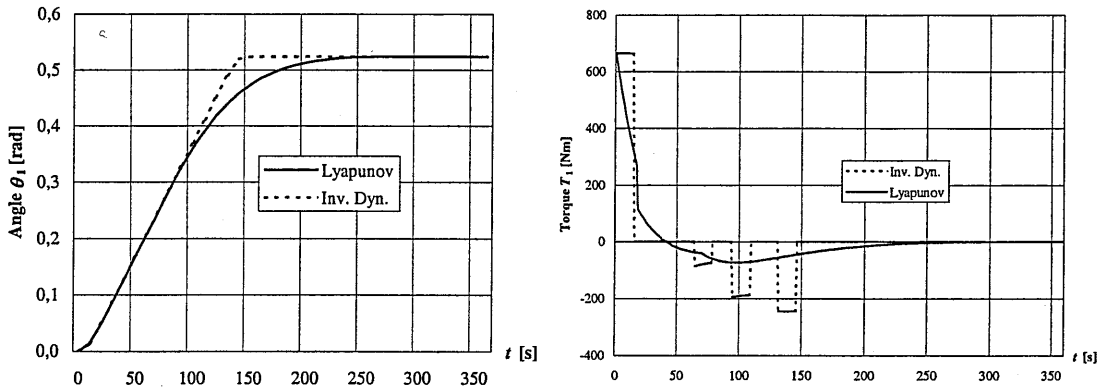

Figures 8.19 and 8.20: Time-history of θ_1 and T_1
for inverse dynamics and Lyapunov method

It is seen that the inverse dynamics method fulfils the desired manoeuvre in about 145 seconds, while the proposed Lyapunov control law needs about 280 seconds.
A remarkable difference between the inverse dynamics method and Lyapunov's method is that with Lyapunov's method all states are brought to the desired target at the same point of time, see figure 8.16. For example, if Link1 has to rotate through a very large angle to the target state and Link2 through a very small angle, Link2 does not reach its final state earlier than Link1, but together with Link1. By contrast, if the RMS slew is calculated with the inverse dynamics method, every link reaches its final state independent from the others, see figure 8.9.
Another important difference between the two methods is that the inverse dynamics method always utilises the maximum accelerations as set prior to the manoeuvre, for the acceleration as well as the deceleration phase, whereas the control law obtained with Lyapunov's method has configuration dependent angular accelerations.
Using Lyapunov's control law, the target states are approached more or less slowly, depending on the chosen velocity and position feedback gains. Therefore the torque profiles of the closed-loop control law for a desired manoeuvre are much smoother than the profiles of the open-loop control law, yielding smaller vibration amplitudes in dynamic response analyses than bang-bang accelerations.

The advantages of the inverse dynamics method are:
- fast computation (linear algebraic equations)
- the differential equations of motion do not have to be solved
- no overshoot at the desired final positions

The disadvantages are:
- the maximum torques may not be fully utilised with the proposed method, but more sophisticated algorithms to compute the maximum angular accelerations can be invented
- the inverse dynamic method only gives the necessary torques for a desired manoeuvre, a real-time control of the RMS attitude is not possible (open-loop control).

The advantages of the Lyapunov method are:
- the control algorithm can be used for closed-loop real-time control
- a control law obtained by Lyapunov's direct method is robust to modelling errors
- the equations of motion do not have to be solved to obtain the control law

The disadvantage is:
- slow computation (non-linear differential equations).

8.5 SUMMARY

This section introduces two methods of rigid body motion control of the triple articulated RMS / Shuttle system. The two methods are derived using Lagrange's equation to obtain the equations of motion for this system.
The first method presented is commonly known as the inverse dynamics method, which makes use of the fact that the equations of motion, once set up, are already explicitly solved for the generalised forces. Thus by inserting the desired accelerations, the equations of motion automatically yield the necessary generalised forces to produce those accelerations. In practice the application of this method can be complicated by taking into account certain boundary conditions such as maximum allowed generalised velocities, generalised forces or accelerations. The inverse dynamics method can only be used for open-loop control of the RMS.
The second method derives a control law using Lyapunov's direct method, which is a very sophisticated way to derive control laws for dynamical systems without having to solve the equations of motion.
Similar to the first control law, this control law is formulated to allow for boundary conditions like maximum velocities and forces. The control law can be used for closed-loop attitude control of the RMS.
The two control laws are compared by the performance of an example slew manoeuvre. The results show that a desired manoeuvre is performed faster using the inverse dynamics control law, since with this method the time-history of the accelerations and thus motions and thus the configuration dependent mass matrix is known a priori, whereas the closed-loop control law has to adopt to the actual configuration without being able to look into the future.
With the open-loop control law, each link is brought to its target state independent from the other links, whereas the closed-loop control law brings the links to their targets at the same time.
Furthermore, the open-loop control law always utilises the maximum allowed angular accelerations, for the acceleration and deceleration. By contrast, the closed-loop control law approaches the target state more or less slowly, depending on the chosen damping coefficient. Therefore the torque profiles of the closed-loop control law for a desired manoeuvre are much smoother than the profiles of the open-loop control law.
If the equations of motion allow for the Shuttle motion, as is the case in the presented example, the Shuttle control forces to perform a desired motion or to keep its position in space while operating the RMS, can also be obtained from the two control methods. Thus a computer controlling the RMS motions can be linked to the Shuttle control system to also give a desired Shuttle motion.

CHAPTER 9: FLEXIBLE RMS WITH PASSIVE AND ACTIVE DAMPING

The previous chapters 2 to 7 of this thesis have concentrated on undamped, open-loop dynamic response analysis of planar vibrations of flexible RMS with varying number of links. It has been shown that slewing with one or more joints free to revolute leads to very small amplitudes of vibration with typical magnitudes of millimetres or less. Significant amplitudes of vibration only occur due to Shuttle thruster firing with all joints locked or for example with only the wrist joint unlocked and perpendicular to the straight RMS, as well as in the case of a sudden application of the joint brakes (emergency braking), and only if the payload mass is sufficiently large.

As discussed in the introduction, long periods of time waiting for payload / RMS vibrations to decay are a great disadvantage in space construction and make some form of improved damping desirable, for example using active damping control systems. A literature search reveals very few papers dealing with active damping control of the Space Shuttle Remote Manipulator System (SRMS), for example [5] and [9]. [70] examines means to enhance the passive structural damping of the SRMS, using additional viscoelastic layers on the SRMS links.

The usually proposed control method using the high gear ratio SRMS joint motors to actively damp out vibrations, as proposed in [5] and [9], seem to be superfluous, since with the joints unlocked, as they must obviously be to use the joint motor for active damping control, the dynamic responses have been shown to be negligibly small, and there is no point in considering this method. Besides it is assumed that this method would rapidly cause wear and fatigue in the gear boxes, and gear backlash and other nonlinearities present additional problems. Finally the question arises how deflections with smaller vibration amplitudes than the SRMS end effector positioning precision itself, which is ± 5.08 cm ([3]), can be actively damped out with the existing joint drives.

However, all the proposed control methods have, to the author's knowledge, not been used in current Shuttle missions, and it seems that works like [13], [14], [15], [19], [24], [59] and many others are not applicable to manipulators similar to the SRMS.

Although the application was shown to be at least somewhat problematic in chapter 2, just as an example we consider again the use of reaction wheels (RW), one on each main RMS arm, with collocated sensors providing velocity feedback to damp out the predominant lowest frequency mode of vibration. Only very few references exist on using reaction wheels or other inertia actuators for active damping control of flexible manipulators, for example [20] and [51], but for space manipulators similar to the SRMS, [8] also proposes additional collocated sensors / actuators for active damping control instead of using the joint motors.

As mentioned in chapter 2, the main disadvantage here is that additional hardware has to be installed on the SRMS. In particular the mass of the reaction wheels is expected to be comparable to that of the unloaded SRMS, as well as being fairly bulky, if the reaction wheels are to provide significant damping ratios.

It is proposed to use active damping only for the joint configurations mentioned above, for example with all joints locked and the RMS / payload raised from the Shuttle payload bay, when the Shuttle thrusters are fired for payload positioning, and when the payload mass is sufficiently large.

Since vibration amplitudes are small during slew manoeuvres with free joints it is not considered important to damp out these vibrations during a slew with active damping

control, and the structural damping, which can be assumed to provide an overall damping ratio of at least 1% ([1], [70]) for all joint configurations, is assumed to be sufficient. An example will show this subsequently.
The prime aim is to place the reaction wheel on each link to provide damping torques proportional to structural velocity and to give significant damping ratios for the fundamental mode, say 2% - 5%, for the mentioned joint configurations.
RMS elastic velocities can be measured using accelerometers and integrators or by strain gauges, collocated with the wheels. Unwanted noise arising from higher modes should be filtered out to clean up the feedback signals. If the sensors / actuators are collocated and the actuators are capable of giving quasi-instantaneous response, as is the case for the fundamental mode, then the system is automatically stable ([61], [62], [65]), which will be proved subsequently.
Since the dynamic analysis considered up to this point concerns only planar vibrations, the reaction wheels are assumed to apply corresponding damping torques, in the same plane. However out of plane oscillations may also arise in certain configuration and one possibility is to have the ability of rotating the wheel about the arms to provide damping torques in various planes. Of course this raises much more complex issues.
One practical point of importance is that installation of fairly bulky reaction wheels should not impede the slewing and stowage of the RMS. The proposed system is shown in figure 9.1, where the reaction wheels are located on Link1 near to the elbow joint and near to the end effector on Link2. In principal the wheel torques should be applied at a location where the elastic slope of the links is a maximum, so as to provide the greatest damping effect, which for the fundamental mode is shown in figure 9.1.

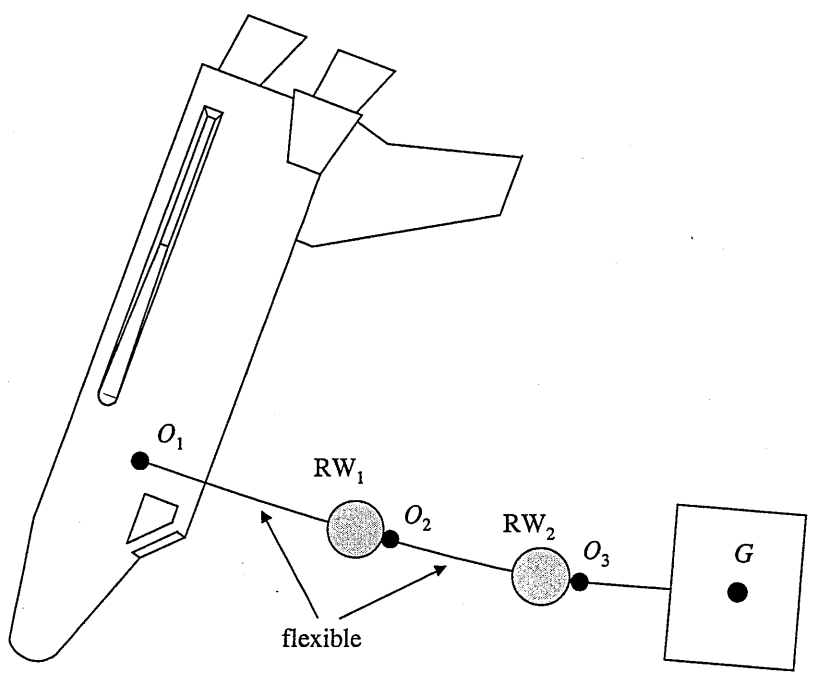

Figure 9.1: Location of reaction wheels on the flexible RMS

9.1 EQUATIONS OF MOTION

The equations of motion of the Shuttle / RMS system in matrix form are always

$$\mathbf{M}\ddot{\mathbf{p}} + \mathbf{K}\mathbf{p} = \mathbf{P} \tag{9.1}$$

where $\mathbf{M} = \mathbf{M}(\mathbf{p})$, $\mathbf{K}$ = const. and where the vector of the generalised coordinates $\mathbf{p}$ represents the elastic deflections of Link1 and Link2 (and their rigid body motions for unlocked joints), the rigid body motion of Link3, and the rigid body motions of the Shuttle. For various joint configurations and degrees of freedom, the elements of the system matrices and vectors $\mathbf{M}$, $\mathbf{K}$, $\mathbf{P}$ and $\mathbf{p}$ are given in chapter 7.
In the presence of damping, equation (9.2) becomes

$$\mathbf{M}\ddot{\mathbf{p}} + \mathbf{D}\dot{\mathbf{p}} + \mathbf{K}\mathbf{p} = \mathbf{P} \tag{9.2}$$

where $\mathbf{D}$ is the damping matrix, containing the damping coefficients. For the following explanations M_{nm}, K_{nm} and D_{nm} denote the element in the n-th row and m-th column of the matrices $\mathbf{M}$, $\mathbf{K}$ and $\mathbf{D}$. If the a-th and b-th degree of freedom in equation (9.2) represent the flexibility of Link1 and Link2 and the c-th degree of freedom the rigid body deflection of Link3 against the joint stiffness of Joint3 and assuming that the Shuttle motions are neither passively nor actively damped, the elements D_{nm} of $\mathbf{D}$ are

$$\begin{aligned} D_{aa} &= 2\beta_1\sqrt{M_{aa}\,K_{aa}} \\ D_{bb} &= 2\beta_2\sqrt{M_{bb}\,K_{bb}} \\ D_{cc} &= 2\beta_3\sqrt{M_{cc}\,K_{cc}} \\ D_{nm} &= 0 \text{ else} \end{aligned} \tag{9.3}$$

where β_1, β_2 and β_3 are the damping ratios of Link1, Link2 and Link3. To get an estimate of the modal damping coefficient achieved with these damping ratios for the various degrees of freedom of the RMS, equation (7.11) can be used. Then absolute value $|d_i|$ of the modal damping coefficient d_i for mode i is approximately

$$|d_i| \approx \mathbf{ev}_i^{\mathrm{T}}\,\mathbf{D}\,\mathbf{ev}_i \tag{9.4}$$

where $\mathbf{ev}_i$ is the eigenvector of the undamped system for mode i calculated by equation (2.50). Note that although the actual eigenvalues are complex since damping is existent, equation (9.4) is a very good approximation for small damping ratios β_1, β_2 and β_3, see also the following paragraph.
For the following simulations, the exact mode shapes for the actual joint configurations are used in the equations of motion. Although these mode shapes are calculated without damping, it is known that the relation of the natural frequency ω_u of an undamped single degree of freedom system to the corresponding natural frequency ω_d of a damped system is ([41])

$$\omega_d = \omega_u \sqrt{1-\beta^2} \tag{9.5}$$

where β is the damping ratio. With 5% damping ratio, equation (9.5) yields ω_d = 0.9995 ω_u, and it is seen that the fundamental frequency and thus the first mode shapes of the flexible links do practically not change for small damping ratios, as confirmed by BEAM and SIMPACK.

9.2 STABILITY ANALYSIS

For a stability analysis of the actively damped RMS system, we use Lyapunov functions as defined in chapter 8 and introduce one additional theorem.

Theorem:
Let $L(\mathbf{p})$ *be a Lyapunov function for the dynamical system* $\dot{\mathbf{x}} = f(\mathbf{x})$ $\left(\mathbf{x} = [\mathbf{p}, \dot{\mathbf{p}}]^T\right)$ *and* Ω *be the non-empty set of state vectors so that* $\mathbf{x} \in \Omega \Rightarrow \dot{L}(\mathbf{x}) = 0$.
Then if the first k - 1 *derivatives of* $L(\mathbf{x})$, *if evaluated on the set* Ω, *are zero,*

$$\frac{\mathrm{d}^i L(\mathbf{x})}{\mathrm{d}\mathbf{x}^i} = 0 \qquad \forall \mathbf{x} \in \Omega \qquad i = 1, 2, ..., k-1$$

and the k-th derivative is negative definite on the set

$$\frac{\mathrm{d}^k L(\mathbf{x})}{\mathrm{d}\mathbf{x}^k} < 0 \qquad \forall \mathbf{x} \in \Omega$$

then the system $\mathbf{x}(t)$ *is asymptotically stable if k is an odd number* ([61], [62], [65]).

To show that the stability analyses hold true also in the presence of Coriolis and centrifugal and other second order effects we write the general standard equations of motion for a natural system with stiffnesses and damping in the absence of external forces (for example at the end of a RMS or Shuttle manoeuvre) as ([61])

$$\mathbf{M}\ddot{\mathbf{p}} + \dot{\mathbf{M}}\dot{\mathbf{p}} + \tfrac{1}{2}\dot{\mathbf{p}}^T \mathbf{M}_p \dot{\mathbf{p}} + \mathbf{D}\dot{\mathbf{p}} + \mathbf{K}\mathbf{p} = \mathbf{0} \tag{9.6}$$

where $\mathbf{M}_p$ is the derivative of $\mathbf{M}$ with respect to $\mathbf{p}$. We use the total kinetic and potential energy as a radially unbounded Lyapunov function, thus

$$L = \tfrac{1}{2}\dot{\mathbf{p}}^T \mathbf{M}\dot{\mathbf{p}} + \tfrac{1}{2}\mathbf{p}^T \mathbf{K}\mathbf{p} \tag{9.7}$$

Since $\mathbf{M}$ and $\mathbf{K}$ are symmetrical, and $\dot{\mathbf{K}} = \mathbf{0}$, the time derivative of L is

$$\dot{L} = \dot{\mathbf{p}}^T \mathbf{M}\ddot{\mathbf{p}} + \tfrac{1}{2}\dot{\mathbf{p}}^T \dot{\mathbf{M}}\dot{\mathbf{p}} + \dot{\mathbf{p}}^T \mathbf{K}\mathbf{p} \tag{9.8}$$

or $$\dot{L} = \dot{\mathbf{p}}^{\mathrm{T}} \left(\mathbf{M}\ddot{\mathbf{p}} + \mathbf{K}\mathbf{p} + \tfrac{1}{2}\dot{\mathbf{M}}\,\dot{\mathbf{p}} \right) \tag{9.9}$$

Recalling that $\dot{\mathbf{p}}^{\mathrm{T}} \dot{\mathbf{M}}\, \dot{\mathbf{p}} = \sum_{j=1}^{J} \dot{p}_j \left(\dot{\mathbf{p}}^{\mathrm{T}} \mathbf{M}_{p_j}\, \dot{\mathbf{p}} \right) = \dot{\mathbf{p}}^{\mathrm{T}} \left(\dot{\mathbf{p}}^{\mathrm{T}} \mathbf{M}_{p}\, \dot{\mathbf{p}} \right)$, see equation (8.44) and text, and substituting the equations of motion, equation (9.9) finally yields

$$\dot{L} = \dot{\mathbf{p}}^{\mathrm{T}} \left(-\mathbf{D}\dot{\mathbf{p}} \right) \tag{9.10}$$

It is seen that $\dot{L}$ is only negative semi-definite, which allows only for the conclusion of Lyapunov stability at this point. With the theorem introduced above, we investigate the higher order time derivatives of L to prove asymptotical stability. The set of states $\boldsymbol{\Omega}$ where $\dot{L} = 0$ is $\boldsymbol{\Omega} = \left\{ (\mathbf{p}, \dot{\mathbf{p}}) \,|\, \dot{\mathbf{p}} = \mathbf{0} \right\}$.

Since $\mathbf{D}$ is symmetrical and $\dot{\mathbf{D}} = \mathbf{0}$, the second time derivative of L is given as

$$\ddot{L} = -2\dot{\mathbf{p}}^{\mathrm{T}} \mathbf{D}\, \ddot{\mathbf{p}} \tag{9.11}$$

Inserting the equations of motion, equation (9.11) becomes

$$\ddot{L} = 2\dot{\mathbf{p}}^{\mathrm{T}} \mathbf{D} \left(\mathbf{M}^{-1} \mathbf{D}\dot{\mathbf{p}} + \mathbf{M}^{-1} \mathbf{K}\mathbf{p} \right) = 2\dot{\mathbf{p}}^{\mathrm{T}} \mathbf{D}\mathbf{M}^{-1} \left(\mathbf{D}\dot{\mathbf{p}} + \mathbf{K}\mathbf{p} \right) \tag{9.12}$$

where $\mathbf{M}^{-1}$ is the inverse of $\mathbf{M}$. $\ddot{L}$ is zero on the set $\boldsymbol{\Omega}$. The third derivative of L is

$$\dddot{L} = 2\ddot{\mathbf{p}}^{\mathrm{T}} \mathbf{D}\mathbf{M}^{-1} \left(\mathbf{D}\dot{\mathbf{p}} + \mathbf{K}\mathbf{p} \right) + 2\dot{\mathbf{p}}^{\mathrm{T}} \mathbf{D}\mathbf{M}^{-1} \left(\mathbf{D}\ddot{\mathbf{p}} + \mathbf{K}\dot{\mathbf{p}} \right) \tag{9.13}$$

Inserting the equations of motion, we obtain

$$\dddot{L} = -2\left(\mathbf{M}^{-1} \left(\mathbf{D}\dot{\mathbf{p}} + \mathbf{K}\mathbf{p} \right) \right)^{\mathrm{T}} \mathbf{D}\mathbf{M}^{-1} \left(\mathbf{D}\dot{\mathbf{p}} + \mathbf{K}\mathbf{p} \right) + 2\dot{\mathbf{p}}^{\mathrm{T}} \mathbf{D}\mathbf{M}^{-1} \left(\mathbf{D}\ddot{\mathbf{p}} + \mathbf{K}\dot{\mathbf{p}} \right) \tag{9.14}$$

Evaluating equation (9.14) on the set $\boldsymbol{\Omega}$, it reduces to

$$\dddot{L} = -2\left(\mathbf{M}^{-1} \mathbf{K}\mathbf{p} \right)^{\mathrm{T}} \mathbf{D}\mathbf{M}^{-1} \mathbf{K}\mathbf{p} \leq 0 \tag{9.15}$$

which is negative definite for the state vector $\mathbf{p}$. As the first non-zero higher order derivative of L is of odd order, the system is globally asymptotically stable. This result agrees with the findings of [61] for a single-degree-of-freedom system.

From this stability analysis it can be seen that if the state vector $\dot{\mathbf{p}}$ is used as a feedback input, the system remains (or becomes) stable ([62], [65]). This however assumes instantaneous response, but for the fundamental mode in joint configurations where active damping is necessary, this assumption is justified due to the very low frequencies involved.

9.3 RELEVANT RMS CONFIGFURATIONS

At this point we briefly summarise the RMS configurations that are relevant for active damping control. Basically there are only three cases where the elastic deflections can reach a magnitude that make active damping control desirable, (1) Shuttle thruster firing, (2) payload capturing and (3) emergency braking during slew manoeuvres (see next chapter).
For Shuttle thruster firing only two joint configurations have to be taken into account, all joints locked and wrist joint locked or unlocked with end effector perpendicular to the RMS. Figure 9.2 shows the two cases.

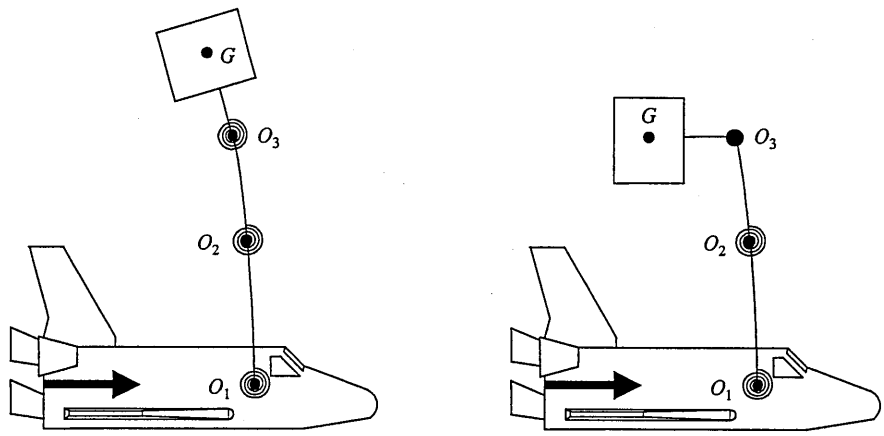

Figure 9.2: RMS joint configurations relevant for active damping for thruster firing

From figure 9.2 it is clear that the RMS links can be in any position within their mechanical work range, and the vibration amplitudes are smaller for non-straight RMS configurations, since the effective cantilever length gets smaller.
It is obvious that the payload mass also determines the dynamic responses due to Shuttle thruster firing. In chapter 7.1, the vibration amplitude of the payload centre of mass *G* relative to the Shuttle for the case of a Shuttle accelerating linearly and perpendicularly to the straight RMS with all joints locked, was shown to be 18.84 cm for the maximum payload size. This figure is the very worst case deflection for a step-input acceleration
Since the reaction force on the RMS due to the payload inertia is a linear function of the payload mass, see equation (7.12), we can easily calculate the necessary payload mass to cause a minimum vibration amplitude. If for simplicity we only consider amplitudes larger than about 2 cm, then the payload mass must at least be about 10% of the maximum payload mass, thus 3000 kg. This is already a relatively large payload and covers many common payload masses such as equipment tools or small satellites.
In practice, the decision whether active damping is used in addition to structural damping can be left to a computer, which would process the incoming data from the sensors, and which would activate the collocated actuators if the measured vibration amplitudes exceeded a given magnitude, say 1 or 2 cm or so.
Programming the computer so as to deactivate active damping control if the vibration amplitudes become smaller than a given magnitude would furthermore avoid chattering of the actuators around the target state for small vibration amplitudes.

9.4 EXAMPLES FOR PASSIVE AND ACTIVE DAMPING

To examine the effects of damping, one example of structurally damped vibrations caused by a RMS slew manoeuvre, and one example of actively damped vibrations arising from Shuttle thruster firing is given.

9.4.1 PASSIVE DAMPING

We consider a slew manoeuvre about Joint2 through 90° with Joint1 and Joint3 locked, starting from the straight RMS position, with the base inertially fixed and with the maximum payload M_p = 30000 kg for a worst case scenario.
The simulation is carried out using the equations of motion given in chapter 7.2.4 for the fixed RMS base.
With [1] and [70], a minimum overall RMS passive damping ratio of 1% is assumed, thus we let $\beta_1 = \beta_2 = \beta_3 = 0.01$ in equation (9.3) (the rigid body motion of Link2 is undamped). Figures 9.3 and 9.4 show the time history of θ_2 (to prove that the desired manoeuvre is performed correctly) and the deflection y_{32} of Link3 relative to the tangential extension of Link2 at O_3 for the data set (B).

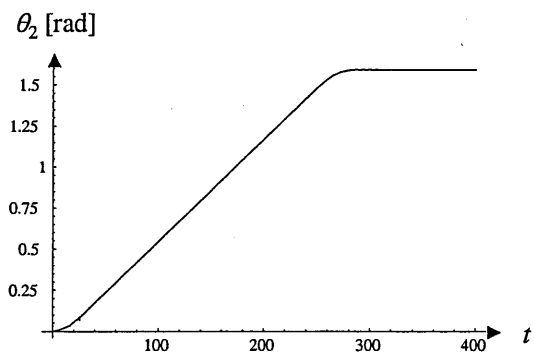

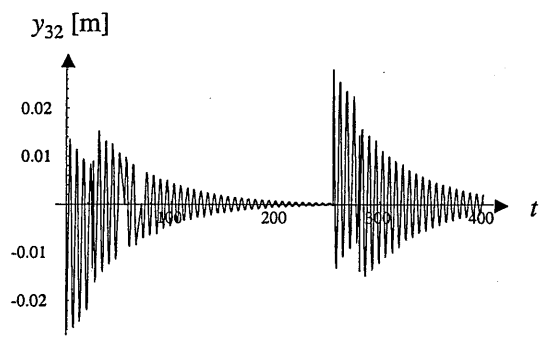

Figures 9.3 and 9.4: 90° slew about Joint2 and passively damped deflection y_{32}

The figures show how with a passive damping ratio of only 1%, the vibrations arising from RMS slew manoeuvres are damped out. Figure 9.4 for example shows that it only takes about 120 seconds to reduce a vibration amplitude of about 1 cm of the tip of Link3 to 2 mm.
For the present slew example, the maximum elastic deflection of the payload centre of mass G relative to the undeformed configuration is about 1.2 mm, and with structural damping is damped quickly to practically zero.

9.4.2 ACTIVE DAMPING USING REACTION WHEELS

The second example considers the case of a straight RMS and the Shuttle accelerated linearly and perpendicularly to the RMS holding the maximum payload. As shown in chapter 7.1, this configuration gives the very maximum elastic vibration amplitudes of the link tips and the payload centre of mass.
For the calculation of the reaction wheel power requirements the maximum response

of the generalised coordinates must be calculated. To get the worst case response the small damping ratios are neglected and using equation (7.11), the modal form of equation (9.1) for mode i is thus

$$m_i \ddot{p}_i + k_i p_i = f_i \tag{9.16}$$

Assuming a step function input $f_i(t)$, the solution to equation (9.16) is given by

$$p_i = \frac{f_i}{k_i}(1 - \cos \omega_i t) \tag{9.17}$$

where

$$\omega_i = \sqrt{\frac{k_i}{m_i}} \tag{9.18}$$

From equation (9.17) the maximum $p_{i,\max}$ of the modal coordinate p_i is

$$p_{i,\max} = \frac{2 f_i}{k_i} \tag{9.19}$$

and the maximum velocity $\dot{p}_{i,\max}$ of the generalised velocity $\dot{p}_i$ is obtained from differentiating equation (9.17) to give

$$\dot{p}_{i,\max} = \omega_i \frac{f_i}{k_i} \tag{9.20}$$

Reversing the modal decomposition with

$$\dot{\mathbf{p}}_{i,\max} = \dot{p}_{i,\max} \mathbf{ev}_i \tag{9.21}$$

yields the maxima of the generalised velocities $\dot{p}_{1,\max} \ldots \dot{p}_{n,\max}$ for mode i.
Let the m-th degree of freedom be the flexibility of link l (l = 1, 2) and let $W_l(x_l)$ and $W_l'(x_l)$ be the exact first mode shape and its first derivative with respect to x_l. Then using the principles derived in equations (2.71) through (2.81), the feedback gain g_m for a constant damping ratio β and for a reaction wheel axis close to the link tip is

$$g_m = \frac{2 \omega_i M_{mm} \beta}{W_l'(L_l)} \tag{9.22}$$

The RW damping torque is

$$M_w = g_m \dot{p}_m \tag{9.23}$$

Due to the harmonic motion of the RW, the maximum inertia torque is equal to the maximum damping torque, thus

$$M_{w,\max} = g_m \dot{p}_{m,\max} = I_m \omega_1^2 \theta_m \tag{9.24}$$

where I_m is the RW moment of inertia and θ_m the amplitude of oscillatory motion in [rad]. Let m_m be the mass of the solid RW$_m$ and d_m its diameter, then I_m is

$$I_m = \tfrac{1}{8} m_m d_m^2 \tag{9.25}$$

Equations (9.24) and (9.25) are used to calculate θ_m. The maximum power consumption dW/dt is

$$\frac{\mathrm{d}W}{\mathrm{d}t}(\max) = M_{w,\max} \theta_m \omega_i \tag{9.26}$$

From the previous equations it is seen that M_w is a linear function of β. θ_m is a linear function of m_m and β and a quadratic function of d_m. The maximum power consumption dW/dt is a linear function of m_m and a quadratic function of β and d_m.
Given two reaction wheels with specific physical data, one can either define a desired damping ratio and calculate the necessary power consumption, or define a maximum allowed power consumption and calculate the possible damping ratio for each wheel.
It is noted that a damping ratio of say 5% for the three links does not lead to a damping ratio of 5% for RMS configurations with free base (= Shuttle), since the Shuttle motions are not damped. In this case the modal damping ratio β_i for mode i is

$$\beta_i = \frac{|d_i|}{2\sqrt{m_i k_i}} \tag{9.27}$$

where $|d_i|$ is given by equation (9.4) and m_i and k_i are given by equation (7.11).
Now the simulation described in chapter 7.1 for the RMS with linearly moving base or Shuttle is reproduced, taking into account damping. The equations of motion are given in chapter 7.1, and the chosen step input function for the Shuttle thrusters is shown in figure 7.2. All data are taken from data set (C).
To be able to compare the results for this worst case scenario of elastic deflections for a passively damped RMS with an actively damped RMS, the simulations are performed once letting $\beta_1 = \beta_2 = \beta_3 = 0.01$ in equation (9.3) (passive damping) and once letting let $\beta_1 = \beta_2 = 0.05$ and $\beta_3 = 0.01$ (active damping). The reason why $\beta_3 = 0.01$ even when active damping is present is because the two reaction wheels can only enhance the damping ratios of Link1 and Link2, but not of the rigid body motion of Link3 against the joint stiffness λ_3.
Figure 9.5 shows the deflection y_G of G around the static offset of 18.84 cm relative to the Shuttle for the passive damping case, and figure 9.6 shows the results for the case of active damping.

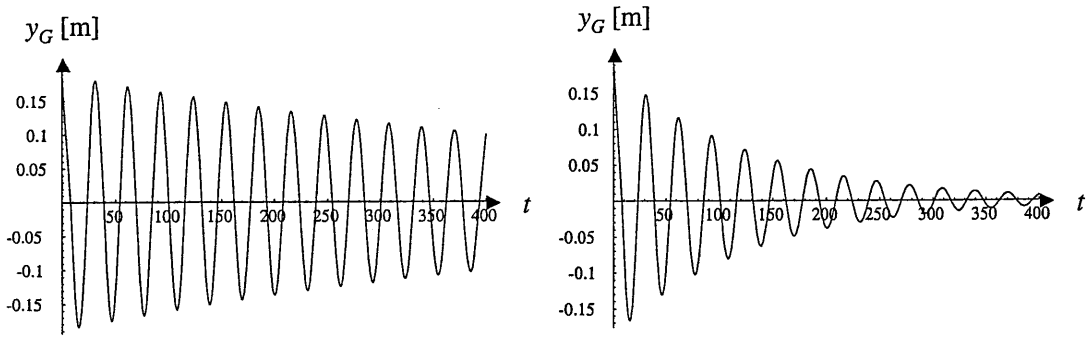

Figures 9.5 and 9.6: y_G for passive and active damping

The decay of a damped vibration is given by ([41])

$$A(t) = A(0)e^{-\beta\omega t} \tag{9.28}$$

where $A(t)$ and $A(0)$ denote the vibration amplitude at t and at $t = 0$, and where β and ω are the damping ratio and vibration frequency. The time t to damp a vibration from $A(0)$ down to $A(0)/x$ is thus

$$t = \frac{\ln x}{\beta\omega} \tag{9.29}$$

With equations (9.28) and (9.29) the time to damp down the vibration shown in figure 9.5 to an amplitude of 1 cm is 1859 seconds, and for figure 9.6 the time is 387 seconds.

Although equation (9.29) shows that the damp out time is an inversely linear function of the damping ratio, the two results above are not perfectly in the ratio 1 / 5 because Link3 is always damped with only 1% structural damping, as mentioned before, therefore the modal damping ratio as obtained with equation (9.28) for the active damping case is not perfectly 5 times the damping ratio for the case of only structural damping.

Equation (9.29) also shows that the time to damp a vibration from $A(0)$ down to $A(0)/x$ is a logarithmic function of the fraction x. Assuming a worst case of total addition of the four step input responses due to one complete Shuttle acceleration / deceleration manoeuvre, that is acceleration start and stop and deceleration start and stop, the initial vibration amplitude is 4×18.84 cm in the present case, if the damping only starts after the last step input. With 5% link damping ratio, the time to damp the amplitude down to 1 cm is 570 seconds.

Using equations (9.16) through (9.26), it is possible to give estimates of the necessary power consumption for a given wheel size.

We choose two identical wheels of mass m = 200 kg and diameter d = 1 m, and assuming a heavy material like iron, equation (2.84) yields a thickness of the wheels of 3.19 cm.

It is noted that the additional reaction wheel masses can be included in M_1 and M_2 in the equations of motion. Doing so however yields a difference of only 0.3 mm or 0.16% in the deflection of G for the present example.

For the chosen wheel data and the present example, the desired additional damping ratio of 4% for Link1 and Link2 leads to a maximum power consumption of 7021 W for RW_1 and 733 W for RW_2.
Restricting the maximum allowed power consumption for example to 500 W for each RW, Link1 can be damped with an additional minimum damping ratio of 1.07% and Link2 with a minimum of 3.30%.
It is stressed here that the terms "maximum power consumption" and "minimum damping ratio" are used because the maximum power consumption for a desired damping ratio only occurs at the very beginning of the active damping phase, and, similar to the vibration amplitude, the decay of the sinusoidal power consumption amplitude with time is

$$P(t) = P(0)\,e^{-\beta\omega t} \tag{9.30}$$

where $P(t)$ and $P(0)$ denote the amplitude at t and at $t = 0$, thus $P(0) = P_{max}$. For improved damping the reaction wheel feedback gains can be made time dependent. β_1 and β_2 of Link1 and Link2 in equation (9.3) are then given by

$$\beta_1 = \beta_{10}\,e^{\beta_i \omega t} \quad \text{and} \quad \beta_2 = \beta_{20}\,e^{\beta_i \omega t} \tag{9.31}$$

where β_i in the exponents is given by equation (9.27) for $t = 0$ and where β_{10} and β_{20} are the damping ratios at $t = 0$, which are identical with the damping ratios above, 1.07% and 3.30%, and it becomes clear now why they were called "minimum damping ratios". With equation (9.31) the peaks of the sinusoidal power consumption are constant, so that the maximum allowed power consumption is always fully utilised.
Figures 9.7 and 9.8 show y_G for the case where the damping ratios of the two reaction wheels are computed with equation (9.32) and the corresponding damping ratio β_1 for Link1. Note that only by coincidence the results in figures 9.6 and 9.7 are almost identical.

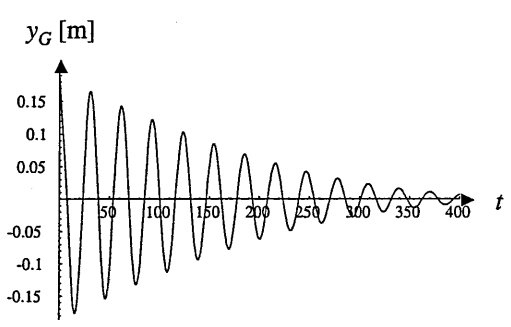

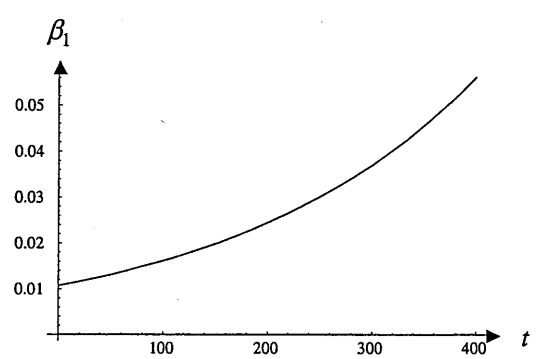

Figures 9.7 and 9.8: y_G and β_1 for time dependent feedback gains (= damping ratios)

In the present configuration it takes 370 seconds to damp the vibration amplitude down to 1 cm, thus the vibrations are damped out faster than with 5% constant damping for the two links, see figure 9.6, while the maximum allowed power

consumption is not exceeded.
In practice the feedback gains can be computed on-line so as not to exceed the maximum allowed power consumption.
It is seen from the above results that with relatively small reaction wheels and a moderate power consumption, the damp out time for the present example is reduced by a factor 5.02, when using the time dependent feedback gains. The additional size of the reaction wheels can still be reduced for example by mounting two identical discs on one axis on either side of the two main SRMS links, which would also avoid asymmetry, and by making them thicker but with smaller diameter (note that the example RW thickness is only 3.19 cm). Thus the additional size could be optimised. The additional mass of the reaction wheels does not affect the SRMS performance, and the change in the dynamic responses due to the additional RW masses is negligibly small with 0.16% in the present case, as mentioned.
However in practice the SRMS would oscillate also out-of-plane, giving rise to the necessity of mounting yet another reaction wheel on each flexible link tip whose axis is perpendicular to that of the first so as to be able to damp out vibrations in all directions. Thus with increasing complexity and space taken up by such an active control system in the SRMS payload bay, the implementation of such a system is less and less practical. The best active control systems would probably use piezoelectric strain gauges that are light and do practically not take up any space.
With the results above we are now able to assess the method of improved passive damping by using constrained viscoelastic layers on the SRMS main links as proposed in [70]. The authors state that the achievable additional damping ratio for the low- frequency modes is about 2.2% for the whole SRMS system. According to [70] the total weight increase due to the additional layers is only 2.47% of the momentary SRMS weight, and considering the other advantages like power independence and practically no increase in size, this method seems to be feasible, simple, easily realisable and of great benefit.
A maximum increased damping ratio could be achieved by using an active damping system together with the constrained layer method. This is also proposed in [70].

9.5 SUMMARY

The present section examines the feasibility of active damping using reaction wheels (RW) and collocated sensors. A literature search reveals that although there exist many papers dealing with active damping control of flexible manipulators, such as [13], [14], [15], [16], [19], [24], [56], [58], [59] and many more, most of the works only deal with single link systems, and most of the works propose control schemes using the joint drives themselves to damp out elastic vibrations. Apparently only very few works deal with the use of reaction wheels or other inertia actuators for active damping control of flexible manipulators, for example [20] and [51].
In view of the results presented in chapter 7 however, it becomes clear that in the case of the SRMS the dynamic response to SRMS slew manoeuvres is very small for all joint configurations and payloads, and assuming a minimum SRMS damping ratio of 1% with [1] and [70], active damping control seems to be unnecessary for these cases. Only the configuration with all joints locked or with only the wrist joint unlocked and the end effector perpendicular to the straight SRMS, see figure 9.2, lead to elastic

vibration amplitudes that make active damping control desirable, when the Shuttle control thrusters are fired.
Therefore control schemes for the SRMS as proposed for example in [5], [9] or [69] seem to be superfluous. Also the question arises how elastic vibrations with an amplitude smaller than the end effector positioning precision of the SRMS, being ± 5.08 cm ([3]), can be actively damped out with the existing SRMS joint drives. Furthermore it is assumed that the proposed control schemes would rapidly cause wear and fatigue of the joint gear boxes, bearings and so on, and gear backlash and other nonlinearities would probably present additional problems, and this control method has apparently not been used in current Shuttle missions. For active damping control of space manipulators comparable to the SRMS, [8] also proposes the use of collocated actuators / sensors instead of the joint drives.
Another method to improve damping ratios of the SRMS is to use additional constrained viscoelastic layers , attached to the two SRMS main links. This method is presented in [70], and the given figures indicate that the method is feasible, simple, easily realisable, probably cheap, not affecting the present size of the SRMS, and of considerable benefit. Furthermore the layer method would be power independent, and the additional weight, according to the authors, would only be 2.47% of the present SRMS weight. However, the layer method alone may not assumed to be sufficient, but it can be used together with an active damping control system, as proposed by the authors.
For the proposed method of using collocated reaction wheels and sensors to provide velocity feedback, the SRMS / Shuttle system is proven to be stable, in agreement with the findings of [61], [62] and [65]. An example shows that the structural SRMS damping, which is assumed to be a minimum of 1% ([1], [70]), is sufficient to quickly damp out the typical elastic vibrations due to a SRMS slew manoeuvre. For the worst case of Shuttle thruster firing and the SRMS in the straight configuration with all joints locked and with the maximum payload, the second example shows that the waiting time for the vibrations to damp down to a vibration amplitude of 1 cm is about 30 minutes with only structural damping.
The application of reaction wheels with constant feedback gains lead to temporarily very high power consumption of the reaction wheels, if additional damping ratios of 4% or more for the two SRMS main links are desired. The best way is to make the feedback gains time dependent, which leads to a better utilisation of a maximum allowed power consumption. With this method and using two relatively small reaction wheels and allowing for a moderate power consumption, the damping ratios of the two main links can be improved so that for the presented worst case example the damp out time can be reduced by a factor 5.024, which is a considerable improvement. The design of the reaction wheels can be optimised in view of desired damping ratios, weight and size. The additional masses of the RW do not affect the performance of the SRMS and change its dynamic responses only to a negligibly small degree. However, the proposed method would make the installation of additional hardware and software necessary, and if vibrations of the SRMS in all directions is considered, as in reality, another reaction wheel would have to be mounted at each flexible link tip, with its axis perpendicular to the axis of the first wheel. Thus the problems with this control scheme seem to become very large, and other actuators like piezoelectric strain gauges seem preferable.

CHAPTER 10: PAYLOAD CAPTURING AND EMERGENCY BRAKING

A literature survey sheds little light on the problem of payload capturing or the consequences of an emergency braking with a sudden application of the joint locks of the SRMS while holding a payload. Of all the available literature on space manipulators similar to the SRMS apparently only [69] deals with the simulation of a payload capturing sequence of a flexible RMS with rigid or flexible payloads.
This chapter presents some simulations and a simple method of estimating the elastic deflections of the RMS due to payload capturing or emergency braking.

10.1 END EFFECTOR DESIGN

Here we only consider the design of the Shuttle Remote Manipulator System, since literature on possible end effector designs other than that of the SRMS can apparently not be found.
Picture 10.1 shows the SRMS end effector design together with some designations.

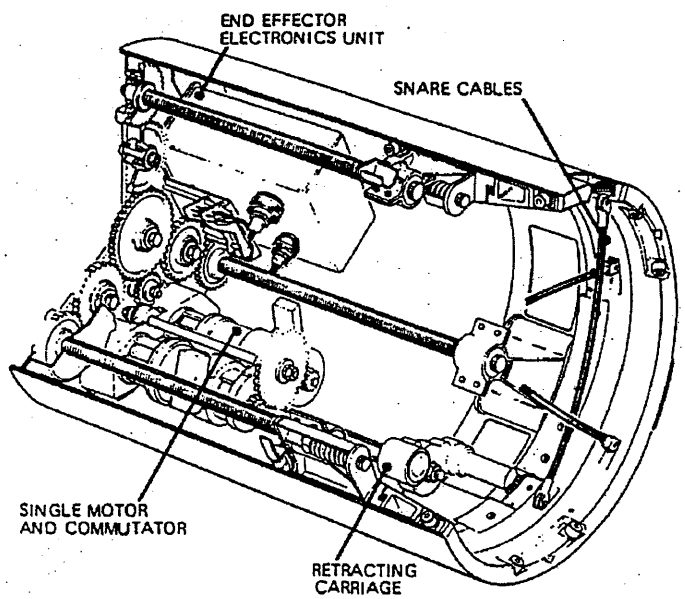

Figure 10.1: Cut away view of the SRMS end effector ([3])

The function of the end effector is to grapple the payload and to secure it to the SRMS. To this end the payload has a so-called standard grapple shaft, which is basically a short bar with a head. When the payload shaft is surrounded by the end effector, its three snare cables close like the aperture of a camera, and the head on the shaft prevents its sliding back. Once the snare cables have closed around the shaft, they are pulled back into the end effector until the base plate of the shaft has full contact with the end effector.
It is noted that the SRMS literature does not report any flexibility between the end effector and the payload, and the connection is commonly taken as rigid.
Figure 10.2 shows the capturing and "rigidising" sequence of the SRMS end effector.

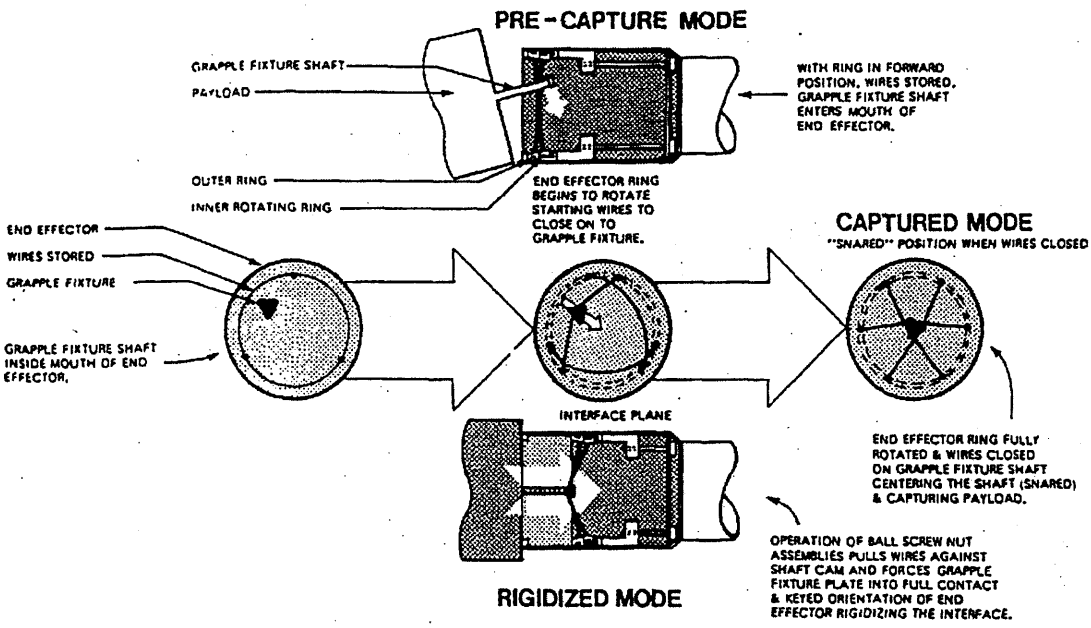

Figure 10.2: Capturing and "rigidising" sequence of the SRMS end effector ([3])

From figures 10.1 and 10.2 and the previous explanations it is clear that capturing a payload with the SRMS standard end effector takes some time and the payload will not be rigidised to the SRMS instantly, but the available data give no idea of how long the sequence shown above may take in practice.
It becomes clear however that the relative velocity between the payload and the end effector must be very small, otherwise it is probably impossible to perform the sequence shown above with the necessary accuracy or in time before the payload bounces off or the grapple shaft is in a position which makes rigidising impossible.

10.2 PAYLOAD CAPTURING SCENARIO

Since the Shuttle / SRMS system and the payload are free to move in space, the velocity vector of the payload relative to the Shuttle at the beginning of the capturing sequence can theoretically have an infinite number of directions and magnitudes. However, in practice the directions and especially the magnitudes of the relative velocity vector will be restricted to avoid overload of the SRMS and to prevent a collision of the payload with the Shuttle.
Also the joints of the SRMS can either be locked or unlocked. Unlocked joints will lead to negligibly small elastic deflections of the SRMS and allow for utilisation of the joint motors and the natural joint friction to dynamically decelerate the payload to a standstill. On the other hand unlocked joints give rise to the risk that the payload can not be decelerated quickly enough, thus driving one or more SRMS links to a mechanical stop or even causing collision with the Shuttle.
No information can be found in the literature about this aspect, and it is therefore assumed that in order to create a maximum of safety, the joints are always locked while capturing a payload. This assumption automatically yields worst case scenarios in view of the elastic deflections of the RMS.

Since it is not assumed feasible to model the complete payload capturing sequence of the end effector, the grappling sequence will be taken as instantaneous. This agrees with the assumption of [69], apparently the only paper available on capturing dynamics with flexible links.
Figure 10.3 shows two possible initial configurations for a payload capturing simulation.

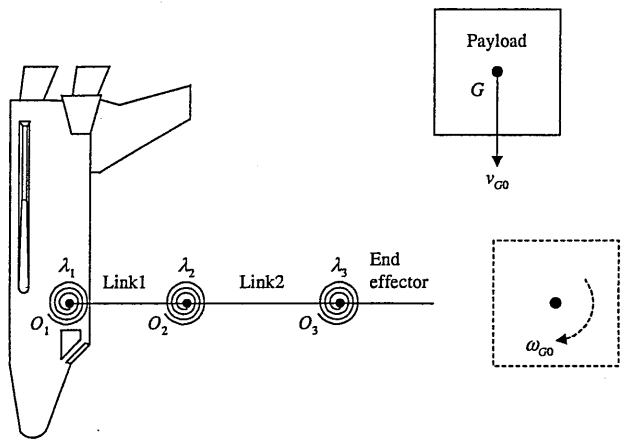

Figure 10.3: Two possible initial configurations for payload capturing simulation

We consider (1) the payload flying perpendicular to the straight RMS with an initial velocity v_{Gi}, crossing the end effector, and (2) the payload initially rotating at angular velocity ω_{Gi} about its centre of mass G with zero translation when being grappled.

10.3 VARIOUS METHODS OF COMPUTING THE DYNAMIC RESPONSE

Obviously the simplest way to perform a payload capturing simulation is to insert a new joint between the end effector tip and the payload. With this joint, the payload can then be given its desired initial rotatory and translatory velocities, and the grappling can be simulated either by locking the joint degrees of freedom or by using very stiff springs so as to effectively produce a rigid connection between the payload and the end effector, when the distance between the payload surface and the end effector is zero. The method of stiff springs, with high damping ratio to avoid unnecessary computational burdens, is used for the SIMPACK model, with which the reference results are calculated for the following simulations.
By contrast, [69] uses the conservation law of generalised momenta to substitute the unknown impact forces due to the payload initial velocities and thus to compute the payload velocities after the impact. In view of the number of necessary calculations to finally obtain the desired results it is questionable if the proposed method is preferable to an additional joint. [69] also proposes a control scheme using the joint motors to damp out the vibrations arising from the capture impact. The impracticality of such control schemes was discussed earlier.
It is noted however that due to the complexity even in SIMPACK, only two of the ten available integration methods are stable when performing the present simulations with the described method of using stiff springs. Thus to have a quick and safe tool for estimating the dynamic response, the following method is introduced.

10.4 MAXIMUM RESPONSE ESTIMATION METHOD

The following method to estimate maximum responses is presented here to have some reference to results obtained with professional software.
The method is based on the fact that the total energy of the system is conserved. Thus the inertial kinetic energy of the payload is transformed into kinetic and potential energy of the whole Shuttle / SRMS / payload system.
It is also noted that if we let the system eigenmodes vibrate with a certain amount of energy, that is if the sum of the potential and kinetic energy is one fixed value for each mode, then the elastic deflections, or the deflections of the masses, is maximum in the fundamental mode, second greatest in the second mode and so on.
The idea is now to let the fundamental mode vibrate with the whole energy initially provided by the payload initial rotatory and translatory velocity, giving an upper limit for the elastic deflections of the RMS in response to payload capture. This is equivalent to the assumption that the whole initial payload kinetic energy is converted into vibrations in the fundamental mode.
The payload initial kinetic energy E_0 is given by

$$E_0 = \tfrac{1}{2} M_p v_{G0}^2 + \tfrac{1}{2} I_p \omega_{G0}^2 \tag{10.1}$$

Equations (7.8) and (7.9) give the system matrices **M** and **K** for an RMS with all joints locked and free floating base or Shuttle. For a fixed RMS base the system matrices are obtained by deleting the rows and columns representing the Shuttle degrees of freedom in equations (7.8) and (7.9). Using equation (7.11) and the notation of previous chapters, a modal decomposition for the first non-zero mode in the absence of external forces and damping yields

$$m_1 \ddot{p}_1 + k_1 p_1 = 0 \tag{10.2}$$

with m_1 and k_1 being the generalised mass and stiffness of the first vibration mode. The system kinetic and potential energy E_S in the fundamental mode is

$$E_S = \tfrac{1}{2} m_1 \dot{p}^2 + \tfrac{1}{2} k_1 p^2 \tag{10.3}$$

From equation (10.3) it is clear that the maximum modal coordinate $p_1 = p_{1,\max}$, occurs when $\dot{p}(t) = 0$. Thus since

$$E_S \overset{!}{=} E_0 \tag{10.4}$$

we have

$$p_{1,\max} = \sqrt{\frac{2E_0}{k_1}} \tag{10.5}$$

Using the kinematics of the double flexible link RMS system with end effector and with fixed or free base or Shuttle as derived in chapters 5 and 6, in the present case of

a straight RMS the deflection y_G of G relative to the free Shuttle or the fixed RMS base is

$$y_G = p_1[(L_2 + L_3 + a)W_1'(L_1) + W_1(L_1) + (L_3 + a)W_2'(L_2) + W_2(L_2) + \Delta\bar{\theta}_2(L_3 + a) + \Delta\bar{\theta}_1(L_1 + L_2 + L_3 + a)] \quad (10.6)$$

where $W_1(x_1)$ and $W_2(x_2)$ are the first exact mode shape for Link1 and Link2 and where $\Delta\bar{\theta}_1$ and $\Delta\bar{\theta}_2$ are given in chapters 5 and 6 and can be calculated with the respective determinants for each mode. Insertion of the maximum of the generalised modal coordinate from equation (10.5) gives

$$y_{G,\max} = p_{1,\max}[...] \quad (10.7)$$

As stated before, equations (10.1) through (10.7) always give an upper limit for y_G. It will be shown subsequently that except for the case of a fixed RMS base and a payload initial rotary velocity, equation (10.7) gives good estimates of the elastic deflections.

10.5 EXAMPLE SIMULATIONS OF PAYLOAD CAPTURING

The following examples consider the RMS elastic deflections due to sudden grappling of a payload. To give ideas of the upper limits of the deflections, we always consider the worst case of the straight RMS with all joints locked and with the maximum SRMS payload for the data in data sets (B) and (C) from chapters 5 and 6 are used for the fix and free RMS base.
It is noted that the figures used may be too large, especially the payload initial rotary velocity, which in reality could prevent a proper payload grappling. Smaller initial payload velocities yield smaller vibration amplitudes, and an unlocked joint also yields very small vibration amplitudes comparable to the dynamic responses due to a RMS slew manoeuvre as presented in chapter 7. Note also that the assumption of an instant payload grappling probably yields bigger dynamic responses than the real rigidising sequence shown in figure 10.2.

10.5.1 LINEARLY MOVING PAYLOAD

We consider the case of a linearly moving payload, suddenly being grappled by the straight RMS as shown in figure 10.3. The initial payload velocity is estimated to be v_{G0} = 0.02 m/s, since [7] states that the maximum allowed velocity of a 15000 kg payload relative to the Shuttle is 0.03 m/s prior to capturing.

Free base results

For the free Shuttle, SIMPACK yields an elastic vibration amplitude of 4.67 cm of the payload centre of mass G relative to the Shuttle. The upper limit calculation using equations (10.1) through (10.8) yields 4.43 cm.
As explained before, the maximum response estimation method gives always results that are equal or bigger than the real results. The reason why in the present case the SIMPACK results are bigger is due to the fact that in SMIPACK three mode shapes of a cantilever beam are used for each of the two flexible links. Although the convergence of the fundamental frequency towards the exact value is very good, see table 6.4, it is known that for assumed mode shapes the elastic deflections can still deviate from the real values even if the natural frequencies are already close to the exact values ([62], [65], [66], [67], [68]), as mentioned in chapter 2.8.2. It is inferred that here such a deviation due to assumed mode shapes is the reason for the difference in the two results. However, the dimension of the result is clearly confirmed.

Fixed base results

For a RMS with fixed base the SIMPACK simulation yields a vibration amplitude y_G of 10.06 cm, by contrast to the maximum response estimation method result of 10.84 cm. Again the results are in reasonable agreement, confirming the dimension of the deflections.
The good agreement between the SIMPACK and the maximum response method results for both the fixed and the free RMS base indicates that in the present example the biggest part of the initial payload kinetic energy is transformed into kinetic and potential energy in the fundamental mode.

10.5.2 ROTATING PAYLOAD

Now we consider the case of a payload rotating stationary with an angular velocity ω_{G0} when suddenly being grappled by the straight RMS with all joints locked, see figure 10.3. The payload initial angular velocity is chosen to be ω_{G0} = 0.008333 rad/s, a figure used in [69]. This value corresponds to 0.5 revolutions per minute.

Free base results

In the case of a RMS with free base or Shuttle, SIMPACK gives a vibration amplitude for y_G of 6.72 cm. The result obtained with the maximum response estimation method is 6.74 cm, and thus in very close agreement.

Fixed base results

For the fixed base RMS the simulation with SIMPACK gives a y_G vibration with an

amplitude of 5.93 cm. The corresponding result obtained with the maximum response method is 16.49 cm.
It is seen that only for this case the two results are not in good agreement. The reason is that only in this case the response of the second mode is considerable, compared with the response in the first mode. Therefore the result obtained with the maximum response method is far too great. Assuming however that the SIMPACK result is approximately exact, one can compute a correction factor to allow for the fact that only a part of the initial payload kinetic energy is transformed into vibrations in the fundamental mode. In the present example the correction factor would be 5.93 / 16.49 = 0.36.
Computing the correction factor for a couple of payload mass cases would allow for setting up an interpolation curve covering the whole range of payload masses.

10.6 EMERGENCY BRAKING OF RMS

Finally we consider the case of an emergency braking of the RMS while slewing a payload. In a Lagrangian formulation, the simulation can be performed using springs with very high stiffness λ_b (b = 1, 2, 3) with typical values of 10^{10} Nm/rad or so and high damping to reduce the computation time between the links. These springs would be activated if the angle between the links reach a desired value. This is analogous to the method mentioned before for the payload / end effector connection for payload grappling simulations.
For the worst case we assume that the two flexible main links and the rigid end effector are moving with the maximum allowed joint velocities, that all brakes are applied simultaneously when the RMS is straight, and that the RMS is holding the maximum payload, using the data from data sets (B) and (C).
The simulation in SIMPACK is identical to the simulation of a payload grappling, only that the payload initial velocities are different in the present case.
According to [7], the translatory and angular maximum velocities of the SRMS are 3 cm/s and 0.238 deg/s respectively for a 30000 kg payload. Using these figures for the payload initial velocities we have v_{G0} = 0.03 m/s and ω_{G0} = 0.004154 rad/s, and for the maximum response estimation method the payload initial kinetic energy computed with equation (10.1) is E_0 = 17 Nm.

Free base results

For the RMS with free base or Shuttle, the emergency braking simulation performed with SIMPACK yields a vibration amplitude y_G of the payload centre of mass G relative to the Shuttle of 9.20 cm. The maximum response estimation method yields a vibration with an amplitude of 7.46 cm.
Similar to the simulation of the grappling of a linearly moving payload with free RMS base, see section 10.5.1 above, SIMPACK gives a slightly bigger vibration amplitude than the maximum response estimation method. As explained before, this is due to the fact that in SIMPACK the assumed mode shape approximation is used, which does not allow for an exact a priori assessment of the convergence of the

elastic deflections. It is found that other mode shapes, for example those of a pinned-pinned beam, and other numbers of mode shapes yield different results, although the convergence of the natural frequencies is always very good.
However, the dimension of the result is clearly confirmed.

Fixed base results

For the fixed base RMS the SIMPACK result is 15.08 cm for the vibration amplitude of the payload centre of mass relative to the base, and the maximum response estimation method gives 18.25 cm. The results are in reasonable agreement, thus confirming that in the present case the payload initial kinetic energy is mainly transformed into vibrations in the fundamental mode.
It is seen that the case of emergency braking yields dynamic responses that are comparable to those arising due to Shuttle thruster firing. Thus these two scenarios produce the biggest RMS vibration amplitudes.
It is noted that the SRMS is designed with the ability to stop the end effector within 0.6 m from the maximum allowed speed under all payload conditions ([7]). Therefore it is inferred that the cases in which emergency braking is the only possibility are very rare, and the SRMS related literature does not report that the emergency braking mode has ever been used.
For the present case, which gives the biggest vibration amplitudes, the results for a small payload are given for comparison. Therefore we let M_p = 1000 kg, I_p = 166.667 kgm^2 and $a = b/2$ = 0.5 m. The other data are as above. Using [7], the maximum initial translatory and rotatory velocities of the payload are estimated to be v_{G0} = 0.1 m/s and ω_{G0} = 0.0174533 rad/s, which using equation (10.1) gives an initial kinetic energy of E_0 = 5.03 Nm.
With these data, the maximum response estimation method gives a vibration amplitude of the payload centre of mass G relative to the base of 8.63 cm, and the corresponding SIMPACK result is 8.11 cm. This shows that with decreasing payload mass, the absolute and relative error between the SIMPACK result, which is assumed to be fairly accurate, and the maximum response estimation method also decreases.

10.7 SUMMARY

This chapter deals with the problem of RMS payload grappling and the dynamic response to a sudden application of the joint brakes in the case of emergency braking during a slew manoeuvre. The problem of emergency braking is apparently not addressed in the SRMS related literature, and only [69] deals with the problem of payload grappling. Since the whole sequence of "rigidising" the payload to the end effector, see figure 10.2, cannot be modelled sufficiently accurate, the grappling is assumed to take place instantaneously, in agreement with [69]. This assumption does not devalue the results, since it gives dynamic responses that are at least equal or greater than reality, thus providing a worst case scenario.
An additional joint between the end effector and payload in a Lagrangian formulation allows for an initial payload rotary and / or translatory velocity relative to the end

effector or RMS. The rigid connection between the end effector and the payload can be modelled using very stiff springs (typical value 10^{10}) and very high damping ratios to reduce the computational burden. These springs would be activated when the payload has the desired distance to the end effector, which in the present case is zero. This method of using stiff and highly damped springs to imitate time or state dependent rigid connections is known from extended use of professional software packages ([66], [67], [68]).
It turns out that MATHEMATICA cannot be used for the simulations, since the integration step size becomes so small at the beginning of the simulation that the computation times are unacceptable with the provided hardware. Also of the ten integrators available in SIMPACK, only two are stable and sufficiently efficient to obtain results in a reasonable amount of time.
To obtain an idea of the maximum dynamic response due to payload grappling or emergency braking an estimation method is introduced that will give dynamic response results that are always bigger than in reality, thus providing an upper limit for elastic deflections.
The basis of the maximum response method is to consider only the dominant fundamental mode vibration with an energy equivalent to the payload initial kinetic energy. Thus contributions of the higher modes to the maximum response as discussed in earlier chapters are considered negligibly small. Since in reality also the modes higher than the fundamental will always be excited, albeit to a minute degree, this will give the aforementioned upper limit for the elastic deflections.
It is found that except for the case of a fixed RMS base and only an initial rotatory payload velocity, the maximum response method gives results in good agreement with the SIMPACK simulations. The reason why only for the aforementioned case the maximum response result can be up to three times greater than the SIMPACK result, depending on the payload case, is the fact that only for this case the second mode is excited to a non-negligible degree, thus leading to elastic deflections considerably smaller than obtained with the maximum response method.
To get better estimates for this RMS configuration, correction factors can be computed, and a series of correction factors would allow for setting up of an interpolation curve giving the necessary correction factors for the whole payload range.
Using the SRMS data and initial payload translatory and rotatory velocities v_{G0} and ω_{G0} at its centre of mass G of 0.02 m/s and 0.008333 rad/s (corresponding to 0.5 revolutions per minute, a figure proposed in [69]), the amplitudes of vibration of G relative to the Shuttle or fixed RMS base for the worst case of maximum payload mass and straight RMS are typically smaller than 10 cm.
The worst case scenario for an emergency braking is the simultaneous application of all RMS joint brakes while slewing the maximum payload mass with the maximum allowed rotatory and translatory velocities when the RMS is straight. With the SRMS data, this scenario yields vibration amplitudes of G relative to the Shuttle or the fixed base of about 8 cm and 16 cm, respectively.
The main advantage of the maximum response estimation method is its very fast computation, since the differential equations of motion do not have to be solved, but the result can be obtained purely analytically with very few calculation steps.

In view of the achievable agreement with the SIMPACK results, which are assumed to be close to the exact values, and the ratio of computation times needed by SIMPACK and the maximum response estimation method, the proposed method appears to be very efficient and sufficiently accurate.

CHAPTER 11: SPACE STATION / MRMS INTERACTION

The assembly and maintenance of the International Space Station (ISS) after completion will be performed using the Mobile Remote Manipulator System (MRMS) and its Mobile Transporter (MT). Figure 11.1 shows the ISS in its completed state and the *xyz* reference frame used in this section.

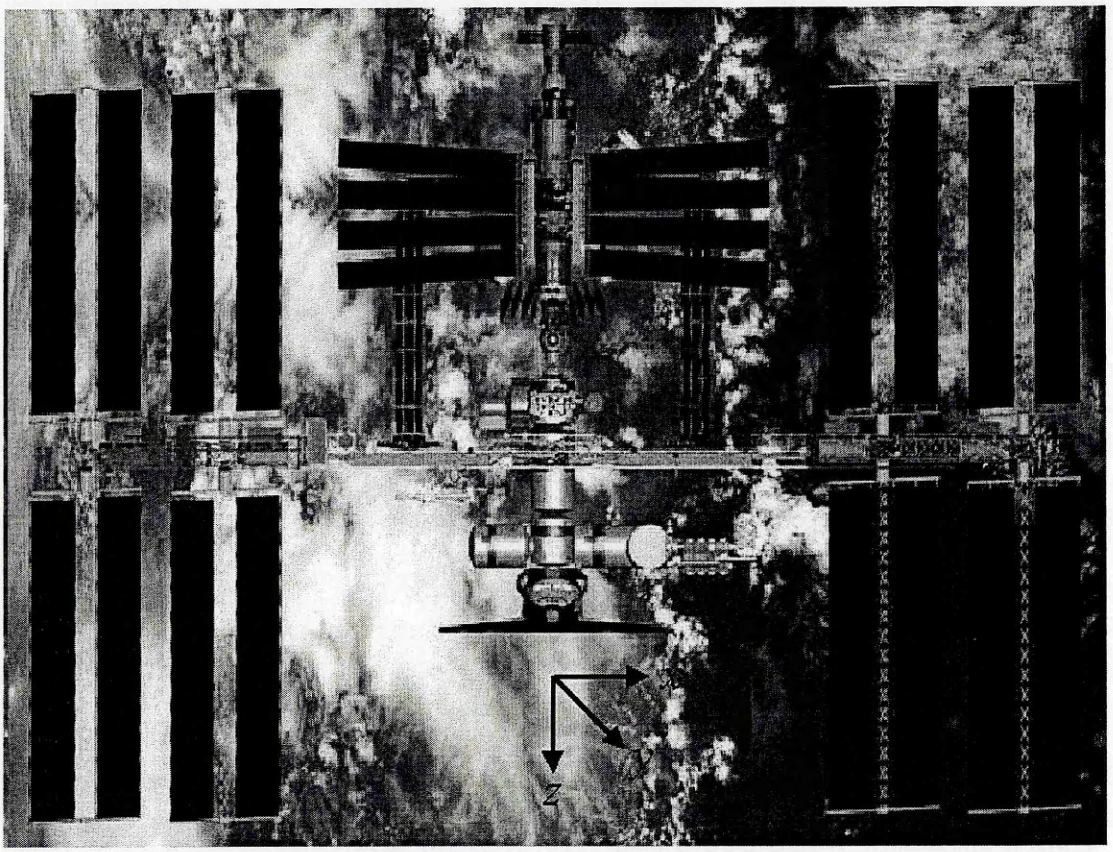

Figure 11.1: The International Space Station

Payloads of 15000 kg and more can be manoeuvred about the two main articulated joints of the robot as well as translated along the main truss beam. The MT track is along the main truss of the ISS, facing the reader, in figure 11.1. Thus for large payloads and different locations on the truss and different configurations of the robot arms, a wide range of moments of inertia for the space station can exist. This aspect alone poses many problems involving multi-body interaction of concern for the space station control system design. The interaction of vibration modes is also of concern.
The interaction problem has been considered by [74], taking account of a rigid space station structure and rigid robot manipulator. Numerous papers on control of a rigid space station using control momentum gyros (CMG) exist, for instance [75].
The effect of flexural modes on the main truss and solar panels for example has received much less attention, being a much more complex problem, which has been addressed by [76]. It is shown that there are many appendage and framework modes below 12.6 rad/s (2 Hz), in particular a solar array mode at 0.63 rad/s (0.1 Hz) exists with negligible main truss motion and the fundamental main truss mode occurs at

1.26 rad/s (0.2 Hz). In [76] the dynamics of the ISS are represented by 101 elastic modes and 6 rigid-body modes. A three axis attitude control system using CMG's with attitude and rate signals was used to orientate the station in [76]. To attenuate the effect of low frequency elastic mode feedback, low pass first order lag filters were used in the compensated control system. A simultaneous command of attitude change of 1° about each axis was studied. The uncompensated closed-loop control system gave a flexural response at the outer solar array tip of about ± 4 m, being reduced to about 1 m when compensation was included. The most prominent modes to be excited were at 0.63 rad/s (0.1 Hz) and 4.59 rad/s (0.73 Hz), the former being antisymmetric solar array modes and the second being due to torsion of the main truss. Thus [76] illustrates the importance of minimising flexural mode response due to attitude changes from say, thrusters, Shuttle docking or CMG torques. Such vibrations may be detrimental to experiments involving micro-gravity, crystal growth or biology, and dynamic response, of say the solar arrays, could lead to structural damage and fatigue.

The influence of flexural modes on the attitude stability of a generic space station main truss, with its local axis along the local horizon, has been studied in [77] and [78].

It is therefore concluded that the effect of a translating, slewing robotic manipulator, either rigid or flexible on a flexible space station has not been reported in the open literature. On the completed ISS it may still be necessary to manoeuvre the MRMS along the main truss with various payloads, thereby creating rigid body and flexural motion. Clearly a rigorous study of the complete problem is extremely complex and could be investigated by various flexible multi-body computer programmes.

Motion of the MRMS along the main truss in a fixed configuration, say perpendicular to the truss will produce time varying moments of inertia of the space station. Here the shoulder joint is expected to be locked with brakes on, leading to flexible joints. During acceleration and deceleration of the MT transient forces on the flexible robot arm with payload, will lead to rigid body and flexural motion of the truss.

A similar result will arise for a stationary MT with the robot arm performing various slews with say the shoulder joint free and the elbow locked. Since the back torque from the slew torque motor will be negligibly small, due to the high reduction gear ratio, it will be the reaction force on the truss that causes vibration, particularly when the robot arm is nearly parallel to the boom.

In view of the complexity of a space station with six rigid body degrees of freedom and many elastic modes, solution with the coupled robot arm, rigid or flexible, is a formidable problem. Therefore considerable simplification is required to gain insight on the influence of MRMS motion on space station dynamics.

[74] shows that the MT performs bang-bang accelerations of 2.2×10^{-4} m/s^2, which is expected to produce very small torques on the supporting main truss. Such small vibrations will not lead to structural problems but could have detrimental effects on micro-gravity experiments. For this reason alone such vibrations are worthy of study.

Note that the following analyses neglect any damping of the MRMS and the space station, which would not significantly reduce the initial maximum vibration levels due to the step input excitations, but which would minimise their effect over time.

Also note that in the following, the offset of the MRMS base from the main truss centre axis due to the physical size of the truss and MT is neglected.

11.1 SIMPLIFIED DYNAMIC MODEL OF FLEXIBLE SPACE STATION

To simplify the actual ISS configuration in figure 11.1 we consider two approximate dynamic models (1) and (2) shown in figures 11.2 and 11.3.

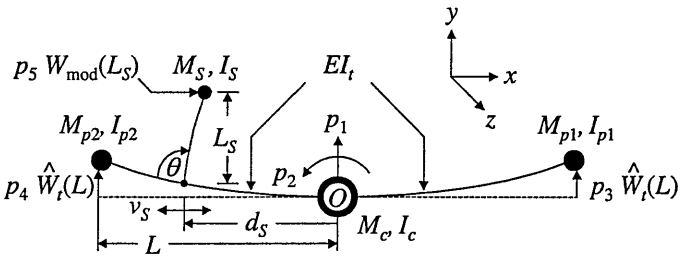

Figure 11.2: Simplified dynamic model (1)

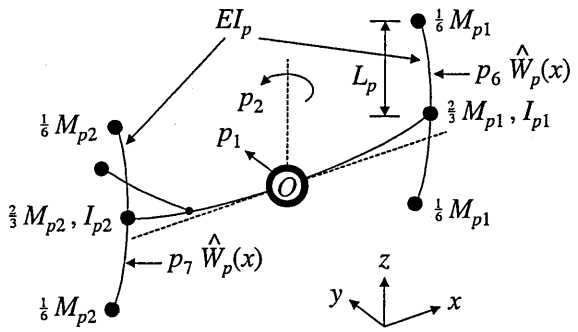

Figure 11.3: Simplified dynamic model (2)

Vibration of the main truss is modelled by the elastic degrees of freedom $p_3 \hat{W}_t(x)$ and $p_4 \hat{W}_t(x)$, allowing for the first symmetric and anti-symmetric truss vibration modes. The mode shape of each half of the truss is assumed to be identical despite the fact that due to the MRMS being positioned on one side of the truss, the masses and rotary inertias on the two truss halves are different. With the MRMS perpendicular to the truss, its payload mass M_S and effective rotary inertia about its root are directly transferred to the truss at distance d_S from O. However, the choice of one degree of freedom for each half of the truss should allow for the mass asymmetry. Since the two truss halves are cantilevered relative to the central cluster, the mode shape defined by equation (2.69) is used. The truss halves of length L have a flexural stiffness EI_t.
[21] states that the MRMS is of similar design to the SRMS and that the two articulated MRMS arms have a total length of 17 m. Therefore we use the SRMS properties given in the previous chapters together with the desired payload properties M_S and I_S and perform a modal decomposition for the fundamental mode, yielding amongst others the modal stiffness k_{mod} and exact modal mode shape $W_{\mathrm{mod}}(x)$.
The simpler model (1) in figure 11.2 assumes that the solar arrays are rigid, having masses M_{pi} and moments of inertia I_{pi}. The five degrees of freedom of this model are:

- p_1: rigid body translation of station central cluster with mass M_c in Oy direction
- p_2: rigid body rotation of central cluster with rotary inertia I_c about Oz direction
- p_3 and p_4: elastic deflections of the two main truss halves in Oy direction
- p_5: elastic deflection of MRMS in the fundamental mode.

Model (2) in figure 11.3 allows for the two extra degrees of freedom p_6 and p_7 due to solar array flexibility, thus giving a total of seven degrees of freedom. The two halves of each solar array are modelled for simplicity as single cantilever beams fixed to the outer booms at the centre of the four arrays with flexural stiffness EI_p. Therefore the mode shape of each half of one solar array is also approximated using the mode shape in equation (2.69), where L is replaced by L_p, the length of one half of one solar array as shown in figure 11.3. Noting that the distributed mass m of a flexible cantilever beam can be represented by $\frac{1}{3}m$ at its tip ([41]), see also equation (7.7) in chapter 7.1, we choose the tip mass of each half of one solar array to be one third of half the total array mass, or $\frac{1}{3}\times\frac{1}{2}M_{pi} = \frac{1}{6}M_{pi}$, and since in both models the mass and moment of inertia of the solar arrays at the main truss ends should be equal we choose the masses at the main truss ends to be $\frac{2}{3}M_{pi}$ with moments of inertia I_{pi}. Note also that since we only allow for one flexible degree of freedom for each complete solar array, the two identical halves of each solar array effectively yield a factor 2 in the kinetic and potential energy expressions for the respective degrees of freedom.
Note that the mobile transporter (MT) traverses along the truss in a crab-like manner with constant acceleration / deceleration over each truss section of length d_t ([74]). This is to avoid excessive build up of velocity, which could be dangerous if the MT brakes failed. Thus a bang-bang acceleration $\pm\, a_S(t)$ gives a velocity profile $v_S(t) = a_S(t)\, t$, which increases linearly to a maximum at the mid-point of a truss section and then decreases linearly to zero at the end of the section. The time t_m to section mid-point is thus $t_m = \sqrt{d_t / a_S(t)}$. Thus the function of the MT position $d_S(t)$ during the acceleration phase ($0 \le t \le t_m$) is given by $d_S(t) = d_0 \pm \frac{1}{2}a_S(t)t^2$, and during the deceleration phase ($t_m \le t \le 2\ t_m$) by $d_S(t) = d_0 \pm \left[\frac{1}{2}d_t + \frac{1}{2}a_S(t)\left(t - t_m\right)^2\right]$. With these equations the time histories of $v_S(t)$ and $d_S(t)$ can be computed and inserted into the kinetic energy expression for Lagrange's equation. Collecting the terms with respect to the MT velocity $v_S(t)$ and formally differentiating $v_S(t)$ with respect to time, which yields $a_S(t)$, will furthermore give the exciting force coefficients, which are multiplied by $a_S(t)$ to give the elements of the generalised force vector. This however assumes a prescribed motion of the MT along the main truss without any coupling with the various vibrations (in particular those of the MRMS), which may be approximately the case if the MT is driven for example by high reduction gear systems, but available literature does not give details of the MT drive system. With $d_S = d_S(t)$ for brevity and neglecting the distributed masses of the main truss and the MRMS, the total kinetic energy expression for model (2) for a MT translation simulation is

$$
\begin{aligned}
T = {} & \tfrac{1}{2}M_c\,\dot{p}_1^2 + \tfrac{1}{2}I_c\,\dot{p}_2^2 + \tfrac{1}{3}M_{p1}\left[\dot{p}_1 + \dot{p}_2 L + \dot{p}_3 \hat{W}_t(L)\right]^2 + \tfrac{1}{2}I_{p1}\left[\dot{p}_2 + \dot{p}_3 \hat{W}_t'(L)\right]^2 + \\
& \tfrac{1}{6}M_{p1}\left[\dot{p}_1 + \dot{p}_2 L + \dot{p}_3 \hat{W}_t(L) + \dot{p}_6 \hat{W}_p(L_p)\right]^2 + \tfrac{1}{3}M_{p2}\left[\dot{p}_1 - \dot{p}_2 L + \dot{p}_4 \hat{W}_t(L)\right]^2 + \\
& \tfrac{1}{6}M_{p2}\left[\dot{p}_1 + \dot{p}_2 L + \dot{p}_4 \hat{W}_t(L) + \dot{p}_7 \hat{W}_p(L_p)\right]^2 + \tfrac{1}{2}I_{p2}\left[\dot{p}_2 - \dot{p}_4 \hat{W}_t'(L)\right]^2 + \\
& \tfrac{1}{2}M_S\left[\dot{p}_1 - \dot{p}_2 d_S + \dot{p}_4 \hat{W}_t(d_S)\right]^2 + \tfrac{1}{2}I_S\left[\dot{p}_2 - \dot{p}_4 \hat{W}_t'(d_S) - \dot{p}_5 W'_{\mathrm{mod}}(L_S)\right]^2 + \\
& \tfrac{1}{2}M_S\left[\dot{p}_5 W_{\mathrm{mod}}(L_S) - \dot{p}_2 L_S + \dot{p}_4 \hat{W}_t'(d_S) L_S + v_S(t)\right]^2
\end{aligned}
\qquad (11.1)
$$

where the first M_S term gives the payload velocity components in y and the second in x. Applying Lagrange's equation yields the equations of motion for model (2) with the 7×7 mass matrix elements M_{nm}, where for sake of brevity we let again $d_S = d_S(t)$.

$$
\begin{aligned}
M_{11} &= M_c + M_{p1} + M_{p2} + M_S \\
M_{12} = M_{21} &= L\left(M_{p1} - M_{p2}\right) - d_S M_S \\
M_{13} = M_{31} &= M_{p1} \hat{W}_t(L) \\
M_{14} = M_{41} &= M_S \hat{W}_t(d_S) + M_{p2} \hat{W}_t(L) \\
M_{15} = M_{51} &= 0 \\
M_{16} = M_{61} &= \tfrac{1}{3} M_{p1} \hat{W}_p(L_p) \\
M_{17} = M_{71} &= \tfrac{1}{3} M_{p1} \hat{W}_p(L_p) \\
M_{22} &= I_c + I_{p1} + I_{p2} + I_S + L^2\left(M_{p1} + M_{p2}\right) + \left(L_S^2 + d_S^2\right) M_S \\
M_{23} = M_{32} &= L M_{p1} \hat{W}_t(L) + I_{p1} \hat{W}_t'(L) \\
M_{24} = M_{42} &= -d_S M_S \hat{W}_t(d_S) - L M_{p2} \hat{W}_t(L) - \left(I_S + L_S^2 M_S\right) \hat{W}_t'(d_S) - I_{p2} \hat{W}_t'(L) \\
M_{25} = M_{52} &= -I_S W'_{\mathrm{mod}}(L_S) - L_S M_S W_{\mathrm{mod}}(L_S) \\
M_{26} = M_{62} &= \tfrac{1}{3} L M_{p1} \hat{W}_p(L_p) \\
M_{27} = M_{72} &= \tfrac{1}{3} L M_{p1} \hat{W}_p(L_p) \\
M_{33} &= M_{p1} \left[\hat{W}_t(L)\right]^2 + I_{p1} \left[\hat{W}_t'(L)\right]^2 \\
M_{34} = M_{43} &= 0 \\
M_{35} = M_{53} &= 0 \\
M_{36} = M_{63} &= \tfrac{1}{3} M_{p1} \hat{W}_p(L_p) \hat{W}_t(L) \\
M_{37} = M_{73} &= 0 \\
M_{44} &= M_S \left[\hat{W}_t(d_S)\right]^2 + M_{p2} \left[\hat{W}_t(L)\right]^2 + \left(I_S + L_S^2 M_S\right) \left[\hat{W}_t'(d_S)\right]^2 + I_{p2} \left[\hat{W}_t'(L)\right]^2 \\
M_{45} = M_{54} &= \hat{W}_t'(d_S) \left[I_S W'_{\mathrm{mod}}(L_S) + L_S M_S W_{\mathrm{mod}}(L_S)\right] \\
M_{46} = M_{64} &= 0 \\
M_{47} = M_{74} &= \tfrac{1}{3} M_{p2} \hat{W}_p(L_p) \hat{W}_t(L) \\
M_{55} &= M_S \left[W_{\mathrm{mod}}(L_S)\right]^2 + I_S \left[W'_{\mathrm{mod}}(L_S)\right]^2 \\
M_{56} = M_{65} &= 0 \\
M_{57} = M_{75} &= 0 \\
M_{66} &= \tfrac{1}{3} M_{p1} \left[\hat{W}_p(L_p)\right]^2 \\
M_{67} = M_{76} &= 0 \\
M_{77} &= \tfrac{1}{3} M_{p2} \left[\hat{W}_p(L_p)\right]^2
\end{aligned}
\tag{11.2}
$$

The elements of the 7×7 stiffness matrix **K** for model (2) due to flexural stiffnesses EI_t of the main truss halves, EI_p of the solar panel arrays and the MRMS are

$$\begin{aligned} K_{33} &= K_{44} = EI_t \int_0^L \left[\hat{W}_t''(x)\right]^2 \mathrm{d}x \ \text{(truss)} \\ K_{55} &= k_{\mathrm{mod}} \ \text{(MRMS)} \\ K_{66} &= K_{77} = 2EI_p \int_0^{L_p} \left[\hat{W}_p''(x)\right]^2 \mathrm{d}x \ \text{(solar arrays)} \\ K_{nm} &= 0 \quad \text{else} \end{aligned} \tag{11.3}$$

where k_{mod} denotes the modal stiffness in the fundamental mode of the straight RMS with the desired payload, all joints locked and fixed base.
The generalised force vector is obtained by collecting the terms remaining after applying Lagrange's equation to the kinetic energy with respect to the MT bang-bang acceleration $a_S(t)$, which gives the 7×1 generalised force vector **P** as

$$\mathbf{P} = a_S(t)\left\{0, -L_S M_S, 0, L_S M_S \hat{W}_t'(d_S(t)), M_S W_{\mathrm{mod}}(L_S), 0, 0\right\}^{\mathrm{T}} \tag{11.4}$$

To obtain the equations of motion for model (1) for a MT translation the sixth and seventh rows and columns, corresponding to the flexible degrees of freedom of the two solar arrays, are deleted in the mass and stiffness matrices **M** and **K** in equations (11.2) and (11.3), together with the sixth and seventh element in the generalised force vector **P** in equation (11.4)
For the simulation of the rotational or slew manoeuvre about the shoulder joint with d_S = constant, we note that due to the previous analyses of the RMS it can be assumed that the flexible dynamic response of the similar MRMS is negligibly small with an unlocked shoulder joint and allows for the assumption of a rigid MRMS. Also note that torques are not transmitted through unlocked joints, so that the effective rotary inertia of the MRMS and the payload about the MRMS root on the main truss has no influence on the other space station degrees of freedom. Thus for the slew manoeuvre the MRMS elastic degree of freedom can be deleted, and the equations of motion for model (1) and (2) are obtained by taking the respective equations of motion for the MT translation, striking the fifth row and column in the mass and stiffness matrices and letting $I_S = L_S = 0$ in the mass matrix. Note that d_S is now a constant. To obtain the generalised force we assume the worst scenario of a slew about the MRMS shoulder joint with the straight MRMS initially parallel to the main truss, so that the reaction force F_0 is perpendicular to the truss, hence

$$F_0 = \ddot{\theta} L_S M_S = \frac{M_0 L_S M_S}{I_S + M_S L_S^2} \tag{11.5}$$

where $\ddot{\theta}$ is the MRMS angular acceleration due to the shoulder joint torque M_0. Since the MRMS design is similar to the SRMS, the reaction torques at a driven and thus unlocked joint are negligibly small due to the high gear ratios. Thus the generalised

force vector for model (2) for the slew manoeuvre simulation is

$$\mathbf{P} = \left\{0,0,0,F_0\,\hat{W}_t(d_S)\cos\theta,0,0\right\}^{\mathrm{T}} \tag{11.6}$$

where, according to the above explanations, **P** has only six elements since the MRMS elastic degree of freedom is deleted, and where θ is the MRMS angle relative to the truss. For model (1), the generalised force vector is obtained from equation (11.6) by deleting the fifth and sixth element, which after deleting the MRMS degree of freedom correspond to the elastic degrees of freedom of the two solar panel arrays.

11.2 RESULTS

The necessary data for the simulations are taken from or estimated using [76] and [80] and are as follows.
(Solar panels) $M_{p1} = M_{p2} = 2.1\times10^4$ kg , $I_{p1} = I_{p2} = 7\times10^6$ kgm^2, $L_p = 31.6$ m, (central cluster) $M_c = 1.48\times10^5$ kg, $I_c = 2.28\times10^7$ kgm^2, and $L = 40$ m. With these data, the total rotary inertia of the space station (without the RMS and payload) about the axis Oz of the rigid body degree of freedom q_2 is 1.04×10^8 kgm^2, thus being in exact agreement with the corresponding value given in [76]. EI_t and EI_p are computed to give a fundamental frequency of 0.63 rad/s mainly due to solar array bending modes, and also so as to give a fundamental truss natural frequency of 1.26 rad/s, in exact agreement with the corresponding values in [76]. Thus $EI_t = 6.8\times10^8$ Nm^2 and $EI_p = 1.4\times10^7$ Nm^2.

MT translation

Figure 11.4 shows the bang-bang acceleration / deceleration profile of the MT over one main truss bay as given in [74].

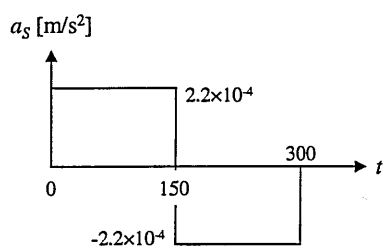

Figure 11.4: MT acceleration / deceleration profile over one bay ([74])

With the MT kinematic equations given in the text above, the length of one bay can be calculated from figure 11.4 to be $d_t = 5$ m. For the worst case we assume a MRMS payload with $M_S = 30000$ kg, $I_S = 4\times10^5$ kgm^2 (about G), and $L_S = 17.5$ m, which could represent a large component of a new space structure to be stored temporarily on the ISS prior to construction, say a Mars mission vehicle component. Also, since the dynamic response of the main truss will be maximum for a torque input at the maximum slope, we let $d_0 = 35$ m, which is as close to the left hand truss extremity as

possible with the data given in [76] and [80]. Note that due to the sign convention of the mode shapes, the acceleration $a_S(t)$ has a positive sign, but the MT motion is subtracted from d_0. Figures 11.5 and 11.6 show the time history of $\ddot{p}_1$, the rigid body translatory acceleration of the central cluster, for model (1) and model (2).

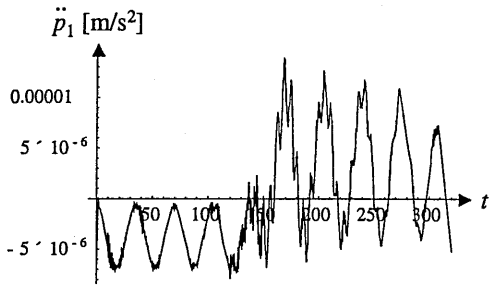

Figure 11.5: $\ddot{p}_1$ for model (1) MT translation

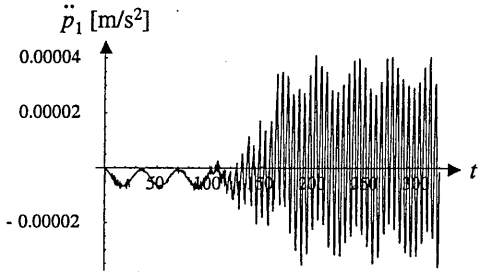

Figure 11.6: $\ddot{p}_1$ for model (2) MT translation

Figures 11.5 and 11.6 show that the higher modes are also excited to a visible level. The maximum absolute value in model (1) occurs at t = 169.01 s and is $\ddot{p}_{1,max}$ = 1.33479×10^{-5} m/s^2, and in model (2) the maximum occurs for example at t = 268.95 s with $\ddot{p}_{1,max}$ = 4.03868×10^{-5} m/s^2. Noting that g = 9.81 m/s^2, the maximum translatory accelerations of the central cluster of the space station in model (1) and model (2) are 1.36 μg and 4.12 μg, respectively.
For a relatively small and probably more realistic payload with M_S = 1000 kg, I_S = 166.67 kgm^2, and L_S = 16 m, the maximum absolute accelerations for model (1) and model (2) are 0.84 μg and 2.76 μg, respectively.

MT emergency braking

For the simulation of a MT emergency braking the equations of motion are identical to those for the simulation of a normal MT translation, but the MT acceleration / deceleration profile differs from that shown in figure 11.4 in that the deceleration takes place in a shorter period of time but with greater magnitude. Assuming that in case of an emergency braking the deceleration phase lasts 1 second instead of 150, we have a deceleration of -0.033 m/s^2 instead of -2.2×10^{-4} m/s^2. Figure 11.7 shows the profile.

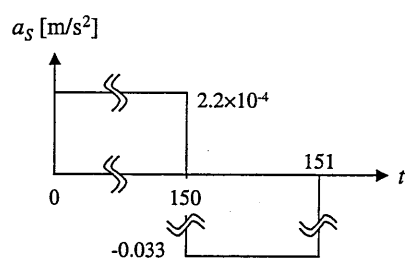

Figure 11.7: MT acceleration / deceleration profile for emergency braking case

Figures 11.8 and 11.9 show the time history of $\ddot{p}_1$ for model (1) and model (2) for M_S = 30000 kg, $I_S = 4\times10^5$ kgm^2, and L_S = 17.5 m.

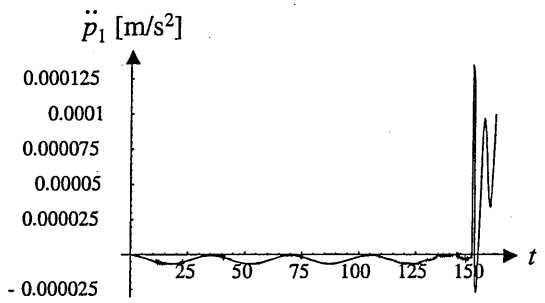

Figure 11.8: $\ddot{p}_1$ for model (1)
MT emergency braking

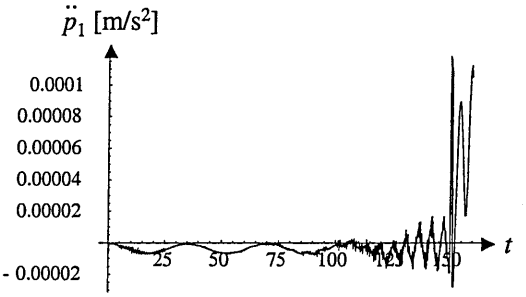

Figure 11.9: $\ddot{p}_1$ for model (2)
MT emergency braking

The absolute maxima for model (1) and model (2) are 13.78 μg and 60.25 μg, respectively.
For the 1000 kg payload case, the respective figures are 45.35 μg and 29.57 μg.

MRMS slew

For the simulation of the MRMS slew manoeuvre we calculate the generalised force in the generalised force vector **P** according to equation (11.5), where we assume an application of the maximum RMS shoulder joint torque with M_0 = 1298 Nm. For the case M_S = 30000 kg, $I_S = 4\times10^5$ kgm^2, and L_S = 17.5 m equation (11.5) then yields F_0 = 71 N. This value is inserted into equation (11.6), where d_S = 35 m is now a constant, as already stated. Taking account of the maximum allowed shoulder joint velocity of the SRMS, figure 11.10 shows the MRMS angular acceleration profile for the actual configuration for a 90° slew manoeuvre of the straight MRMS being initially parallel to the main truss.

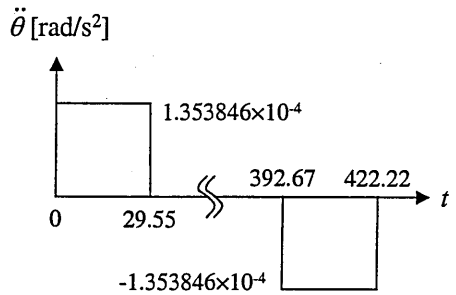

Figure 11.10: MRMS angular acceleration for maximum payload case

Note that the force F_0 in equation (11.6) has to be switched on and off, respectively, according to the acceleration as shown in figure 11.10. Figures 11.11 and 11.12 show the time histories of $\ddot{p}_1$ for model (1) and (2).

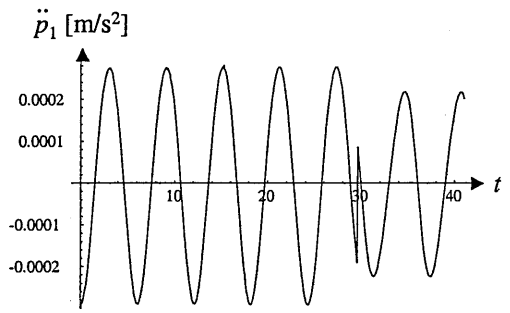

Figure 11.11: $\ddot{p}_1$ for model (1) MRMS 90° slew

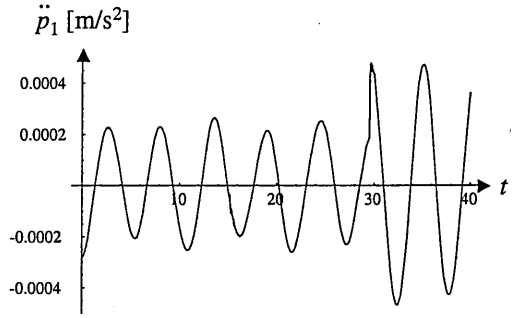

Figure 11.12: $\ddot{p}_1$ for model (2) MRMS 90° slew

Figure 11.11 shows that in model (1), only one mode is dominant, whereas in model (2) at least two modes are visible. The maximum absolute value in model (1) is 29.75 μg, and in model (2) 47.47 μg.
For the small payload case with M_S = 1000 kg, I_S = 166.67 kgm^2, and L_S = 16 m, the MRMS angular acceleration / deceleration profile differs from that for the maximum payload case shown in figure 11.10 due to the different total moment of inertia of the payload about the MRMS shoulder joint, and equation (11.5) now yields F_0 = 81 N to be inserted into equation (11.6). The profile is shown in figure 11.13, where the maximum allowed joint velocity of the RMS is again taken account of.

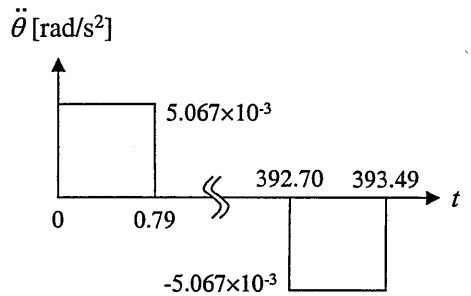

Figure 11.13: MRMS angular acceleration for small payload case

For the small payload, the maximum absolute values for the translatory acceleration of the space station central cluster in model (1) and in model (2) are 23.99 μg and 22.05 μg, respectively.
All the above results are of the same magnitude as those given in [79], but it is noted that in [79] the robot payload was very much smaller, whereas on the other hand the robot accelerations were much larger. Also the robot position was assumed stationary within the laboratory cluster. Thus due to a lack of further information, it is impossible at this point to evaluate the quality of the results presented above.
To give an idea of an acceleration of say, $1\mu G$, we refer to [79], in which it is claimed that an astronaut pushing off a wall in the space station causes disturbances of about $18\mu G$, and using the treadmill, the astronaut causes disturbances of about $750\mu G$.

11.3 SUMMARY

This chapter investigates the magnitudes of possible interactions of a space station and a manipulator, assuming properties similar to the International Space Station (ISS) and its Mobile Remote Manipulator System (MRMS).
Since the available literature on the ISS does not allow for a detailed modelling, and since this is assumed to be impossible within the boundaries of this thesis, two very much simplified dynamic models are set up to allow some initial assessments of the vibration levels to be expected. The two models differ in that in model (1) the solar panel arrays are modelled to be point masses at the end of the main truss, whereas in model (2) they are modelled as a pair of cantilever beams at the ends of the main truss.
With the simplified models, the translatory accelerations of the ISS central cluster with the laboratories and other facilities due to a MRMS normal bay to bay motion along the ISS main truss as described in [74] and due to an emergency braking during the MRMS bay to bay motion are computed for two payload cases with 30000 kg and 1000 kg, respectively. For the normal MRMS motion along one bay, the values for the central cluster acceleration in both models and with both payloads are between 1 μg and 4 μg. In the emergency braking case, the absolute maximum accelerations in model (1) for the big and small payload are about 13 μg and 45 μg, and in model (2) about 60 μg and 30 μg.
A 90° slew manoeuvre of the MRMS about the shoulder joint with the MRMS being as close to one main truss end as possible causes disturbances of typically about 26 μg in model (1) for both payload cases, and about 48 μg and 22 μg in model (2) for the big and small payload, respectively.
The magnitude of these results agree with the magnitude of the results given in [79], but it is noted that in [79] the robot is assumed to be stationary in the central cluster, holding a much smaller payload but accelerating much faster, so that the results can not directly be compared.
Due to a lack of more detailed information, the validation of the present results can not be made, but a qualitative comparison with [79] indicates that they are probably of the correct order of magnitude.
The above analyses neglect any damping of the MRMS or the ISS, which would not significantly reduce the initial maximum vibration levels due to the step input excitations, but which would in reality ensure that the vibrations amplitudes reduce to zero in time.

CHAPTER 12: SUMMARY, DISCUSSION AND RECOMMENDATIONS

Method: This thesis investigates the vibration response of a flexible space manipulator modelled on the Shuttle Remote Manipulator System (SRMS) for motion of its two main flexible links and the rigid end effector coupled to a large rigid payload, and a wide range of payloads and link configurations is considered. In contrast to research into multi-link earth based rigid robots the study of the vibration of articulated flexible space robotic systems due to rotation manoeuvres about the joints and positioning of the payload by Shuttle thruster induced motion, has not been reported widely in the literature. Also interaction effects of a slewing payload with the Space Shuttle rigid body motion does not appear in published work.
The thesis is restricted to planar motions of the SRMS in the plane of symmetry. However, the influence of a rigid straight SRMS slew on Shuttle out of plane motion in roll and surge and the influence of a Shuttle being free to move in all spatial degrees of freedom on the lateral acceleration of the payload in the inertia frame is studied.
The major contribution of this thesis consists of obtaining an exact analytical solution to the vibration modes and natural frequencies of a three-link system with two flexible links and one rigid end effector / payload, for various cases of joints locked or free. Allowance for joint flexibility and interaction with the Shuttle motion is also considered and the feasibility of using reaction wheel dampers is examined. The exact solution of the two articulated flexible beam eigenvalue problem is obtained by solving the Bernoulli beam partial differential equation for both beams using the appropriate boundary conditions at the three joints, allowing for any configuration of the SRMS. For dynamic response analyses the modelling of the SRMS / payload using the exact mode shapes has considerable advantage over the use of many assumed modes, which are necessary to get a good convergence towards the exact fundamental frequency, since inclusion of a relatively large number of assumed modes creates a large order dynamic model with increasing complexity and computational burden.
A chapter on numerical accuracy when using the proposed determinant method shows the limits of the method when the system complexity grows very large. Thus ill-conditioning of the eigenvalue determinant caused problems of incorrectly computed natural frequencies for the higher modes for the very complex systems. The difficulties appear to be due to the steepness of the determinant at the zero crossing points and due to some of the terms in the determinant dominating the others. However, since in practice only the first mode of systems with a very low fundamental frequency yields non-negligible dynamic responses, the described problems do not affect the analyses in this thesis. In this respect the accuracy of the method is rigorously validated for all the presented results and natural frequencies.
In the last chapters of this thesis, additional aspects that are rarely mentioned in other publications are addressed, namely the problem of SRMS dynamic response when capturing a satellite with relative velocity and the interaction of the MRMS with a reduced order flexible model of the ISS.

Results: One of the most important findings of this thesis is the fact that when the kinematic and dynamical boundary conditions for the SRMS flexible links and end

effector, as far as they are known and/or published, are correctly taken into account for dynamic response analyses, the vibration levels are very small with typical amplitudes of millimeters or less when one or more joints are unlocked. Only the situation all joints locked with the SRMS straight and perpendicular to the Shuttle yields vibration levels in the magnitude of centimeters or decimeters when the Shuttle thrusters are fired. This result seems to invalidate the analyses of previous researchers, because they all propose control schemes using the joint motors themselves to damp out flexible vibrations. But if the joint motors are free to revolute, as they must obviously be to act as damping actuators, the vibration levels are negligibly small, as mentioned.
In this respect the backdriveability of the SRMS joint gear trains from the output side is found to be the most important dynamical aspect for a correct formulation of the boundary conditions for the flexible links. This is because if a joint is free to revolute its backdriveability essentially leads to pinned-free boundary conditions for the flexible link connected to its output side, giving rise to only small levels of flexible vibration. It is inferred that previous researchers did not account for these facts, and, in agreement with other authors, assumed boundary conditions of a cantilever beam for the flexible links. This might be the explanation why in these papers the control aspect is stressed so much whereas the present thesis shows that except for one or two worst case scenarios, the elastic vibration levels are practically negligible.
Due to these findings it becomes clear that when an active damping control is desired, the use of additional actuators is necessary. The analyses show that the use of reaction wheels is impractical mainly due to the space taken up by the wheels in the payload bay and during operation, and piezoelectric elements would be preferable.
However, in view of the vibration levels to be generally expected it is possible that the advantage of an active damping control system (less waiting time for vibrations to damp down to an acceptable level for precision positioning) does not necessarily match the disadvantages (available space in the Shuttle cargo bay, additional hardware and software and thus increased probability of failure, increased costs, ...), and these reasons probably explain why NASA has not employed active damping on the SRMS or the Mobile Remote Manipulator System (MRMS) on the ISS.

Future work: It is recommended that the presented aspects of SRMS vibration response be the subject of future research, using simplified dynamic modelling as in this thesis for comparison with multi-body computer programmes.
Also, the problem of ill-conditioning of determinants arising from systems with very large masses and inertias constituting the dynamical boundary conditions of a slender link system is proposed for future work.

Conclusion: In conclusion this thesis presents a unique method of vibration analysis of a two-link flexible space manipulator with a third rigid link, coupled to the Space Shuttle. The aim has been an attempt to simplify the analyses and explain the basic dynamics of the system so as to be able to realistically interpret and explain the results of more complex and comprehensive multi-body programmes. It is believed that all research of this nature should follow this simplifying approach wherever possible without losing the most important features of the system.

LIST OF REFERENCES

[1] D. M. Gossain, E. Quittner, S. S. Sachdev, *Analysis and Design of the Shuttle Remote Manipulator System Mechanical Arm for Launch Dynamic Environment*, Shock and Vibration Bulletin, 1980.

[2] D. R. Dunbar, A. R. Robertson, *Graphite / Epoxy Booms for the Shuttle Remote Manipulator*, Proceedings of the 2nd International Conference on Composite Materials, April 16-20, 1978, Toronto, Canada.

[3] D. J. Hedley, *Design Characteristic and Design Feature Analysis of the Shuttle Remote Manipulator Arm*, Society of Automotive Engineers, 1987.

[4] J. A. Hunter, T. H. Ussher, D. M. Gossain, *Structural Dynamic Design of the Shuttle Remote Manipulator System*, AIAA.

[5] O. Prakash II, N. J. Adams, B. D. Appleby, *Multivariable Control of the Space Shuttle Remote Manipulator System*, AIAA Guidance, Navigation and Control Conference, August 12-14, New Orleans, Louisiana, 1991,Volume 3.

[6] P. Kumar, P. Truss, C. G. Wagner-Bartak, *System Design Features of the Space Shuttle Remote Manipulator*, Proceedings of the 5th World Congress on Theory of Machines and Mechanisms, July 1979, Montreal, Canada.

[7] R. Ravindran, K. H. Doetsch, *Design Aspects of the Shuttle Remote Manipulator Control*, American Institute of Aeronautics and Astronautics, 1982.

[8] Y. Chen, L. Meirovitch, *Control of a Flexible Space Robot Executing a Docking Maneuver*, Journal of Guidance and Control, Vol. 18, No. 4, July-August 1995.

[9] M. A. Scott, M. G. Gilbert and M. E. Demeo, *Active Vibration Damping of the Space Shuttle Remote Manipulator System*, AIAA Guidance, Navigation and Control Conference, New Orleans, August 12-14, 1991, pp.194-204.

[10] E. C. Wu, J. C. Wang, J. T. Chladek, *Fault-Tolerant Joint Development for the Space Shuttle Remote Manipulator System: Analysis and Experiment*, IEEE Transactions on Robotics and Automation, Vol. 9, No. 5, October 1993.

[11] B. Pond, I. Sharf, *Motion Planning for Flexible Manipulators*, IEEE Transactions on Robotics and Automation, 1/95, pp.2103-2108, 1995.

[12] A. Konno, M. Uchiyama, *Modeling of a Flexible Manipulator Dynamics Based upon Holzer's Model*, Proceeding of IROS, 1996.

[13] F. Matsuno, M. Tanaka, M. Ikeda, *Force and Vibration Control of a Flexible Arm Without Vibration Sensor*, Proceedings of the 33rd Conference on Decision and Control, Lake Buena Vista, Florida, December 1994.

[14] S. K. Biswas, R. D. Klafter, *Dynamic Modeling and Optimal Control of Flexible Robotic Manipulators*, IEEE paper CH2555-1/88/0000/0015, 1988.

[15] K. S. Rattan, V. Feliu, *Feedforward Control of Flexible Manipulators*, Proceedings of the 1992 IEEE International Conference on Robotics and Automation, Nice, France, May 1992.

[16] S. Yurkovich, K. L. Hillsley, A. P. Tzes, *Identification and Control for a Manipulator with Two Flexible Links*, Proceedings of the 29th Conference on Decision and Control, Honolulu, Hawaii, December 1990.

[17] S.-T. Hwang, A. Eltimsahy, *Simulation Studies on Near Minimum Time Control of Planar Flexible Manipulators with Multiple Links*, Proceedings of the 1993 IEEE / RSJ International Conference on Intelligent Robots and Systems, Yokohama, Japan, July 26-30, 1993.

[18] J. C. Doyle, K. Glover, P. P. Khargonekar, B. A. Francis, *State-Space Solutions to Standard H(2) and H(infinite) Control Problems*, IEEE Transactions on Automatic Control, Vol. 34, No. 8, August 1989.

[19] C.-W. Jen, S. Nicosia, P. Valigi, *Theoretical and Experimental Study of Dynamics and Control of a Two-Link Flexible Robot Manipulator of Revolute Joints*, IEEE paper 0-8186-7352-4/96, 1996.

[20] S. Jain and F. Khorrami, *Vibration Suppression of Unknown Flexible Payloads Using a Wrist Mounted Force/Torque Sensor for Remote Manipulator Systems*, IEEE International Conference on Robotics and Automation, 1994, Proceedings, pages 2119-2124, vol.3.

[21] D. G. Hunter, *The Space Station Freedom Special Purpose Dexterous Manipulator Arm*, IEEE paper CH3010-6/91/0371, 1991.

[22] D. K. Robertson, *Three-Dimensional Vibration Analysis of a Uniform Beam With Offset Inertial Masses at the Ends*, NASA Technical Memorandum 86393, 1985.

[23] C. J. Damaren, *Approximate Inverse Dynamics and Passive Feedback for Flexible Manipulators with Large Payloads*, IEEE paper 1042-296X/96, 1996.

[24] F. Khorrami, S. Jain, A. Tzes, W. Grossman, W. Blesser, *Nonlinear Control with Input Preshaping for Flexible-Link Manipulators*, IEEE paper 7803-0078/91/0600-0096, 1991.

[25] R. Ravindran, P. K. Nguyen, *Control of the Shuttle Remote Manipulator*, Proceedings of the 6th Canadian Congress of Applied Mechanics, Vancouver, May 29-June 3, 1977.

[26] F. Matsuno, K. Yamamoto, *Dynamic Hybrid Position / Force Control of a Flexible Manipulator*, IEEE paper 1050-4729/93, 1993.

[27] A.R. Fraser, R. W. Daniel, *Perturbation Techniques for Flexible Manipulators*, Kluwer Academic Publishers.

[28] H. B. Hablani, *Hinges-Free and Hinges-Locked Modes of Deformable Multi-Body Space Station – a Continuum Approach*, paper AIAA-87-0925-CP, AIAA Dynamics Specialist Conference, Monterey, California, April 1987.

[29] W. L. Hallauer, *Recent Literature on Experimental Structural Dynamics Control Research*, in: Mechanics and Control of Large Flexible Structures, Progress in Astronautics and Aeronautics, Vol.129, Ed. By J. L. Junkins, 1990, pp.465-489.

[30] W. J. Book, *Recursive Lagrangian Dynamics of Flexible Manipulator Arms*, The International Journal of Robotics Research, Vol.3, No.3, Fall 1984, pp.87-101.

[31] S. M. Joshi, *Robustness Properties of Colocated Controllers for Flexible Spacecraft*, AIAA Guidance, Vol.9, No.1,Jan.-Feb. 1986, pp.85-91.

[32] Jen-Kuang Huang, Li-Farn Yang and Jer-Nan Juang, *Large Planar Manoeuvres For Articulated Flexible Manipulators*, AIAA Guidance, Navigation and Control Conference, Aug.15-17, 1988, Paper 88-4119-CP, Minneapolis, USA.

[33] H. Baruh and S. S. K. Tadikonda, *Issues in the Dynamics and Control of Flexible Robot Manipulators*, AIAA J. Guidance, Vol.12, No.5, Sept.-Oct. 1989, pp.659-671.

[34] E. Garcia and D. J. Inman, *Modelling of the Slewing Control of a Flexible Structure*, J.Guidance, Vol.14, No.4, July-August 1991, pp.736-742.

[35] M. K. Kwak and L. Meirovitch, *New Approach to the Manoeuvering and Control of Flexible Multibody Systems*, Journal of Guidance, Control and Dynamics, Vol.15, No.6, November-December 1992, pp.1342-1353.

[36] L. Meirovitch and S. Lim, *Manoeuvering and Control of Flexible Space Robots*, J. Guidance, Control and Dynamics, Vol.17, No.3, May-June 1994, pp.520-528.

[37] R. Montgomery, D. Gosh, et al., *Testing of an End-Point Control Unit Designed to Enable Precision Control of Manipulator-Coupled Spacecraft*, AIAA-94-4612, AIAA Space Programmes and Technologies Conference, September 27-29,1994, Huntsville, AL, USA.

[38] C. L. Kirk and F. L. Doengi, *Closed-Loop Vibration Control of Flexible Space Shuttle Manipulator*, ACTA Astronautica Vol.32, No.9, 1994, pp.561-576.

[39] P. C. Hughes, *Dynamics of a Chain of Flexible Bodies*, The Journal of the Astronautical Sciences, Vol.27,No.4, October-December 1979, pp.359-380.

[40] P. C. Hughes, *Modal Identities for elastic Bodies, With Application to Vehicle Dynamics and Control*, Trans. ASME, Journal of Applied Mechanics, Vol.47, 1980, pp.177-184.

[41] S. Timoshenko, D. H. Young and W. Weaver, Jr., *Vibration Problems in Engineering*, 4th Ed. John Wiley and Sons, 1974, p.105.

[42] Sharf and C. Damaren, *Simulation of Flexible-Link Manipulators: Basis Functions and Nonlinear Terms in the Motion Equations*, Proceedings of the IEEE International Conference on Robotics and Automation, Nice, France, May 1992, pp.1956-61.

[43] D. M. Gossain, *Dynamics of an Articulated Structure with a High Gear Ratio Joint*, Canadian Aeronautics and Space Journal, Vol.25, No.3, 1979, pp.234-41.

[44] J. A. Hunter, T. H. Ussher and D. M. Gossain, *Structural Dynamics Considerations of the Shuttle Remote Manipulator System*, AIAA 23rd Structures, Structural Dynamics and Materials Conference, May 1982, paper 82-0762, pp.499-505.

[45] R. J. Roark, *Formulas for Stress and Strain*, p.99, case 29, McGraw-Hill Book Company, Inc.1938.

[46] L. Alder and S. Rock, *Adaptive Control of a Flexible-Link Manipulator with Unknown Payload Dynamics*, Proceedings of the 1993 American Control Conference, June 1993, pages 2088-2092.

[47] R. Schwertassek, O. Wallrapp, *Dynamik flexibler Mehrkoerpersysteme*, Friedrich Vieweg & Sohn Verlagsgesellschaft mbH, Braunschweig/ Wiesbaden, 1999.

[48] S. H. Farghaly, *Bending Vibrations of an Axially Loaded Cantilever Beam with an Elastically Mounted End Mass of Finite Length*, Journal of Sound and Vibration, Nr. 156, Vol. 2, 1992.

[49] J. C. Bruch, T. P. Mitchell, *Vibrations of a Mass-Loaded Clamped-Free Timoshenko Beam*, Journal of Sound and Vibration, Nr. 114, Vol. 2, 1987.

[50] P. A. A. Laura, J. L. Pombo, E. A. Susemihl, *A Note on the Vibrations of a Clamped-Free Beam with a Mass at the Free End*, Journal of Sound and Vibration, Nr. 37, Vol. 2, 1974.

[51] F. Khorrami, A. A. Gomez, M. D. Hills, *Utilization of Torque Wheels for Active Damping of Flexible Manipulators*, IEEE paper 1050-4729/94, 1994.

[52] Dorf (Editor), *International Encyclopaedia of Robotics*, pp. 943-963 and 1669-1683, 1988.

[53] D. Li, J. W. Zu, A. A. Goldenberg, *Dynamic Modeling and Mode Analysis of Flexible-Link, Flexible-Joint Robots*, Mechanic Machines Theory, Vol. 33, No. 7, pp.1031-1044, 1998.

[54] G.-B. Yang, M. Donath, *Dynamic Model of a One-Link Robot Manipulator with Both Structural and Joint Flexibility*, IEEE paper CH2555-1/88/0000/0476, 1988.

[55] J. P. Den Hartog, *Mechanical Vibrations*, Dover Publications Inc., New York, 1985.

[56] S. Cetinkunt, W.-L. Yu, *Accuracy of Finite Dimensional Dynamic Models of Flexible Manipulators for Controller Design*, Journal of Robotic Systems, paper CCC 0741-2223/92/030327-024, John Wiley and Sons, Inc., 1992.

[57] A. C. Aitken, *Determinants and Matrices*, Oliver and Boyd, Edinburgh and London, 1946.

[58] S. Cetinkunt, S. Wu, *Discrete-Time Tip Position Control of a Flexible One Arm Robot,* Journal of Dynamic Systems, Measurements and Control, Vol. 114, pp. 428-435, September 1992.

[59] T. Kokkinis, M. Sahraian, *Inverse Dynamics of a Flexible Robot Arm by Optimal Control*, Proceedings of the ASME Design Technical Conferences – 21st Biennial Mechanisms Conference, Chicago, Illinois, September 16-19, 1990.

[60] K. Gatland, M. Hewish, P. Wright, *The Space Shuttle Handbook*, Sackett Publishing Services Ltd., London, 1979.

[61] J. L. Junkins, H. Schaub, *Analytical Mechanics of Aerospace Systems*, 1999.

[62] J. L. Junkins, Y.Kim, *Introduction to Dynamics and Control of Flexible Structures*, Washington D.C.: AIAA Education Series, 1993.

[63] S. Dubowsky, E. Vance, M. Torres, *The Control of Space Manipulators Subject to Spacecraft Attitude Control Saturation Limits*, Proceedings of the NASA Conference on Space Telerobotics, Jet Propulsion Lab., Pasadena, CA., 1989.

[64] E. Barbieri, S. P. Kenny, *Nonlinear Modelling of a Long Flexible Manipulator and Control by Inertia Devices*, IEEE, 11th American Control Conference, Chicago, 1992 ACC/TAU, pp.1695-1699.

[65] L. Meirovitch, *Dynamics and Control of Structures*, John Wiley & Sons, 1990.

[66] O. Wallrapp, S. Wiedemann, *Deployment of Flexible Satellite Solar Array*, 4th International Conference on Dynamics and Control of Structures in Space, Cranfield University Press, Cranfield, May 1999.

[67] S. Wiedemann, *Entfaltanalyse Solargenerator unter Beruecksichtigung von Elastizitaeten mit SIMPACK*, Munich, 1999.

[68] O. Wallrapp, S. Wiedemann, *Simulation of Deployment of a Flexible Solar Array*, NATO Advanced Workshop, Pultusk, Poland, July 2-7, 2000.

[69] X. Cyril, A. K. Misra, M. Ingham, G. J. Jaar, *Postcapture Dynamics of a Spacecraft-Manipulator-Payload System*, Journal of Guidance, Control and Dynamics, Vol. 23, No. 1, January-February 2000.

[70] T. E. Alberts, H. Xia, Y. Chen, *Dynamic Analysis to Evaluate Viscoelastic Passive Damping Augmentation for the Space Shuttle Remote Manipulator System*, Journal of Dynamic Systems, Measurement and Control, September 1992, Vol.114, pp. 468-475.

[71] L. Collatz, *Differentialgleichungen*, B. G. Teubner, Stuttgart, 1981.

[72] O. Verlinden, P. Dehombreux, C. Conti, *New Component Modes for Flexible Multibody Systems*, Proceedings of the Design Engineering Technical Conferences, DETC, September 14-17, 1997, Sacramento, California.

[73] A. A. Shabana, *Resonance Conditions and Deformable Body Coordinate Systems*, Journal of Sound and Vibration, No. 192 (1), pp. 389-398, 1996.

[74] Wie, Hu, S. N. Singh, *Multi-body Interaction Effects on Space Station Attitude Control and Momentum Management*, Journal of Guidance and Control, Vol.13, No. 6, Nov.- Dec. 1990, pp. 993-999.

[75] S. N. Singh, T. C. Bossart, *Feedback Linearisation and Nonlinear Ultimate Boundness Control of the Space Station Using CMG*, Guidance, Navigation and Control Conference, Portland, Oregon, August 20-22, 1990, pp 369-376.

[76] T. R. Sutter, P. A. Cooper, J. W. Young, *Dynamic and Control Characteristics of a Reference Space Station Configuration*, AIAA International Space Station Conference, Williamsburg, Virginia, April 21-22, 1988, technical paper A88-31376-12-18.

[77] P. M. Bainum, V. K. Kumar, *Dynamics of a Flexible Body in Orbit, Journal of Guidance and Control*, Engineering Note, No. 3, pp 90-92, 1980.

[78] P. M. Bainum, V. K. Kumar, *Dynamics of Orbiting Flexible Beams and Platforms in Horizontal Orientation*, ACTA Astronautica, Vol. 9, No. 3, pp 119-127, 1982.

[79] J. H. Miller, C. Lawrence, D. A. Rohn, *The Dynamic Effects of Internal Robots on Space Station Freedom*, Guidance, Navigation and Control Conference, New Orleans, April 12-14, 1991, paper no. AIAA-91-2822-CP.

[80] L. DeRyder, P. Troutman, M. Heck, *The Impact of Asymmetric Physical Properties on Large Space Structures*, AIAA International Space Station Conference, Williamsburg, Virginia, April 21-22, 1988.

[81] J. W. S. Rayleigh, *The Theory of Sound*, Dover Publications, New York, 1945.

[82] C. L. Kirk, S. M. Wiedemann, *Natural Frequencies and Mode Shapes of a Free-free Beam With Large End Masses*, submitted, Journal of Sound and Vibration, 2001.

[83] O. Wallrapp, *Beam – A Pre-processor for Mode Shape Analysis of Straight Beam Structures and Generation of the SID File for MBS Codes*, User Manual, INTEC GmbH, Wessling, Report Version 3.0, March 1994.